Quantum effects in two-dimensional nanostructures

Adrián Ceferino

A thesis submitted to the University of Manchester for the degree of Doctor of Philosophy in the Faculty of Science and Engineering

School of Physics and Astronomy

2021

Contents

Word count: 57180

List of Figures

List of Tables

The University of Manchester

Adrián Ceferino

Doctor of Philosophy

Quantum effects in two-dimensional nanostructures

Two-dimensional van der Waals semiconductors have emerged as one of the most promising class of materials in the field of nanoelectronics. Among them, InSe has excelled in providing all the requirements needed for technological applications, demonstrating superior flexibility[1, 2, 3], ambient stability[4] and exceptional band gap tunability[5, 6, 7, 8]. In this thesis, we explore using $\mathbf{k} \cdot \mathbf{p}$ and tight-binding calculations, a plethora of quantum effects observed in few-layer InSe and we analyse transverse magnetic focusing data measured in twisted bilayer graphene.

We studied the intersubband energy dependence on the number of layers and the applied electric field in the lowest conduction subband of multilayer InSe. From the subband energies, we extracted the intersubband optical absorption properties of n-doped InSe. Using a quantum well model, the intersubband energies in the conduction band were found to range in the infrared and far-infrared part of the optical spectrum. The dependence on the electric field was self-consistently calculated for the different number of layers and an analytical expression for the intersubband optical absorption coefficient was derived using the Fermi golden rule.

Using the self-consistent algorithm previously developed to study the intersubband energy dependence on the applied electric field, the spin-orbit coupling (SOC) strength in the bottommost conduction subband was calculated at different applied displacement fields. The calculations performed were complemented with density functional theory (DFT) studies of ferroelectric charge transfer[9] in InSe which indicated a very weak ferroelectric contribution to the overall SOC strength. Finally, our calculated SOC strengths were compared with those extracted from weak antilocalization measurements in a dual-gated device. We found a very good agreement between our theoretical predictions and the experimental data.

We used the quantum harmonic oscillator basis to calculate the excitonic dispersion in InSe films ranging from the monolayer to the bulk limit. Both the excitonic dispersion and the binding energies in different film thicknesses were calculated taking into account the sombrero dispersion in the valence band. The effect of such band flatness was to generate a minimum in the excitonic dispersion at a finite centre of mass momentum which vanishes with an increasing number of layers[10]. When the InSe film thickness surpasses the six-layer limit, a transition from a dark to a bright exciton was predicted. The proposed procedure was demonstrated to be effective to calculate the excitonic binding energies in any van der Waals heterostructure[11, 12] using an extension of the proposed procedure.

Finally, we demonstrated how magnetic focusing can be used to probe the band structure of any 2D material. This technique was used to investigate the band structure profile of twisted bilayer graphene, where the application of an externally applied electric field generates a visible minivalley splitting.

BLANK PAGE

Declaration of originality

I hereby confirm that no portion of the work referred to in the thesis has been submitted in support of an application for another degree or qualification of this or any other university or other institute of learning.

Copyright statement

1. The author of this thesis (including any appendices and/or schedules to this thesis) owns certain copyright or related rights in it (the "Copyright") and s/he has given The University of Manchester certain rights to use such Copyright, including for administrative purposes.

2. Copies of this thesis, either in full or in extracts and whether in hard or electronic copy, may be made *only* in accordance with the Copyright, Designs and Patents Act 1988 (as amended) and regulations issued under it or, where appropriate, in accordance with licensing agreements which the University has from time to time. This page must form part of any such copies made.

3. The ownership of certain Copyright, patents, designs, trademarks and other intellectual property (the "Intellectual Property") and any reproductions of copyright works in the thesis, for example graphs and tables ("Reproductions"), which may be described in this thesis, may not be owned by the author and may be owned by third parties. Such Intellectual Property and Reproductions cannot and must not be made available for use without the prior written permission of the owner(s) of the relevant Intellectual Property and/or Reproductions.

4. Further information on the conditions under which disclosure, publication and commercialisation of this thesis, the Copyright and any Intellectual Property and/or Reproductions described in it may take place is available in the University IP Policy (see `http://documents.manchester.ac.uk/DocuInfo.aspx?DocID=24420`), in any relevant Thesis restriction declarations deposited in the University Library, The University Library's regulations (see `http://www.library.manchester.ac.uk/about/regulations/`) and in The University's policy on Presentation of Theses.

Acknowledgements

Firstly, I would like to thank my PhD supervisor Prof.Vladimir I. Fal'ko for giving me the chance to work on such an exciting project and for his mentoring. I would also like to acknowledge my colleague and collaborator Kok Wee Song for his deep understanding and advice during most of my doctorate. I am also grateful to Samuel Magorrian and Viktor Zólyomi for their DFT calculations necessary for Chapters 3,4 and 5 as well as their wide and valuable expertise in the computational modelling of InSe. I am also thankful to Vladimir Enaldiev, David Ruiz-Tijerina and Sergey Slizovskiy, for all their valuable knowledge and experience. I would also like to acknowledge the two talented experimentalists Denis A. Bandurin and Alexey Berdyugin with whom I had the honour to collaborate. Moreover, I would like to thank Irina V.Grigorieva and Amalia Patanè for their feedback on the manuscript on SOC in InSe. I also want to thank my colleagues Charlotte Bull, Lee Hague, Aitor García Fuentes, Harry Waring, Johanna Zultak, Lucas Mogg, James Howarth and Julien Barrier for their invaluable support and company during my entire PhD. Finally, I would like to thank as well my advisor Mark Hughes for his priceless recommendations and general support during my PhD.

Chapter 1

Introduction

The family of post-transition metal monochalcogenides (InSe and GaSe) has recently been a primary focus of attention in the 2D materials scientific community[13, 14] due to their unique optical and transport properties[6]. These materials are capable of not only transitioning from an indirect to direct band gap[15, 16] in increasing the number of layers or in applying strain[17] but they have also shown a large modulation in their spin-orbit coupling strength with the applied electric field, the number of layers, and crystal stacking[18, 19]. In addition to that, their superior flexibility[20, 21], ambient condition stability[4] and tunable intersubband energy in the infrared (IR) and far-infrared (FIR) part of the optical spectrum, makes them a very promising family of materials for optoelectronic applications such as tunnelling devices, light-emitting diodes, or quantum cascade lasers[22, 23, 24]. Finally, the very flat valence band in these materials strongly enhances the electron-electron[25] and electron-phonon[26] interaction, making *p*-doped InSe and GaSe very interesting platforms to study strongly correlated physics[15].

In few-layer InSe, the intersubband energy splitting in the conduction band is uniquely determined by the degree of confinement of the particle along the sample growth direction. Consequently, one can model the formation of energy subbands using a quantum well model and calculate the intersubband energies from the quantised energy levels. The most straightforward mechanism to externally control the intersubband energies and the optical absorption peaks due to such subbands is by applying a perpendicular electric field. An electric field would not only enhance the oscillator strength between the different subbands but also enlarge the number of electrons participating in the process of optical absorption. Finally, the thermal broadening in the absorption peaks can be studied at different applied electric fields.

The very large and layer-number-dependent SOC both in the conduction and

in the valence band of few-layer InSe makes this material a very interesting candidate for spintronic device applications with the possibility to control its SOC with the number of layers, stacking and applied displacement field. Using the previously discussed quantum well model, the intrinsic SOC strength due to the lack of inversion symmetry in γ-stacked InSe can be analytically computed from the discretised values of k_z in this approximate framework. Furthermore, as the applied displacement field can either enhance or counteract the overall $z \to -z$ asymmetry of the electron's wavefunction, InSe permits fabricating devices with vanishing SOC at sufficiently large applied displacement fields.

From the interband optics viewpoint, InSe has the rather peculiar characteristic of an indirect to direct band gap transition when the number of layers is increased from the monolayer to the bulk limit[6]. This is due to the large wavevector mismatch (of the order of 0.2Å^{-1} in monolayer InSe) between the lowest energy point in the conduction band and the highest energy point in the top of the valence band, resulting in a significant suppression of the recombination probability. In addition to this unique dark to bright exciton transition in the 2D limit, recently, bulk InSe excitons have displayed an exotic 2D to 3D crossover due to its very high effective mass anisotropy resulting in an unconventional sequence of photoluminescence peaks and surprising stability of the exciton bound state at very high temperatures[27]. In addition to the many exotic properties of InSe, the combination of InSe with other 2D materials also has promising applications in the realm of optics, with the possibility to create direct Γ-point excitons in hBN-encapsulated InSe/TMDs heterostructures[28] when appropriately engineered.

This thesis is aimed at providing a coherent and consistent explanation of a wide realm of optical and transport phenomena due to the interplay between quantum confinement, strong spin-orbit coupling and the unique sombrero dispersion present in the topmost valence band of multilayer InSe. Using the tight-binding[29] and $\mathbf{k} \cdot \mathbf{p}$ models previously developed[30], a complete theoretical description often supported by *ab initio* calculations is available for both theorist and experimentalists working on this field of research. The first chapter of this thesis is devoted to an introductory overview of the analytical tools necessary to understand the

content of this investigation. Chapters 3-6 are presented starting from an introductory description of the material under consideration and followed by a scientific manuscript on each topic. An additional supplementary material subsection is added to clarify and support any relevant claim made in each manuscript. Finally, a conclusion stating the most relevant results and the prospects of this field of research is presented. The chapters of this thesis are therefore organised as follows:

Chapter 2

Chapter 2 provides a general overview of the crystalline structure and the orbital composition of few-layer InSe. The SOC properties of monolayer InSe are also discussed with a particular emphasis on its effect in the interband optical selection rules. The 14-band hybrid $\mathbf{k} \cdot \mathbf{p}$ tight-binding Hamiltonian used for this investigation is also presented.

Chapter 3

In Chapter 3 a self-consistent analysis of multilayer InSe under an applied displacement field is presented and its impact on the intersubband optical absorption is studied. The application of an electric field is demonstrated to have an interesting role to manipulate the optical absorption properties of this material as it modifies both the number of states participating in the process of optical absorption and the resonant frequencies.

Chapter 4

In Chapter 4 the spin-orbit coupling (SOC) strength in multilayer InSe was calculated for various multilayer systems at different applied displacement fields. Its magnitude was compared with the SOC strengths extracted from weak antilocalization measurements.

Chapter 5

In Chapter 5 the exciton dispersion and binding energies calculated for various

hBN-encapsulated InSe thin films are presented. A crossover from an indirect to direct exciton was predicted when the number of InSe layers exceeded 6-7 layers. In bulk InSe, a similar direct to indirect transition was found when the exciton acquired a finite centre of mass momentum in the z-direction. Additionally, using the method presented we calculated binding energies in suspended TMDs and in TMD heterostructures.

Chapter 6

In Chapter 6 the technique of magnetic focusing is presented and it is shown how it can be used to probe the Fermi surface of twisted bilayer graphene under an applied displacement field. By changing both the displacement field and the perpendicularly applied magnetic field, both the shape and the radius of the cyclotron orbits were hugely altered. In twisted bilayer graphene, this technique allowed us to observe valley-split currents due to an opposite shift in the energies at the two different **K**-points.

Chapter 7

In this final chapter, a summary of the main conclusions of this investigation is presented and the main results are highlighted. A particular emphasis is put on the potential optoelectronic applications of this investigation and the prospects of this field of research.

Chapter 2

Background and Theory

2.1 Crystalline structure of two-dimensional InSe

To fully understand the optoelectronic properties of any 2D material, the first step is to consider the symmetries present in the crystal structure as well as their dynamical symmetries such as invariance under time-reversal. Such symmetries dictate any conserved quantity the system may have such as topologically invariant quantities or the presence of spin-split bands. The constraints imposed by the crystal symmetries were studied in monolayer transition metal dichalcogenides (TMDs)[31, 32] allowing to formulate a $\mathbf{k} \cdot \mathbf{p}$ Hamiltonian around the $\mathbf{K}$ and $\mathbf{K}'$ points. Similarly, a very systematic analysis of the broken symmetries in monolayer graphene allowed to predict the form of the spin-split bands in a very wide realm of different situations combining both tight-binding calculations and group theory considerations[33].

Monolayer InSe is an element of the family of the post-transition metal monochalcogenides with point group symmetry D_{3h}. This implies a 3-fold rotational symmetry along its vertical axis and a mirror-plane symmetry with respect to the central plane of the monolayer (see Fig.2.1). Its primitive lattice vectors are given by $\vec{a}_1 = a(1, 0)$ and $\vec{a}_2 = \frac{a}{2}(1, \sqrt{3})$, where $a = 3.95$Å is the length of the hexagonal side conforming the unit cell in real space (see Fig.2.1). Given the hexagonal unit cell of the crystal, a Brillouin zone defined by the vectors $\vec{b}_1 = \frac{2\pi}{a}(1, \frac{-1}{\sqrt{3}})$ and $\vec{b}_2 = \frac{2\pi}{a}(0, \frac{2}{\sqrt{3}})$ is expected. Twelve symmetry elements characterise the D_{3h} point group, among them, the three most relevant are the C_3 rotational symmetry, the σ_h mirror plane reflection symmetry along the central xy-plane and the three reflections along the three major axes. As shown in Section. 2.2, the lack of inversion symmetry ($\vec{\mathbf{r}} \to -\vec{\mathbf{r}}$) in monolayer InSe crucially determines the presence of spin-split bands in its band structure.

In going from monolayer to multilayer InSe, the crystal stacking most often

reduces the symmetries previously present in the monolayer form. Three different stackings are most commonly found in InSe multilayer structures: γ, ε and β stackings, with their atomic distribution along the unit cell shown in Fig.2.1. Among them, γ-stacked InSe is the most stable configuration, although recent studies[18] have demonstrated a large presence of stacking faults in γ-stacked InSe multilayers when grown by the Bridgman method[36, 37]. In addition to the very common stacking fault defects which may alter the overall symmetry of the crystal, InSe is also a very sensitive material to point-like defects such as adatoms and vacancies[38] which have been shown to originate much larger trigonal defects[39]. Among all the different stacking phases, γ and ε-stacked InSe do not have inversion symmetry while the β and δ stacking do have an inversion centre. As demonstrated in Section.4.2, the presence or absence of inversion symmetry dictates the possibility of having or not a finite SOC splitting and the $z \to -z$ asymmetry of the multilayer crucially determines whether such splitting is linear

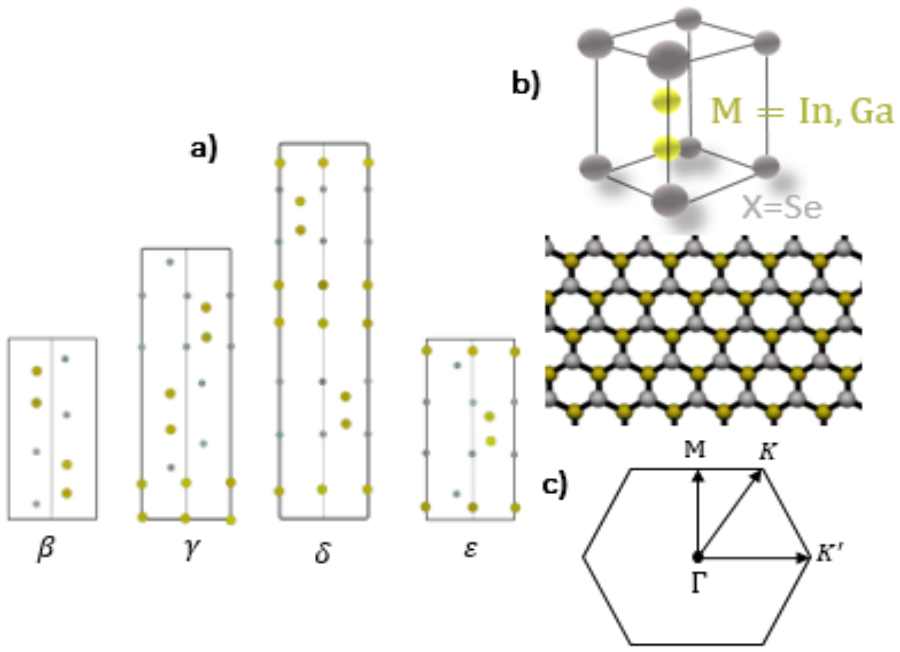

Figure 2.1: a) Bulk unit cell of the different stackings in multilayer InSe as shown in Ref.[34, 35]. The yellow spheres indicate the metal atoms M=In, Ga while the smaller grey spheres label the chalcogen atoms X=Se. While neither ε nor γ-stacked InSe are inversion symmetric, ε-stacked InSe is clearly shown to be $z \to -z$ symmetric for even number of layers. b) Top and profile view of monolayer MSe. c) Brillouin zone of monolayer InSe with the high-symmetry points indicated.

or cubic in k. Furthermore, the absence of inversion symmetry is also responsible for the γ-stacked InSe bilayer to host a slight ferroelectric polarisation as due to interlayer charge transfer[9]. Such transfer of charge generates a very clear hysteresis loop in the electric polarisation with the externally applied electric field, and, as shown experimentally in InSe/GaSe heterostructures[40], it could allow for very high-quality non-volatile memory devices.

2.2 Electronic band structure of monolayer InSe

In order to study the optoelectronic properties of InSe, it is crucial to scrutinize the orbital composition of the bands under consideration. Indium atoms ($Z = 49$) are post-transition metal atoms with an electronic configuration given as: $[\mathrm{Kr}]4d^{10}5s^25p^1$, which prescribes their two most common oxidation states to be In^{3+} and In^{1+}. Selenium atoms belong to the family of the chalcogenides, and have an electronic configuration of the form: $[\mathrm{Ar}]3d^{10}4s^24p^4$, which dictates its three most common oxidation states to be Se^{2-}, Se^{4+} and Se^{6+}. The electronic structure of these elements therefore allows for several compounds to occur, the most notable ones being $\mathrm{In_2Se_3}$, InSe and $\mathrm{In_6Se_7}$[41]. In InSe, The valence s and p orbital states in both the Indium and Selenium atoms determine the orbital composition of the different InSe bands. While the lowest monolayer conduction band c and the topmost valence band v (see Fig. 2.2 and Table 2.1) are mainly composed of equally distributed s and p_z orbitals from both Indium and Selenium atoms, the upper conduction band c_1 is only made of Indium s and p_z orbitals states while the deeper valence bands v_1 and v_2 are only composed of Selenium p_x

D_{3h}	E	σ_h	$2C_3$	$2S_3$	$3C'_{2i}$	$3\sigma_{vi}$	$basis$
Γ_1	1	1	1	1	1	1	1
Γ_2	1	1	1	1	-1	-1	xy
Γ_3	1	-1	1	-1	1	-1	xyz
Γ_4	1	-1	1	-1	-1	1	z
Γ_5	2	-2	-1	1	0	0	(xz, yz)
Γ_6	2	2	-1	-1	0	0	(x, y)

Table 2.1: Character table of the point group D_{3h} as tabulated in Ref.[35].

and p_y orbital states. Given that we will be mostly interested in bands c and v, we can evaluate the effect of the various crystal symmetries on the wavefunctions of bands c and v respectively (i.e. Φ^c and Φ^v) by looking at the character table presented in Table 2.1 for the D_{3h} point group. Starting from the rotational C_3 symmetry, the effect of a 3-fold rotation in the wavefunctions Φ^c and Φ^v is

$$\hat{C}_3|\Phi^c\rangle = |\Phi^c\rangle \quad \text{and} \tag{2.1}$$

$$\hat{C}_3|\Phi^v\rangle = |\Phi^v\rangle. \tag{2.2}$$

Similarly, the horizontal mirror-plane reflection σ_h (i.e. $z \to -z$ symmetry) leads to

$$\hat{\sigma}_h|\Phi^c\rangle = -|\Phi^c\rangle \quad \text{and} \tag{2.3}$$

$$\hat{\sigma}_h|\Phi^v\rangle = |\Phi^v\rangle. \tag{2.4}$$

Finally, the σ_{vi} symmetry coming from the mirror reflection along the three major crystallographic axes impose

$$\hat{\sigma}_{vi}|\Phi^c\rangle = |\Phi^c\rangle \quad \text{and} \tag{2.5}$$

$$\hat{\sigma}_{vi}|\Phi^v\rangle = |\Phi^v\rangle. \tag{2.6}$$

In the absence of an applied magnetic field, time-reversal symmetry is needed to be considered as Kramer's theorem imposes at least a double-degeneracy constraint on every energy level. The electron Hamiltonian, therefore, satisfies $[\hat{H}, \hat{T}] = 0$ while the wavefunction of a half-integer spin $\sigma \equiv \{\uparrow, \downarrow\} = \{1, -1\}$ must obey [33]

$$\hat{T}|\Phi, \sigma\rangle = (-1)^{\frac{1-\sigma}{2}}|\Phi, (-\sigma)\rangle. \tag{2.7}$$

A very remarkable feature of both InSe and GaSe is its very flat topmost valence band (band v in Fig.2.2) which persists from the monolayer to the bulk limit. Such valence band flatness can be understood as originating from a competition between $\mathbf{k} \cdot \mathbf{p}$ interactions involving higher conduction bands and deeper valence

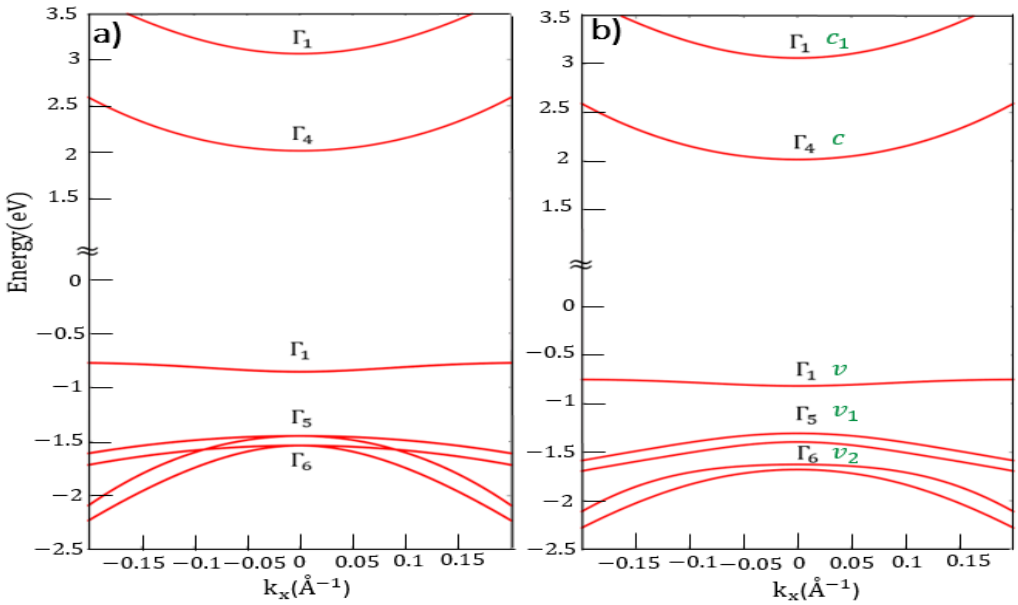

Figure 2.2: a) Monolayer InSe band structure in the absence of SOC with the appropriate irreducible representation Γ^{α} (see Table 2.1) for each band clearly labelled. b) Monolayer InSe band structure when SOC is included with the band nomenclature labelled in green and the corresponding irrep labelled in black.

bands[42]. While the former tries to push the band v lower in energy, the latter tries to push band v to higher energies, resulting in an energetic minimum exactly at the Γ-point followed by a maximum in energy at a finite wavevector. Such dispersion profile commonly referred to as a "Mexican hat" or a "sombrero" dispersion, is particularly prominent in monolayer InSe. In going from monolayer to multilayer InSe, the formation of subbands due to the different quantum confined eigenstates suppresses the Mexican hat dispersion because of the greater influence of the p_z orbitals of the interlayer chalcogen atoms. Such orbitals dominate the valence band dispersion around the Γ-point therefore raising in energy the bottom of the sombrero dispersion[42]. This results in a vanishing Mexican hat dispersion with increasing number of layers which, as will be shown in Section.5, leads to a transition from dark to bright excitons in increasing the number of layers.

To fully understand the optoelectronic properties of monolayer InSe, it is necessary to account for the effect of spin-orbit coupling. Atomic spin-orbit coupling is a relativistic effect coupling the angular momentum and the spin component of an electron[43], resulting in a term in the electron's Hamiltonian of the form

$\xi\hat{\mathbf{L}}\cdot\hat{\mathbf{S}}$. In InSe, both the In and Se atoms possess a very strong SOC due to their very large atomic number ($Z_{In} = 49$ and $Z_{Se} = 34$). Such interaction is therefore capable of mixing the different spins of the p_x and p_y orbital components of the v_1 and v_2 bands, therefore shifting the bands with total angular momentum $J = \frac{3}{2}\hbar$ higher in energy compared to the ones with $J = \frac{1}{2}\hbar$. As well as splitting the v_1 and v_2 bands, SOC allows for the mixing of the p_z orbital states in c and v with the p_x and p_y orbital states of the v_1 and v_2 bands. This has a huge impact on the Mexican hat dispersion of the topmost valence band as it significantly flattens the sombrero dispersion[44], reducing the energy difference between the rim and the bottom of the Mexican hat from approximately 70 to 40meV in monolayer InSe. Due to the $z \to -z$ symmetry (labelled as σ_h in Table 2.1) of the monolayer crystal, the spin Pauli operator $\hat{s}_z$ is a good quantum number ($[\hat{H}, \hat{s}_z] = 0$). Given such constraint, the s and p_z orbital dominated bands c and v must have a momentum-dependent spin-splitting proportional to $\hat{s}_z$. Given the lack of inversion and σ_h symmetry, the lowest order SOC-splitting of bands c and v must have the form[42]

$$H_{so} = \gamma k^3 \sin(3\phi)\hat{s}_z, \tag{2.8}$$

where ϕ is the polar angle with respect to the $\Gamma - M$ direction. Note that Eq. (2.8) takes into account the three-fold rotational symmetry of the crystal as well as the lack of inversion symmetry and predicts exactly zero spin splitting in the $\Gamma - M$ direction.

2.3 Optical properties of monolayer InSe

One of the most relevant features of post-transition metal monochalogenides is their interaction with light and the selection rules derived from it[16]. In the absence of SOC, two very clear absorption peaks are expected from group theoretical arguments[30]. Firstly, an absorption peak of z-polarised light is expected from the v to c optical transition, as clearly seen from the direct product

of their two irreducible representations ($\Gamma_1 \bigotimes \Gamma_4 = \Gamma_4 \sim z$). Similarly, an in-plane polarization absorption peak is expected for the v_1 to c optical transition. This is again proven from the direct product of their irreducible representations ($\Gamma_5 \bigotimes \Gamma_4 = \Gamma_6 \sim (x, y)$).

In using a $\mathbf{k} \cdot \mathbf{p}$ expansion around the Γ-point, it can be shown how the incorporation of spin-orbit coupling hugely alters the optical absorption properties of monolayer InSe[30, 45]. Using the $\mathbf{k} \cdot \mathbf{p}$ formalism, the light-matter coupling can be obtained replacing any momentum $\mathbf{p}$ by $\mathbf{p} \to \mathbf{p} + \mathbf{A}$ where $\mathbf{A}$ is the magnetic vector potential. Our starting point is the monolayer $\mathbf{k} \cdot \mathbf{p}$ Hamiltonian including the various light-matter couplings (see Section.2.4 for a thorough derivation of the monolayer $\mathbf{k} \cdot \mathbf{p}$ Hamiltonian)

$$\hat{H} = \begin{pmatrix} H_c \mathbf{s}_0 & \mathcal{E}_z d_z \mathbf{s}_0 & \frac{ie\beta_1}{cm_e}(\mathbf{s}_0 \bigotimes \mathbf{A}) & i\lambda_{c,v_2}(\mathbf{s} \times \mathbf{\Lambda}) \\ \mathcal{E}_z d_z \mathbf{s}_0 & H_v \mathbf{s}_0 & i\lambda_{v,v_1}(\mathbf{s} \times \mathbf{\Lambda}) & \frac{ie\beta_2}{cm_e}(\mathbf{s}_0 \bigotimes \mathbf{A}) \\ \frac{-ie\beta_1}{cm_e}(\mathbf{s}_0 \bigotimes \mathbf{A})^T & -i\lambda_{v,v_1}(\mathbf{s} \times \mathbf{\Lambda})^\dagger & H_{v_{1(2)}} \mathbf{s}_0 + \lambda_{v_1} \tau_y s_z & 0 \\ -i\lambda_{c,v_2}(\mathbf{s} \times \mathbf{\Lambda})^\dagger & \frac{-ie\beta_2}{cm_e}(\mathbf{s}_0 \bigotimes \mathbf{A})^T & 0 & H_{v_{1(2)}} \hat{s}_0 + \lambda_{v_2} \tau_y s_z \end{pmatrix}, \tag{2.9}$$

where $H_c = \frac{\hbar^2 k^2}{2m_c}$, $H_v = E_v + E_{v_2} k^2 + E_{v_4} k^4$ and $H_{v_{1(2)}} = \left[E_{v_{1(2)}} + \frac{\hbar^2 k^2}{2m_{v_{1(2)}}} \right] \tau_0 + \frac{\hbar^2 (k_x^2 - k_y^2)}{2m'_{1(2)}} \tau_z + \frac{2\hbar^2 k_x k_y}{2m'_{1(2)}} \tau_x$. The matrices τ_i label the 2×2 Pauli matrices in the space of the p_x and p_y orbital components of the v_1 and v_2 bands, while τ_0 is the identity matrix in that same basis. The vector $\mathbf{A}$ labels the magnetic vector potential and the vector $\mathbf{\Lambda}$ labels the p_x and p_y orbital component of the v_1 and v_2 bands (the p_x component being $\Lambda_x = [1, 0]$ and the p_y being $\Lambda_y = [0, 1]$) such that $(\mathbf{s} \times \mathbf{\Lambda}) = (-\mathbf{s}_y, \mathbf{s}_x)$. The matrices $\mathbf{s}$ are the spin Pauli matrices with $\mathbf{s}_0$ being the identity matrix in spin space and any SOC strength is labelled by the greek letter λ. Finally, the term $\mathcal{E}_z$ is the component of the electric field in the z-direction coming from the incident electromagnetic wave and d_z is the interband dipole moment defined as $d_z \equiv e\langle c|z|v\rangle$. The parameters $\beta_{1(2)}$ are the different interband matrix elements of the momentum operator $\beta_{1(2)} \equiv |\langle c(v)|\mathbf{P}|v_1(v_2)\rangle|$. From this expression, the light-matter absorption for each interband optical transition can

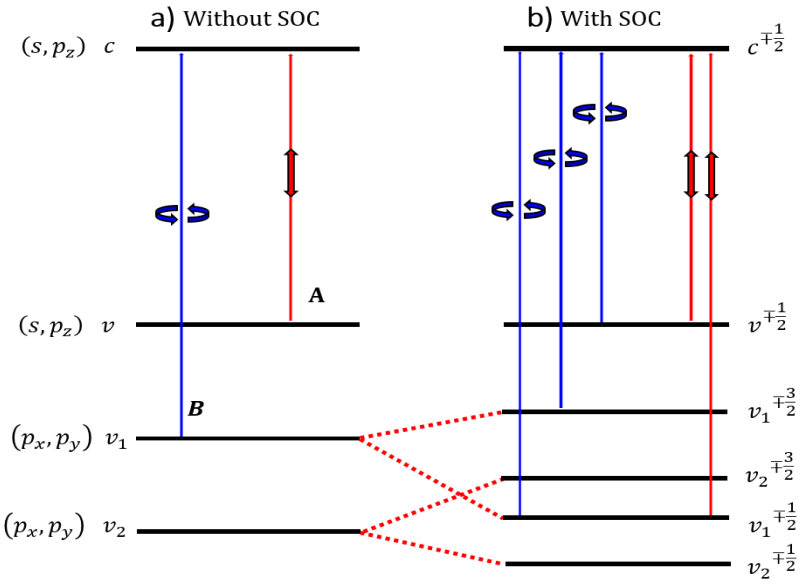

Figure 2.3: a) Optical absorption diagram in monolayer InSe when spin-orbit coupling is not considered inspired from Fig.1 of Ref.[30]. Circularly polarised light is required for the B-absorption line while for the A-absorption line, light polarised in the z-direction couples bands c and v. b) New set of optical absorption resonant frequencies when SOC is included. As due to SOC, both the v_1 and v_2 bands split, creating different absorption lines for the $J_z = \pm\frac{1}{2}\hbar$ and $J_z = \pm\frac{3}{2}\hbar$ eigenstates.

be evaluated using the Fermi golden rule,

$$\Gamma_{i\to f} = \frac{2\pi}{\hbar}|\langle f|\delta\hat{H}|i\rangle|^2\rho(E), \tag{2.10}$$

where $\langle f|$ is the band c and $|i\rangle$ is any of the v, v_1 or v_2 bands. The term δH is the light to matter coupling term between $|i\rangle$ and $\langle f|$ with or without SOC included. This term is given by $\delta\hat{H} = -\frac{e}{mc}\vec{p}\cdot\vec{A}$ in the absence of SOC, and by $\delta\hat{H} = \frac{-e}{mc}\frac{\beta_1\lambda_{v_1v}}{E_v - E_{v_1}}(\mathbf{s}_x A_y - \mathbf{s}_y A_x)$ in the presence of SOC, coupling the spin and the light polarisation perpendicular to each other. Finally, $\rho(E)$ is defined as the density of states at a given energy E. As shown in Fig.2.3, the overall result was that SOC-mediated spin-flip transitions were capable of not only coupling bands with different total angular momentum ($c^{\pm\frac{1}{2}}$ and $v_1^{\pm\frac{3}{2}}$), but also the v to c bands with in-plane polarised light[30] and the v_1 to c bands with out-of-plane polarised light. Exact analytical expressions for the absorption coefficient can be obtained considering the ratio of the absorbed light by the interband transition divided by the energy flux of the incident electromagnetic radiation[46, 29, 30]. In the

absence of spin-orbit coupling, the absorption coefficient α for v to c and for v_1 to c can be obtained from

$$\alpha = \frac{16\pi^2 e^2}{m_e^2 c\omega}|\langle c|\mathbf{p}|v'\rangle|^2 \rho_{cv'}(\hbar\omega), \tag{2.11}$$

where ω is the optical frequency, $\mathbf{p}$ is the momentum operator and $\rho_{cv}(\hbar\omega)$ is the joint density of states between bands c and an arbitrary valence band v'. In two dimensions, this quantity equals to $\rho_{cv} = \frac{m_r}{\pi\hbar^2}$ where m_r is the reduced effective mass between bands c and v'. The above expression would yield to the following expression for α_{cv}^z (maximum absorption coefficient between bands c and v due to z-polarised light) and for $\alpha_{cv_1}^{\sigma^\pm}$(maximum absorption coefficient between bands c and v_1 due to circularly polarised light)[44],

$$\begin{aligned} \alpha_{cv}^z &= \frac{8\pi e^2}{\hbar c}\left|\frac{d_z}{e}\right|^2 \frac{\hbar\omega m_c}{\hbar^2}, \\ \alpha_{cv_1}^{\sigma^\pm} &= \frac{8\pi e^2}{\hbar c}|\beta_1|^2 \frac{m_c}{\hbar\omega m_e^2}. \end{aligned} \tag{2.12}$$

On including the SOC term mixing bands v_1 and v, the following additional term[30] can be obtained for the circularly polarised optical absorption between bands c and v,

$$\alpha_{cv}^{\sigma^\pm} = \frac{8\pi e^2}{\hbar c}\left|\beta_1 \frac{\sqrt{2}\lambda_{vv_1}}{\left(E_v - E_{v_1} + \lambda_{v_1}\right)}\right|^2 \frac{m_c}{\hbar\omega m_e^2}. \tag{2.13}$$

2.4 Hybrid $\mathbf{k}\cdot\mathbf{p}$ tight-binding model of few-layer InSe

To study both the optical and spin-orbit coupling properties of multilayer InSe around the Γ-point, a 14×14-band $\mathbf{k}\cdot\mathbf{p}$ Hamiltonian capable of catching all

the relevant dispersion features from monolayer to bulk InSe was used[47]. The 7-bands (each one has two possible spin states, therefore making 14 bands in total) of the 14-band $\mathbf{k}\cdot\mathbf{p}$ monolayer InSe Hamiltonian are the two c_1, c bands in the conduction band and the $v, v_{1x}, v_{1y}, v_{2x}, v_{2y}$ bands in the valence band (see Fig.2.2). From the character table shown in Table 2.1 for the point group D_{3h}, a general $\mathbf{k}\cdot\mathbf{p}$ Hamiltonian capturing all the symmetries of the D_{3h} point group can be formulated using the usual technique of invariants[35]. According to such methodology, the Hamiltonian is required to remain invariant under all the symmetries present in the crystal, therefore forcing it to obey[35]

$$D^{\alpha}(g)H^{\alpha\beta}(\hat{P}_g\mathcal{K}\hat{P}_g^{-1})D^{\beta}(g^{-1}) = H^{\alpha\beta}(\mathcal{K}), \tag{2.14}$$

where $D^{\alpha}(g)$ is the matrix representation of the operator g in the irreducible representation Γ^{α} (see Table 2.1 for the symmetries of each irrep) and $\hat{P}_g\mathcal{K}\hat{P}_g^{-1}$ is the effect of the operator g in the (k_x, k_y)-dependent polynomial $\mathcal{K}$. The procedure of invariants therefore constructs the $\mathbf{k}\cdot\mathbf{p}$ matrix Hamiltonian from elements invariant under all the symmetries prescribed by the crystal lattice such that each irrep Γ_{γ} has invariants of the form[35]

$$I_{\gamma}^{\alpha\beta} = \sum_{l} X_{\gamma l}^{\alpha\beta} K_{\gamma l}, \tag{2.15}$$

where $K_{\gamma l}$ are irreducible tensor operators obtained from $\mathcal{K}$ which under D_{3h} are required to obey $\hat{P}_g K_{\gamma l}\hat{P}_g^{-1} = \sum_{l'} K_{\gamma l'} D_{l'l}^{\gamma}(g)$. Finally, the tensor $X_{\gamma l}^{\alpha\beta}$ are D_{3h}-symmetrized matrices which transform according to the l^{th} column of Γ_{γ}, i.e. $D^{\alpha}(g)X_{\gamma l}^{\alpha\beta}D^{\beta}(g^{-1}) = \sum_{l'} X_{\gamma l'}^{\alpha\beta} D_{l'l}^{\gamma}(g)$. The term in the Hamiltonian $H^{\alpha\beta}$ is therefore given by a proportionality constant with respect to a linear combination of the invariants $I_{\gamma}^{\alpha\beta}$ such that

$$H^{\alpha\beta}(\mathcal{K}) = \sum_{\gamma} c_{\gamma}^{\alpha\beta} I_{\gamma}^{\alpha\beta}(\mathcal{K}). \tag{2.16}$$

In addition to the crystal symmetries, it is necessary to take into consideration the time-reversal symmetry present in the absence of an applied magnetic field.

This can be written as

$$\hat{\theta}H^{\alpha\beta}(\mathcal{K})\hat{\theta}^{-1} = H^{\alpha\beta}(\mathcal{K}), \tag{2.17}$$

where $\hat{\theta}$ is the time-reversal operator. This condition is only strictly necessary in the diagonal elements of the $\mathbf{k}\cdot\mathbf{p}$ matrix Hamiltonian[48]. Using this method, the 14-band Hamiltonian describing both monolayer InSe and GaSe around the Γ-point can be written as

$$\hat{H} = \begin{pmatrix} \hat{H}_{cc} & \hat{H}_{cv} \\ \hat{H}_{vc} & \hat{H}_{vv} \end{pmatrix}, \tag{2.18}$$

where $\hat{H}_{cc}$ is defined as

$$\hat{H}_{cc} = \begin{pmatrix} (\varepsilon_c + \alpha_c k^2)\mathbf{s}_0 & 0 \\ 0 & (\varepsilon_{c_1} + \alpha_{c_1} k^2)\mathbf{s}_0 \end{pmatrix}, \tag{2.19}$$

operating on the $c^{\uparrow}, c^{\downarrow}, c_1^{\uparrow}$ and $c_1^{\downarrow}$ band basis of monolayer InSe (see Fig.2.2). In Eq. (2.19), the 2×2 matrix $\mathbf{s}_0$ is defined as the identity matrix in spin space. The term $\hat{H}_{cv}$ couples bands v, v_1 and v_2 with bands c_1 and c. Its matrix representation can be proven to have the form

$$\hat{H}_{cv} = \begin{pmatrix} 0 & i\beta_{c,v_1}(\mathbf{k}\cdot\mathbf{\Lambda}) & i\lambda_{c,v_2}(\mathbf{s}\times\mathbf{\Lambda}) \\ \beta_{c_1,v}k^2 & 0 & i\beta_{c_1,v_2}(\mathbf{k}\cdot\mathbf{\Lambda}) \end{pmatrix}. \tag{2.20}$$

In the above expression, the vectors $\mathbf{\Lambda} = (\Lambda_x, \Lambda_y)$ are the unit vectors $\Lambda_x = [1, 0]$ and $\Lambda_y = [0, 1]$ operating in the space of p_x and p_y orbital components of the v_1 and v_2 bands, while the matrices $\mathbf{s} = (\mathbf{s}_x, \mathbf{s}_y, \mathbf{s}_z)$ are the spin Pauli matrices in the x, y and z-direction respectively. Note that the matrix $\hat{H}_{cv}$ is related to $\hat{H}_{vc}$ by hermiticity. The matrix $\hat{H}_{vv}$ written in the basis of v,v_1 and v_2 states can be

proven to have the form

$$\hat{H}_{vv} = \begin{pmatrix} (\varepsilon_v + \alpha_v k^2)\mathbf{s}_0 & i\lambda_{v,v_1}(\mathbf{s}\times\mathbf{\Lambda}) & i\beta_{v,v2}(\mathbf{k}\cdot\mathbf{\Lambda}) \\ -i\lambda_{v,v_1}(\mathbf{s}\times\mathbf{\Lambda})^\dagger & \mathbf{s}_0\gamma_{v_1} + \lambda_{v_1}\tau_y s_z & 0 \\ -i\beta_{v,v_2}(\mathbf{k}\cdot\mathbf{\Lambda})^T & 0 & \mathbf{s}_0\gamma_{v_2} + \lambda_{v_2}\tau_y s_z \end{pmatrix}, \tag{2.21}$$

where the $\tau_{x,y,z}$ are Pauli matrices operating in the p_x, p_y orbital components of the v_1, v_2 bands and τ_0 is the identity matrix in that same basis. In Eq. (2.21), γ_{v_1} is defined as $\gamma_{v_1} \equiv D_{v_1}\tau_0 + D'_{v_1}\tau_x + D''_{v_1}\tau_z$ and γ_{v_2} as $\gamma_{v_2} \equiv D_{v_2}\tau_0 + D'_{v_2}\tau_x + D''_{v_2}\tau_z$. The term D_{v_1} is defined as $D_{v_1} \equiv (\varepsilon_{v_1} + \alpha_{v_1}k^2)$ while D_{v_2} as $D_{v_2} \equiv (\varepsilon_{v_2} + \alpha_{v_2}k^2)$. The terms D'_{v_1} and D'_{v_2} are defined as $D'_{v_1} \equiv -2\alpha'_{v_1}k_xk_y$ and $D'_{v_2} \equiv -2\alpha'_{v_2}k_xk_y$ respectively (see Table 2.2 for their numerical values). Finally, the terms D''_{v_1} and D''_{v_2} have the form $D''_{v_1} \equiv \alpha'_{v_1}(k_y^2 - k_x^2)$ and $D''_{v_2} \equiv \alpha'_{v_2}(k_y^2 - k_x^2)$ respectively. In this Hamiltonian it is important to point out the $(\mathbf{s}\times\mathbf{\Lambda})$ form of the SOC terms mixing bands c and v_2 as well as bands v and v_1. This form of the SOC comes from invariants whose product of the irreps had functional form $\sim (xz, yz)$, forcing the SOC matrix elements between c and v_2 as well as between v and v_1 to have the cross product form $(-\mathbf{s}_y, \mathbf{s}_x)$. This crossed form of the SOC is an important feature for the investigation of SOC in multilayer InSe and GaSe thin films as it prescribes the electron's spin texture, which is a physical observable responsible for transport phenomena such as the spin-galvanic effect[49, 50, 51, 52].

In the hybrid $\mathbf{k}\cdot\mathbf{p}$ tight-binding Hamiltonian, the interlayer hoppings are given by the tunnelling amplitude between neighbouring Selenium atoms. Neglecting any interlayer spin-flip hopping term, the hopping Hamiltonian between layers $i+1$ and i in the basis $[c, c_1, v, v_1, v_2]$ therefore has the following form:

$$\hat{H}_{i,i+1} = \begin{pmatrix} t_c & t_{c_1,c} & t_{c,v} & 0 & 0 \\ -t_{c_1,c} & t_{c_1} & 0 & 0 & 0 \\ -t_{c,v} & 0 & t_v & 0 & 0 \\ 0 & 0 & 0 & t_{v_{1,2}} & t_{v_{1,2}} \\ 0 & 0 & 0 & -t_{v_{1,2}} & t_{v_{1,2}} \end{pmatrix}. \tag{2.22}$$

The hybrid $\mathbf{k}\cdot\mathbf{p}$ tight-binding Hamiltonian parameters were extracted from fitting density functional theory computed bands taking into account electron-electron interaction effects in the GW approximation[53, 54] (see Table 2.2 for their numerical values). Such parameterisation unavoidably overestimated the effective mass of the electron in the monolayer but provided a very accurate description of the global properties of the band structure including the spin-orbit splittings in bands v_1 and v_2 as well as an accurate description of the sombrero dispersion in band v (see Fig. 2.4).

While this 14-band Hamiltonian is a very useful tool to study the optoelectronic properties of InSe in the vicinity of the Γ-point, it may sometimes be more convenient to use a simplified model to reduce the required time needed for computations. As we are mostly interested in looking at the properties of the c and v band, one usual procedure is to formulate a 2-band hybrid $\mathbf{k}\cdot\mathbf{p}$ tight-binding Hamiltonian from the 14-band model. This is done by projecting both the upper c_1 conduction band and the deeper v_1, v_2 valence bands into a 2-band basis composed of c and v monolayer eigenstates. The projection is done applying Löwdin renormalisation (see Section. 4.2) of both the linear in momentum terms and the various interlayer hoppings in both the c and v bands ignoring the effects of SOC. Such renormalization procedure leads to the following 2-band Hamiltonian

$$\hat{H}_{k.p} = \begin{pmatrix} \frac{E_g}{2} + \frac{\hbar^2 k^2}{2m_c} & t_{cc}^{(2)} & 0 & t_{cv}^{(2)} \\ t_{cc}^{(2)} & \frac{E_g}{2} + \frac{\hbar^2 k^2}{2m_c} & -t_{cv}^{(2)} & 0 \\ 0 & -t_{cv}^{(2)} & -\frac{E_g}{2} + \gamma_2 k^2 + \gamma_4 k^4 & t_{vv}^{(2)} \\ t_{cv}^{(2)} & 0 & t_{vv}^{(2)} & -\frac{E_g}{2} + \gamma_a k^2 + \gamma_4 k^4 \end{pmatrix}, \tag{2.23}$$

where $\frac{1}{2m_c} = \frac{\beta_{c,v_1}^2}{E_c - E_{v_1}}$, $t_{vv}^{(2)} \equiv t_v + t_{vv_2} k^2$, $t_{vv2} = \frac{\beta_{v,v_2}^2 t_{v_{1,2}}}{(E_v - E_{v_2})^2} - \frac{\beta_{v,v_2}^2 t_v}{(E_v - E_{v_2})^2}$, $t_{cc}^{(2)} = t_c + t_{cc2} k^2$, $t_{cc2} = \frac{\beta_{c,v_1}^2 t_{v_{1,2}}}{(E_c - E_{v_1})^2} - \frac{\beta_{c,v_1}^2 t_c}{(E_c - E_{v_1})^2}$, $t_{cv}^{(2)} = t_{c,v} + t_{cv2} k^2$, and $t_{cv2} = \frac{\beta_{c,v_1}\beta_{v,v_2} t_{v_{1,2}}}{(E_c - E_{v_1})(E_v - E_{v_2})} - \frac{\beta_{c,v_1}^2 t_{cv}}{2(E_c - E_{v_1})^2} - \frac{\beta_{v,v_2}^2 t_{cv}}{2(E_v - E_{v_2})^2}$.

Using this simplified hybrid $\mathbf{k}\cdot\mathbf{p}$ tight-binding Hamiltonian, the subband energies and optical absorption amplitudes can be easily extracted and, in combination with a self-consistent calculation of the externally applied electrostatic potential,

ε_{c_1}	3.064 eV
ε_c	2.015 eV
ε_v	−0.855 eV
ε_{v_1}	−1.449 eV
ε_{v_2}	−1.538 eV
$\lambda_{v_{1(2)}}$	0.142 eV
λ_{v,v_1}	0.119 eV
λ_{c,v_2}	-0.09 eV
t_{c_1}	−0.011 eV
t_c	0.333 eV
t_v	−0.420 eV
$t_{v_{1,2}}$	−0.048 eV
$t_{c_1,c}$	0.019 eV
$t_{c,v}$	0.251 eV

α_{c_1}	1.54 eVÅ^2
α_c	−18.7 eVÅ^2
α_v	−4.95 eVÅ^2
α_{v_1}	6.48 eVÅ^2
α'_{v_1}	−10.51 eVÅ^2
α_{v_2}	−0.28 eVÅ^2
α'_{v_2}	−4.20 eVÅ^2
$\beta_{c_1,v}$	3.77 eVÅ^2
β_{c_1,v_2}	8.51 eVÅ
β_{c,v_1}	10.54 eVÅ
β_{v,v_2}	−2.78 eVÅ

Table 2.2: Model parameters provided by S.J.Magorrian used in Chapter.4 and 5. They were obtained from fitting these parameters to bulk QSGW computed bands from Ref.[53, 54]. The SOC parameter λ_{c,v_2} was obtained from fitting λ_{c,v_2} from the QSGW data as shown in Section 4.2.

one could study the effect of an applied external electric field in the vicinity of the Γ-point. A similar 2-band model was successfully used for the calculation of intersubband energies and optical absorption coefficients in the lowest conduction subband, neglecting any effect of spin-orbit coupling due to its limited impact in the energetics and dispersion features of the lowest conduction subband.

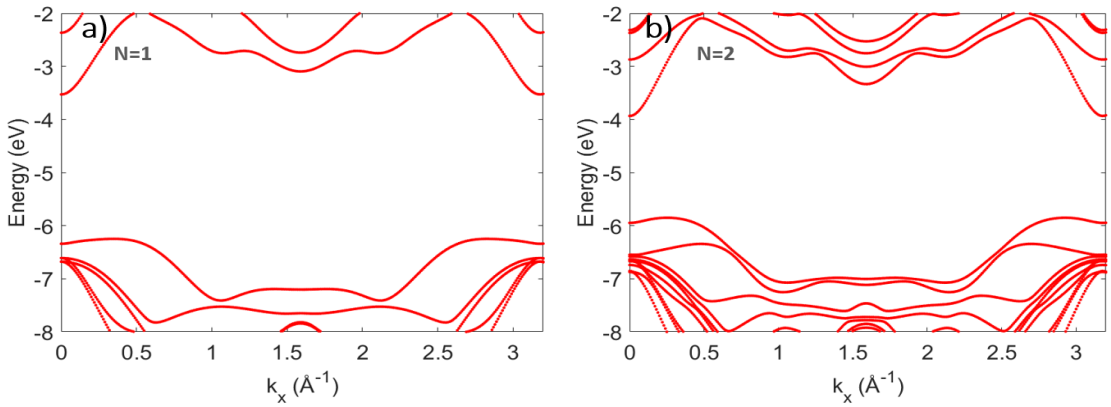

Figure 2.4: (Left) Tight-binding calculation of the monolayer InSe band structure in the absence of SOC. (Right) Tight-binding calculation of the band structure of bilayer InSe in the absence of SOC.

Chapter 3

Subband optics in InSe

3.1 Introduction

In going from bulk to monolayer InSe, the allowed values of the out-of-plane momentum k_z are discretised due to the confinement of the electrons in the z-direction [42]. The discrete set of k_z values leads to a finite number of energy levels in the electronic band structure known as subbands. To model the formation of such states in InSe, a quantum well model was developed for multilayer InSe and the intersubband energy dependence on the number of layers was described using such formalism. The boundary conditions applied to both InSe/vacuum interfaces corresponded to the generalised Dirichlet-Neumann boundary conditions (also known as Robin boundary conditions[55]) which considers the multilayer crystal as an effective quantum well with a slight overextension compared to the actual thickness of the film. From the subband energies, the intersubband oscillator strengths and optical absorption coefficients were calculated as well as their thermal broadening.

Using a self-consistent algorithm that models each monolayer as an infinitely thin film (see Appendix.A.1 of this thesis for the self-consistent analysis of bilayer InSe), a toy-model for the intersubband energy dependence on the applied electric field was developed for different multilayer systems and the effect of an applied displacement field on the optical absorption peaks was studied. The intersubband energies were found to range from the infrared to the far-infrared part of the optical spectrum when going from the bilayer to the bulk limit. In applying an electric field, tunability in the resonant peak was demonstrated due to the dependence of the intersubband energy, the intersubband dipole moment and the in-plane conduction band effective mass on carrier density.

3.2 Hybrid $\mathbf{k} \cdot \mathbf{p}$ tight-binding model for intersubband optics in atomically thin InSe films

The results of this investigation were presented in Ref.[23]: "Hybrid $\mathbf{k}\cdot\mathbf{p}$ tight-binding model for intersubband optics in atomically thin InSe films". In:Phys. Rev. B97 (16 Apr. 2018).

My contribution to this work: A. Ceferino performed the self-consistent calculation to account for the effect of an electric field in the intersubband energies in multilayer InSe and computed the optical absorption coefficient in different InSe multilayer thin films at various carrier densities.

Full author list: S. J. Magorrian, A. Ceferino, V. Zólyomi and V. I. Fal'ko.

Author contribution: S. J. Magorrian calculated the subband energies, optical absorptions in the absence of an applied electric field, developed the quantum well model and wrote the paper. A. Ceferino and S. J. Magorrian calculated the intersubband energy dependence on carrier density.

Hybrid k · p tight-binding model for intersubband optics in atomically thin InSe films

S. J. Magorrian, A. Ceferino, V. Zólyomi, and V. I. Fal'ko
National Graphene Institute, University of Manchester, Booth St E, Manchester M13 9PL, United Kingdom
and School of Physics and Astronomy, University of Manchester, Oxford Road, Manchester M13 9PL, United Kingdom

(Received 19 January 2018; published 12 April 2018)

We propose atomic films of n-doped γ-InSe as a platform for intersubband optics in the infrared and far-infrared range, coupled to out-of-plane polarized light. Depending on the film thickness (number of layers) and the amount of n-doping of the InSe film, these transitions span from ∼0.7 eV for bilayer to ∼0.05 eV for 15-layer InSe. We use a hybrid $\mathbf{k}\cdot\mathbf{p}$ theory and tight-binding model, fully parametrized using density-functional theory, to predict their oscillator strengths and thermal linewidths at room temperature.

DOI: 10.1103/PhysRevB.97.165304

I. INTRODUCTION

Atomically thin layers of van der Waals (vdW) materials and their heterostructures [1,2], generally branded as two-dimensional materials (2DMs), attracted attention due to their promise for creating multifunctional electronic devices and, more generally, as a new materials base for optoelectronics [3]. This class of materials features strong covalent bonding of atoms in the 2D planes and a weak vdW attraction between the layers, permitting fabrication of stable films of such materials down to a monolayer (sub-nm) thickness and creation of their various heterostructures. The ongoing studies of 2DMs broadly address graphene [1] and hexagonal boron nitride (hBN, a wide-band-gap insulator) [4], narrow-gap semiconductor black phosphorus [5,6], and various transition-metal dichalcogenides [7].

Among all 2DMs, a special place is taken by two post-transition-metal chalcogenides (PTMCs): InSe and GaSe. This closely lattice-matched pair of optically active 2D compounds (with a monolayer stoichiometric formula $M_2\mathrm{Se}_2$, M = In or Ga) was found, both theoretically [8,9] and experimentally [10], to have a band gap that varies widely from the monolayer to multilayer films, densely covering the range of energies $E_g \sim 1.3$–3 eV. Also, these 2DMs have relatively light ($m_c \sim 0.2m_e$) conduction-band electrons [8–10] with very high mobility, even in the case of atomically thin films. While the recent optical studies of 2D InSe and GaSe crystals [10,11] have been performed using mechanically exfoliated films, manufacturability of 2D crystals of PTMCs using molecular-beam epitaxy [12] and chemical vapor deposition [13] has already been demonstrated, and the potential of various PTMCs for optoelectronics applications was identified in terms of their implementation in high-sensitivity [14] and fast [15] broadband photodiodes. Here, we show that optical transitions between subbands in n-doped PTMC films of various thicknesses, active in the same out-of-plane polarization [9] as the interband transitions, can extend the range of their optical functionality into the IR/FIR range.

Theoretical studies of 2D InSe have largely focused on the monolayer, with DFT studies finding a slightly indirect band gap due to an offset in the valence-band maximum [8], with a Lifshitz transition presenting the possibility of ferromagnetism on hole-doping [16]. Meanwhile, $\mathbf{k}\cdot\mathbf{p}$ theory and tight-binding studies [9,17,18] have been employed to further understand the band structure, symmetries, optical properties, and highly sensitive strain response of monolayer InSe.

Here, we use a hybrid $\mathbf{k}\cdot\mathbf{p}$ theory and tight-binding (HkpTB) model to study in detail the subbands and intersubband transitions in atomically thin films of post-transition-metal chalcogenides. In particular we find that, in InSe films with thicknesses from $N = 2$ to 15 layers, transitions between the lowest and first excited subbands cover the range of photons from $\lambda \sim 2$ μm to $\lambda \sim 25$ μm (between ∼680 and ∼50 meV); see Fig. 1. We analyze thermal broadening of the intersubband absorption spectra caused by the variation of the 2D (in-plane) dispersion of electrons in consecutive subbands, and we also develop the self-consistent description of the subband energies for the films doped n-type by gates.

II. HYBRID k · p TIGHT-BINDING MODEL

The crystal structure of few-layer InSe is shown in Fig. 2, with successive Se-In-In-Se layers arranged in the γ polytype—each layer is shifted with respect to the layer below such that selenium atoms in the upper layer lie above the indium atoms in the lower layer. The wave functions at the conduction-band edge in InSe are predominantly composed of s and p_z orbitals on In and Se [9]. Electrons in the monolayer have a light in-plane effective mass $m_c \sim 0.2m_e$, while strong interlayer hopping between the layers leads to a strong band gap dependence on the number of layers, varying from ∼1.3 eV in the bulk to ∼2.0 eV in the bilayer [9,10].

To describe subbands of electrons in the conduction band in few-layer InSe, we construct a two-band hybrid ($\mathbf{k}\cdot\mathbf{p}$)-tight-binding Hamiltonian in a basis of the $\mathbf{k}\cdot\mathbf{p}$ conduction and valence bands of the monolayer, with successive layers coupled by tight-binding hoppings between monolayer $\mathbf{k}\cdot\mathbf{p}$ states. These bands and hoppings are chosen as those in the region of the band edge with non-negligible strength interlayer electronic couplings and subband splittings. The Hamiltonian

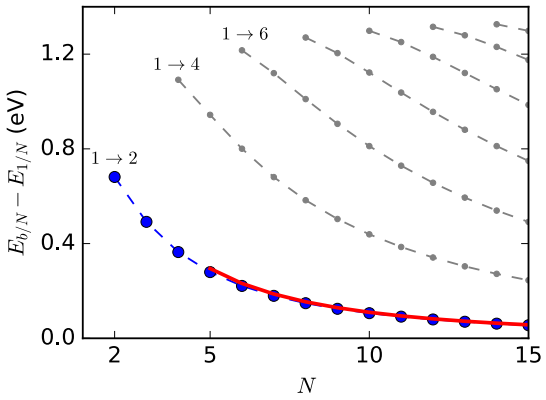

FIG. 1. Intersubband energies for an allowed electric dipole transition for excitation from the lowest subband in weakly n-doped ($N = 2$–15)-layer InSe. Transitions to the second lowest subband (marked in blue) are expected to be significantly stronger than transitions to higher subbands. The red line shows the $1|N \to 2|N$ intersubband transition energies in lightly n-doped films approximated by an asymptotic ($N \gg 1$) formula, $\hbar\omega \approx \frac{\hbar^2\pi^2}{2m_{Az}a_z^2}\frac{3}{(N+2v)^2}$, derived from Eq. (8). The lowest intersubband transition energy increases for heavily doped films (see Fig. 5 in Sec. V).

takes the form

$$\hat{H} = \sum_n^N \Big[\Big(\Delta_c(2 - \delta_{n,1} - \delta_{n,N}) + \frac{\hbar^2 p^2}{2m_c} \Big) a_{nc} a_{nc}^\dagger + [E_v + \Delta_v(2 - \delta_{n,1} - \delta_{n,N})] a_{nv} a_{nv}^\dagger \Big] + \sum_n^{N-1} \big[(t_c^\Gamma + t_c' p^2) a_{(n+1)c}^\dagger a_{nc} + t_v a_{(n+1)v}^\dagger a_{nv} + (t_{cv}^\Gamma + t_{cv}' p^2)(a_{(n+1)v}^\dagger a_{nc} - a_{(n+1)c}^\dagger a_{nv}) + \text{H.c.} \big]. \quad (1)$$

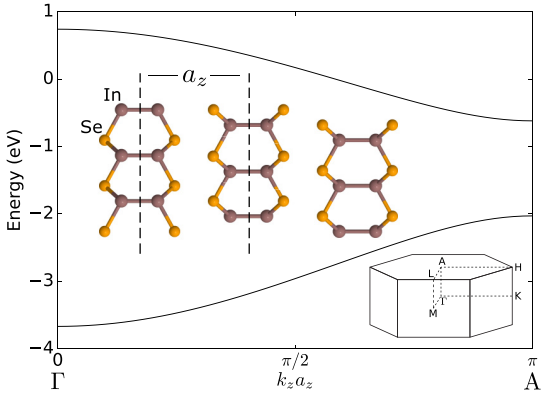

FIG. 2. Γ-A dispersion in bulk γ-InSe ($k_x = k_y = 0$), from the two-band HkpTB model, Eq. (1). Zero of energy set to the conduction-band edge in a monolayer. Inset center: crystal structure of γ-InSe. The monolayer has a hexagonal structure, with point-group symmetry D_{3h}. The point group of the bulk crystal is C_{3v}, with each layer shifted with respect to the layer below such that selenium atoms in the upper layer lie above the indium atoms in the lower layer. $a_z = 8.32$ Å is the experimentally known interlayer distance [19]. Inset bottom right: Brillouin zone of a conventional unit cell of InSe (three layers); bands plotted here have been unfolded.

TABLE I. HkpTB theory parameters in Eq. (1), and Γ-point transition energies between two lowest subbands.

E_v	−2.79 eV	t_c^Γ	0.34 eV
m_c	0.17 m_e	t_v	−0.41 eV
Δ_c	0.03 eV	t_{cv}^Γ	0.29 eV
Δ_v	−0.03 eV	t_c'	−5.91 eV Å^2
		t_{cv}'	−5.36 eV Å^2

N	$E_{2\|N} - E_{1\|N}$
2	680 meV
3	490 meV
4	360 meV
5	280 meV

Here, operators $a_{nc/v}^{(\dagger)}$ annihilate (create) electrons in the conduction (valence) bands of the individual layers (indexed by $n = 1, \ldots, N$) of the N-layer crystal. Since the Γ-point dispersion of electrons in the conduction band of monolayer InSe changes negligibly upon inclusion of spin-orbit coupling (SOC) [20], we neglect spin-orbit effects and describe the monolayer conduction band with a parabolic dispersion with effective mass m_c, while approximating the valence band as flat, with constant energy E_v. $t_{c(v)}$ is an interlayer conduction-conduction (valence-valence) hop, and t_{cv} describes interlayer conduction-valence and valence-conduction hybridization. Our earlier studies [9] showed that the interlayer coupling is dominated by Se-Se interlayer pairs on the outside adjacent monolayers, and hence we assume that the valence-conduction and conduction-valence hops can be related as $t_{vc} = -t_{cv}$. The p dependence of the conduction-conduction and conduction-valence interlayer hops, which helps account for the differing effective masses in the subbands within the conduction band, is introduced as $t_{c(cv)} = t_{c(cv)}^\Gamma + t_{c(cv)}' p^2$. Finally, $\Delta_{c(v)}$ are on-site energy shifts to the conduction (valence) states, included to take account of the different environment of states on the inside of the crystal compared with those on the surface.

We parametrize the interlayer hops (t_α) and on-site energy shifts (Δ) using dispersion curves obtained by means of density-functional theory (DFT) as implemented in VASP [21] for bulk and few-layer InSe [9,20]. The cutoff energy for the plane-wave basis is 600 eV and the Brillouin zone is sampled by a 12 × 12 **k**-point grid. We complement DFT by a "scissor correction" adjustment of the monolayer band gap (having the effect $E_v \to E_v - 0.99$ eV), chosen to correct for the difference between the LDA band gap and the value known from experiment for bulk InSe, as described in Ref. [9]. The parameters obtained are listed in Table I. This procedure is chosen since the underestimation of the gap by DFT would lead to the overestimation of the effect of the interband interlayer hop t_{cv} on the value of the electron effective mass in the z direction in the bulk, and on the subband spectra of multilayer films. To illustrate this effect, we consider the out-of-plane conduction-band-edge effective mass in the bulk, given by Eq. (3). Using the parameters in Table I with the LDA band gap $E_g = 0.41$ eV, we obtain an effective mass $m_{Az} = 0.043m_e$, while with the corrected gap $E_g = 1.40$ eV we find an effective mass $m_{Az} = 0.088m_e$, which is much

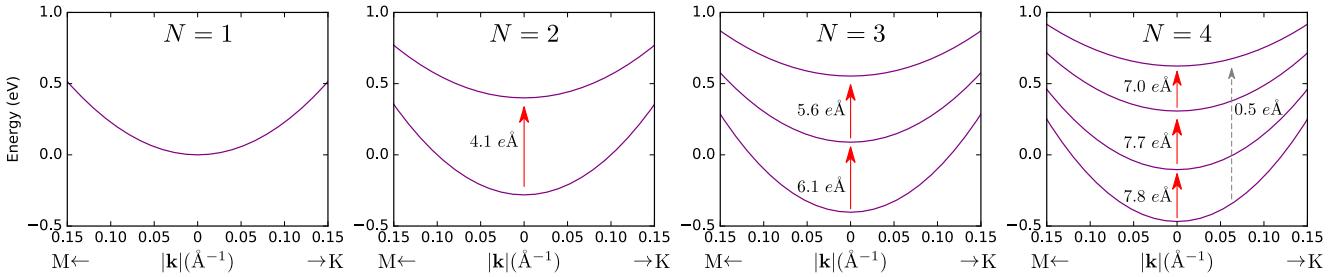

FIG. 3. Subbands of the conduction band in the $N = 1 - 4$-layer InSe near the Γ point, from Eq. (1). 0 of energy set to the conduction-band minimum in the monolayer. Red arrows denote the strongest intersubband optical-absorption transitions, coupled to the out-of-plane electric dipole, while the dashed gray arrow for four-layer InSe indicates a much weaker transition. Arrows are labeled with the intersubband out-of-plane electric dipole moment of the transition, d_z [Eq. (10)].

closer to the experimental value of $0.081(9)m_e$ [22]. Having noted this change to the dispersion in the bulk crystal, we also expect changes to the energies of the subbands in the few-layer crystal. For example, correction of the monolayer gap reduces the splitting between the two lowest subbands in six-layer InSe from 250 to 220 meV.

Each band in the monolayer generates N subbands in N-layer InSe, with the subband dispersions of the conduction band for $N = 1$–4 shown in Fig. 3, and the Γ-point separation between the lowest subbands shown in Table I. In all of these cases, electrons in the lower-energy subbands have lighter effective masses than those in the higher subbands. This difference in effective masses gives a finite thermal linewidth to the absorption lines, at high doping and/or elevated temperatures.

III. BAND-EDGE EXPANSION IN BULK InSe

In bulk InSe, both conduction- and valence-band edges are located at the A-point (see Fig. 2), $k_x = k_y = 0, k_z = \pi/a_z$ (where $a_z = 8.32$ Å is the experimentally known interlayer distance [19]). The **k** · **p** expansion in the vicinity of the A-point can be written as

$$E_c(\mathbf{p}, p_z) = \left(\frac{\hbar^2}{2m_A} + \eta p_z^2 a_z^2\right) p^2 + \frac{\hbar^2 p_z^2}{2m_{Az}}, \tag{2}$$

where $p = |\mathbf{p}| = |(p_x, p_y)|$, while $p_z = k_z - \pi/a_z$. The xy plane and z-axis effective masses, m_A and m_{a_z}, are given by

$$\frac{1}{m_A} = \frac{1}{m_c} - \frac{4t_c'}{\hbar^2}, \quad \frac{1}{m_{Az}} = \frac{2a_z^2}{\hbar^2}\left[t_c^\Gamma + \frac{4t_{cv}^{\Gamma 2}}{E_g}\right], \tag{3}$$

respectively, where $E_g = 2\Delta_c - (E_v + 2\Delta_v) - 2(t_c - t_v)$ is the bulk band gap. These give $m_A = 0.11m_e$ and $m_{Az} = 0.09m_e$, respectively, close to the experimentally known values of $m_A = 0.14m_e$ and $m_{Az} = 0.08m_e$ [22]. The additional parameter,

$$\eta = t_c' - \frac{2\hbar^2}{m_A}\frac{t_{cv}^{\Gamma 2}}{E_g^2} + \frac{8t_{cv}^\Gamma t_{cv}'}{E_g} \simeq -0.63\frac{\hbar^2}{2m_A}, \tag{4}$$

takes into account the anisotropic nonparabolicity of the electron dispersion at the A-point.

For a crystal slab of finite thickness $L = Na_z$, the general form of the boundary conditions at the crystal surfaces can be written as

$$\psi \pm \nu a_z \partial_z \psi = 0, \tag{5}$$

where ν is a dimensionless constant ~ 1, and it allows the wave function to extend a little beyond the surface of the crystal. $+$ $(-)$ corresponds to the upper (lower) surface of the crystal. Substitution of a general plane-wave wave function, $\psi = ue^{ip_z z} + ve^{-ip_z z}$, where u and v are constants, yields the requirement

$$Np_z a_z + 2\arctan(\nu p_z a_z) = n\pi, \tag{6}$$

where n is an integer. Expansion for small p_z thus gives the quantization condition for small momenta,

$$p_z = \frac{n\pi}{(N + 2\nu)a_z}. \tag{7}$$

Within the bulk CB edge expansion, Eq. (2), the 2D Γ-point energy of subband n in N-layer InSe (denoted $n|N$) can then be expressed as

$$E_{n|N}(n \ll N) \approx \frac{\hbar^2\pi^2}{2m_{Az}a_z^2}\frac{n^2}{(N + 2\nu)^2}. \tag{8}$$

Using subband energies calculated from the HkpTB model, we find that $\nu = 1.42$, as fitted to the intersubband transition energies for the transition from subband 1 to 2, $E_{2|N} - E_{1|N}$. The energies obtained from Eq. (8) are plotted in Fig. 1 alongside those obtained from the few-layer HkpTB model [Eq. (1)]. Additionally, the difference in effective masses for the electron dispersion in different subbands, shown in Fig. 3, arises from the nonparabolicity of the electron dispersion at the A-point. Also, quantization of p_z in a thin film leads to heavier effective masses in higher subbands (for $n \ll N$),

$$\frac{1}{m_{n|N}} \approx \frac{1}{m_A}\left[1 - \frac{6.2n^2}{(N + 2\nu)^2}\right], \tag{9}$$

which produces the difference between the 2D effective masses in the lowest subbands shown in Fig. 4.

IV. INTERSUBBAND TRANSITIONS

For the intersubband transitions between the subbands of the conduction band of n-doped InSe, the population of holes in the valence band is negligible, so excitonic effects do not need to be considered, and the energy of an intersubband optical transition can be taken as that of the subband splitting. The oscillator

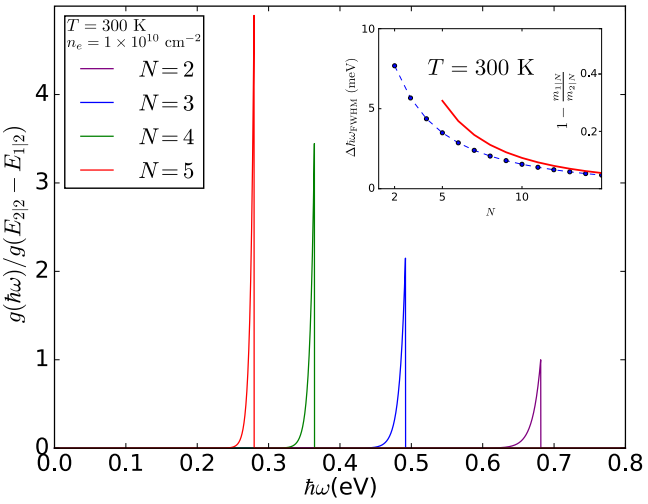

FIG. 4. Intersubband line shapes (normalized to the Γ-point transition in the bilayer) for N-layer InSe for excitation from lowest subband $(1|N)$ to next-lowest subband $(2|N)$, for a very light doping at $T = 300$ K. Inset: thermal broadening ($T = 300$ K, left-hand axis) of absorption lines at light doping due to the difference between subband effective masses (right-hand axis), Eq. (14). The red line was calculated using effective masses approximated by Eq. (9) for $N > 4$.

strength of coupling to z-polarized photons is determined by the electric dipole matrix element,

$$d_z(1|N,b|N) = e\sum_n^N \langle 1|N|\, z(n)(a_{nc}^\dagger a_{nc} + a_{nv}^\dagger a_{nv})\, |b|N\rangle\,, \tag{10}$$

where $z(n) = a_z[n - (N+1)/2]$. Due to the $z \to -z$ symmetry of the HkpTB model, $d_z(1|N,b|N) = 0$ when b is odd (a consequence of setting $t_{vc} = -t_{cv}$). Since the true crystal structure does not have this symmetry, we check the validity of the latter assumption using values from a DFT calculation for the trilayer case—this gives $\frac{|d_z(1|3,3|3)|^2}{|d_z(1|3,2|3)|^2} \sim 10^{-4}$, so the transitions forbidden by the HkpTB model can be safely neglected. In Fig. 3, the nonzero intersubband dipole matrix elements are labeled alongside their respective transitions, and we note that the matrix element for transitions between adjacent subbands is much larger than that for transitions between more distant subbands.

With the subband energies, dipole matrix elements, and effective masses obtained by diagonalizing the Hamiltonian in Eq. (1), we can describe the line shape for intersubband absorption of IR/FIR photons by a slightly n-doped N-layer InSe, from the $n = 1$ subband to the $n = 2$ subband as

$$g(\hbar\omega) \propto |d_z(1|N,2|N)|^2\hbar\omega \times \mathrm{DOS} \times F_T, \tag{11}$$

where the joint density of states of the excitation is given by $\mathrm{DOS}(\hbar\omega) = [\pi\hbar^2(1/m_{1|N} - 1/m_{2|N})]^{-1} \times \Theta(E_{2|N} - E_{1|N} - \hbar\omega)$, while the factor reflecting the occupancy of initial states is

$$F_T = \left\{\exp\left[\frac{1}{k_BT}\left(\frac{E_{2|N} - E_{1|N} - \hbar\omega}{1 - \frac{m_{1|N}}{m_{2|N}}} - E_F\right)\right] + 1\right\}^{-1}, \tag{12}$$

where

$$E_F = k_BT \ln\left[\exp\left(\frac{\pi\hbar^2 n_e}{m_{1|N}k_BT}\right) - 1\right] \tag{13}$$

is the Fermi energy in the lowest subband, relative to the band minimum, of an n-doped InSe film with carrier density n_e. Here we assume that $E_{2|N} - E_{1|N} - E_F \gg k_BT$. The thermal linewidth can be estimated as

$$\Delta\hbar\omega_{\rm FWHM} \approx \max\left\{\left[1 - \frac{m_{1|N}}{m_{2|N}}\right]k_BT\ln 2, E_F\right\}, \tag{14}$$

resulting in the thermal linewidths shown in the inset to Fig. 4, which shows the line shapes (normalized to the Γ-point transition in the bilayer) determined by Eq. (11) for the $1|N \to 2|N$ IR/FIR optical transitions as a function of the transition energy for ($N = 2$–5)-layer InSe at 300 K for a very light doping.

V. EFFECTS OF INTERLAYER SCREENING IN GATED *n*-DOPED InSe

For the intersubband transitions to be active, the system must be n-doped. In the earlier transport experiments on 2D InSe, n-doping was introduced using electrostatic gates. In bulk systems (or thick films), doping by the gates induces accumulation layers of electrons near the surface, where the form of the confinement potential and, therefore, the subband structure of the effective quantum well is determined by the density profile of confined electrons [23]. In a thin film, the doping by the gate applied on one side introduces an asymmetry of potential distribution inside it, increasing the energy separation between the lowest two subbands, while the change in the corresponding lowest subband wave function leads to a partial screening of such potential. Below, we offer a self-consistent analysis of the potential profile and subband splittings induced by the voltage applied to the gate for doping the film with electrons, taking into account the screening (by the induced electrons) of the electric field of the gate. For this, we calculate the excess charges on each layer in the conduction band as

$$n_e(n) = \sum_j \frac{1}{\pi}\int \sum_{\alpha=c,v} |c_{jn}(\alpha,\hat{H}')|^2 F_{Tj}(\hat{H}',k)k\,dk, \tag{15}$$

where $F_{Tj}(\hat{H}',k)$ are the Fermi occupation factors in the jth subband at momentum $\mathbf{k}$, and $c_{jn}(c/v,H')$ are the amplitudes of the jth subband wave function on the nth layer (in terms of the monolayer basis states), evaluated using Eq. (1) with an additional potential energy term added to the on-layer "monolayer" Hamiltonian for each layer,

$$\hat{H}' = \hat{H} + \sum_n U_n(a_{nc}^\dagger a_{nc} + a_{nv}^\dagger a_{nv}). \tag{16}$$

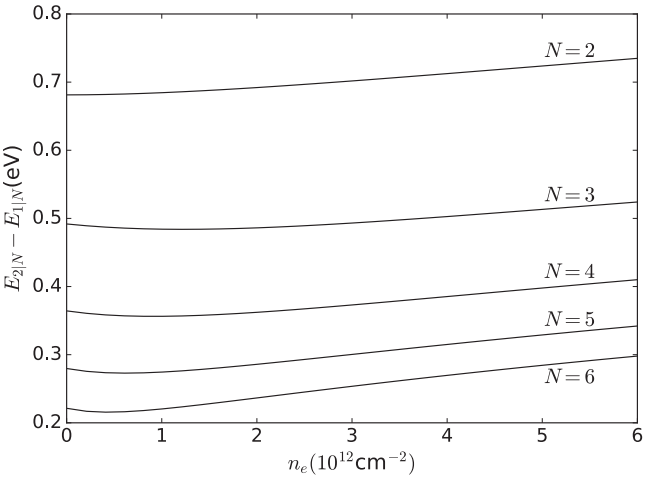

FIG. 5. Intersubband transition energies as a function of total gate-induced carrier density (n_e) for two- to six-layer InSe.

The potential energy profile in $\hat{H}'$ is related to the electron density distribution over the layers as

$$U_{n>1} = U_1 + ea_z \sum_{n'=2}^{n} E_{n'-1,n'}, \quad E_{n-1,n} = \frac{e}{\varepsilon_0} \sum_{n'=n}^{N} n_e(n'),$$

which satisfies the requirement that the total density is determined by the electric field between the top of the film and the gate,

$$E_{\text{ext}} = \frac{e}{\varepsilon_0} n_e, \quad n_e = \sum_n n_e(n).$$

Then, for each density we converge the potential distribution U_n, setting an additional requirement that U_1 has a value chosen to give the desired total carrier density at self-consistency.

The results of the self-consistent calculation are shown in Fig. 5 for the films with two to six layers, over the density range where only states in the lowest subband are filled. Following a slight decrease in the subband spacing at very small gate voltages (where the density distribution remains peaked in the center of the film), we find a steady increase in the intersubband transition energy. The latter result shows that by doping, one can increase the intersubband spacing, thus broadening the spectrum of IR and FIR transitions in the film with a given number of layers, offering an additional tunability of the spectral characteristics of this system.

VI. CONCLUSIONS

In conclusion, we have used a hybrid **k** · **p** tight-binding model, fully parametrized using DFT, to evaluate the energies, oscillator strengths, and thermal linewidths of optical transitions between the subbands of the conduction band of few-layer InSe. The strongest transitions are found to be from the lowest to next-lowest energy subbands, which broadly cover the optical spectrum from ∼0.7 eV down to the low THz range, with thermal linewidths ∼8–0.5 meV at room temperature arising from the variation of in-plane effective masses between the subbands. Similar properties can also be expected for atomically thin films of transition-metal chalcogenides [24], so that 2D materials offer great potential for applications in IR/FIR optoelectronics.

ACKNOWLEDGMENTS

The authors thank S. Slizovskiy, A. Patanè, D. A. Bandurin, A. V. Tyurnina, M. Potemski, Y. Ye, J. Lischner, and N. D. Drummond for discussions. This work made use of the CSF cluster of the University of Manchester. S.J.M. and A.C. acknowledge support from EPSRC CDT Graphene NOWNANO EP/L01548X. V.F. acknowledges support from ERC Synergy Grant Hetero2D, EPSRC EP/N010345, and Lloyd Register Foundation Nanotechnology grant. V.Z. and V.F. acknowledge support from the European Graphene Flagship Project, the N8 Polaris service, the use of the ARCHER national UK supercomputer (RAP Project e547), and the Tianhe-2 Supercomputer at NUDT. Research data are available from the authors on request.

[1] K. S. Novoselov, V. I. Fal'ko, L. Colombo, P. R. Gellert, M. G. Schwab, and K. Kim, Nature (London) **490**, 192 (2012).
[2] A. K. Geim and I. V. Grigorieva, Nature (London) **499**, 419 (2013).
[3] A. C. Ferrari, F. Bonaccorso, V. I. Fal'ko, K. S. Novoselov, S. Roche, P. Bøggild, S. Borini, F. H. L. Koppens, V. Palermo, N. Pugno *et al.*, Nanoscale **7**, 4598 (2015).
[4] R. V. Gorbachev, I. Riaz, R. R. Nair, R. Jalil, L. Britnell, B. D. Belle, E. W. Hill, K. S. Novoselov, K. Watanabe, T. Taniguchi, A. K. Geim, and P. Blake, Small **7**, 465 (2011).
[5] L. Li, Y. Yu, G. J. Ye, Q. Ge, X. Ou, H. Wu, D. Feng, X. H. Chen, and Y. Zhang, Nat. Nanotechnol. **9**, 372 (2014).
[6] H. Liu, A. T. Neal, Z. Zhu, Z. Luo, X. Xu, D. Tománek, and P. D. Ye, ACS Nano **8**, 4033 (2014).
[7] Q. H. Wang, K. Kalantar-Zadeh, A. Kis, J. N. Coleman, and M. S. Strano, Nat. Nanotechnol. **7**, 699 (2012).
[8] V. Zólyomi, N. D. Drummond, and V. I. Fal'ko, Phys. Rev. B **89**, 205416 (2014).
[9] S. J. Magorrian, V. Zólyomi, and V. I. Fal'ko, Phys. Rev. B **94**, 245431 (2016); **96**, 079905(E) (2017).
[10] D. A. Bandurin, A. V. Tyurnina, L. Y. Geliang, A. Mishchenko, V. Zólyomi, S. V. Morozov, R. K. Kumar, R. V. Gorbachev, Z. R. Kudrynskyi, S. Pezzini, Z. D. Kovalyuk, U. Zeilter, K. S. Novoselov, A. Patanè, L. Eaves, I. I. Grigorieva, V. I. Fal'ko, A. K. Geim, and Y. Cao, Nat. Nanotechnol. **12**, 223 (2017).
[11] D. Terry, V. Zólyomi, M. Hamer, A. V. Tyurnina, D. G. Hopkinson, A. M. Rakowski, S. J. Magorrian, Y. M. Andreev, O. Kazakova, K. Novoselov, S. J. Haigh, V. I. Fal'ko, and R. Gorbachev (unpublished).
[12] Z. Ben Aziza, D. Pierucci, H. Henck, M. G. Silly, C. David, M. Yoon, F. Sirotti, K. Xiao, M. Eddrief, J.-C. Girard, and A. Ouerghi, Phys. Rev. B **96**, 035407 (2017).

[13] R. Browning, N. Kuperman, B. Moon, and R. Solanki, Electronics **6**, 27 (2017).
[14] S. R. Tamalampudi, Y.-Y. Lu, R. Kumar U, R. Sankar, C.-D. Liao, K. Moorthy B, C.-H. Cheng, F. C. Chou, and Y.-T. Chen, Nano Lett. **14**, 2800 (2014).
[15] N. Balakrishnan, Z. R. Kudrynskyi, M. W. Fay, G. W. Mudd, S. A. Svatek, O. Makarovsky, Z. D. Kovalyuk, L. Eaves, P. H. Beton, and A. Patanè, Adv. Opt. Mater. **2**, 1064 (2014).
[16] T. Cao, Z. Li, and S. G. Louie, Phys. Rev. Lett. **114**, 236602 (2015).
[17] P. Li and I. Appelbaum, Phys. Rev. B **92**, 195129 (2015).
[18] M. Zhou, R. Zhang, J. Sun, W.-K. Lou, D. Zhang, W. Yang, and K. Chang, Phys. Rev. B **96**, 155430 (2017).
[19] G. W. Mudd, S. A. Svatek, T. Ren, A. Patanè, O. Makarovsky, L. Eaves, P. H. Beton, Z. D. Kovalyuk, G. V. Lashkarev, Z. R. Kudrynskyi, and A. I. Dmitriev, Adv. Mater. **25**, 5714 (2013).
[20] S. J. Magorrian, V. Zólyomi, and V. I. Fal'ko, Phys. Rev. B **96**, 195428 (2017).
[21] G. Kresse and J. Furthmüller, Phys. Rev. B **54**, 11169 (1996).
[22] E. Kress-Rogers, R. Nicholas, J. Portal, and A. Chevy, Solid State Commun. **44**, 379 (1982).
[23] T. Ando, A. B. Fowler, and F. Stern, Rev. Mod. Phys. **54**, 437 (1982).
[24] M. Danovich, D. A. Ruiz-Tijerina, C. Yelgel, V. Zólyomi, and V. I. Fal'ko (unpublished).

3.3 Supplementary material

3.3.1 Optical absorption

As shown in the above publication, the formation of subbands leads to the possibility of photon absorption at frequencies in the infrared and far-infrared range. The optical absorption rate between subbands i and f can be obtained using the Fermi golden rule,

$$\Gamma_{i\to f} = \frac{2\pi}{\hbar}|\langle f|\delta\hat{H}|i\rangle|^2\rho(E_f), \tag{3.1}$$

where $\Gamma_{i\to f}$ is the transition rate from state $|i\rangle$ to $|f\rangle$, $\rho(E)$ is the density of states at energy E and $\delta\hat{H}$ is the light-matter coupling term defined as $\delta\hat{H} = \frac{-e\vec{A}\cdot\vec{p}}{mc}$ coupling states $|i\rangle$ and $|f\rangle$. To obtain the absorption of light polarised in the z-direction, we use the following identity relating the momentum operator between

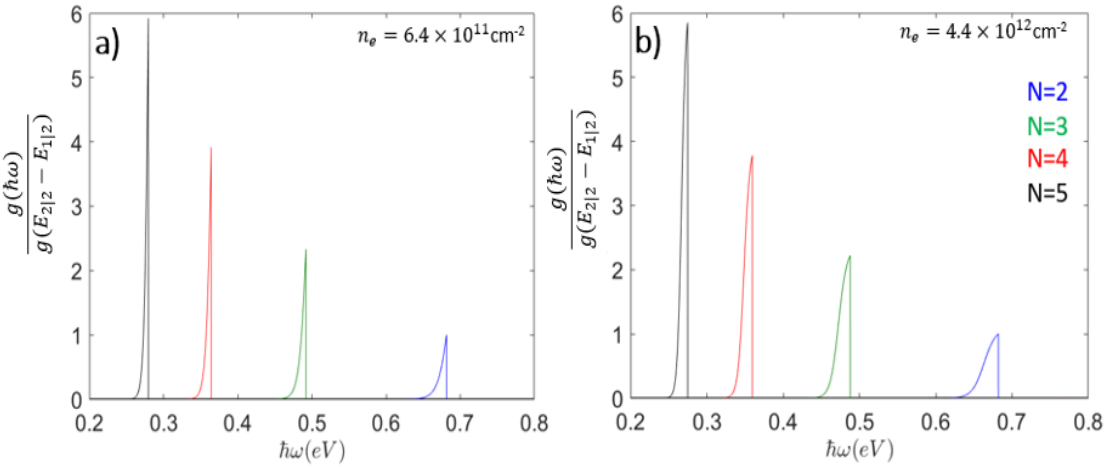

Figure 3.1: Subband optical absorption peaks in different InSe multilayers at two different carrier concentrations. The absorption coefficient of each multilayer thin film was normalised with respect to the absorption coefficient of bilayer at that specific carrier density. A clear broadening of the absorption frequencies as well as a net enhancement of the optical absorption amplitude is observed with increasing carrier density. The dielectric constant used for this calculation was $\epsilon_z = 9.9$ and the temperature used was T=300K.

states $|n\rangle$ and $|k\rangle$ with the dipole moment between them[56]:

$$\hat{x}_{nk} = \frac{-i\hbar\hat{p}^x_{nk}}{m(E_n - E_k)}. \tag{3.2}$$

Integrating the transition rate between the two conduction subbands c^1 and c^i over the totality of occupied states in the conduction band below the Fermi level, we obtain

$$\begin{aligned} W_{i1} &= \frac{2\pi}{\hbar}\int |\langle c^i|\delta H|c^1\rangle|^2 \frac{2}{(2\pi)^2}\delta(E_{c^i} - E_{c^1} - \hbar\omega) f(E_{c^1}(k) - E_F) d^2k \\ &= \frac{2\pi}{\hbar}\int |\langle c^i|\delta H|c^1\rangle|^2 \frac{2}{2\pi}\delta(E_{c^i} - E_{c^1} - \hbar\omega) f(E_{c^1} - E_F) \frac{d(E_{c^i} - E_{c^1})}{\hbar^2|\frac{1}{m_{1|N}} - \frac{1}{m_{i|N}}|}, \end{aligned} \tag{3.3}$$

where $E_{c^i} - E_{c^1}$ is the subband energy difference between the 1^{st} and the i^{th} subband. After integrating over the appropriate energy range effectively limited by the Fermi-Dirac distribution $f(E_{c^1} - E_F)$ assuming that the final state c^i is empty, and dividing by the incident electromagnetic flux given by multiplying the Poynting vector over the visible area, the following expression was obtained for the intersubband optical absorption coefficient

$$\alpha_{i1}(\omega, E_F) = \frac{8\pi d_z^2 \hbar\omega\Theta(E_{i|N} - E_{1|N} - \hbar\omega)}{\hbar^3 c\left|\frac{1}{m_{1|N}} - \frac{1}{m_{i|N}}\right|\left(e^{\frac{1}{k_B T}\left(\frac{E_{i|N} - E_{1|N} - \hbar\omega}{1 - \frac{m_{1|N}}{m_{i|N}}} - E_F\right)} + 1\right)}. \tag{3.4}$$

In the above expression, $E_{i|N} - E_{1|N}$ is the energy difference between the i^{th} and the 1^{st} subband of an N-layer system and $m_{i|N}$ and $m_{1|N}$ are the effective masses of the i^{th} and the 1^{st} conduction subband respectively.

3.3.2 Oscillator strengths

Due to an applied displacement field, the intersubband energies are expected to be altered, leading to a shift in the intersubband absorption frequencies. However, as shown in Eq. (10) and Eq. (11) of the previously presented manuscript,

the optical absorption amplitude hugely depends on the intersubband dipole moment. In applying a displacement field, as well as varying the intersubband energies, it also affects the intersubband dipole moment as well as the in-plane effective masses. To look at the displacement field dependence of the intersubband optical absorption in InSe, it is necessary to look at the electric field dependence of the intersubband dipole moment $d_z^{2,1} \equiv \langle c^2|ez|c^1\rangle$ between the lowest (c^1) and the second lowest (c^2) conduction subband as well as at the effect that the applied displacement field has on the resonant energies. Using perturbation theory, the dependence of the intersubband dipole moment on an applied electric field $\mathcal{E}_z$ can be obtained as

$$\begin{aligned}\tilde{d}_z^{2,1} \equiv \langle c^2|ez|c^1\rangle &= \langle c_0^2 + \frac{c_0^1\mathcal{E}_z d_z^{1,2}}{E_{c^2} - E_{c^1}} + \frac{c_0^3\mathcal{E}_z d_z^{3,2}}{E_{c^2} - E_{c^3}}|ez|c_0^1 + \frac{c_0^2\mathcal{E}_z d_z^{2,1}}{E_{c^1} - E_{c^2}}\rangle \\ &= d_z^{2,1} + \frac{-\mathcal{E}_z^2 d_z^{1,2} d_z^{2,1}}{(E_{c^2} - E_{c^1})^2} + \frac{\mathcal{E}_z^2 d_z^{1,2} d_z^{2,3}}{(E_{c^1} - E_{c^2})(E_{c^2} - E_{c^3})}.\end{aligned} \tag{3.5}$$

As shown in Eq. (3.4), as well as depending on the intersubband oscillator strength, the optical absorption coefficient depends very strongly on the effective mass through the joint density of states.

3.3.3 Effective masses

As shown in Eq. (14) of the above publication, the thermal broadening of the intersubband optical transition crucially depends on the effective masses of the different subbands. Its dependence on the displacement field can be obtained using perturbation theory. Considering the momentum dependence of the $c-c$ interlayer hopping (i.e. t_{cc2}, defined in Eq. (2.23)) as a perturbation and using 1^{st} order perturbation theory on the lowest conduction subband wavefunction Ψ, the following expression can be obtained for the corrections to the conduction band energy dependence on wavevector k

$$\Delta E(k) = \langle\Psi|\delta\hat{H}|\Psi\rangle = \langle\Psi_0 + \delta\Psi|\delta\hat{H}|\Psi_0 + \delta\Psi\rangle. \tag{3.6}$$

In the above expression, the perturbation term $\delta\Psi$ accounts for the effect of a displacement field in the wavefunction distribution of the lowest conduction subband Ψ_0. Considering the limit where the electrostatic potential can be treated as a perturbation due to its smallness compared to the intersubband energy difference, the wavefunctions are modified as

$$|\Psi\rangle = |\Psi_0\rangle + |\Psi_0^j\rangle \sum_{j=2}^{j=N} \frac{\mathcal{E}_z \langle \Psi_0^j | ez | \Psi_0 \rangle}{\Delta E_{1j}} = |\Psi_0\rangle + |\Psi_0^j\rangle \sum_{j=2}^{j=N} \frac{e\mathcal{E}_z \sum_{i=1}^{i=N} z_i \alpha_i \alpha_i^j}{\Delta E_{1j}}. \quad (3.7)$$

The following expression is therefore obtained for the corrections of the subband energy-wavevector dependence with the penultimate term being the corrections linear in the applied electric field

$$\Delta E(k) = \sum_{i=1}^{i=N} k^2 \Big(t_{cc2}\alpha_i(\alpha_{i+1} + \alpha_{i-1}) + 2t_{cc2}\alpha_i(\alpha_{i+1}^j + \alpha_{i-1}^j) \sum_{j=2}^{j=N} \frac{e\mathcal{E}_z \sum_{l=1}^{l=N} z_l \alpha_l \alpha_l^j}{\Delta E_{1j}} \quad (3.8)$$

$$+ O(\mathcal{E}_z^2) \Big).$$

The above expression automatically implies a renormalisation of the in-plane conduction band effective mass with respect to the applied electric field of the form

$$\delta m_c = - \sum_{i=1}^{i=N} \frac{4m_c^2 \Big(t_{cc2}\alpha_i(\alpha_{i+1}^j + \alpha_{i-1}^j) \sum_{j=2}^{j=N} \frac{e\mathcal{E}_z \sum_{i=1}^{i=N} z_l \alpha_l \alpha_l^j}{\Delta E_{1j}} \Big)}{\hbar^2}, \quad (3.9)$$

where m_c is the effective mass of the lowest conduction subband in the unperturbed situation.

Chapter 4

Tunable spin-orbit coupling in two-dimensional InSe

4.1 Introduction

Inversion asymmetric 2D materials have spin-split bands even in the absence of an applied electric or magnetic field. The application of an external displacement field can either enhance or suppress the overall asymmetry of the electron wavefunction[57, 58], resulting in an exceptionally useful tool to easily manipulate the spin-splitting in any given system. Using the method of Löwdin partitioning[59, 60, 61] in combination with the self-consistent algorithm presented in Section.3, the SOC was calculated in the lowest conduction subband of different γ-stacked InSe multilayers, and its dependence on the applied displacement field and carrier density was studied.

The ferroelectric charge transfer in bilayer InSe was calculated using DFT to evaluate its impact on the SOC strength. To account for the intrinsic lack of $z \rightarrow -z$ symmetry, bulk SOC vs k_z was fitted to small interlayer $z \rightarrow -z$ symmetry breaking parameters which take into account the effect that the In atoms have in the interlayer hopping terms. Three mechanisms were found to

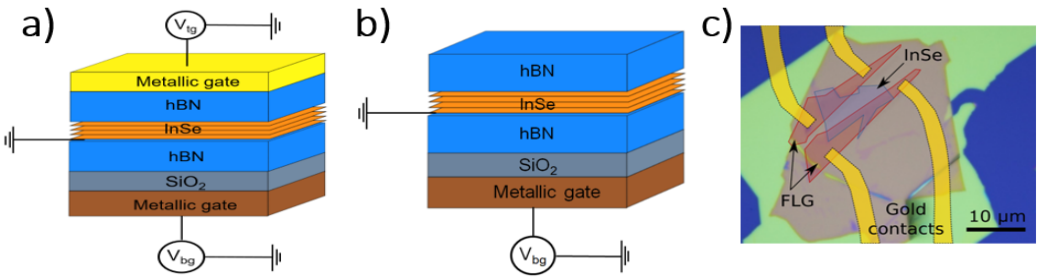

Figure 4.1: a) Schematic diagram of a dual-gated device made of multilayer InSe. b) Schematic diagram of an hBN-encapsulated InSe single-gated device. c) Optical image of the dual-gated device analysed in Section.3 for its SOC properties.

heavily contribute to the overall SOC strength. The first one is the intrinsic lack of inversion symmetry of the crystal, then the overall $z \to -z$ asymmetry of the wavefunction due to the applied electrostatic potential in the thin film, and finally the mixing between different z-parity bands due to the various interband dipole moments. The 14-band Hamiltonian including all these $z \to -z$ symmetry breaking hopping parameters and the SOC terms mixing the different bands was used to calculate the SOC strength in the lowest conduction subband.

Applying such methodology, it was demonstrated how an applied displacement field could completely suppress any intrinsic spin-splitting in multilayer InSe by counteracting the intrinsic $z \to -z$ asymmetry of the thin film. At displacement fields of the order of $D_z = 1.5\text{Vnm}^{-1}$, the SOC was found to completely vanish in the few-layer limit (4-8 layers). The direction of the stacking relative to that of the displacement field generated two branches in the SOC-displacement field dependence. In a single-gated configuration where the application of an electric field implies an increase in the carrier density of the thin film, a complete suppression of the SOC was found a lot more complicated due to the large effect of screening inside the multilayer. It was found necessary to n-dope the system up to carrier densities of the order of $\sim 10^{13}\text{cm}^{-2}$ to completely suppress SOC, which is experimentally very challenging and would require ionic-liquid-gating. Finally, from group-theoretical arguments, a quantum well model was formulated and a generalised expression for the SOC was obtained for any arbitrarily applied electric field $\mathcal{E}_z$ and number of layers N.

The perturbation theory analysis performed to extract the SOC strength was compared with the exact solution obtained from an exact diagonalisation of the 14-band Hamiltonian with good agreement between the two. Finally, the calculated SOC strengths were compared with experimentally extracted SOC splittings obtained from weak antilocalization measurements (see Appendix.B.1 of this thesis) in a high-mobility dual-gated device[6].

4.2 Tunable spin-orbit coupling in two-dimensional InSe

The results of this investigation were presented in Phys.Rev.B (currently under review): "Tunable spin-orbit coupling in two-dimensional InSe"[62].

My contribution to this work: A. Ceferino performed the calculation of SOC in multilayer InSe and analysed the weak antilocalization data provided by D. A. Bandurin. A. Ceferino wrote the manuscript.

Full author list: A. Ceferino, S. J. Magorrian,V. Zólyomi, D. A. Bandurin, A. K. Geim, A. Patanè, Z. D. Kovalyuk, Z. R. Kudrynskyi, I. V. Grigorieva and V. I. Fal'ko.

Author contribution: S. J. Magorrian contributed to the theoretical understanding of SOC in multilayer InSe and computed the ferroelectric charge transfer in bilayer InSe as well as providing DFT data together with V. Zólyomi for few-layer and bulk InSe. D. A. Bandurin provided the experimental data necessary for the comparison with our calculations. Both Z. D. Kovalyuk, Z. R. Kudrynskyi fabricated the InSe device. V. I. Fal'ko, I. V. Grigorieva and A. Patanè contributed to the writing of the manuscript and, together with A. K. Geim supervised the project.

Tunable spin-orbit coupling in two-dimensional InSe

A. Ceferino,[1,2,*] S.J. Magorrian,[2] V. Zólyomi,[3] D.A. Bandurin,[4,1] A.K. Geim,[1,2]
A. Patanè,[5] Z.D. Kovalyuk,[6] Z.R. Kudrynskyi,[5] I.V. Grigorieva,[1,2] and V.I. Fal'ko[1,2,7]

[1]*Department of Physics and Astronomy, University of Manchester, Oxford Road, Manchester, M13 9PL, United Kingdom*
[2]*National Graphene Institute, Booth Street East, Manchester, M13 9PL, United Kingdom*
[3]*STFC Hartree Centre, Daresbury Laboratory, Daresbury, Warrington, WA4 4AD, United Kingdom*
[4]*Department of Physics, Massachusetts Institute of Technology, Cambridge, Massachusetts 02139, USA*
[5]*School of Physics and Astronomy, University of Nottingham, Nottingham, NG7 2RD, UK*
[6]*Institute for Problems of Materials Science, The National Academy of Sciences of Ukraine, Chernivtsi, 58001, Ukraine*
[7]*Henry Royce Institute for Advanced Materials, Manchester, M13 9PL, United Kingdom*

We demonstrate that spin-orbit coupling (SOC) strength for electrons near the conduction band edge in few-layer γ-InSe films can be tuned over a wide range. This tunability is the result of a competition between film-thickness-dependent intrinsic and electric-field-induced SOC, potentially, allowing for electrically switchable spintronic devices. Using a hybrid $\mathbf{k}\cdot\mathbf{p}$ tight-binding model, fully parameterized with the help of density functional theory computations, we quantify SOC strength for various geometries of InSe-based field-effect transistors. The theoretically computed SOC strengths are compared with the results of weak antilocalization measurements on dual-gated multilayer InSe films, interpreted in terms of Dyakonov-Perel spin relaxation due to SOC, showing a good agreement between theory and experiment.

I. INTRODUCTION

Indium selenide (InSe) is a layered semiconductor with already demonstrated high mobility and versatile optical properties[1–8]. Atomically thin InSe films (exfoliated from bulk crystals[9] or produced by chemical vapour deposition[10]) have already been used to fabricate field-effect transistors (FET devices). Moreover, the persistence of high mobility[11–13] of electrons in n-type doped γ-InSe to only few atomic layers[3,4,9] in thickness makes it feasible to implement InSe in spintronic devices[14]. In contrast to the conventional InAs[15] or HgTe[16] quantum wells, in γ-InSe it is possible to completely suppress the conduction band SOC using applied displacement field, allowing for exceptionally tunable spintronic devices. One of the methods to control the electron spin in semiconductors is to manipulate its spin-orbit coupling (SOC)[17–23], and, in this paper, we study the dependence of SOC for two dimensional (2D) electrons near the conduction band edge of InSe films on the number of layers and on the gate-controlled electrostatic doping in the films implemented in the FET geometry[24–31].

Below, we use the earlier developed hybrid $\mathbf{k}\cdot\mathbf{p}$ tight-binding (HkpTB) model for InSe[33,34], taking into account the s and p_z orbital composition of the lowest conduction subband and self-consistent analysis of the electrostatic potential on each layer[35], and show that the dominant term in the SOC in γ-stacked InSe multilayer thin film (any number of layers) has the generic form,

$$\hat{H}_{SOC} = \alpha(\mathbf{s}\times\mathbf{k})\cdot\hat{\mathbf{z}}. \qquad (1)$$

This is the only linear in wavevector $\mathbf{k}=(k_x,k_y)$ of electron (in the vicinity of the Γ-point) term allowed by C_{3v} point-group symmetry of the lattice of γ-stacked multilayer (the next term in the $\mathbf{k}\cdot\mathbf{p}$ theory expansion would be of the third order[36] in k, hence, much weaker for a

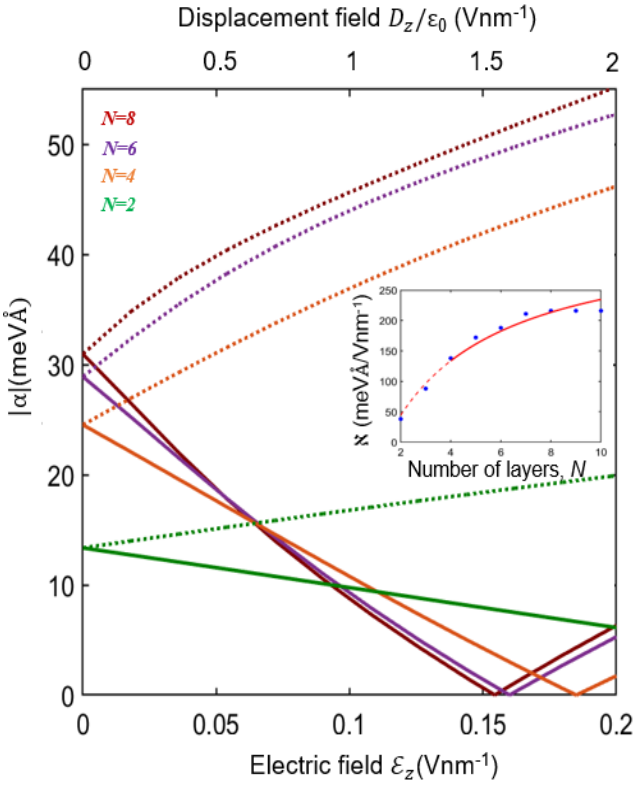

FIG. 1. SOC strength dependence on displacement field and number of layers N at $n_e = 0$ in a dual-gated FET geometry. InSe dielectric constant[32] used here is $\epsilon_z = 9.9$. The inset shows the layer-number-dependence of parameter ℵ used to take into account the influence of an electric field $\mathcal{E}_z$ in Eq. (2). The solid and dotted lines indicate respectively when the applied displacement field suppresses or enhances the Dresselhaus SOC.

E_v	-2.79 eV	t^{Γ}_{cc}	0.34 eV	m_c	0.266 m_0
t^{Γ}_{vv}	-0.41 eV	t_{cc_2}	-3.43 eVÅ^2	E_{v_1}	-3.4 eV
E_{v_2}	-3.5 eV	t^{Γ}_{cv}	0.25 eV	t_{cv_2}	-3.29 eVÅ^2

E_{cv}	2.79 eV
E_{c_1c}	1.09 eV
E_{vv_1}	0.54 eV
E_{vv_2}	0.683 eV
b_{54}	10.54 eVÅ
λ_{15}	0.119 eV
b_{16}	-2.77 eVÅ
$b^{c_1v_2}_{16}$	8.51 eVÅ
d_{cv}	-1.68 eÅ
$d_{v_1v_2}$	-2.56 eÅ
d_{c_1c}	0.86 eÅ
t^{Γ}_{cc}	0.34 eV
t^{Γ}_{vv}	-0.41 eV
t^{Γ}_{cv}	0.25 eV
t_{cc_1}	0.019 eV
$t_{v_1v_2}$	0.048 eV
δ_{cv}	0.014 eV
δ_{c_1c}	0.022 eV
$\delta_{v_1v_2}$	-0.001 eV
λ_{46}	-0.09 eV
a_z	8.32 Å

TABLE I. (Top) Two-band hybrid $\mathbf{k}\cdot\mathbf{p}$ tight-binding parameters extracted from the 14-band model in the bottom table. (Bottom) Hybrid $\mathbf{k}\cdot\mathbf{p}$ tight-binding model parameters used in the perturbation theory analysis. Numerical indices in the b and λ terms label the symmetry group shown in the character table in Fig. 4. The magnitude of the out-of-plane dipole moments d_{cv}, $d_{v_1v_2}$ and d_{c_1c} were obtained from the tight-binding model developed in Ref. 33. The SOC parameter λ_{46} was calculated from the fits performed in Appendix A and the interlayer distance $a_z = 8.32$Å was obtained from the experimental measurements shown in Ref. 40.

feasible doping of the film)[37–39]. In Eq. (1), $\mathbf{s} = (\sigma_x, \sigma_y)$ is a vector composed of Pauli matrices, and α is a layer-number-dependent factor,

$$\alpha(\mathcal{E}_z, N) \approx \alpha_\infty \left(1 - \frac{\chi}{(N+2.84)^2}\right) \pm \mathcal{E}_z \aleph. \qquad (2)$$

Here, $\alpha_\infty \approx 34.5$ meVÅ is the value of SOC at the conduction band edge of 3D bulk γ-InSe, N is the number of layers in a thin film, $\chi \approx 14.9$ accounts for the non-linear dependence of bulk SOC on the out-of-plane momentum k_z counted from the bulk A-point band edge, at $k_A = \frac{\pi}{a_z}$. Also $\mathcal{E}_z$ is the electric field piercing the film, and parameter $\aleph$ quantifies the dependence on the electric field, as shown in the inset of Fig. 1.

The overall strength of SOC in Eq. (2) is determined by the interplay between the intrinsic lattice asymmetry of the crystal (known as Dresselhaus contribution[41]) and the electric-field-induced symmetry breaking (the so-called Bychkov-Rashba term[42]). This interplay allows for the tunability of the SOC value, both by choosing the film thickness (Nd), and by applying a displacement field in the double-gated (both top- and bottom-gated) devices. The results of our analysis are exemplified in Fig. 1, indicating that a vertically applied electric field $\mathcal{E}_z \sim 0.15$-0.20 Vnm^{-1} would be enough to switch SOC off and on, opening new avenues towards the design of spintronic devices. This form of SOC in a film is the result of $\mathbf{k}\cdot\mathbf{p}$ and tight-binding model analysis[43], parameterized using density functional theory (DFT) computations of the band structure. The theoretically calculated SOC size was compared with the values of SOC strength extracted from weak antilocalization magnetoresistance, measured in a FET based on a six-layer InSe device. We find a good agreement between theory and experiment in the available range of device parameters.

Below, the paper is organized as follows. In Section II, we compute the SOC coefficient in the lowest conduction subband of InSe using DFT *ab intio* calculations, in Section III, we perform simple perturbative calculations of SOC strength in the lowest conduction subband of bilayer InSe and, in Section IV, we generalise the bilayer formalism for an arbitrary number of layers. Finally, in Section V, we compare the theoretically obtained SOC coefficient with the values experimentally measured in an available InSe-based FET device.

II. FIRST PRINCIPLES CALCULATIONS OF InSe PARAMETERS

As a background to the hybrid $\mathbf{k}\cdot\mathbf{p}$ tight-binding (HkpTB) model presented in this manuscript, we overview the density functional theory bandstructure of monolayer and few-layer InSe.

Monolayer InSe has pairs of vertically aligned metal

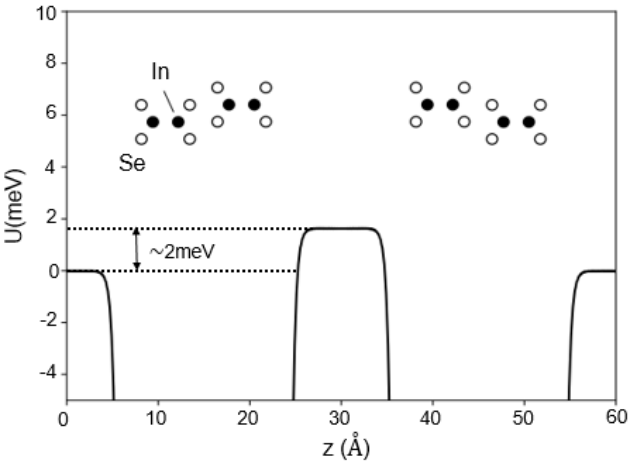

FIG. 2. Plane-averaged electrostatic potential accounting for ionic and Hartree contributions in a double-bilayer InSe supercell (supercell structure shown as inset).

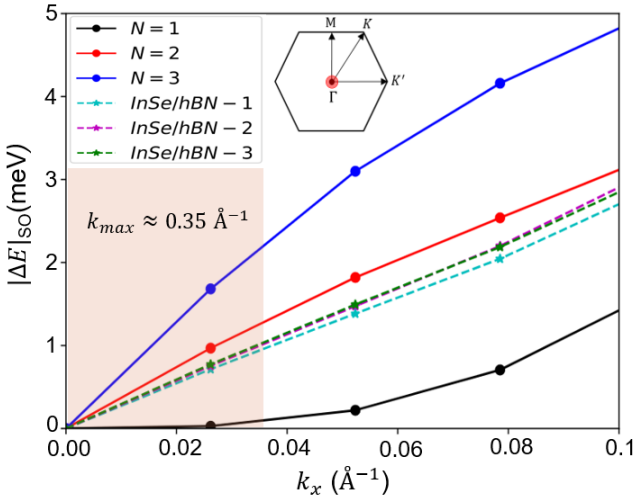

FIG. 3. DFT-calculated conduction band spin-orbit splitting for mono-, bi-, and tri-layer InSe in for small k_x near the Γ-point. The finite thickness of the film discretizes k_z while k_x and k_y remain continuous variables. While the cubic Dresselhaus SOC splitting is expected to be zero in the $\Gamma - M$ direction, in the $(k_x, 0)$ orientation a finite contribution is expected. In contrast to the orientation-dependent cubic SOC, the expected form of the linear SOC splitting (see Eq. (1)) makes this contribution isotropic in $\mathbf{k}$. The shaded region labels the range in k_x below the Fermi level of a device doped with a carrier density of $n_e \approx 2 \times 10^{12}\text{cm}^{-2}$. The clear linear spin splitting with k_x indicates the dominance of the linear SOC terms near the Brillouin zone (BZ) center. Also plotted using stars connected by dashed lines are values of splitting for a monolayer InSe/monolayer hBN heterostructure for three different in-plane stacking configurations. (Inset) Hexagonal BZ of monolayer InSe. The red circle indicates the region in the BZ with wavevector magnitude in the range presented.

D_{3h}	E	σ_h	$2C_3$	$2S_3$	$3C_{2i}^{'}$	$3\sigma_{vi}$	*basis*	*orbitals*	*bands*
$A_1'(\Gamma_1)$	1	1	1	1	1	1	1	(s^+, p_z^-)	v, c_1
$A_2'(\Gamma_2)$	1	1	1	1	-1	-1	xy		
$E'(\Gamma_6)$	2	2	-1	-1	0	0	(x, y)	(p_x^+, p_y^+)	v_2
$A_1''(\Gamma_3)$	1	-1	1	-1	1	-1	xyz		
$A_2''(\Gamma_4)$	1	-1	1	-1	-1	1	z	(s^-, p_z^+)	c
$E''(\Gamma_5)$	2	-2	-1	1	0	0	(xz, yz)	(p_x^-, p_y^-)	v_1

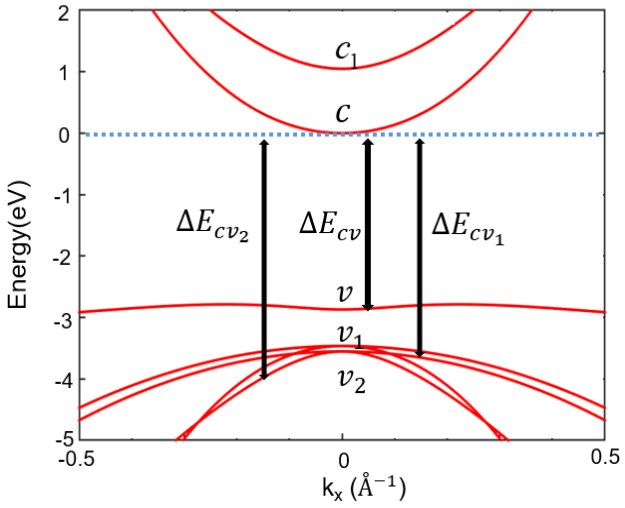

FIG. 4. (Top) Character table of the point-group D_{3h} which captures the symmetries of monolayer InSe. In parenthesis, the Bethe notation for each irrep is shown. Both the basis function of each irreducible representation as well as the orbital composition of any band relevant for our analysis are displayed in the final columns. The σ_h conjugacy class in the character table labels the $z \to -z$ symmetry of each irreducible representation. This crucially determines which bands are mixed due to an applied electric field. The superscripts on top of the orbitals indicate the parity with respect to the $z \to -z$ symmetry calculated in Ref. 46. (Bottom) Band structure of monolayer InSe without SOC.

atoms in the middle sublayers and chalcogens in the outer sublayers, arranged on a plane into a honeycomb structure. Such a lattice has a D_{3h} point-group symmetry which includes mirror plane symmetry, rotations by 120°, but not inversion symmetry. In any few-layer γ-InSe film, the $z \to -z$ mirror symmetry is broken. This opens a possibility for a weak "ferroelectric" charge transfer between the layers due to layer-asymmetric hybridization between the conduction and valence bands and the resulting built-in electric field in the film which may be relevant for the self-consistent analysis of the on-layer potential in a film with a finite thickness. To find out whether this is of relevance for InSe, or not, we carry out DFT calculations on a supercell with a large vacuum separating two mirror reflected images of a γ-InSe bilayer, to satisfy periodic boundary conditions without affecting the mismatch between vacuum potentials, produced by the double-charge layer due to the charge transfer (see Fig. 2 and inset). For the DFT calculations, we used the generalized gradient approximation (GGA) of Perdew, Burke and Ernzerhof[44], with an $12 \times 12 \times 1$ k-point grid and a plane-wave cutoff energy of 600 eV, implemented in the VASP code[45]. Monolayer atomic structure parameters, and interlayer distances, are taken from an experimental reference for the bulk crystal[40]. We find that the charge transfer between the layers is small, yielding a ≈ 2 meV vacuum potential difference across the bilayer in Fig. 2, which is so small that it will be neglected for the rest of the manuscript.

Due to its mirror symmetry, the monolayer Hamiltonian cannot include s_x, and s_y operators, that is, it does not display a 2D SOC. However, its symmetry allows for spin-orbit splitting in the form of[41,46]

$$\hat{H}_{so} = \gamma k^3 \sin(3\phi)\hat{s}_z \tag{3}$$

where ϕ is the polar angle with respect to the $\Gamma - M$ direction and $\hat{s}_z$ is the third Pauli matrix. This is reflected by the results of DFT computations of conduction band dispersion in mono-, bi-, and trilayers shown in Fig. 3(a). Note that the spin polarization of the computed states is in z-direction only for monolayers, whereas for bi- and trilayers, where it has a linear dependence announced in Eq. (1), it reflects in-plane spin splitting. In fact, for the

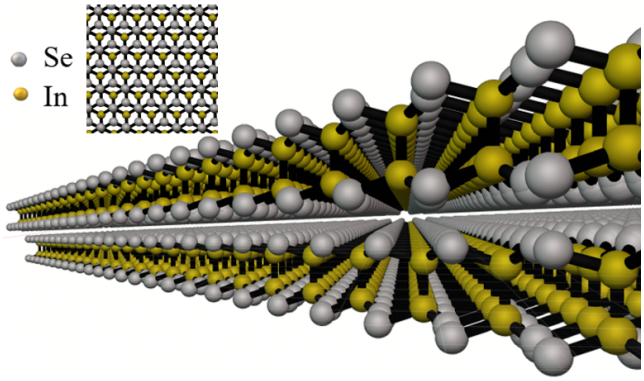

FIG. 5. Profile and top view of bilayer γ-stacked InSe. The Se atom of the top layer is shown to sit above the In atom of the bottom layer but not the other way around. This crystallographic z-asymmetry is responsible for an effective "electric field" at the origin of the Dresselhaus SOC in bilayer InSe.

range of in-plane wavenumbers corresponding to feasible doping densities, the spin splitting in the monolayer is negligibly small.[47]. We also carried out DFT calculations for a heterobilayer consisting of monolayer of InSe, and monolayer of hBN (the latter was strained to give commensurability with a lattice constant $a_{\rm hBN} = a_{\rm InSe}/\sqrt{3}$ and rotated to align the armchair direction of hBN with the zigzag direction of the InSe). We take the interlayer distance as 0.333 nm between the middle of hBN and the nearest plane of Se atoms. A dipole correction was applied, and we considered three in-plane configurations: (1) boron directly above indium, (2) nitrogen above indium (the hBN is inverted in-plane), and (3) configuration (1) with the hBN shifted in-plane by half the B-N vector. The spin-orbit splitting near Γ in the (InSe-dominated) conduction band edge is plotted for all 3 configurations in Fig. 3. For the monolayer InSe/monolayer hBN heterostructure, we obtain a SOC which depends very weakly on the configuration, with a strength similar to that of the isolated InSe bilayer.

III. SPIN-ORBIT COUPLING IN InSe BILAYER

InSe belongs to the family of group-III metal-monochalcogenides with the s and p orbitals of In and Se dominating the low-energy dispersion in the vicinity of the Γ-point[33,43,46]. In the bottomost conduction band c and in the topmost valence band v, the atomic orbital composition is mainly dominated by the s and p_z orbitals of both In and Se. The deeper valence bands v_1 and v_2 are prominently Se p_x and p_y orbitals which are naturally split by the atomic SOC of the Se atoms.

In going from monolayer to bilayer γ-stacked InSe (see Fig. 5), the mirror plane symmetry is broken, reducing the symmetry from the point-group D_{3h} to C_{3v}. This allows for a linear in momentum SOC splitting in the form presented in Eq. (1) prescribed by the third-order rotation symmetry axis[48]. Consequently, the interlayer hoppings need to account for the reduction of the global symmetries of the bilayer, leading to a finite Dresselhaus SOC. This appears via the interlayer mixing of the opposite z-parity bands.

We construct a bilayer Hamiltonian using monolayer Hamiltonians described in Ref. 33 taking into account interlayer hopping[33] and the intralayer interband spin-orbit coupling[49],

$$\hat{H} = \hat{H}^{(0)} + \delta\hat{H} = \begin{pmatrix} \hat{H}^{(0)}_{11} + \delta\hat{H}_{11} & \hat{H}^{(0)}_{12} + \delta\hat{H}_{12} \\ \hat{H}^{(0)}_{21} + \delta\hat{H}_{21} & \hat{H}^{(0)}_{22} + \delta\hat{H}_{22} \end{pmatrix}, \quad (4)$$

For the analysis of SOC in the bilayer, band edge states in the constituent monolayers,

$$\Psi^{\rm T} \equiv [c^{\uparrow}, c^{\downarrow}; c_1^{\uparrow}, c_1^{\downarrow}; v^{\uparrow}, v^{\downarrow}; v_1^{\uparrow,p_x}, v_1^{\downarrow,p_x}; v_1^{\uparrow,p_y}, v_1^{\downarrow,p_y}; v_2^{\uparrow,p_x}, v_2^{\downarrow,p_x}; v_2^{\uparrow,p_y}, v_2^{\downarrow,p_y}],$$

for the bands described in Section II, will be characterised by their respective band energies, neglecting an almost parabolic band dispersion,

$$\hat{H}^{(0)}_{11(22)} = \begin{pmatrix} -U_{1(2)} & 0 & 0 & 0 & 0 \\ 0 & E_{c_1} - U_{1(2)} & 0 & 0 & 0 \\ 0 & 0 & E_v - U_{1(2)} & 0 & 0 \\ 0 & 0 & 0 & (E_{v_1} - U_{1(2)})\hat{\mathbf{I}}_\nu & 0 \\ 0 & 0 & 0 & 0 & (E_{v_2} - U_{1(2)})\hat{\mathbf{I}}_\nu \end{pmatrix}. \quad (5)$$

Here $\hat{\mathbf{I}}_\nu$ is the identity operator in the 2×2 space of atomic p_x, p_y orbital components of v_1 and v_2.

E_{c_1}, E_v, E_{v_1} and E_{v_2} are the energy differences between the lowest conduction band and the c_1, v, v_1 and v_2 bands, respectively, (see Fig. 4). In addition, we take into account linear in momentum interband terms in the monolayer Hamiltonian , discussed earlier in relation to the optical selection rules for the interband transitions[49],

$$\delta\hat{H}_{11(22)} = \begin{pmatrix} 0 & 0 & 0 & ib_{54}\mathbf{k}\cdot\mathbf{\Lambda} & i\lambda_{46}(\mathbf{s}\times\mathbf{\Lambda}) \\ 0 & 0 & 0 & 0 & ib_{16}^{c_1v_2}(\mathbf{k}\cdot\mathbf{\Lambda}) \\ 0 & 0 & 0 & i\lambda_{15}(\mathbf{s}\times\mathbf{\Lambda}) & ib_{16}(\mathbf{k}\cdot\mathbf{\Lambda}) \\ -ib_{54}(\mathbf{k}\cdot\mathbf{\Lambda})^T & 0 & -i\lambda_{15}(\mathbf{s}\times\mathbf{\Lambda})^\dagger & 0 & 0 \\ -i\lambda_{46}(\mathbf{s}\times\mathbf{\Lambda})^\dagger & -ib_{16}^{c_1v_2}(\mathbf{k}\cdot\mathbf{\Lambda})^T & -ib_{16}(\mathbf{k}\cdot\mathbf{\Lambda})^T & 0 & 0 \end{pmatrix}, \tag{6}$$

Here 1×2 matrices $\mathbf{\Lambda_y}$=[0,1] and $\mathbf{\Lambda_x}$=[1,0] operate in the p_x, p_y orbital components of v_1 and v_2 valence bands and the coefficients b_{45}, b_{16} and $b_{16}^{c_1v_2}$ characterise the $c-v_1$, $v-v_2$ and c_1-v_2 intra-layer couplings (associated with interband optical transitions excited by the in-plane polarised photons). Spin Pauli matrices $\mathbf{s_{x,y}}$ produce spin flips upon the interband mixing which can be rooted to atomic $\mathbf{S}\cdot\mathbf{L}$ coupling (between $p_{x/y}$ and p_z orbitals which contribute to c, v, v_1, v_2 bands captured by parameters λ_{15} and λ_{46}). Note that $\mathbf{k}\cdot\mathbf{\Lambda} \equiv k_x\mathbf{\Lambda_x} + k_y\mathbf{\Lambda_y}$ and $\mathbf{s}\times\mathbf{\Lambda} \equiv \mathbf{s_x}\mathbf{\Lambda_y} - \mathbf{s_y}\mathbf{\Lambda_x}$.

Hopping between neighbouring layers is accounted for by the following two terms,

$$\hat{H}_{12}^{(0)} = \begin{pmatrix} t_{cc}^\Gamma & 0 & 0 & 0 & 0 \\ 0 & 0 & 0 & 0 & 0 \\ 0 & 0 & t_{vv}^\Gamma & 0 & 0 \\ 0 & 0 & 0 & 0 & 0 \\ 0 & 0 & 0 & 0 & 0 \end{pmatrix}, \tag{7}$$

$$\delta\hat{H}_{12} = \begin{pmatrix} 0 & (t_{cc_1}+\delta_{c_1c}) & (t_{cv}^\Gamma+\delta_{cv}) & 0 & 0 \\ (-t_{cc_1}+\delta_{c_1c}) & 0 & 0 & 0 & 0 \\ (-t_{cv}^\Gamma+\delta_{cv}) & 0 & 0 & 0 & 0 \\ 0 & 0 & 0 & 0 & 0 \\ 0 & 0 & 0 & 0 & 0 \end{pmatrix}. \tag{8}$$

The first of them describes the resonant interlayer hybridization of separately lower conduction and the top valence band edges, which was identified[33] as the strongest hybridization effect, determined by the substantial weight of s and p_z chalcogen orbitals in the sublattice composition of the band edge states. The second term takes into account interband interlayer hybridization, which produces a much weaker effect on the band edge energies, but is sensitive to the mirror symmetry breaking set by stacking of the layers (see Fig. 4).

According to the table in Fig. 4, the on-layer states in bands c are odd under $z\to-z$ reflection while bands v and c_1 are even under the same transformation. Because of this, for a mirror symmetric arrangement of the layers, the corresponding interband interlayer couplings would obey the relation $t_{cv}^\Gamma = -t_{vc}^\Gamma$ and $t_{c_1c} = -t_{cc_1}$. To capture the mirror plane symmetry breaking for γ-stacking, we introduce parameters $\delta_{\alpha\beta}$ such that $t_{cv}^\Gamma = t_{cv}^\Gamma + \delta_{cv}$, $t_{vc}^\Gamma = -t_{cv}^\Gamma + \delta_{cv}$, $t_{v_1v_2} = t_{v_1v_2} + \delta_{v_1v_2}$, $t_{v_2v_1} = -t_{v_1v_2} + \delta_{v_1v_2}$, $t_{cc_1} = t_{cc_1} + \delta_{c_1c}$, and $t_{c_1c} = -t_{cc_1} + \delta_{c_1c}$. Overall, the $z\to-z$ symmetry breaking in the bilayer (which gives rise to the 2D SOC in the lowest conduction subband of the bilayer) is produced by the interplay between δH_{11} and the contributions from $\delta_{\alpha\beta}$ in Eq. (9). For this we use 3^{rd} order pertubation theory with respect to parameters $\delta_{c_1c}, \delta_{cv}, b_{54}, b_{16}, b_{16}^{c_1v_2}, \lambda_{15}$, and λ_{46}, and this results in the spin-orbit coupling constant,

$$\alpha_0 = 2\left(\frac{b_{54}\lambda_{15}\delta_{cv}}{\Delta E_{cv_1}\Delta E_{g^1}} + \frac{b_{16}\lambda_{46}\delta_{cv}}{\Delta E_{cv_2}\Delta E_{g^1}} + \frac{b_{16}^{c_1v_2}\lambda_{46}\delta_{c_1c}}{\Delta E_{cc_1}\Delta E_{cv_2}}\right). \tag{9}$$

Here we also account for asymmetry induced by an external electric field so its effect on the on-layer energy of the orbitals in Eq. (5), captured by $\Delta E_{cv_1} \equiv -(t^{\Gamma}_{cc} + E_{v_1})$, $\Delta E_{cv_2} \equiv -(t^{\Gamma}_{cc} + E_{v_2})$ and $\Delta E_{cc_1} \equiv -(t^{\Gamma}_{cc} + E_{c_1})$ are the energy differences between the lowest conduction subband and v_1, v_2 and c_1 bands while $\Delta E_{g^{1(2)}} = -(t^{\Gamma}_{cc} + E_v) \pm t^{\Gamma}_{vv}$ is the energy difference between the lowest conduction subband and the 1^{st} or 2^{nd} topmost valence subband, respectively.

In the absence of external electric field, $U_1 = U_2 = 0$, and using parameters in Table III, we estimate that $\mathcal{E}_z(\alpha_0 = 0) = 0.35\text{Vnm}^{-1}$. The dependence on a perpendicularly applied electric field $\mathcal{E}_z$ is approximated by

$$\aleph \equiv \left.\frac{d\alpha}{d\mathcal{E}_z}\right|_{U_1=U_2=0} = \frac{(b_{54}\lambda_{15} + b_{16}\lambda_{46})ea_z t^{\Gamma}_{cv}}{\Delta E_{cv_1}} \times \left(\frac{2t^{\Gamma}_{vv}}{\Delta E_{g^1}\Delta E_{g^2}}\right)\left(\frac{1}{2t^{\Gamma}_{cc}} - \frac{1}{2t^{\Gamma}_{vv}}\right). \quad (10)$$

Here, $a_z = 8.32$ Å is the interlayer distance between the central planes of two neighbouring InSe monolayers. Using parameters in Table I we estimate that for a bilayer $\aleph = 38\text{meVÅ/Vnm}^{-1}$, this also means that an electric field $\mathcal{E}_z = 0.35$ Vnm^{-1} would reduce the 2D SOC coupling strength to zero.

In addition to the above-discussed effects, mirror symmetry breaking may be caused by the encapsulation environment[50] coupling on the Se orbitals in the outer top/bottom sublayers of the crystal. This asymmetry may be due to the difference between the encapsulating materials, or even due to a different orientation of the top/bottom encapsulating layers of the same compound, e.g., hexagonal boron nitride (hBN). To describe this effect, we introduce an additional term in the bilayer Hamiltonian responsible for $c-v$, v_1-v_2 band mixing with randomly different strength in the top and bottom layers,

$$\delta\hat{H}^{(I)}_{11(22)} = \begin{pmatrix} \Delta E_{c1(2)} & 0 & \pm\Upsilon^{t/b}_{cv} & 0 & 0 \\ 0 & 0 & 0 & 0 & 0 \\ \pm\Upsilon^{t/b}_{cv} & 0 & \Delta E_{v1(2)} & 0 & 0 \\ 0 & 0 & 0 & \Delta E_{v_1 1(2)}\hat{\mathbf{I}}_\nu & \pm\Upsilon^{t/b}_{v_1v_2}\hat{\mathbf{I}}_\nu \\ 0 & 0 & 0 & \pm\Upsilon^{t/b}_{v_1v_2}\hat{\mathbf{I}}_\nu & \Delta E_{v_2 1(2)}\hat{\mathbf{I}}_\nu \end{pmatrix}. \quad (11)$$

Here, $\Delta E_{c1(2)}$ and $\Delta E_{v1(2)}$ are the energy shifts of the c and the v bands in the 1^{st} and 2^{nd} layer respectively; $\Delta E_{v_1 1(2)}$ and $\Delta E_{v_2 1(2)}$ are the energy shifts of the bands v_1 and v_2 and $\hat{\mathbf{I}}_\nu$ is the identity operator in the 2×2 space of atomic p_x, p_y orbital components of the v_1 and v_2 bands. The terms Υ^{t}_{cv} and $\Upsilon^{t}_{v_1v_2}$ are responsible for $c-v$ and v_1-v_2 band mixing in the top layer: the interfacial $z \to -z$ symmetry breaking couples states of opposite parities. In the bottom surface, the interfacial effect is inverted, which is the reason for the inverted signs, $-\Upsilon^{b}_{cv}$ and $-\Upsilon^{b}_{v_1v_2}$ of the corresponding terms in $\delta\hat{H}^{(I)}_{11(22)}$. In Table II, we quote values of all those parameters obtained using DFT modelling described in Section II. In order to extract those parameters, the wavefunctions of bands c and v_1 were obtained for the three different atomic arrangements described in Section II. By comparing their wavefunction distribution with the DFT-computed wavefunctions of suspended monolayer InSe, the mixing terms between opposite z-parity bands Υ_{cv} and $\Upsilon_{v_1v_2}$ was extracted for each configuration. Finally, from the DFT energy eigenvalues, the shifts in energy of bands c and v were obtained for each of the three different configurations; the energy shifts of bands v_1 and v_2 were neglected due to the very weak interlayer hybridization of those bands which results in a negligible contribution to the conduction band SOC strength. Using pertubation theory, we calculate the contribution of these additional terms towards bilayer SOC and find that the dominant effect comes from the $c-v$ band mixing, resulting in,

$$\alpha^{(I)} = \Big[\frac{b_{45}\lambda_{15}}{\Delta E_{g^1}\Delta E_{cv_1}} + \frac{b_{16}\lambda_{46}}{\Delta E_{g^1}\Delta E_{cv_2}}\Big]\Big(\Upsilon^{t}_{cv} - \Upsilon^{b}_{cv}\Big). \quad (12)$$

The above equation suggests that encapsulation of InSe with the same material in the top and bottom would

InSe/hBN stacking	ΔE_c	ΔE_v	$\lvert\Upsilon_{cv}\rvert$	$\lvert\Upsilon_{v_1v_2}\rvert$
1	140meV	141meV	35.6meV	36.98meV
2	155meV	95meV	20.5meV	32.77meV
3	146meV	141meV	35.6 meV	39.37meV

TABLE II. DFT-estimated parameters describing the effect of hBN substrate or overlay on an InSe monolayer in Eq. (11).

result in the cancellation of the main part of such an additional contribution. Due to misalignement or an offset of the encapsulating crystals, this cancelation would never be exact leaving a residual effect due to the variation of InSe and, e.g., hBN stacking. Taking into account the random nature of such a variation, in the mechanically assembled structures, we estimate characteristic size of the residual SOC contribution using the characteristic difference of the Υ_{cv} parameters for two InSe/hBN stackings analysed in Section II (Configuration 1 and 2 in Table II and Fig. 3). This gives $|\alpha^{(I)}| \sim 3.5$meVÅ, which is an order of magnitude smaller than $\alpha_0 = 13$meVÅ. As a result, for InSe bilayer encapsulated with hBN on both sides, the value and displacement field dependence of SOC can be well described using Eq. (9) and (10).

IV. SPIN-ORBIT COUPLING IN MULTILAYER InSe

Here, we combine the analysis of two factors that determine the strength of SOC in multilayer γ-InSe: the asymmetry embedded into the interlayer hybridization and the effect of an externally controllable electric field.

A. Self-consistent analysis of subband electrostatics in doped multilayer InSe films

In this section, the effect of an externally applied electrostatic potential (gating) for electrons in the lowest conduction subband is calculated self-consistently, and its effect on the charge distribution and on the band gap is discussed for the dual and single-gated FET geometry as sketched in insets of Fig. 11 and Fig. 13, respectively. To quantify the SOC in the lowest conduction subband of few-layer InSe films, we describe the subband structure of the latter (both dispersion and wavefunctions) taking into account the electrostatic potential profile induced by doping and gating. Our 'workhorse' is a 2-band hybrid $\mathbf{k}\cdot\mathbf{p}$ tight-binding (HkpTB) model previously discussed in Ref. 35, formulated in the basis of conduction, c and valence, v band states in each layer $[c_1, v_1, c_2, v_2, ...]$. The HkpTB Hamiltonian has the form,

$$\hat{H}^N_{\mathbf{k}\cdot\mathbf{p}} \approx \begin{pmatrix} \frac{\hbar^2k^2}{2m_c}+U_1 & 0 & t_{cc} & t_{cv} & \cdots \\ 0 & E_v+U_1 & -t_{cv} & t_{vv} & \cdots \\ t_{cc} & -t_{cv} & \frac{\hbar^2k^2}{2m_c}+U_2 & 0 & \cdots \\ t_{cv} & t_{vv} & 0 & E_v+U_2 & \cdots \\ 0 & 0 & t_{cc} & 0 & \cdots \\ \vdots & \vdots & \vdots & \vdots & \end{pmatrix} \tag{13}$$

Here, $t_{cc(vv)}$ parameterize the interlayer conduction-conduction (valence-valence) hops ($t_{cc} \equiv t^{\Gamma}_{cc} + t_{cc_2}k^2$), while t_{cv} ($t_{cv} \equiv t^{\Gamma}_{cv} + t_{cv_2}k^2$) is the conduction to valence band hop. The zero of energy is set to the monolayer conduction band edge, so that $E_v \approx -2.8$ eV is the energy of the monolayer's topmost valence band at the Γ-point. We neglect the valence band dispersion in InSe monolayers, as earlier studies[1,51–53] have shown that it is approximately flat over a large central part of the Brillouin zone. We also neglect any k-dependence in t_{vv} for the same reason. The terms U_η account for the electrostatic potential in layer η, and they are calculated as[35],

$$U_{\eta>1} = U_1 + ea_z \sum_{\kappa=2}^{\kappa=\eta} \mathcal{E}_{(\kappa-1)\kappa}, \tag{14}$$

where $a_z = 8.32$ Å is the distance between adjacent layers and $\mathcal{E}_{(\kappa-1)\kappa}$ is the electric field between layers $\kappa-1$ and κ. $\mathcal{E}_{(\kappa-1)\kappa}$ is obtained from the electron density on each InSe layer, n_η, as

$$\mathcal{E}_{(\kappa-1)\kappa} = \frac{e}{\epsilon_z\varepsilon_0} \sum_{\eta=\kappa}^{\eta=N} n_\eta, \tag{15}$$

where N is the total number of InSe layers in the device, n_η is the carrier concentration at the η^{th} layer and ϵ_z is the dielectric constant of InSe in the z-direction. We then approximate the electric field across a single layer as the mean of the fields either side of it,

$$\mathcal{E}_\kappa \simeq (\mathcal{E}_{(\kappa-1)\kappa} + \mathcal{E}_{\kappa(\kappa+1)})/2. \tag{16}$$

Values of the parameters in the above Hamiltonian are listed in Table III. They are obtained by fitting the results of the numerical analysis of the 14-band model described in Ref. 33, 35, 55, and 56. It is also common, in order to obtain more flexibility in gating, to have both a back gate and a top gate applied to the device as shown in the dual-gated geometry in the inset of Fig. 11. To demonstrate the behaviour of the SOC coefficient in the dual-gated case, we reproduce the gating configuration used for transport experiments on a six-layer device studied in Ref. 11. In that work, a fixed positive top gate voltage was applied to dope the system. At $V_{bg} = 0$, the carrier density in the InSe films was measured to be $n_e \sim 4\times10^{12}$ cm^{-2} indicating that the charge density in the top plate was that same amount. To include a fixed top gate in our electrostatic calculations, we amend Eq. (15) to read

$$\mathcal{E}_{(\kappa-1)\kappa} = \frac{e}{\epsilon_z\varepsilon_0}\left[\sum_{\eta=\kappa}^{\eta=N} n_\eta - n_{tg}\right], \tag{17}$$

where n_{tg} is the fixed top gate carrier density and n_η the carrier density in layer η. In considering the single-gated

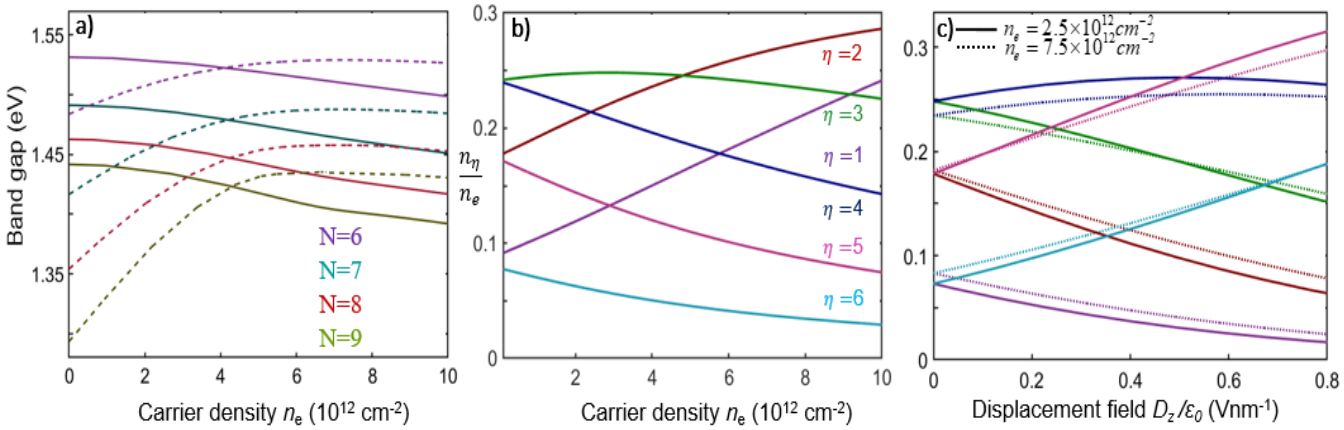

FIG. 6. (a) Band gap dependence on carrier density for a single (solid) and dual-gated (dashed) device with a fixed top gate carrier density $n_{tg} = 4 \times 10^{12}$cm^{-2}. A reduction in the band gap with increasing electric field is expected from the displacement of electrons towards lower energies along with an increase in electrostatic energy of the holes (quantum-confined Stark effect)[8,54]. (b) Fraction of the total carrier density at each layer η in a single-gated six-layer InSe device. The first layer is defined as the one closest to the metallic gate. (c) Fraction of the total carrier density at each layer η against displacement field in a six-layer InSe device in a dual-gated configuration at two fixed carrier concentrations of $n_e = 2.5 \times 10^{12}$cm^{-2} for the solid line and $n_e = 7.5 \times 10^{12}$cm^{-2} for the dotted line. The same color to layer correspondence applies as in Fig. 2(b).

FET geometry, a band gap modulation in the range of 10−20 meV is obtained for carrier densities in the range of $0 - 3 \times 10^{12}$cm^{-2} for 6−9 layers as shown in Fig. 6(a). Such band gap tunability[11] is a lot more efficient in the dual-gated configuration, due to a reduced electrostatic screening, with the band gap increasing up to 50 meV for an 8 layer device with a doping density of 2×10^{12} cm^{-2} and an applied top gate carrier density of $n_{tg} = 4 \times 10^{12}$ cm^{-2}. This reduction in screening also makes the charge redistribution more efficient in the dual-gated FET device compared with the single-gated configuration, see Fig. 6(b) and 6(c).

L	*Band gap* (eV)	m_c/m_0
1	2.87	0.266
2	2.14	0.220
3	1.83	0.204
4	1.67	0.197
5	1.58	0.192
6	1.52	0.189
7	1.48	0.187
8	1.46	0.186
9	1.44	0.185
10	1.42	0.184

TABLE III. Dependence of the energy gap and of the effective mass of the lowest conduction subband as a function of the number of layers L; m_0 is the free electron mass.

B. SOC in multilayer films from few-layer HkpTB

In analyzing the SOC in multilayer InSe, two main mechanisms are found to determine the SOC strength. First, there are the intralayer dipole moments which mix wavefunctions of opposite parities within each layer under an applied electric field. Second, there is an interplay between the intrinsic inversion asymmetry of the lattice structure of γ-InSe, and the overall wavefunction $z \to -z$ symmetry breaking due to the applied electrostatic potential. For the analysis of SOC in multilayer InSe it is necessary to include deeper valence bands v_1 and v_2 dominated by the p_x, p_y orbitals necessary for atomic SOC mixing with the p_z orbitals in c and v (see the orbital composition of each band in the character table on top of Fig. 4). On including the deeper valence bands, the hybrid $\mathbf{k} \cdot \mathbf{p}$ tight-binding Hamiltonian $\hat{H}$ of an N-layer InSe[43] in the vicinity of the Γ-point ($k_x, k_y \to 0$) previously discussed in Section III is rewritten as the sum of an unperturbed $\hat{H}^{(0)}$ and a perturbative part $\delta\hat{H}$,

$$\hat{H} = \hat{H}^{(0)} + \delta\hat{H}. \tag{18}$$

Writing the wavefunction eigenstates of the multilayer Hamiltonian $\hat{H}$ in a $14 \times N$ band basis as $\Psi = [\Phi_1, \Phi_2, \Phi_3, \Phi_4, ..., \Phi_N]$, where Φ_w is the 14-band monolayer basis in layer w defined as

$$\Phi_w \equiv [c^{\uparrow(w)}, c^{\downarrow(w)}, c_1^{\uparrow(w)}, c_1^{\downarrow(w)}, v^{\uparrow(w)}, v^{\downarrow(w)}, v_1^{\uparrow,p_x(w)}, v_1^{\downarrow,p_x(w)}, v_1^{\uparrow,p_y(w)}, v_1^{\downarrow,p_y(w)}, v_2^{\uparrow,p_x(w)}, v_2^{\downarrow,p_x(w)}, v_2^{\uparrow,p_y(w)}, v_2^{\downarrow,p_y(w)}], \tag{19}$$

yields the following expression for $\hat{H}$, $\hat{H}_0$ and $\delta\hat{H}$

$$\hat{H} = \begin{pmatrix} \hat{H}^{(0)}_{11} + \delta\hat{H}_{11} & (\hat{H}^{(0)}_{12} + \delta\hat{H}_{12}) & 0 & 0 & \cdots \\ (\hat{H}^{(0)}_{12} + \delta\hat{H}_{12})^T & \hat{H}^{(0)}_{22} + \delta\hat{H}_{22} & (\hat{H}^{(0)}_{23} + \delta\hat{H}_{23}) & \cdots & \cdots \\ 0 & (\hat{H}^{(0)}_{23} + \delta\hat{H}_{23})^T & \ddots & (\hat{H}^{(0)}_{(\eta-1)\eta} + \delta\hat{H}_{(\eta-1)\eta}) & \cdots \\ 0 & \vdots & (\hat{H}^{(0)}_{(\eta-1)\eta} + \delta\hat{H}_{(\eta-1)\eta})^T & \hat{H}^{(0)}_{\eta\eta} + \delta\hat{H}_{\eta\eta} & \cdots \\ \vdots & \vdots & \vdots & \vdots & \ddots \end{pmatrix} \tag{20a}$$

$$\hat{H}^{(0)}_{\eta\eta} = \begin{pmatrix} -U_\eta & 0 & 0 & 0 & 0 \\ 0 & (E_{c_1} - U_\eta) & 0 & 0 & 0 \\ 0 & 0 & (E_v - U_\eta) & 0 & 0 \\ 0 & 0 & 0 & (E_{v_1} - U_\eta)\hat{\mathbf{I}}_\nu & 0 \\ 0 & 0 & 0 & 0 & (E_{v_2} - U_\eta)\hat{\mathbf{I}}_\nu \end{pmatrix} \tag{20b}$$

$$\delta\hat{H}_{\eta\eta} = \begin{pmatrix} 0 & \mathcal{E}_\eta d_{c_1c} & \mathcal{E}_\eta d_{cv} & ib_{54}(\mathbf{k}\cdot\mathbf{\Lambda}) & i\lambda_{46}(\mathbf{s}\times\mathbf{\Lambda}) \\ \mathcal{E}_\eta d_{c_1c} & 0 & 0 & 0 & ib^{c_1v_2}_{16}(\mathbf{k}\cdot\mathbf{\Lambda}) \\ \mathcal{E}_\eta d_{cv} & 0 & 0 & i\lambda_{15}(\mathbf{s}\times\mathbf{\Lambda}) & ib_{16}(\mathbf{k}\cdot\mathbf{\Lambda}) \\ -ib_{54}(\mathbf{k}\cdot\mathbf{\Lambda})^T & 0 & -i\lambda_{15}(\mathbf{s}\times\mathbf{\Lambda})^\dagger & 0 & \mathcal{E}_\eta d_{v_1v_2}\hat{\mathbf{I}}_\nu \\ -i\lambda_{46}(\mathbf{s}\times\mathbf{\Lambda})^\dagger & -ib^{c_1v_2}_{16}(\mathbf{k}\cdot\mathbf{\Lambda})^T & -ib_{16}(\mathbf{k}\cdot\mathbf{\Lambda})^T & \mathcal{E}_\eta d_{v_1v_2}\hat{\mathbf{I}}_\nu & 0 \end{pmatrix} \tag{20c}$$

$$\hat{H}^{(0)}_{(\eta-1)\eta} = \begin{pmatrix} t^\Gamma_{cc} & 0 & 0 & 0 & 0 \\ 0 & 0 & 0 & 0 & 0 \\ 0 & 0 & t^\Gamma_{vv} & 0 & 0 \\ 0 & 0 & 0 & 0 & 0 \\ 0 & 0 & 0 & 0 & 0 \end{pmatrix}, \delta\hat{H}_{(\eta-1)\eta} = \begin{pmatrix} 0 & (t_{cc_1} + \delta_{c_1c}) & (t^\Gamma_{cv} + \delta_{cv}) & 0 & 0 \\ (-t_{cc_1} + \delta_{c_1c}) & 0 & 0 & 0 & 0 \\ (-t^\Gamma_{cv} + \delta_{cv}) & 0 & 0 & 0 & 0 \\ 0 & 0 & 0 & 0 & (t_{v_1v_2} + \delta_{v_1v_2}) \\ 0 & 0 & 0 & (-t_{v_1v_2} + \delta_{v_1v_2}) & 0 \end{pmatrix}. \tag{20d}$$

Here, indices η and κ label layers. The basis of each matrix $\hat{H}^{(0)}_{\eta\kappa}$ and $\delta\hat{H}_{\eta\kappa}$ is the 14-band monolayer InSe basis. In $\hat{H}^{(0)}_{\eta\eta}$, U_η is the electrostatic potential in the η^{th} layer, E_v is the monolayer topmost valence band energy as previously defined in the 2-band model, E_{v_1}, E_{v_2} and E_{c_1} are the energies of the v_1 v_2 and c_1 bands, and $\hat{\mathbf{I}}_\nu$ is the identity operator in the space of atomic p_x, p_y orbitals. In $\hat{H}^{(0)}_{(\eta-1)\eta}$, parameters t^Γ_{cc} and t^Γ_{vv} are the neighbouring conduction-conduction (valence-valence) interlayer hoppings; no spin index has been included in Eq. (20d) and in Eq. (20b) as all non-zero matrix elements are spin independent. In $\delta\hat{H}_{(\eta-1)\eta}$, t^Γ_{cv} and δ_{cv} are the z-symmetric and z-antisymmetric $c-v$ mixing interlayer hoppings, respectively (see Appendix A). In $\delta\hat{H}_{\eta\eta}$, d_{cv}, $d_{v_1v_2}$ and d_{c_1c} are the out-of-plane dipole moments (see Fig. 4). Coefficients b_{45}, b_{16} and $b^{c_1v_2}_{16}$ are $\mathbf{k}\cdot\mathbf{p}$ mixing terms between $c-v_1$, $v-v_2$ and c_1-v_2 respectively, while λ_{46} and λ_{15} are the atomic orbital SOC strengths for $c-v_2$ and $v-v_1$ spin-flip mixing, with values given in Table I. The latter is included using spin matrices $\mathbf{s_x}$ and $\mathbf{s_y}$. Matrices $\mathbf{\Lambda_y}$ and $\mathbf{\Lambda_x}$ are 1×2 matrices $[0,1]$ and $[1,0]$, respectively, operating in the p_x, p_y orbital component of the v_1 and v_2 valence bands and $\mathbf{k}\cdot\mathbf{\Lambda} \equiv k_x\mathbf{\Lambda_x} + k_y\mathbf{\Lambda_y}$ and $\mathbf{s}\times\mathbf{\Lambda} \equiv \mathbf{s_x}\mathbf{\Lambda_y} - \mathbf{s_y}\mathbf{\Lambda_x}$.

In the absence of interband hoppings, and having neglected the interlayer hoppings between the deeper valence bands v_1 and v_2 and between band c and the upper conduction band c_1, the subband eigenstates formed by $\hat{H}_0$ define the orthogonal basis used in the Löwdin projection. The eigenstates of the j^{th} conduction and valence subband states in this unperturbed Hamiltonian therefore have the form $|c^j\rangle = \sum_{\eta=1}^{\eta=N} \alpha^j_\eta |c_\eta\rangle$, $|v^j\rangle = \sum_{\eta=1}^{\eta=N} \beta^j_\eta |v_\eta\rangle$, $|v^j_{1(2)}\rangle = |v_{1(2)\eta}\rangle$, $|c^j_1\rangle = |c_{1\eta}\rangle$ where $|c_\eta\rangle$, $|v_\eta\rangle$, $|v_{1(2)\eta}\rangle$ and $|c_1\rangle$ are the c, v, $v_{1(2)}$ and c_1 monolayer eigenstates in layer η, respectively. In the following analysis we will only focus on the lowest conduction subband $\alpha^1_\eta \equiv \alpha_\eta$. For the purpose of calculating the SOC coefficient as a function of carrier density, the v_1, v_2 and c_1 subbands are approximated as all being located at $E'_{v_1} \equiv E_{v_1} - U_{av}$, $E'_{v_2} \equiv E_{v_2} - U_{av}$ and $E'_{c_1} \equiv E_{c_1} - U_{av}$ respectively, where U_{av} is the average electrostatic potential per layer. This is due to a small change in the on site electrostatic potential, $\Delta U_{(\eta-1)\eta} = U_{\eta-1} - U_\eta$, as compared with the E_{v_1}, E_{v_2} and E_{c_1} energy denomina-

tors (0.1−0.3 eV, as compared to about 3.5 eV for c to $v_{1(2)}$ energy denominator terms and to about 1.4 eV for the c to c_1 terms). When applying the Löwdin partitioning method[57,58] (see Appendix D), the A block is chosen to act on the ↑ and ↓ spin states of the lowest conduction subband and the B block on every other subband in the InSe multiband structure.

In order to obtain the SOC term perturbatively, we account for three effects: an inversion symmetry breaking (such as an electric field or the interlayer pseudopotentials); SOC interband mixing; and $\mathbf{k}\cdot\mathbf{p}$ mixing elements. Consequently, the lowest-order non-zero terms in the perturbation theory have to be third-order in the expansion. Defining,

$$H'_{\rho\omega} \equiv \langle\rho|\delta\hat{H}|\omega\rangle, \tag{21}$$

where $|\rho\rangle$ and $|\omega\rangle$ are two eigenstates of $\hat{H}_0$, the corresponding third-order terms in quasi-degenerate perturbation theory have the form,

$$\begin{aligned}\Delta H^{(3)}_{mm'} = &-\frac{1}{2}\sum_{l,m''}\frac{H'_{ml}H'_{lm''}H'_{m''m'}}{(E_{m'}-E_l)(E_{m''}-E_l)}\\
&-\frac{1}{2}\sum_{l,m'''}\frac{H'_{mm''}H'_{m''l}H'_{lm'}}{(E_m-E_l)(E_{m''}-E_l)}\\
&+\frac{1}{2}\sum_{l,l'}\frac{H'_{ml}H'_{ll'}H'_{l'm'}}{(E_m-E_l)(E_m-E_{l'})}\\
&+\frac{1}{2}\sum_{l,l'}\frac{H'_{ml}H'_{ll'}H'_{l'm'}}{(E_{m'}-E_l)(E_{m'}-E_{l'})},\end{aligned} \tag{22}$$

where the m, m' indices correspond to $\hat{H}_0$ subband eigenstates in block A and the l, l' index to any subband eigenstate in block B (see Appendix D). Energies $E_{m(l)}$ correspond to the energy of the m^{th} or l^{th} eigenstate. Contributions to SOC originate from the 3-step loop Feynman diagrams in Fig. 7-10, with spin reversed initial and final states $c^{\uparrow(\downarrow)}$ and $c^{\downarrow(\uparrow)}$.

The Feynman diagrams, originating from the inversion asymmetric parameter δ_{cv} and δ_{c_1c} in combination with the mixing with deeper valence bands and SOC as shown in Fig. 7 and Fig. 8, give a term,

$$\begin{aligned}\Delta H'''_{11} = 2\Bigg[&\sum_{j=1}^{j=N}\sum_{\kappa=1}^{\kappa=N}\left(\frac{b_{54}\lambda_{15}\delta_{cv}}{\Delta E_{cv_1}\Delta E_{cv^j}}+\frac{b_{16}\lambda_{46}\delta_{cv}}{\Delta E_{cv_2}\Delta E_{cv^j}}\right)\\
&\times\alpha_\kappa(\beta^j_{\kappa+1}+\beta^j_{\kappa-1})\sum_{\xi=1}^{\xi=N}\alpha_\xi\beta^j_\xi+\sum_{\eta=1}^{\eta=N}\left(\frac{b^{c_1v_2}_{16}\lambda_{46}\delta_{c_1c}}{\Delta E_{cc_1}\Delta E_{cv_1}}\right)\times\\
&\alpha_\eta(\alpha_{\eta+1}+\alpha_{\eta-1})\Bigg)\Bigg](\mathbf{s}\times\mathbf{k}),\end{aligned} \tag{23}$$

where δ_{cv} and δ_{c_1c} is the z-asymmetric parameters between c and v and between c_1 and c defined in Eq. (20d) and further discussed in Appendix A. In the presence of an external electrostatic potential, the signs of δ_{cv} and δ_{c_1c} become important, as it can be related to placing a single electrostatic gate on one of the surfaces and the orientation (up/down) of externally controlled electric field, $\mathcal{E}_z$.

The two diagrams in Fig. 9, give a SOC term in the

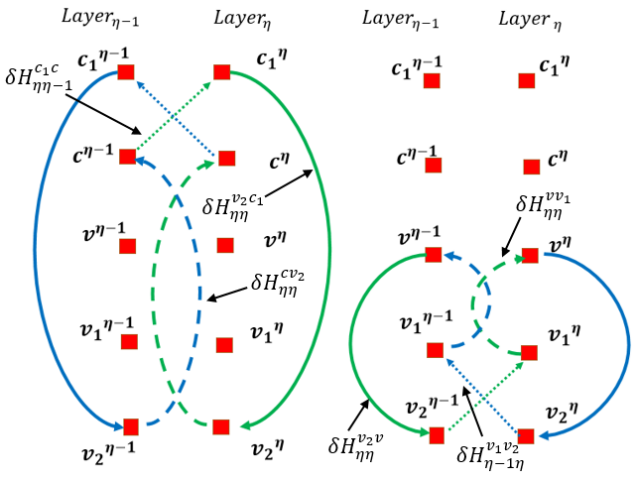

FIG. 7. (Left) Feynman diagram of the interlayer spin-flip loops due to the γ-stacking involving the upper conduction band c_1. (Right) Feynman diagram of the interlayer spin-flip loops due to the γ-stacking involving the deeper valence bands v_1 and v_2. Such contribution is only relevant for the Dresselhaus SOC in the valence band v as shown in Appendix A. Doted lines $(\cdots)$ label the terms in $\delta\hat{H}$ responsible for inversion symmetry breaking. Dashed lines $(---)$ label the intra-atomic SOC mixing between different bands. Solid lines label the $\mathbf{k}\cdot\mathbf{p}$ interband mixing terms in $\delta\hat{H}$. Different colors label pairs of loops that produce competing contributions in the same order of perturbation theory.

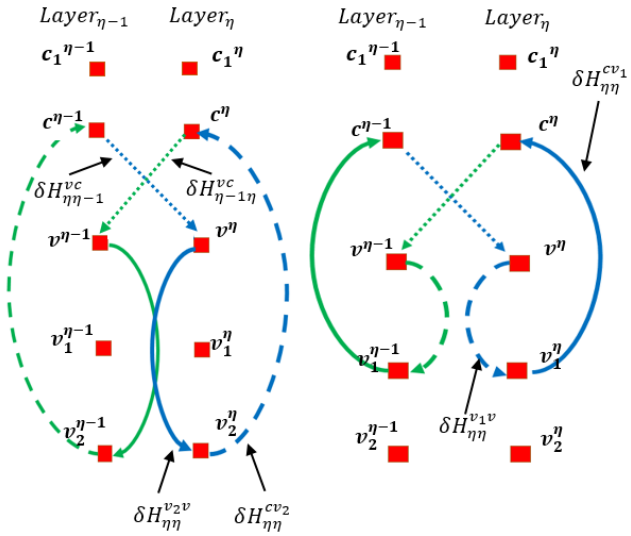

FIG. 8. Feynman diagram of the interlayer spin-flip loops due to the γ-stacking responsible for breaking the $z\to -z$ symmetry in the c to v hopping parameters t_{cv} and t_{vc}. Doted, dashed and solid lines follow the same convention as in Fig. 7.

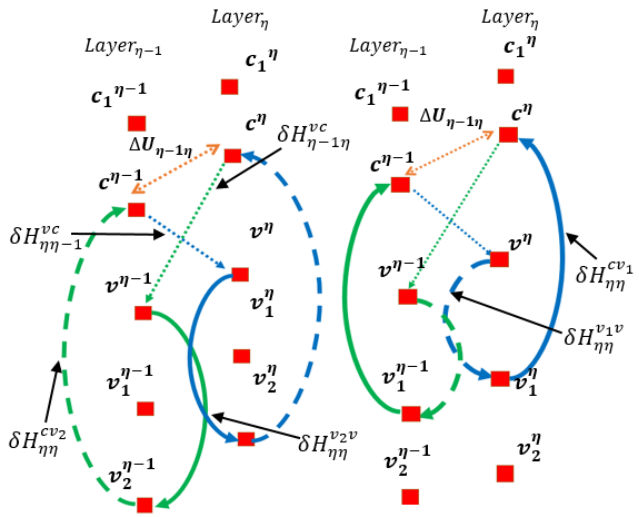

FIG. 9. Feynman diagram of the SOC originated from the asymmetry induced by the electrostatic potential distribution U_i combined with the $z \to -z$ symmetric interband hopping parameter t_{cv}. Doted, dashed and solid lines follow the same convention as in Fig. 7.

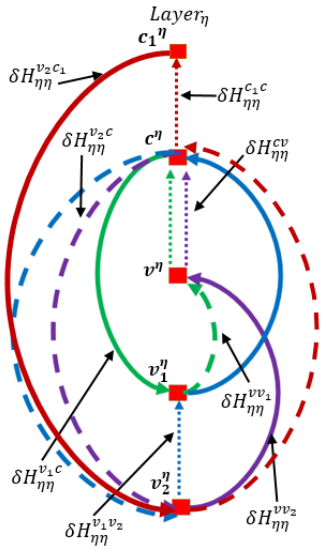

FIG. 10. Feynman diagram of the SOC from the dipolar mixing terms. Dots, dashed and solid lines follow the same convention as in Fig. 7. Different colors label the different 3-step loops included in Eq. (22) in the same order of perturbation theory.

form of,

$$\Delta H'_{11} = 2\Bigg[\sum_{j=1}^{j=N}\sum_{\kappa=1}^{\kappa=N}\left(\frac{b_{54}\lambda_{15}t^{\Gamma}_{cv}}{\Delta E_{cv_1}\Delta E_{cv^j}} + \frac{b_{16}\lambda_{46}t^{\Gamma}_{cv}}{\Delta E_{cv_2}\Delta E_{cv^j}}\right) \times \alpha_\kappa(\beta^j_{\kappa+1} - \beta^j_{\kappa-1})\left(\sum_{\xi=1}^{\xi=N}\alpha_\xi\beta^j_\xi\right)\Bigg](\mathbf{s}\times\mathbf{k}), \tag{24}$$

where α_κ and β^j_κ are the components of the lowest conduction subband and the j^{th} valence subband respectively; κ labels the layer index. $\Delta E_{cv^j} \equiv E_c - E_{v^j}$ is the energy difference between the lowest conduction subband and the j^{th} valence subband and $\Delta E_{cv_{1(2)}} \equiv E_c - E'_{v_{1(2)}}$ is the energy gap between the lowest conduction subband and the v_1 and v_2 subbands located at $E_{v_{1(2)}} - U_{av}$. The loops shown in Fig. 10 for the dipolar mixing terms give a SOC term in the form of

$$\Delta H''_{11} = 2\Bigg[\sum_{j=1}^{j=N}\sum_{\kappa=1}^{\kappa=N}\left(\frac{d_{cv}\lambda_{15}b_{54}}{\Delta E_{cv^j}\Delta E_{cv_1}} + \frac{d_{cv}\lambda_{46}b_{16}}{\Delta E_{cv^j}\Delta E_{cv_2}}\right) \times (\mathcal{E}_\kappa\alpha_\kappa\beta^j_\kappa)\left(\sum_{\xi=1}^{\xi=N}\alpha_\xi\beta^j_\xi\right) + \sum_{\eta=1}^{\eta=N}\alpha^2_\eta\mathcal{E}_\eta \times \left(\frac{d_{v_1v_2}b_{54}\lambda_{46}}{\Delta E_{cv_1}\Delta E_{cv_2}} + \frac{d_{c_1c}b^{c_1v_2}_{16}\lambda_{46}}{\Delta E_{cc_1}\Delta E_{cv_2}}\right)\Bigg](\mathbf{s}\times\mathbf{k}), \tag{25}$$

where d_{cv} is the matrix element of the out-of-plane dipole operator between the monolayer conduction and valence bands, $d_{v_1v_2}$ is the out-of-plane dipole moment between v_1 and v_2 and d_{c_1c} the out-of-plane dipole between c_1 and c. $\mathcal{E}_\eta$ is defined as the electric field in layer η and $\Delta E_{cc_1} \equiv E_c - E'_{c_1}$ is the energy difference between the lowest conduction subband and the set of c_1 subbands located at $E_{c_1} - U_{av}$. In accounting for the dipolar terms, some care must be taken in choosing its sign in the few-layer case, as is further explained in Appendix B.

Combining all these contributions enables us to describe the dependence of SOC strength, α, on the number of layers, electric field, and doping in the film as shown in Figs. 11,12 and 13. For example, as illustrated in Fig. 12, in multilayer InSe in a single-gated FET, doping the device to carrier densities $> 10^{13}$cm^{-2} can lead to the compensation of the intrinsic SOC by the contribution of the gate-induced electric field.

C. SOC analysis in InSe films using a quantum well model

To describe thicker films, it is more practical to use a quantum well model for InSe films[8,35]. For this, we describe the dispersion of electrons in the $\mathbf{k}\cdot\mathbf{p}$ theory expansion near the A-point conduction band edge of bulk InSe as

$$E_c(\mathbf{p}, p_z) = \left(\frac{\hbar^2}{2m_A} + \xi p_z^2 a_z^2\right)p^2 + \frac{\hbar^2 p_z^2}{2m_{Az}} + \alpha_\infty\left(1 - \frac{\chi a_z^2 p_z^2}{\pi^2}\right)(\mathbf{s}\times\mathbf{p}), \tag{26}$$

where m_A and m_{Az} are the in-plane and out-of-plane effective mass at the A-point and the parameters ξ and χ take into account the anisotropic non-parabolicity of the electron's dispersion characteristic for layered systems.

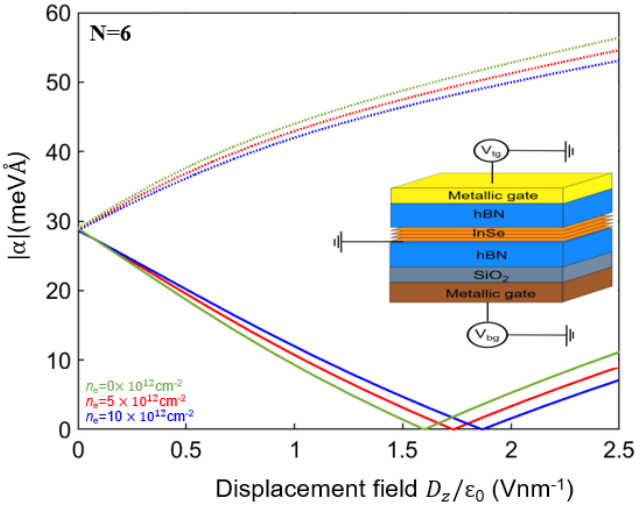

FIG. 11. SOC strength dependence on displacement field and carrier density for a six-layer InSe dual-gated FET device as shown in the inset. The solid and dotted lines indicate respectively when the applied displacement field suppresses or enhances the Dresselhaus SOC.

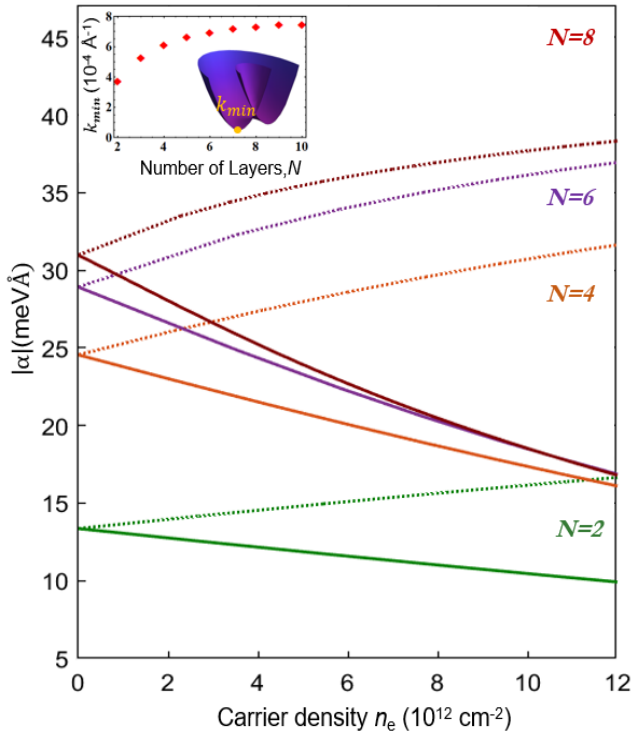

FIG. 12. 2D SOC coefficient α in the lowest conduction subband of N-layer InSe film against carrier density for different number layers in a single-gated FET geometry. Inset: shift in momentum of the minimum of the lowest conduction subband as a function of the number of layers when no electrostatic doping is present. The dielectric constant, used for this calculation, was ϵ_z=9.9. The solid and dotted lines indicate respectively when the applied displacement field suppresses or enhances the Dresselhaus SOC.

In Fig. 13(b) we show the p_z-dependence (around the A-point) of the linear in k_x, k_y spin-orbit coupling computed by DFT for bulk InSe using QSGW approach[55,59], to compare with the SOC form in Eq. (26). This has to be complemented with the generalised Dirichlet-Neumann boundary conditions for the quantum well wavefunction $\Psi(z)$ at the encapsulating interfaces,

$$\Psi \pm \nu a_z \partial_z \Psi = 0, \quad \nu \approx 1.42. \tag{27}$$

The latter determines the values for the wave numbers of the electron's standing waves,

$$p_z = \frac{n\pi}{(N+2\nu)a_z}, \tag{28}$$

which determines the subband and layer-number-dependence of the subband mass and SOC parameter,

$$\frac{1}{m_n} \approx \frac{1}{m_A}\left(1 - \frac{6.2n^2}{(N+2\nu)^2}\right), \tag{29}$$
$$\alpha_{n|N}(n << N) \approx \alpha_\infty\left(1 - \frac{\chi}{(N+2\nu)^2}\right).$$

By fitting $\alpha_{1|N}$ described in Eq. (2) to the values of the lowest subbands SOC strength in Fig. 13 we find that α_∞=34.5 meVÅ and χ=14.9 respectively. Additionally, the results of the calculations, performed in the same films subjected to an electric field $\mathcal{E}_z$ perpendicular to the layers shown in Fig. 1 and 11 show an approximately linear SOC strength dependence on $\mathcal{E}_z$. We describe the latter as

$$\alpha(N, \mathcal{E}_z) = \alpha(N) - \mathcal{E}_z \aleph(N), \tag{30}$$

with the vales of $\aleph(N)$ for $N \geq 2$ shown in the inset of Fig. 1. Further to the DFT calculations for the few-layer case, in Fig. 3(b) we use previous quasiparticle self-consistent GW (QSGW) calculations for bulk γ-InSe[55,59] to extract the k_z-dependence of the coefficient of the linear component of SOC for small in-plane momentum near $k_x = k_y = 0$, for both the conduction and valence bands. This shows that as k_z approaches the bulk band edge (located at $k_z = \pi/a_z$) the SOC strength increases, implying that as k_z is restricted by confinement in thin films of InSe, the SOC strength can be expected to decrease from its bulk value, with smaller strengths for thinner films.

V. MAGNETOTRANSPORT STUDIES OF InSe FILMS IN THE FET GEOMETRY AND THEIR COMPARISON WITH THEORY

In order to probe the nature of SOC in InSe, we fabricated a dual-gated multiterminal 6 layer γ-InSe device using mechanical exfoliation and hexagonal boron nitride (hBN) encapsulation, which were carried out in an inert atmosphere of a glovebox[60]. Such encapsulation was

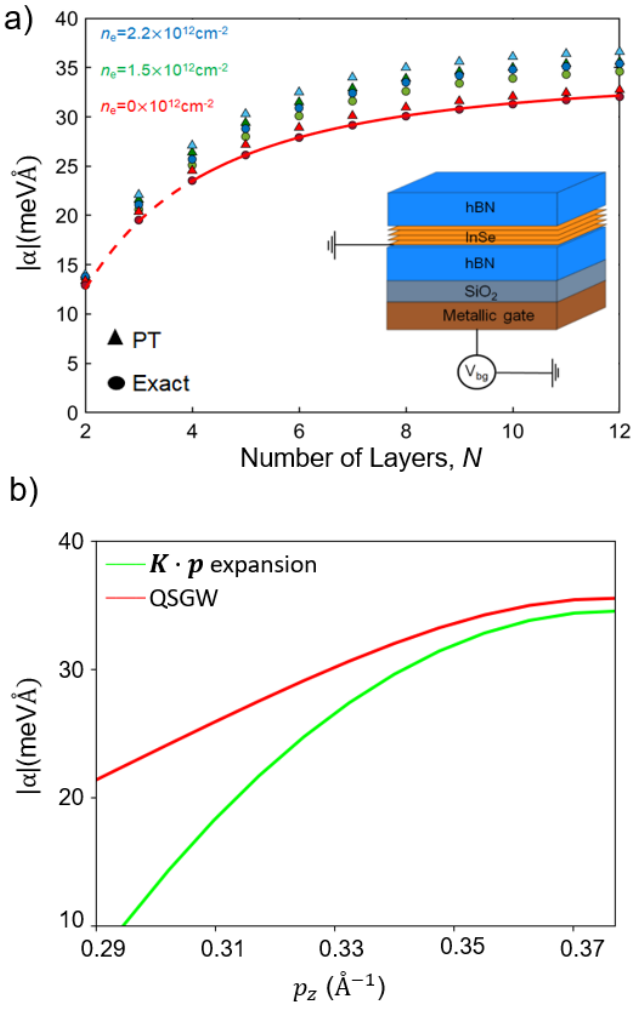

FIG. 13. (a) SOC coefficient α computed for InSe films with various thicknesses and carrier densities in a single-gated FET geometry (inset), calculated assuming ϵ_z=9.9 for the InSe. The data shown in circles (◯) were obtained by exact diagonalization of the 14-band Hamiltonian in Ref. 55 and compared with the perturbation theory results obtained by Löwdin partitioning (△) (note that for N=1, $\alpha = 0$ for $n_e = 0 \times 10^{12}$cm^{-2}). Inset shows the usual configuration of a single-gated FET device. The solid and dashed lines indicate the fitted dependence of the Dresselhaus term as a function of the number of layers when the quantum well approximation holds ($N \geq 4$) and when it does not respectively. (b) In red, the QSGW-calculated SOC strength as a function of p_z in bulk γ-InSe for the conduction band[56,59]. As p_z approaches the band edge located at $p_z = \frac{\pi}{a_z} = 0.378$ Å^{-1}, the SOC strength increases following a quadratic dependence on momentum p_z shown in green $\left(\alpha(p_z) = \alpha_\infty\left(1 - \frac{\chi a_z^2 p_z^2}{\pi^2}\right)\right.$, where $\alpha_\infty = 34.5$meVÅ and $\left.\chi = 14.9\right)$. This increasing trend indicates that for greater confinement under a decreasing number of layers, a weaker linear Dresselhaus SOC is expected.

needed to protect air-sensitive InSe flakes from the environment (see Fig. 14(a)). In addition, electrical contact to InSe was provided by few-layer graphene (FLG) flakes which in turn were connected to metal leads by standard nanofabrication techniques as illustrated in Fig. 14(a) (see Ref. 11 for further details). The gate-tunable work function of graphene ensured ohmic contacts between FLG and 2D InSe[61] and thus enabled us to explore InSe properties using conventional four-terminal measurements. To characterize the fabricated device, we first measured its longitudinal resistivity, ρ_{xx}, as a function of gate-induced carrier density, n_e. The latter was obtained via Hall-effect measurements that provided full $n_e(V_{bg})$ dependence presented in Fig. 15. In contrast to earlier studies of the quantum Hall effect in InSe/graphene interfaces[62], the perfectly linear n_e vs V_{bg} trend shown in the inset of Fig. 15 does not indicate any substantial charge transfer from the InSe to the gating surface.

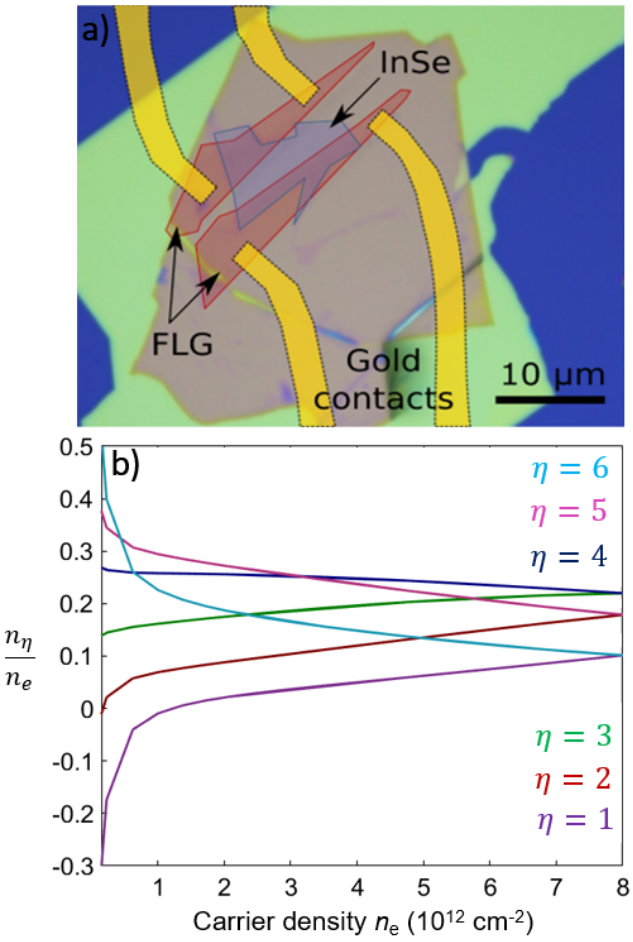

FIG. 14. (a) Optical photograph of an encapsulated InSe flake (light blue) equipped with few-layer graphene (FLG) contacts (red). Yellow polygons illustrate gold leads contacting FLG. Green colour corresponds to the bottom hBN flake deposited on top of an oxidized Si wafer (dark blue). (b) Calculated charge density distribution along the different layers in the dual-gated device under study. At a carrier concentration of $n_e = 8 \times 10^{12}$ cm^{-2}, the distribution of charges becomes $z \to -z$ symmetric as the top plate carrier density is fixed at $n_{tg} = 4 \times 10^{12}$ cm^{-2}.

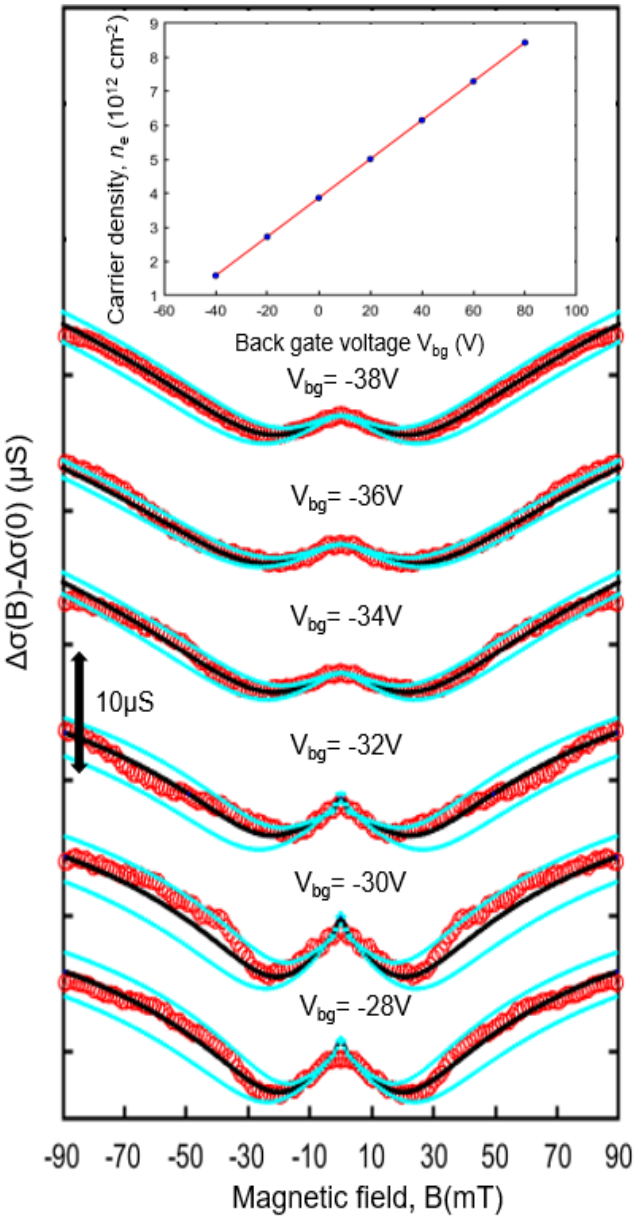

FIG. 15. Weak antilocalization feature in conductivity measured in a 6-layer dual-gated InSe device with corresponding optimal fits (Black). Carrier densities were measured in the range from $1.7-2.2\times10^{12}$ cm^{-2} in steps of 0.1×10^{12} cm^{-2}. Blue indicates the upper and lower bound fits of the corrections to magnetoconductivity. Top inset shows the carrier density at each back gate voltage obtained from Hall-effect measurements. The finite carrier density at V_{bg}=0 is due to the applied top gate voltage corresponding to $V_{tg}=8$ V. The linear relation between the carrier density and the back gate voltage for a fixed top gate of $V_{tg}=8$ V was found to be $n_e=\Upsilon(V_{bg}-V'_{bg(V_{tg}=8\mathrm{V})})$ where $V'_{bg(V_{tg}=8\mathrm{V})}=-67.6$V and $\Upsilon=5.71\times10^{10}$ V^{-1}cm^{-2}.

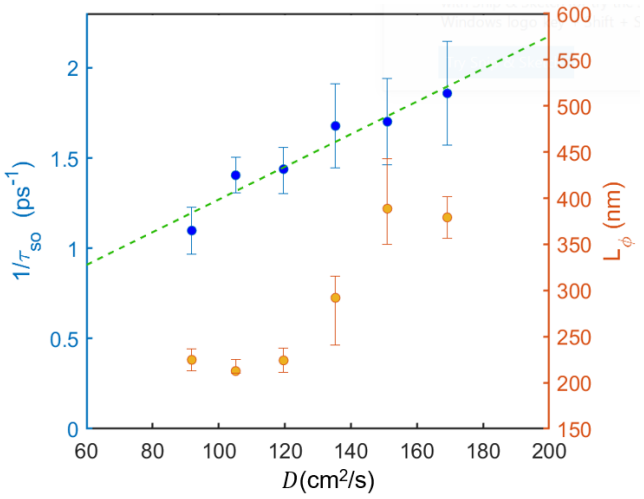

FIG. 16. Inverse spin relaxation time and phase relaxation length *vs* diffusion coefficient. The proportionality relation between the diffusion coefficient obtained by varying the carrier density n_e and the inverse of the spin relaxation time indicates Dyakonov-Perel mechanism of spin relaxation.

Using Drude formula we determined the mean free path of charge carriers, λ, and respective scattering time, τ, important parameters critical for further analysis. The effective mass for the lowest conduction subband used to extract τ was $m_c=0.12m_e$, obtained from an accurate calculation of the bulk effective mass accounting both for electron-electron and electron-phonon interaction effects in the bulk conduction band.[63].

An experimental manifestation of the SOC strength can be found in the weak antilocalization (WAL) corrections to magnetoconductance[64–67] produced by the interference of electron waves propagating along closed loops of random walks[68,69]. Such behavior has been observed in recent studies of few-layer single-gated GaSe[70] and InSe[71,72].

In Ref. 72, the fitting procedure used to extract the SOC strength from the corrections to magnetoconductance was the formalism developed by Hikami, Larkin and Nagaoka[66] for systems where the spin relaxation mechanism is dominated by scattering with magnetic impurities[73,74]. As the γ-stacked phase in InSe is noncentrosymmetric and therefore the spin relaxation mechanism is expected to be Dyakonov-Perel, their extracted spin relaxation parameters from WAL fits were overestimated. In Ref. 71 the enhancement of the SOC as compared to our estimated bulk SOC strength value at the band edge ($\alpha_\infty\approx34$ meVÅ) is a result of an impurity deposition layer formed at the interface of the suspended device; this forms a sharp potential barrier at the interface and therefore increases the SOC strength.

From our weak antilocalization measurements, the spin and phase relaxation times can be obtained by fitting the corrections to conductivity with respect to these two parameters in the range of magnetic fields where the minimum in magnetoconductance appears.

The WAL corrections to the conductivity of the 6-layer device with the same characteristics as reported in Ref. 11 were measured as a function of the magnetic field with 1 mT magnetic field step. As shown in Fig. 15, at mag-

netic fields 10-30 mT, a clear minimum in the magnetoconductance is observed. The corrections to conductivity $\Delta\sigma(B)-\Delta\sigma(0)$ were measured in the range of 0−90 mT, and both the spin and phase relaxation time were fitted with the formalism developed by Iordanskii, Larkin and Pitaevskii[75,76] (ILP) for systems where the lack of inversion symmetry leads to the electron's spin precessing and to relaxation by Dyakonov-Perel mechanism. Such formalism was used for carrier densities $< 2\times10^{12}$cm^{-2}; above that carrier densities, the assumption of the ILP formalism that the precession angle $\phi=\Omega\tau << 1$ (Ω being the spin precession frequency and τ the momentum relaxation time), and that the magnetic field $B << B_{tr}$ (where $B_{tr}\equiv\frac{\hbar}{2e\lambda^2}$ and λ is the mean free path) breaks down. The spin precession frequency Ω is then related to the spin-orbit coupling strength α through the simple relation $\Omega=\alpha k_F$ where k_F is the Fermi momentum. In these cases, we employ the approach developed by Golub[77,78], which goes beyond the diffusion approximation for arbitrarily large precession angles and for magnetic fields comparable to the transport field B_{tr}.

For the magnetoconductance fits performed at carrier densities $n_e \geq 2\times10^{12}$ cm^{-2}, the non-backscattering corrections to conductivity were found to be negligible, and therefore corrections to conductivity only came from the backscattering loops,

$$\sigma_{back}=-\frac{e^2}{2\pi^2\hbar}\left(\frac{\lambda}{l_B}\right)^2\sum_{N'=0}^{\infty}\left(Tr\left[\hat{A}_{N'}^3(\hat{I}-\hat{A}_{N'})^{-1}\right]-\frac{P_{N'}^3}{1-P_{N'}}\right), \tag{31}$$

$$\hat{A}_{N'}\equiv\begin{pmatrix} P_{N'-2}-S_{N'-2}^{(0)} & R_{N'-2}^{(1)} & S_{N'-2}^{(2)} \\ R_{N'-2}^{(1)} & P_{N'-1}-2S_{N'-1}^{(0)} & R_{N'-1}^{(1)} \\ S_{N'-2}^{(2)} & R_{N'-1}^{(1)} & P_{N'}-S_{N'}^{(0)}\end{pmatrix},$$

$$P_{N'}\equiv\frac{l_B}{\lambda}\int_0^{\infty}\exp\left(-\frac{l_B}{\tilde{l}}x-\frac{x^2}{2}\right)L_{N'}(x^2)dx,$$

$$S_{N'}^{(\mu)}\equiv\frac{l_B}{\lambda}\sqrt{\frac{N'!}{(N'+\mu)!}}\int_0^{\infty}\exp\left(-\frac{l_B}{\lambda}x-\frac{x^2}{2}\right)x^{\mu}L_{N'}^{\mu}(x^2)\sin^2\left(\Omega\tau\frac{l_B}{\lambda}\right)dx,$$

$$R_{N'}^{(\mu)}\equiv\frac{l_B}{\sqrt{2}\lambda}\sqrt{\frac{N'!}{(N'+\mu)!}}\int_0^{\infty}\exp\left(-\frac{l_B}{\lambda}x-\frac{x^2}{2}\right)x^{\mu}L_{N'}^{\mu}(x^2)\sin\left(2\Omega\tau\frac{l_B}{\lambda}\right)dx,$$

Here, $l_B\equiv\sqrt{\frac{\hbar}{eB}}$ is the magnetic length, and in Eq. (31), $\tilde{l}$ is defined as $\tilde{l}\equiv\frac{\lambda}{1+\frac{\tau}{\tau_\phi}}$ where τ_ϕ is the phase relaxation time. The precession frequency is related to the spin relaxation time τ_{SO} through $\frac{1}{\tau_{SO}}=2\Omega^2\tau$. As done previously with the ILP formalism, both the phase and spin relaxation times were taken as fitting parameters. In Fig. 16, the inverse proportionality between the spin relaxation time and the diffusion coefficient D confirms that the spin relaxation mechanism is Dyakonov-Perel[79,80]. From τ_{SO}, the SOC coefficient is extracted and compared with our theoretical calculation in Fig. 18. In Fig. 18 the SOC coefficient at different carrier densities was calculated at the experimentally established dielectric constant $\epsilon_z=9.9$ for InSe[32]. Very good agreement was found between the calculated SOC coefficient and the experimentally extracted SOC strength. Furthermore, by looking at the two different branches originated from the orientation of the crystal being parallel or antiparallel to the applied electric field, it was found that at a carrier density of $n_e=8\times10^{12}$ cm^{-2} the two branches converged at a single point. This indicates no dependence neither on crystal orientation nor on electrostatic profile. As shown in Fig. 14, at that exact carrier density, the electrostatic profile is expected to be $z\rightarrow -z$ symmetric and therefore the only contribution to the SOC must originate from the intrinsic $z\rightarrow -z$ asymmetry of the crystal (see comparison in Fig. 18 with SOC strength at zero electric field).

VI. CONCLUSION

Overall, the description of SOC strength (as a function of the number of layers and the applied electric field piercing the multilayer film) obtained using the few-layer HkpTB study and a quantum well model give the matching results, and the theoretically computed SOC strengths are compared with the results of weak antilocalization measurements on dual-gated multilayer InSe films showing a good agreement between theory and experiment.

The size of SOC constant we compute for InSe films with 2-10 layers thickness is comparable to the SOC strength in quantum wells of conventional semiconduc-

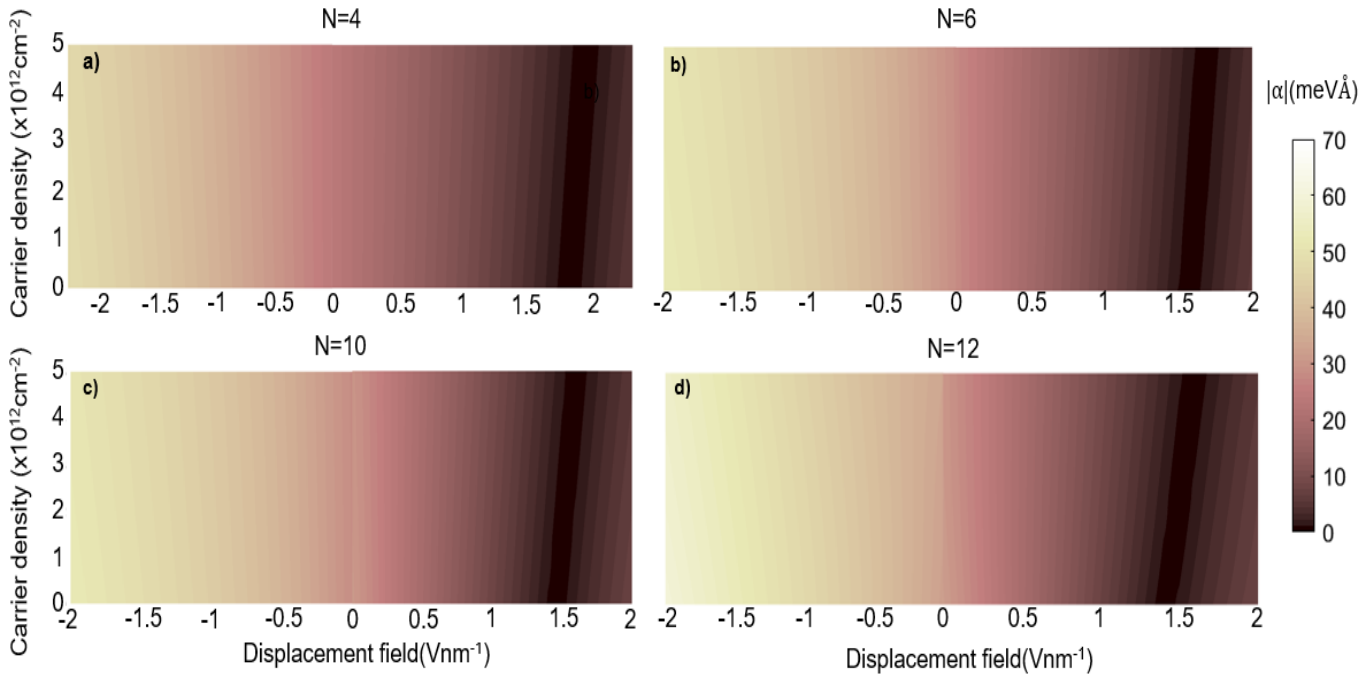

FIG. 17. (a-d) SOC strength as a function of the displacement field and carrier density for different number of layers. Crystal orientation is chosen such that the applied displacement field counteracts the Dresselhaus SOC when the displacement field is positive. The dark black lines indicate the disappearance of SOC due to the application of a displacement field which compensates the SOC from the intrinsic lack of inversion symmetry in the different multilayers.

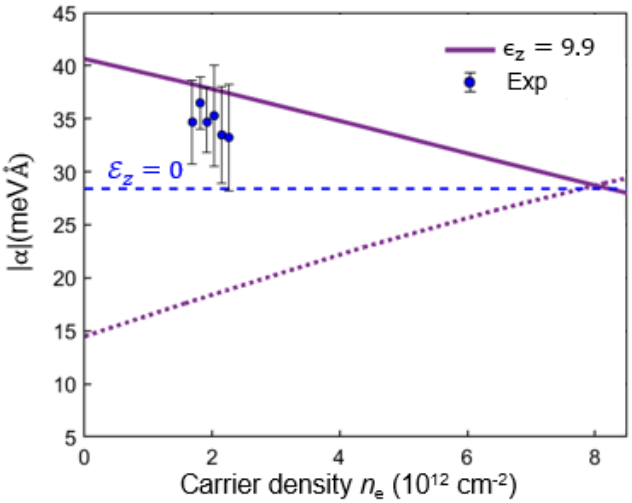

FIG. 18. SOC coefficient α as experimentally extracted from weak antilocalization measurements of the dual-gated 6 layer device[11], compared to the value obtained in the self-consistent calculation. The blue dashed line indicates the value of α in the absence of any electrostatic gating and doping. The same notation for the solid and dotted lines is used as in Fig. 1,12 and 11.

tors, such as GaAs, InAs, HgTe. What makes 2D InSe different from those spintronic systems is that the SOC strength in it can be tuned over a wide range. Additionally contribution originating from the asymmetry of an hBN/InSe interface was analysed and shown to be negligible (as compared with the intrinsic SOC in the film) for InSe encapsulated in hBN both on top and in the bottom, and also to decay as N^{-3}. Moreover we demonstrate that spin-orbit coupling strength for electrons near the conduction band edge in few-layer γ-InSe films can be tuned over a wide range, from α=0 to $\alpha \approx$ 70meVÅ. This tunability illustrated in Fig. 17 for the films of various thicknesses is the result of a competition between film-thickness-dependent intrinsic and electric-field-induced SOC, potentially, allowing for electrically switchable spintronic devices. As shown in Fig. 17 and Fig. 1, displacement fields in the range of 1-2 Vnm^{-1} can turn the SOC on and off.

ACKNOWLEDGMENTS

The authors thank M. Potemski, Y. Ye, J. Lischner, A. Mirlin, V. Enaldiev, K.W. Song, S. Slizovskiy, and N. D. Drummond for discussions. We also thank S.J. Liang and F. Miao for sharing the data in Ref. 72. This work made use of the CSF cluster of the University of Manchester and the N8 Polaris service, the use of the ARCHER national UK supercomputer (RAP Project e547), and the Tianhe-2 Supercomputer at NUDT. We acknowledge support from EPSRC CDT Graphene NOWNANOEP/L01548X, ERC Synergy Grant Hetero2D, grant EP/N010345, Lloyd Register

Foundation Nanotechnology grant, European Quantum Technology Flagship Project 2D-SIPC, and Core 3 European Graphene Flagship Project. Research data are available from the authors on request.

Appendix A: Determination of parameters δ_{cv}, δ_{c_1c} and $\delta_{v_1v_2}$ from bulk SOC

For the calculation of subband energies and dispersions, it was sufficient to approximate the interlayer hops as being entirely between the inversion symmetric sublattices of selenium atoms on the outside of each layer. This causes the hops to be inversion symmetric, which when combined with the opposite z-symmetries of the monolayer conduction and valence under σ_h reflection (i.e. $z \to -z$ symmetry) gives $t_{cv} = -t_{vc}$, $t_{c_1c} = -t_{cc_1}$ and $t_{v_2v_1} = -t_{v_1v_2}$. It is transparent from Eq. (1) that inversion symmetry would prohibit the existence of extrinsic SOC. Consequently, we require terms in our model which break inversion symmetry (such as an applied electric field or the interlayer pseudopotentials arising from the γ-stacking[81]). The indium atoms provide such an asymmetry-in the γ stacking there is a vertically opposite interlayer In/Se pair heading in one direction along the z-direction, while in the other direction the indium atom is opposite an empty space in the adjacent layer. In the $\mathbf{k}\cdot\mathbf{p}$ model, the effect of this symmetry breaking is to give t_{cv}, t_{c_1c} and $t_{v_1v_2}$ slightly different magnitudes as compared with $-t_{cv}$, $-t_{c_1c}$ and $-t_{v_1v_2}$, so we define three new parameters: $2\delta_{cv} \equiv t_{cv}+t_{vc}$ $2\delta_{c_1c} \equiv t_{c_1c}+t_{cc_1}$ and $2\delta_{v_1v_2} \equiv t_{v_1v_2}+t_{v_2v_1}$. In order to obtain the parameters δ_{cv} and δ_{c_1c} relevant for the analysis of the Dresselhaus SOC in the conduction band, the linear SOC splittings at each individual k_z are obtained from the QUESTAAL package by linearly fitting the energy differences between the two spin split bands (see Fig. 19). Firstly, the parameters δ_{cv} and δ_{c_1c} were fitted for the α vs k_z-dependence of band c (red curve in Fig. 19), and then the $\delta_{v_1v_2}$ parameter was fitted from the α vs k_z-dependence of band v (green curve in Fig. 19). Using the same perturbative analysis as in Section IV in the bulk limit, the Dresselhaus SOC at each k_z is obtained both for the c and v bands respectively, namely

$$\alpha_c(p_z) = 4\cos(p_z a_z)\left(\frac{\delta_{cv}b_{54}\lambda_{15}}{\left(E_c-E_v\right)\left(E_c-E_{v_1}\right)}+\frac{\delta_{cv}b_{16}\lambda_{46}}{\left(E_c-E_v\right)\left(E_c-E_{v_2}\right)}+\frac{\delta_{c_1c}b_{16}^{c_1v_2}\lambda_{46}}{\left(E_c-E_{c_1}\right)\left(E_c-E_{v_2}\right)}\right) \tag{A1}$$

and

$$\alpha_v(p_z) = 4\cos(p_z a_z)\left(\frac{\delta_{cv}b_{54}\lambda_{15}}{\left(E_v-E_c\right)\left(E_v-E_{v_1}\right)}+\frac{\delta_{cv}b_{16}\lambda_{46}}{\left(E_v-E_c\right)\left(E_v-E_{v_2}\right)}+\frac{\delta_{v_1v_2}b_{16}\lambda_{15}}{\left(E_v-E_{v_1}\right)\left(E_v-E_{v_2}\right)}\right). \tag{A2}$$

where $p_z = \frac{\pi}{a_z} - k_z$. The fitting parameters considered are the terms δ_{cv}, δ_{c_1c}, $\delta_{v_1v_2}$ and λ_{46} as the 14-band fit applied to the InSe bulk dispersion did not account for any them. The optimal parameters found in order to fit the spin splitting vs k_z-dependence in the vicinity of the band edge where perturbation theory is best applicable were $\delta_{cv} = 0.014$ eV, $\delta_{c_1c} = 0.022$ eV, $\delta_{v_1v_2} = -0.001$ eV and $\lambda_{46} = -0.09$eV.

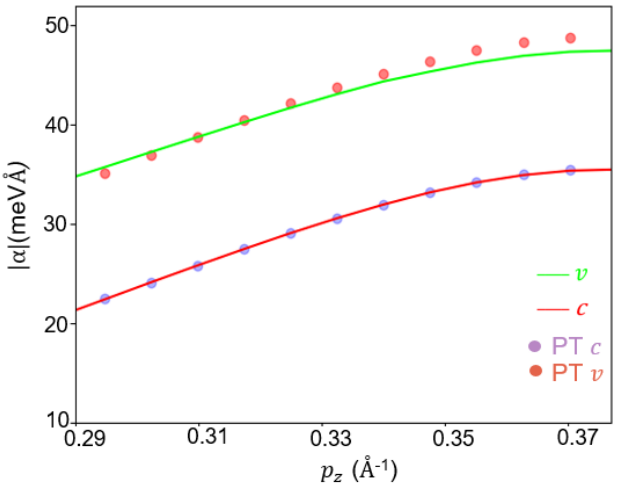

FIG. 19. (Solid) Bulk SOC as a function of p_z for c and v bands. (Dots) SOC strength at different p_z obtained from the perturbative analysis in Eq. (A1) and (A2).

Appendix B: Determination of the signs of d_{cv}, $d_{v_1v_2}$ and d_{c1c}

While on their own the signs of d_{cv} and t_{cv} may be chosen arbitrarily through an appropriate choice of basis in the monolayer Hamiltonian, the product of d_{cv} and t_{cv} does not have such degree of freedom. In order to determine the relative signs of the different dipole moments, it is necessary to look at their k-dependence as we move away from the Γ-point. In considering the conduction to valence band interlayer hopping (both the z-symmetric and z-antisymmetric) as a perturbation to our conduction or valence subband wavefunctions, the k-dependence of the bilayer valence band dipole moment follows easily

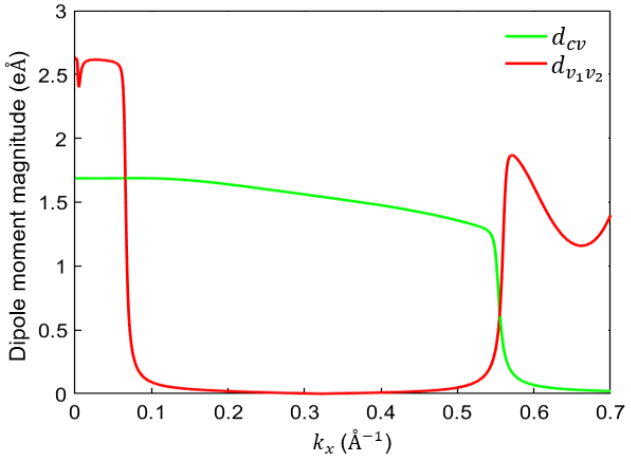

FIG. 20. Dipole moments between monolayer bands c and v (d_{cv}) and between monolayer bands v_1 and v_2 ($d_{v_1v_2}$) computed using the tight-binding model in Ref. 33.

as:

$$\langle v_{2L}|ez|v_{2L}\rangle = 2\delta_{cv}\left[\frac{d_{cv}}{E_{g2L}} + \frac{t_{cv}ea_z}{2E_{g2L}E'_{g2L}}\right] \tag{B1}$$

for the valence band, and

$$\langle c_{2L}|ez|c_{2L}\rangle = -2\delta_{cv}\left[\frac{d_{cv}}{E_{g2L}} + \frac{t_{cv}ea_z}{2E_{g2L}E''_{g2L}}\right] \tag{B2}$$

for the bilayer conduction band. In the above equation, $d_{cv} = |\langle c|ez|v\rangle| = 1.68$ eÅ is the matrix element of the out-of-plane dipole operator between the monolayer conduction and valence bands and v_{2L} and c_{2L} are the topmost valence subband and lowest conduction subband wavefunctions in a bilayer system at the Γ-point. $E_{g2L} = E_c - E_v - (t_{cc} - t_{vv})$, $E'_{g2L} = E_c - E_v + t_{cc} + t_{vv}$, and $E''_{g2L} = E_c - E_v - (t_{cc} + t_{vv})$ are the energy differences between the bilayer bands in the absence of the interband hoppings. Comparison of these expressions with the signs of the quantities calculated using DFT gives, for a choice of positive t_{cv} and negative d_{cv}, a positive δ_{cv} when the $+z$ direction is chosen such that the vertical In-Se interlayer pair in the interface between two layers the Se atom lies above the In atom in the γ-stacking. Conversely, a negative δ_{cv} is obtained for the opposite orientation. On calculating perturbatively the value of d_{cv} at a finite k, the following result is obtained

$$d_{cv}(k) \equiv \langle v|ez|c\rangle = \langle v_0|ez|c_0\rangle + \frac{b_{54}b_{16}k^2 d_{v_1v_2}}{\Delta E_{v_1c}\Delta E_{v_2v}}. \tag{B3}$$

By looking at the negative trend of $|d_{cv}|$ and the hybrid $\mathbf{k}\cdot\mathbf{p}$ tight-binding values quoted in Table III, it is transparent that if d_{cv} is positive $d_{v_1v_1}$ is as well positive. Furthermore, if d_{cv} is negative, the value of $d_{v_1v_2}$ should be negative as well. In order to find the sign of the dipole moment d_{c_1c} a similar perturbative analysis is applied for $d_{v_1v_2}$,

$$d_{v_1v_2}(k) \equiv \langle v_1|ez|v_2\rangle = \langle v_{1,0}|ez|v_{2,0}\rangle + \frac{b_{54}b_{16}k^2 d_{cv}}{\Delta E_{v_1c}\Delta E_{v_2v}} + \frac{b_{54}b_{16}^{c_1v_2}k^2 d_{c_1c}}{\Delta E_{v_1c}\Delta E_{v_2c_1}}. \tag{B4}$$

In comparing the red and the green curve in Fig. 20, the much more pronounced steepness of the red curve as compared to the green curve at low values of k indicates that d_{c_1c} must be negative for a positive $d_{v_1v_2}$ and vice-versa.

Appendix C: Interfacial contribution to multilayer InSe SOC

In addition to the crystalline and the electrostatically induced $z \to -z$ asymmetry, few-layer InSe is a material sensitive to interfacial effects due to its limited thickness. Such effects may have an impact in the SOC strength of multilayer InSe and must therefore be taken into consideration[50]. The same two InSe-hBN configurations used for the analysis of interfacial effects in bilayer InSe shown in Table II (configuration 1 and 2) were also used for the calculation of the interface-induced SOC in multilayer InSe as their contribution in the absence of an external electrostatic potential is only dependent on the encapsulating substrates and on the film thickness. Interface effects are taken into account by adding into the multilayer Hamiltonian two additional contributions identical to Eq. (11). Firstly, bands c and v with a relevant Se p_z orbital composition, experience in the outer layers a shift in energy due to the interaction with the p_z orbitals of the encapsulating hBN. Therefore, an additional energy shift is added to the c,v,v_1 and v_2 bands of the 1^{st} and the N^{th} layer.

Additionally, the hBN interfaces break $z \to -z$ symmetry in the outer layers mixing bands with opposite z-parity but identical in-plane symmetries. The following perturbative term accounting for all these effect is introduced in the multilayer Hamiltonian,

$$\delta\hat{H}^{(I)}_{11(NN)} = \tag{C1}$$
$$\begin{pmatrix} \Delta E_{c1(N)} & 0 & \pm\Upsilon^{t/b}_{cv} & 0 & 0 \\ 0 & \Delta E_{v1(N)} & 0 & 0 & 0 \\ \pm\Upsilon^{t/b}_{cv} & 0 & 0 & 0 & 0 \\ 0 & 0 & 0 & \Delta E_{v_1 1(N)}\hat{\mathbf{I}}_\nu & \pm\Upsilon^{t/b}_{v_1v_2}\hat{\mathbf{I}}_\nu \\ 0 & 0 & 0 & \pm\Upsilon^{t/b}_{v_1v_2}\hat{\mathbf{I}}_\nu & \Delta E_{v_2 1(N)}\hat{\mathbf{I}}_\nu \end{pmatrix},$$

where Υ^t_{cv} and $\Upsilon^t_{v_1v_2}$ are the mixing terms between bands $c-v$ and v_1-v_2 in the top interface and $-\Upsilon^b_{cv}$,$-\Upsilon^b_{v_1v_2}$

are ones mixing bands $c-v$ and v_1-v_2 at the bottom interface. Note that such mixing terms require an opposite sign due to the opposite sign due to the opposite direction of the interfacial effective electric fields at the two InSe/hBN interfaces. Given the very small interfacial energy shift of bands c and v and the very weak hybridization between bands v_1 and v_2, the dominant contribution to the conduction band SOC strength originates from the interfacial terms mixing bands of opposite parity (see Fig. 22). Among them, the most relevant contribution originates from the term Υ_{cv} mixing bands c and v, which, in the absence of an applied electric field, yields to the following contribution to the SOC strength,

$$\Delta H_{11}^{(I)} = 2\Bigg(\Big[\frac{b_{45}\lambda_{15}}{\Delta E_{g^1}\Delta E_{cv_1}} + \frac{b_{16}\lambda_{46}}{\Delta E_{g^1}\Delta E_{cv_2}}\Big](\Upsilon_{cv}^{t}\alpha_1\beta_1 - \Upsilon_{cv}^{b}\alpha_N\beta_N)\Bigg)(\mathbf{s}\times\mathbf{k}), \tag{C2}$$

where ΔE_{g^1} is the energy between the lowest conduction subband and the topmost valence band (i.e. the energy gap) and $\Delta E_{cv_{1(2)}}$ is the energy difference between the lowest conduction subband and the $v_{1(2)}$ subbands. The number of layers dependence of the interfacial SOC strength can be extracted expanding ΔE_{g^1}, $\Delta E_{cv_{1(2)}}$, $\alpha_{1(N)}$ and $\beta_{1(N)}$ as a function of the number of layers in the quantum well approximation presented in Ref. 35. In such approximate framework, the out-of-plane wavevector k_z depends on the number of layers as $k_z = \frac{\pi}{a_z} + \frac{n\pi}{(N+2\nu)a_z}$ and the wavefunctions for both the conduction and the valence bands are approximated as the eigenstates of a quantum well size $L = (N+2\nu)a_z$ ($\Phi_c^n \approx \Phi_v^n \approx \sqrt{\frac{1}{(N+2\nu)a_z}}\cos\left(\frac{n\pi}{(N+2\nu)a_z}\right)$). From this quantum well model, a $\frac{1}{(N+2\nu)^3}$ dependence of the interfacial SOC strength is expected, as confirmed by the fit presented in Fig. 21. Given the smallness of the interfacial SOC strength compared to the layer-number dependent Dresselhaus SOC, any contribution coming from the hBN/InSe interface will be neglected for the rest of our analysis.

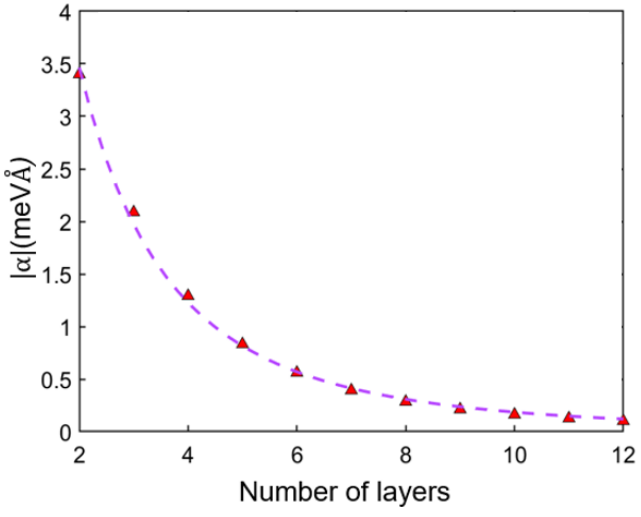

FIG. 21. Interfacial SOC as a function of the number of layers in the absence of an externally applied electric field $\mathcal{E}_z$. (Dashed) Fit of the interfacial SOC strength as a function of the number of layers. A $\frac{1}{(N+2\nu)^3}$ dependence is expected from the quantum well model presented in Ref. 35.

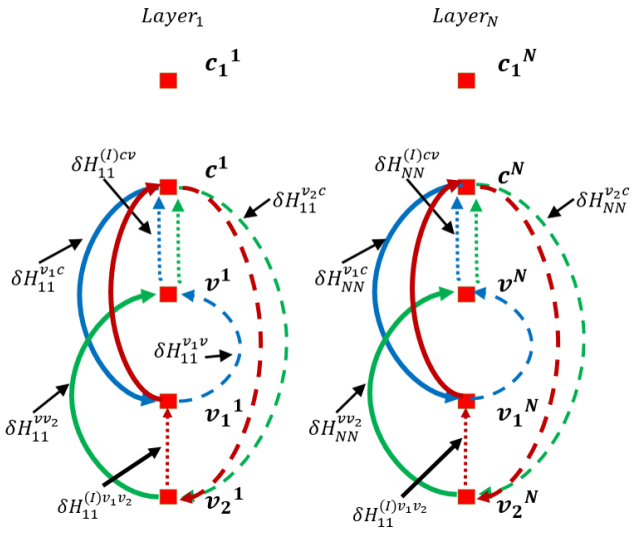

FIG. 22. Feynman diagram of the interlayer spin-flip loops due to the interfacial electric fields experienced by the electrons in the outer Se orbitals of the 1^{st} and N^{th} layer. Dots, dashed and solid lines follow the same convention as in Fig. 7.

Appendix D: Löwdin partitioning method

In order to obtain the 3^{rd} order corrections to the hybrid $\mathbf{k}\cdot\mathbf{p}$ tight-binding Hamiltonian, the standart method of Löwdin partitioning[57] is applied. The total multilayer Hamiltonian is written in the basis of the unperturbed subbands eigenstates obtained from diagonalizing the $\hat{H}_0$ part of the Hamiltonian in Eq. (20b),

$$\hat{H} = \hat{H}_0 + \hat{H}' \tag{D1}$$

where $\hat{H}'$ is the perturbative part, namely the projection of $\delta\hat{H}$ in the orthogonal subband basis formed by $\hat{H}_0$ ($H'_{\rho\omega} \equiv \langle\rho|\delta\hat{H}|\omega\rangle$). In the partitioning method, two diagonal blocks are defined, A and B and a unitary transformation is applied to the entire Hamiltonian matrix in order to remove the non-block-diagonal elements. The set A is defined as the elements within the lowest con-

duction subband c^1

$$\hat{H}_A = \begin{pmatrix} \langle c^{1\uparrow}|\hat{H}_A|c^{1\uparrow}\rangle & \langle c^{1\uparrow}|\hat{H}_A|c^{1\downarrow}\rangle \\ \langle c^{1\downarrow}|\hat{H}_A|c^{1\uparrow}\rangle & \langle c^{1\downarrow}|\hat{H}_A|c^{1\downarrow}\rangle \end{pmatrix}, \tag{D2}$$

while the set B are the matrix elements within the valence subbands or the upper conduction subbands,

$$\hat{H}_B = \begin{pmatrix} \langle v^{1\uparrow}|\hat{H}_B|v^{1\uparrow}\rangle & \langle v^{1\uparrow}|\hat{H}_B|v^{1\downarrow}\rangle & \langle v^{1\uparrow}|\hat{H}_B|v^{2\uparrow}\rangle & \langle v^{1\uparrow}|\hat{H}_B|v^{2\downarrow}\rangle \dots \\ \langle v^{1\downarrow}|\hat{H}_B|v^{1\uparrow}\rangle & \langle v^{1\downarrow}|\hat{H}_B|v^{1\downarrow}\rangle & \langle v^{1\downarrow}|\hat{H}_B|v^{2\uparrow}\rangle & \langle v^{1\downarrow}|\hat{H}_B|v^{2\downarrow}\rangle \dots \\ \langle v^{2\uparrow}|\hat{H}_B|v^{1\uparrow}\rangle & \langle v^{2\uparrow}|\hat{H}_B|v^{1\downarrow}\rangle & \langle v^{2\uparrow}|\hat{H}_B|v^{2\uparrow}\rangle & \langle v^{2\uparrow}|\hat{H}_B|v^{2\downarrow}\rangle \dots \\ \langle v^{2\downarrow}|\hat{H}_B|v^{1\uparrow}\rangle & \langle v^{2\downarrow}|\hat{H}_B|v^{1\downarrow}\rangle & \langle v^{2\downarrow}|\hat{H}_B|v^{2\uparrow}\rangle & \langle v^{2\uparrow}|\hat{H}_B|v^{2\uparrow}\rangle \dots \\ \vdots & \vdots & \vdots & \vdots \end{pmatrix}, \tag{D3}$$

where the numerical indices such as 1 and 2 refer to the 1^{st} or 2^{nd} subbands. The non-block-diagonal elements. H_{nbd} are the elements mixing the terms of the A and B block namely

$$\hat{H}_{nbd} = \begin{pmatrix} \langle c^{1\uparrow}|\hat{H}|v^{1\uparrow}\rangle & \langle c^{1\uparrow}|\hat{H}|v^{1\downarrow}\rangle & \langle c^{1\uparrow}|\hat{H}|v^{2\uparrow}\rangle & \dots \\ \langle c^{1\downarrow}|\hat{H}|v^{1\uparrow}\rangle & \langle c^{1\downarrow}|\hat{H}|v^{1\downarrow}\rangle & \langle c^{1\downarrow}|\hat{H}|v^{2\uparrow}\rangle & \dots \end{pmatrix}. \tag{D4}$$

The expression in Eq. (D1) is rewritten in terms of $\hat{H}_1'$ (the matrix containing the perturbations within block A and B), and $\hat{H}_2'$ (the non-zero perturbations between sets A and B)

$$\hat{H} = \hat{H}_0 + \hat{H}_1' + \hat{H}_2'. \tag{D5}$$

Transforming the Hamiltonian with a unitary transformation of the form $e^{\hat{S}}$,

$$\tilde{H} = e^{-\hat{S}}\hat{H}e^{\hat{S}}, \tag{D6}$$

the deeper valence band states are projected into the lowest conduction subbband. From the definition of the A block, the matrix elements $\langle c^{\uparrow}|\hat{H}|c^{\downarrow}\rangle$ and $\langle c^{\downarrow}|\hat{H}|c^{\uparrow}\rangle$ are the terms responsible for the SOC splitting. We get the following expressions for the block and non-block-diagonal matrix elements,

$$\begin{aligned} \hat{H}_{bd} &= \sum_{j=0}^{\infty} \frac{1}{(2j)!}[\hat{H}^{(0)} + \hat{H}^{(1)}, \hat{S}]^{(2j)} + \\ &\quad \sum_{j=0}^{\infty} \frac{1}{(2j+1)!}[\hat{H}^{(2)}, \hat{S}]^{(2j+1)}, \\ \hat{H}_{nbd} &= \sum_{j=0}^{\infty} \frac{1}{(2j+1)!}[\hat{H}^{(0)} + \hat{H}^{(1)}, \hat{S}]^{(2j+1)} + \\ &\quad \sum_{j=0}^{\infty} \frac{1}{(2j)!}[\hat{H}^{(2)}, \hat{S}]^{(2j)}. \end{aligned} \tag{D7}$$

The non-block-diagonal terms are then set to 0 forcing the third order in the perturbation Hamiltonian ($\Delta H^{(3)}$) to be

$$\begin{aligned} \Delta H^{(3)}_{mm'} &= -\frac{1}{2}\sum_{l,m''}\Big[\frac{H'_{ml}H'_{lm''}H'_{m''m'}}{(E_{m'}-E_l)(E_{m''}-E_l)} + \frac{H'_{mm''}H'_{m''l}H'_{lm'}}{(E_m-E_l)(E_{m''}-E_l)}\Big] \\ &+ \frac{1}{2}\sum_{l,l'}\Big[\frac{H'_{ml}H'_{ll'}H'_{l'm'}}{(E_m-E_l)(E_m-E_{l'})} + \frac{H'_{ml}H'_{ll'}H'_{l'm'}}{(E_{m'}-E_l)(E_{m'}-E_{l'})}\Big], \end{aligned} \tag{D8}$$

where (m, m') are elements within A and (l, l') are elements within B. Having identified the loops responsible for the SOC splitting shown in Figs. 7-9 and 10, the mixing between the conduction and the deeper valence bands projected into the lowest conduction subband has the form,

$$\Delta H_{11}^{(3)} = 2\sum_{j=1}^{j=N}\sum_{\eta=1}^{\eta=N}\frac{\langle c^{\downarrow}|\delta\hat{H}|v_{2,\eta}^{\uparrow}\rangle\langle v_{2,\eta}^{\uparrow}|\delta\hat{H}|v^{j,\uparrow}\rangle\langle v^{j,\uparrow}|\delta\hat{H}|c^{\uparrow}\rangle}{\Delta E_{cv_2}\Delta E_{cv^j}} + 2\sum_{j=1}^{j=N}\sum_{\eta=1}^{\eta=N}\frac{\langle c^{\downarrow}|\delta\hat{H}|v_{1,\eta}^{\downarrow}\rangle\langle v_{1,\eta}^{\downarrow}|\delta\hat{H}|v^{j,\uparrow}\rangle\langle v^{j,\uparrow}|\delta\hat{H}|c^{\uparrow}\rangle}{\Delta E_{cv_1}\Delta E_{cv^j}} \quad \text{(D9)}$$
$$+ 2\sum_{\eta=1}^{\eta=N}\frac{\langle c^{\downarrow}|\delta\hat{H}|v_{2,\eta}^{\uparrow}\rangle\langle v_{2,\eta}^{\uparrow}|\delta\hat{H}|v_{1,\eta}^{\uparrow}\rangle\langle v_{1,\eta}^{\uparrow}|\delta\hat{H}|c^{\uparrow}\rangle}{\Delta E_{cv_1}\Delta E_{cv_2}} + 2\sum_{\eta=1}^{\eta=N}\frac{\langle c^{\downarrow}|\delta\hat{H}|c_{1,\eta}^{\downarrow}\rangle\langle c_{1,\eta}^{\downarrow}|\delta\hat{H}|v_{2,\eta}^{\downarrow}\rangle\langle v_{2,\eta}^{\downarrow}|\delta\hat{H}|c^{\uparrow}\rangle}{\Delta E_{cc_1}\Delta E_{cv_2}}.$$

Knowing the origin of the 3-step loop processes described in Section IV, the Hamiltonian that contributes to the SOC in the absence of a relevant interfacial term can be decomposed as

$$\Delta H_{11}^{(3)} = \Delta H'_{11} + \Delta H''_{11} + \Delta H'''_{11}, \quad \text{(D10)}$$

where the different terms correspond to the different mechanisms behind SOC in band c,

$$\Delta H'_{11} = 2\Bigg[\sum_{j=1}^{j=N}\sum_{\kappa=1}^{\kappa=N}\Big(\frac{b_{54}\lambda_{15}t_{cv}^{\Gamma}}{\Delta E_{cv_1}\Delta E_{cv^j}} + \frac{b_{16}\lambda_{46}t_{cv}^{\Gamma}}{\Delta E_{cv_2}\Delta E_{cv^j}}\Big)\alpha_{\kappa}(\beta_{\kappa+1}^{j} - \beta_{\kappa-1}^{j})\Bigg(\sum_{\xi=1}^{\xi=N}\alpha_l\beta_{\xi}^{j}\Bigg)\Bigg](\mathbf{s}\times\mathbf{k}), \quad \text{(D11)}$$

$$\Delta H''_{11} = 2\Bigg[\sum_{j=1}^{j=N}\sum_{\kappa=1}^{\kappa=N}\Bigg(\frac{\mathcal{E}_{\kappa}d_{cv}\lambda_{15}b_{54}}{\Delta E_{cv^j}\Delta E_{cv_1}} + \frac{\mathcal{E}_{\kappa}d_{cv}\lambda_{46}b_{16}}{\Delta E_{cv^j}\Delta E_{cv_2}}\Bigg)(\alpha_{\kappa}\beta_{\kappa}^{j})\Bigg(\sum_{\xi=1}^{\xi=N}\alpha_{\xi}\beta_{\xi}^{j}\Bigg) + \sum_{\eta=1}^{\eta=N}\alpha_{\eta}^{2}\Bigg(\frac{\mathcal{E}_{\eta}d_{v_1v_2}b_{54}\lambda_{46}}{\Delta E_{cv_1}\Delta E_{cv_2}} +$$
$$\frac{\mathcal{E}_{\eta}d_{c_1c}b_{16}^{c_1v_2}\lambda_{46}}{\Delta E_{cc_1}\Delta E_{cv_2}}\Bigg)\Bigg](\mathbf{s}\times\mathbf{k}),$$

$$\Delta H'''_{11} = 2\Bigg[\sum_{j=1}^{j=N}\sum_{\kappa=1}^{\kappa=N}\Bigg(\frac{b_{54}\lambda_{15}\delta_{cv}}{\Delta E_{cv_1}\Delta E_{cv^j}} + \frac{b_{16}\lambda_{46}\delta_{cv}}{\Delta E_{cv_2}\Delta E_{cv^j}}\Bigg)\alpha_{\kappa}(\beta_{\kappa+1}^{j} + \beta_{\kappa-1}^{j})\Bigg(\sum_{\xi=1}^{\xi=N}\alpha_{\xi}\beta_{\xi}^{j}\Bigg) + \sum_{\eta=1}^{\eta=N}\Bigg(\frac{b_{16}^{c_1v_2}\lambda_{46}\delta_{c_1c}}{\Delta E_{cc_1}\Delta E_{cv_1}}\Bigg)\times$$
$$\alpha_{\eta}(\alpha_{\eta+1} + \alpha_{\eta-1})\Bigg](\mathbf{s}\times\mathbf{k}).$$

Finally, using Eq. (D9) the interfacial contribution to the SOC strength coming from the dominant $\Upsilon_{cv}^{t/b}$ term in Eq. (C2) has the form

$$\Delta H_{11}^{(I)} = 2\Bigg[\sum_{j=1}^{j=N}\Big(\frac{b_{45}\lambda_{15}}{\Delta E_{cv^j}\Delta E_{cv_1}} + \frac{b_{16}\lambda_{46}}{\Delta E_{cv^j}\Delta E_{cv_2}}\Big)(\Upsilon_{cv}^{t}\alpha_1\beta_1^{j} - \Upsilon_{cv}^{b}\alpha_N\beta_N^{j})\Bigg(\sum_{\xi=1}^{\xi=N}\alpha_l\beta_{\xi}^{j}\Bigg)\Bigg](\mathbf{s}\times\mathbf{k}). \quad \text{(D12)}$$

Considering the limit where the applied electric field is zero, this term simplifies to

$$\Delta H_{11}^{(I)} = -2\Big[\frac{b_{45}\lambda_{15}}{\Delta E_{g^1}\Delta E_{cv_1}} + \frac{b_{16}\lambda_{46}}{\Delta E_{g^1}\Delta E_{cv_2}}\Big](\Upsilon_{cv}^{t}\alpha_1\beta_1^{1} - \Upsilon_{cv}^{b}\alpha_N\beta_N^{1})(\mathbf{s}\times\mathbf{k}). \quad \text{(D13)}$$

* adrian.ceferino@postgrad.manchester.ac.uk

[1] M. J. Hamer, J. Zultak, A. V. Tyurnina, V. Zólyomi, D. Terry, A. Barinov, A. Garner, J. Donoghue, A. P. Rooney, V. Kandyba, A. Giampietri, A. Graham, N. Teutsch, X. Xia, M. Koperski, S. J. Haigh, V. I. Fal'ko, R. V. Gorbachev, and N. R. Wilson, ACS Nano **13**, 2136 (2019).

[2] M. Brotons-Gisbert, D. Andres-Penares, J. Suh, F. Hidalgo, R. Abargues, P. J. Rodríguez-Cantó, A. Segura, A. Cros, G. Tobias, E. Canadell, P. Ordejón, J. Wu, J. P. Martínez-Pastor, and J. F. Sánchez-Royo, Nano Letters **16**, 3221 (2016).

[3] N. Ubrig, E. Ponomarev, J. Zultak, D. Domaretskiy, V. Zólyomi, D. Terry, J. Howarth, I. Gutierrez Lezama, A. Zhukov, Z. Kudrynskyi, Z. Kovalyuk, A. Patanè, T. Taniguchi, K. Watanabe, R. Gorbachev, V. I. Fal'ko, and A. Morpurgo, Nature Materials **19**, 299 (2020).

[4] D. J. Terry, V. Zólyomi, M. J. Hamer, A. V. Tyurnina, D. Hopkinson, A. M. Rakowski, S. J. Magorrian, N. Clark, Y. M. Andreev, O. Kazakova, K. S. Novoselov, S. J. Haigh, V. I. Fal'ko, and R. V. Gorbachev, 2D Materials **5**, 041009 (2018).

[5] G. W. Mudd, S. A. Svatek, L. Hague, O. Makarovsky, Z. R. Kudrynskyi, C. J. Mellor, P. H. Beton, L. Eaves, K. S. Novoselov, Z. D. Kovalyuk, E. Vdovin, A. J. Marsden, N. R. Wilson, and A. Patané, Advanced Materials (Deerfield Beach, Fla.) **27**, 3760 (2015).

[6] P. Kang, 2D Materials **7**, 021002 (2020).

[7] Z. Kudrynskyi, J. Kerfoot, D. Mazumder, M. Greenaway, E. Vdovin, O. Makarovsky, Z. Kovalyuk, L. Eaves, P. Beton, and A. Patanè, Communications Physics **3**, 16 (2020).

[8] J. Zultak, S. Magorrian, M. Koperski, A. Garner, M. Hamer, E. Tóvári, K. Novoselov, A. Zhukov, Y. Zou, N. Wilson, S. Haigh, A. Kretinin, V. I. Fal'ko, and R. Gorbachev, Nature Communications **11**, 125 (2020).

[9] G. Mudd, S. Svatek, T. Ren, A. Patanè, O. Makarovsky, L. Eaves, P. Beton, Z. Kovalyuk, G. Lashkarev, Z. Kudrynskyi, and A. Dmitriev, Advanced Materials **25**, 5714 (2013).

[10] H.-C. Chang, C.-L. Tu, K.-I. Lin, J. Pu, T. Takenobu, C.-N. Hsiao, and C.-H. Chen, Small **14**, 1802351 (2018).

[11] D. A. Bandurin, A. V. Tyurnina, L. Y. Geliang, A. Mishchenko, V. Zólyomi, S. V. Morozov, R. K. Kumar, R. V. Gorbachev, Z. R. Kudrynskyi, S. Pezzini, Z. D. Kovalyuk, U. Zeilter, K. S. Novoselov, A. Patanè, L. Eaves, I. V. Grigorieva, V. I. Fal'ko, A. K. Geim, and Y. Cao, Nature Nanotechnology **12**, 223 (2017).

[12] W. Li, S. Ponce, and F. Giustino, Nano Letters **19** (2019).

[13] P.-H. Ho, Y.-R. Chang, Y.-C. Chu, M.-K. Li, C.-A. Tsai, W.-H. Wang, C.-H. Ho, C.-W. Chen, and P.-W. Chiu, Acs Nano **11**, 7362 (2017).

[14] M. Zhou, S. Yu, W. Yang, W.-k. Lou, F. Cheng, D. Zhang, and K. Chang, Phys. Rev. B **100**, 245409 (2019).

[15] K.-H. Kim, H.-j. Kim, H. C. Koo, J. Chang, and S.-H. Han, Applied Physics Letters **97**, 012504 (2010).

[16] M. Schultz, F. Heinrichs, U. Merkt, T. Colin, T. Skauli, and S. Løvold, Semiconductor Science Technology **11**, 1168 (1996).

[17] Z. Wang, D.-K. Ki, J. Y. Khoo, D. Mauro, H. Berger, L. S. Levitov, and A. F. Morpurgo, Phys. Rev. X **6**, 041020 (2016).

[18] S. Omar and B. J. van Wees, Phys. Rev. B **97**, 045414 (2018).

[19] C. Niu, G. Qiu, Y. Wang, Z. Zhang, M. Si, W. Wu, and P. D. Ye, Phys. Rev. B **101**, 205414 (2020).

[20] A. Manchon, H. Koo, J. Nitta, S. Frolov, and R. Duine, Nature Materials **14** (2015).

[21] D. Shcherbakov, P. Stepanov, S. Memaran, Y. Wang, Y. Xin, J. Yang, K. Wei, R. Baumbach, W. Zheng, K. Watanabe, *et al.*, arXiv preprint arXiv:2012.00937 (2020).

[22] D. Liang and X. P. Gao, Nano Letters **12**, 3263 (2012).

[23] R. van Gelderen and C. M. Smith, Phys. Rev. B **81**, 125435 (2010).

[24] K. Premasiri and X. P. Gao, Journal of Physics: Condensed Matter **31**, 193001 (2019).

[25] I. Zutic, J. Fabian, and S. D. Sarma, Acta Phys. Slovaca **57**, 567 (2007).

[26] E. A. de Andrada e Silva, G. C. La Rocca, and F. Bassani, Phys. Rev. B **55**, 16293 (1997).

[27] R. S. Calsaverini, E. Bernardes, J. C. Egues, and D. Loss, Phys. Rev. B **78**, 155313 (2008).

[28] R. Lassnig, Phys. Rev. B **31**, 8076 (1985).

[29] M. Kurpas, M. Gmitra, and J. Fabian, Phys. Rev. B **94**, 155423 (2016).

[30] A. Dankert and S. Dash, Nature Communications **8**, 16093 (2017).

[31] W. Zawadzki and P. Pfeffer, Semiconductor Science and Technology **19**, R1 (2003).

[32] N. Kuroda and Y. Nishina, Solid State Communications **34**, 481 (1980).

[33] S. J. Magorrian, V. Zólyomi, and V. I. Fal'ko, Phys. Rev. B **94**, 245431 (2016).

[34] S. J. Magorrian, *Theory of electronic and optical properties of atomically thin films of Indium Selenide* (Springer, 2019).

[35] S. J. Magorrian, A. Ceferino, V. Zólyomi, and V. I. Fal'ko, Phys. Rev. B **97**, 165304 (2018).

[36] The linear in wavevector SOC presbribed by the C_{3v} point-group has the form $H_{SO}^{(1)} = i\alpha\Big(k_-\mathbf{s}_+ - k_+\mathbf{s}_-\Big)$, where $k_\pm \equiv k_x \pm ik_y$ and $\mathbf{s}_\pm \equiv \frac{1}{2}(\mathbf{s_x} \pm i\mathbf{s_y})$. A higher order invariant in wavevector k can be constructed replacing $k_\pm$ by $k_\pm^3$, therefore leading to a cubic SOC of the form $H_{SO}^{(3)} = -i\beta\Big(k_-^3\mathbf{s}_+ - k_+^3\mathbf{s}_-\Big) = 2\beta\Big((k_x^3 - 3k_xk_y^2)\mathbf{s_y} - (3k_yk_x^2 - k_y^3)\mathbf{s_x}\Big)$.

[37] L. Gerchikov and A. Subashiev, Soviet physics. Semiconductors **26**, 73 (1992).

[38] R. Winkler, S. Papadakis, E. De Poortere, and M. Shayegan, *Spin-Orbit Coupling in Two-Dimensional Electron and Hole Systems*, Vol. 41 (Springer, 2003).

[39] D. Kochan, S. Irmer, and J. Fabian, Phys. Rev. B **95**, 165415 (2017).

[40] J. Rigoult, A. Rimsky, and A. Kuhn, Acta Crystallographica Section B Structural Crystallography and Crystal Chemistry **36**, 916 (1980).

[41] G. Dresselhaus, Phys. Rev. **100**, 580 (1955).

[42] Y. A. Bychkov and É. I. Rashba, JETP Letters **39**, 78 (1984).

[43] M. Zhou, R. Zhang, J. Sun, W.-K. Lou, D. Zhang, W. Yang, and K. Chang, Phys. Rev. B **96**, 155430 (2017).

[44] J. P. Perdew, K. Burke, and M. Ernzerhof, Phys. Rev.

Lett. **77**, 3865 (1996).
[45] G. Kresse and J. Furthmüller, Phys. Rev. B **54**, 11169 (1996).
[46] P. Li and I. Appelbaum, Phys. Rev. B **92**, 195129 (2015).
[47] Note that the SOC coefficients, α, implied by the DFT results, 18.6 meVÅ and 32.3 meVÅ for bilayer and trilayer respectively, are somewhat larger than those predicted by the model presented in this work - this is due to the substantial underestimation of the band gap of InSe by DFT. We therefore base the parametrization of the model on GW results for bulk crystals.
[48] G. Dresselhaus and M. S. Dresselhaus, Phys. Rev. **140**, A401 (1965).
[49] S. J. Magorrian, V. Zólyomi, and V. I. Fal'ko, Phys. Rev. B **96**, 195428 (2017).
[50] D. Wang, W. Ju, T. Li, Q. Zhou, Y. Zhang, Z. Gao, D. Kang, H. Li, and S. Gong, Journal of Physics: Condensed Matter **33**, 045501 (2020).
[51] D. V. Rybkovskiy, A. V. Osadchy, and E. D. Obraztsova, Phys. Rev. B **90**, 235302 (2014).
[52] A. V. Lugovskoi, M. I. Katsnelson, and A. N. Rudenko, Phys. Rev. Lett. **123**, 176401 (2019).
[53] V. Zólyomi, N. D. Drummond, and V. I. Fal'ko, Phys. Rev. B **89**, 205416 (2014).
[54] D. A. B. Miller, D. S. Chemla, T. C. Damen, A. C. Gossard, W. Wiegmann, T. H. Wood, and C. A. Burrus, Phys. Rev. Lett. **53**, 2173 (1984).
[55] A. Ceferino, K. W. Song, S. J. Magorrian, V. Zólyomi, and V. I. Fal'ko, Phys. Rev. B **101**, 245432 (2020).
[56] D. Pashov, S. Acharya, W. R. Lambrecht, J. Jackson, K. D. Belashchenko, A. Chantis, F. Jamet, and M. van Schilfgaarde, Computer Physics Communications **249**, 107065 (2020).
[57] P.-O. Löwdin, J. Chem. Phys. **19**, 1396 (1951).
[58] P.-O. Löwdin, International Journal of Quantum Chemistry **21**, 69 (2004).
[59] D. Pashov, S. Acharya, W. R. Lambrecht, J. Jackson, K. D. Belashchenko, A. Chantis, F. Jamet, and M. van Schilfgaarde, Computer Physics Communications **249**, 107065 (2020).
[60] Y. Cao, A. Mishchenko, G. L. Yu, E. Khestanova, A. P. Rooney, E. Prestat, A. V. Kretinin, P. Blake, M. B. Shalom, C. Woods, J. Chapman, G. Balakrishnan, I. V. Grigorieva, K. S. Novoselov, B. A. Piot, M. Potemski, K. Watanabe, T. Taniguchi, S. J. Haigh, A. K. Geim, and R. V. Gorbachev, Nano Letters **15**, 4914 (2015).
[61] X. Cui, G.-H. Lee, Y. Kim, G. Arefe, P. Huang, C.-H. Lee, D. Chenet, X. Zhang, L. Wang, F. Ye, F. Pizzocchero, B. Jessen, K. Watanabe, T. Taniguchi, D. Muller, T. Low, P. Kim, and J. Hone, Nature Nanotechnology **10**, 534 (2015).
[62] Z. R. Kudrynskyi, M. A. Bhuiyan, O. Makarovsky, J. D. G. Greener, E. E. Vdovin, Z. D. Kovalyuk, Y. Cao, A. Mishchenko, K. S. Novoselov, P. H. Beton, L. Eaves, and A. Patanè, Phys. Rev. Lett. **119**, 157701 (2017).
[63] W. Li and F. Giustino, Phys. Rev. B **101**, 035201 (2020).
[64] T. Koga, J. Nitta, T. Akazaki, and H. Takayanagi, Phys. Rev. Lett. **89**, 046801 (2002).
[65] F. G. Pikus and G. E. Pikus, Phys. Rev. B **51**, 16928 (1995).
[66] S. Hikami, A. I. Larkin, and Y. Nagaoka, Progress of Theoretical Physics **63**, 707 (1980).
[67] Y. Araki, G. Khalsa, and A. H. MacDonald, Phys. Rev. B **90**, 125309 (2014).
[68] B. L. Altshuler, D. Khmel'nitzkii, A. I. Larkin, and P. A. Lee, Phys. Rev. B **22**, 5142 (1980).
[69] B. L. Altshuler, A. Aronov, D. Khmel'nitzkii, A. I. Larkin, and P. A. Lee, JETP Letters **54**, 411 (1981).
[70] S. Takasuna, J. Shiogai, S. Matsuzaka, M. Kohda, Y. Oyama, and J. Nitta, Phys. Rev. B **96**, 161303 (2017).
[71] K. Premasiri, S. K. Radha, S. Sucharitakul, U. R. Kumar, R. Sankar, F.-C. Chou, Y.-T. Chen, and X. P. A. Gao, Nano Letters **18**, 4403 (2018).
[72] J. Zeng, S.-J. Liang, A. Gao, Y. Wang, C. Pan, C. Wu, E. Liu, L. Zhang, T. Cao, X. Liu, Y. Fu, Y. Wang, K. Watanabe, T. Taniguchi, H. Lu, and F. Miao, Phys. Rev. B **98**, 125414 (2018).
[73] R. J. Elliott, Phys. Rev. **96**, 266 (1954).
[74] Y. Yafet, Journal of Physics C: Solid State Physics **14**, 1 (1963).
[75] S. V. Iordanskii, Y. B. Lyanda-Geller, and G. E. Pikus, Soviet Journal of Experimental and Theoretical Physics Letters **60**, 206 (1994).
[76] W. Knap, C. Skierbiszewski, A. Zduniak, E. Litwin-Staszewska, D. Bertho, F. Kobbi, J. L. Robert, G. E. Pikus, F. G. Pikus, S. V. Iordanskii, V. Mosser, K. Zekentes, and Y. B. Lyanda-Geller, Phys. Rev. B **53**, 3912 (1996).
[77] L. E. Golub, Phys. Rev. B **71**, 235310 (2005).
[78] M. M. Glazov and L. Golub, Semiconductors **40**, 1209 (2006).
[79] M. Dyakonov and V. Kachorovskii, Soviet Physics Semiconductors **20**, 110 (1986).
[80] M. Dyakonov and V. Perel, Soviet Physics Solid State **13**, 3023 (1972).
[81] M. Zhou, D. Zhang, S. Yu, Z. Huang, Y. Chen, W. Yang, and K. Chang, Phys. Rev. B **99**, 155402 (2019).

Chapter 5

Crossover from weakly indirect to direct excitons in multilayer InSe thin films

5.1 Introduction

The optical properties of two-dimensional post-transition metal monochalcogenides are fundamentally governed by the formation of strongly correlated electron-hole bound states known as excitons. In such systems, the small thickness of the multilayer film relative to the exciton size has dramatic effects on the excitonic properties of these 2D materials. As the exciton is expected to have a size much larger than the sample thickness, the dielectric constant mediating the electron-hole interaction will be determined both by the dielectric constant of the environment and the in-plane polarisability of the thin film. This hugely modifies the electrostatic interaction, making excitons bind much more strongly when encapsulated in hBN due to the much reduced dielectric constant of the hBN in comparison to the InSe thin film dielectric constant ($\varepsilon^{||}_{hBN} = 6.8$, $\varepsilon^{z}_{hBN} = 3.7$ while $\varepsilon^{||}_{InSe} = 10.9$, $\varepsilon^{z}_{InSe} = 9.9$). Furthermore, in dealing with systems with quantised energy levels, one has to account for any eventual intersubband scattering when the binding energy of the bound pair is larger or comparable to the intersubband energy.

In addition to adding the possibility of intersubband scattering, the formation of subbands broadens the wavefunction distribution along the confinement direction. Such distribution is needed to be taken into account when considering the electron-hole interaction since it substantially differs from the usual point-charge interaction and may increase the binding energy of the exciton. To account

for such effect, two additional forms of the electrostatic interaction were considered (see Appendix.C.1 of this thesis). Firstly, the wavefunction distribution was assumed uniformly distributed over the entire InSe film thickness, then the wavefunction was assumed to follow a sinusoidal distribution in a similar fashion to a quantum well eigenstate. Both electrostatic interactions were demonstrated to generate similar excitonic binding energies with slight increase in the binding energy as compared to the point-like potential originally derived by Keldysh[63]. The calculation of the exciton binding energies and dispersions in multilayer InSe were performed projecting the exciton Hamiltonian in the harmonic oscillator basis. The exciton binding energy was shown to decrease significantly with an increasing number of layers (from ∼200meV in the monolayer to approximately 50meV in a 10-layer film) due to a greater influence of the very large InSe dielectric constant. The excitonic dispersion was shown to transition from having a minimum in energy at a finite centre of mass momentum Q_{min} to becoming a direct exciton with an increasing number of layers. The activation energy of the dispersion (energy difference between $Q_x = 0$ and Q_{min}) was found to transition from approximately 40meV in the monolayer case to 0meV in the 7-layer case, corroborating the observation of an indirect to direct excitonic transition with increasing film thicknesses. Finally, a similar transition was reported in the calculation of excitons in bulk InSe when they acquired a finite centre of mass momentum in the z-direction.

5.2 Crossover from weakly indirect to direct excitons in atomically thin films of InSe

The results presented in this chapter were reported in Ref.[64]: "Crossover from weakly indirect to direct excitons in atomically thin films of InSe". In:Phys. Rev. B 101 (24 June 2020).

My contribution to this work: A. Ceferino performed the calculation of the exciton binding energies, exciton dispersions and exciton radii both in few-layer and in bulk InSe using a real space quantum harmonic oscillator basis. A. Ceferino also extracted the Mexican hat parameters in Appendix.A, calculated the binding energies shown in Table III and contributed to the writing of the manuscript.

Full author list: Adrián Ceferino, Kok Wee Song, Samuel J.Magorrian, Viktor Zólyomi and V.I. Fal'ko.

Author contribution: K.W.Song performed as well every calculation of exciton binding energies, exciton dispersions and exciton radii using an equivalent method to the one used by A. Ceferino. He also calculated the excitonic dispersion using the Fourier transform method presented in Appendix.C and contributed to the writing of the manuscript. K.W. Song developed the package presented in the supplementary material in Ref.[64]. S.J. Magorrian wrote Appendix.B and, together with V. Zólyomi performed the necessary DFT calculations for the parameters in Table II. V.I. Fal'ko supervised the project and contributed to the writing of the manuscript.

Crossover from weakly indirect to direct excitons in atomically thin films of InSe

Adrián Ceferino,[1,2,*] Kok Wee Song,[2,†] Samuel J. Magorrian,[2] Viktor Zólyomi,[3] and Vladimir I. Fal'ko[1,2,4]

[1]*Department of Physics and Astronomy, University of Manchester, Oxford Road, Manchester, M13 9PL, United Kingdom*

[2]*National Graphene Institute, Booth Street East, Manchester, M13 9PL, United Kingdom*

[3]*STFC Hartree Centre, Daresbury Laboratory, Daresbury, Warrington, WA4 4AD, United Kingdom*

[4]*Henry Royce Institute for Advanced Materials, Manchester, M13 9PL, United Kingdom*

(Received 14 January 2020; accepted 23 March 2020; published 22 June 2020)

We perform a $\mathbf{k}\cdot\mathbf{p}$ theory analysis of the spectra of the lowest energy and excited states of the excitons in few-layer atomically thin films of InSe taking into account in plane electric polarizability of the film and the influence of the encapsulation environment. For the thinner films, the lowest-energy state of the exciton is weakly indirect in momentum space, with its dispersion showing minima at a layer-number-dependent wave number, due to an inverted edge of a relatively flat topmost valence band branch of the InSe film spectrum, and we compute the activation energy from the momentum dark exciton ground state into the bright state. For the films with more than seven In_2Se_2 layers, the exciton dispersion minimum shifts to Γ point.

DOI: 10.1103/PhysRevB.101.245432

Two-dimensional (2D) materials create new opportunities for semiconductor optoelectronics [1–3]. Among those new materials, post-transition metal chalcogenides (InSe and GaSe) occupy a special place, as they offer a flexibility to choose a desirable size of their bandgap (in the range from 3 to 1.3 eV) depending on the number of atomic planes in a thin film [4–8]. While the experimental studies of the band gap and optical properties of few layer films of InSe [7,9–11] and GaSe [12–15] have found a reasonably close quantitative interpretation at the single-particle level, based on density functional theory (DFT) [16–22] and the DFT-parametrized tight-binding model [23], the fine tuning of the theory requires taking into account excitonic effects in the system, which remains an open question for atomically thin InSe films.

Here, we develop a mesoscale theory for the binding energies, dispersions, and excited state spectra of excitons in mono-, bi-, tri-, and few-layer InSe films (γ polytype), taking into account the strongly nonparabolic features of the valence band dispersion in these 2D materials and the influence of various encapsulation environments. In particular, we study the role of a weak inversion of the hole dispersion near the top of the valence band [18,19,24–26], established in the thinnest InSe and GaSe films using angle-resolved photoemission spectroscopy [10,27] and high field magneto-optics studies [23], and analyze the crossover of the excitons from weakly indirect to direct in momentum space, as a function of the InSe film thickness. The crossover of the exciton dispersion from indirect [$\varepsilon(Q) = \min$ at $Q \neq 0$] to direct [$\varepsilon(Q) = \min$ at $Q = 0$] exciton was found at $L = 7$ layers. For films with $1 \leqslant L \leqslant 10$, we compute the binding energies of the excitons for hBN-encapsulated InSe films and the activation energies from the momentum-dark excitonic bound states, with the results summarized in Fig. 1.

In the analysis presented below, we describe excitons using two-particle wave functions, $\Psi^\dagger_{\mathbf{Q}} = \sum_{nm}\int d^2k\,\psi_{\mathbf{Q},nm}(\mathbf{k})a^\dagger_{\mathbf{k}+\mathbf{Q},n}c_{\mathbf{k},m}$, written in the wave-number representation for the constituent electrons and holes occupying states with wave numbers $\mathbf{k}+\mathbf{Q}$ and $\mathbf{k}$ in sub-bands [11,28] n and m on the conduction ($a_{\mathbf{k}+\mathbf{Q},n}$) and valence ($c_{\mathbf{k},m}$) band side of few-layer InSe film spectrum. Below, we project all electron and hole states onto the lowest sub-bands ($n = 1$) in the film, which is justified by the much larger inter-sub-band energies, as compared to the exciton binding energies in the thin films (with $L \lesssim 10$ see Fig. 2). As a result, the exciton creation operator takes the approximate form $\Psi^\dagger_{\mathbf{Q}} = \int d^2k\,\psi_{\mathbf{Q}}(\mathbf{k})a^\dagger_{\mathbf{k}+\mathbf{Q},1}c_{\mathbf{k},1}$ where $\psi_{\mathbf{Q}} \equiv \psi_{\mathbf{Q},11}$. This gives the Bethe-Salpeter equation [29–33]:

$$\int_{\mathbf{q}}[(\varepsilon_c(\mathbf{k})-\varepsilon_v(\mathbf{k}-\mathbf{Q})-\Omega)\delta_{\mathbf{q},0}+V(\mathbf{q})]\psi_{\mathbf{Q}}(\mathbf{k}+\mathbf{q})=0, \quad (1)$$

for an effectively 2D exciton with momentum $\mathbf{Q}$ and energy Ω (the latter is a sum $\Omega = E_g + E_b$ of the gap E_g and the binding energy E_b). Here, we use the notation $\int_{\mathbf{q}} \equiv \int \frac{d^2q}{(2\pi)^2}$. The electron-hole (e-h) attraction is accounted for by the Fourier transform of the interaction potential,

$$V(\mathbf{q})=-\frac{4\pi e^2}{\epsilon_0}\iint|\phi_{e\mathbf{k}_e}(z)|^2W(\mathbf{q},z,z')|\phi_{h\mathbf{k}_h}(z')|^2dzdz',$$

$$W(\mathbf{q},z,z')=\frac{\cosh\left[\tilde{q}\left(\frac{d}{2}-z\right)+\eta\right]\cosh\left[\tilde{q}\left(\frac{d}{2}+z'\right)+\eta\right]}{\sqrt{\epsilon_\parallel\epsilon_z}q\sinh(\tilde{q}d+2\eta)};$$

$$\tilde{q}=\sqrt{\epsilon_\parallel/\epsilon_z}q; \quad \eta=\frac{1}{2}\ln\frac{\sqrt{\epsilon_\parallel\epsilon_z}+\sqrt{\kappa_\parallel\kappa_z}}{\sqrt{\epsilon_\parallel\epsilon_z}-\sqrt{\kappa_\parallel\kappa_z}}, \quad (2)$$

designed to take into account both the dielectric polarizability of the 2DM and the dielectric environment [34–37] (e.g., hBN [38,39], with $\kappa_\parallel = 6.9$ and $\kappa_z = 3.7$). For L-layer InSe, film thickness is $d = La_z$, where $a_z = 8.32$ Å is the interlayer distance and $\epsilon_\parallel$ and ϵ_z are the in- and out-of-plane permittivities

*adrian.ceferino@postgrad.manchester.ac.uk

†kokwee.song@manchester.ac.uk

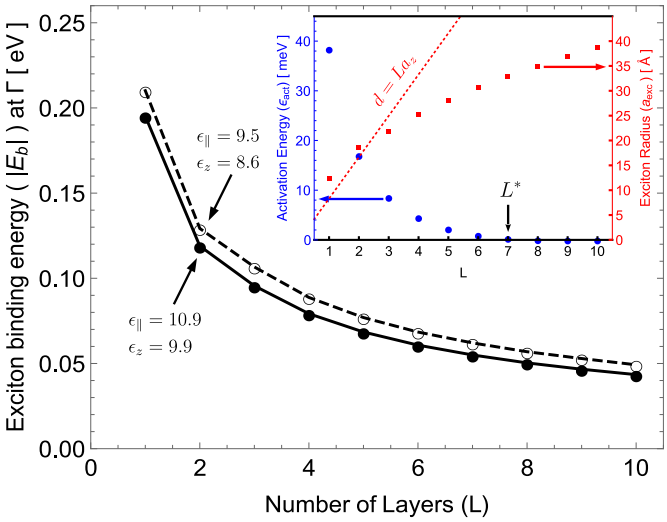

FIG. 1. The dependence of the exciton binding energy on the number of layers (L) for hBN encapsulated InSe films. Binding energies at Γ point, $E_b(0)$ are compared for two values of bulk InSe dielectric constants $\epsilon_\parallel$ and ϵ_z. The inset shows the activation energy $\varepsilon_{\rm act} = E_{\rm b}(0) - E_{\rm b}(Q_{\rm min})$ (closed blue circles) where $Q_{\rm min}$ is approximately the wave vector between the Γ point and the edge of the highest valence band. The radius of the exciton, $a_{\rm exc} = \sqrt{\langle|\mathbf{r}_e - \mathbf{r}_h|^2\rangle}$ is also shown (closed red square). The red dashed line shows the thickness of the InSe film.

of bulk InSe [40]. The above expression takes into account the z dependence of the lowest electron-hole sub-band wave functions $\phi_{e/h,\mathbf{k}}(z)$, and W is quoted for $z \geqslant z'$ (for $z < z'$, z should be interchanged with z'). We note that, for $L = 1$ and 2, the 2D potential $V(\mathbf{q})$ can be simplified to the Keldysh potential [34,35,37,41],

$$V(\mathbf{q}) \approx -\frac{2\pi e^2}{\sqrt{\kappa_z \kappa_\parallel}} \frac{1}{q(1+r_* q)}, \quad r_* = \frac{\sqrt{\epsilon_z \epsilon_\parallel} - 1}{2\sqrt{\kappa_z \kappa_\parallel}} d.$$

In the above equation, r_* is the screening length [42] indicating the region dominated by the logarithmically divergent potential at length scales smaller than r_* and the region dominated by the Coulombic interaction potential at distances greater than r_*. However, for $L \geqslant 3$, the exciton radius ($a_{\rm exc}$) appears to be smaller than the film thickness, so that the electron/hole charge distribution along the z axis in Eq. (2) needs to be taken into account in full details. To do that, we use the quantum-well approximation for the z distribution of the lowest sub-band [28,43], $\phi_{e/h,\mathbf{k}}(z) \approx \sqrt{2/d}\cos(\pi z/d)$. We note that separating wave-function variables and discarding higher energy sub-bands in Eq. (1) is applicable if the quantization energy due to confinement is much larger than the excitonic energy scale, which will be justified later by comparing the inter-sub-band energies to the calculated exciton binding energies.

To implement numerical diagonalization of the Bethe-Salpeter equation (1), we use a basis of harmonic oscillator functions for the bound electron-hole states [44], $\psi_{\mathbf{Q}}(\mathbf{k}) = \sum_{0\leqslant n_x+n_y}^{N_{\rm max}} \mathcal{A}^{\mathbf{Q}}_{n_x,n_y} \varphi_{n_x}(k_x)\varphi_{n_y}(k_y)$ where $\varphi_n(k) = \sqrt{\frac{\lambda}{\pi^{1/2}2^n n!}}(-i)^n e^{-k^2\lambda^2/2} H_n(k\lambda)$ and $H_n(x)$ is the nth Hermite polynomial. In the above described basis, the choice of the length λ and the cutoff $N_{\rm max}$ are optimized for speeding up a converging calculation (see Appendix C for details). We also checked the performance of the developed code by comparing its results to the exact solution of the 2D hydrogen problem, aiming at <2% error as compared to the ground-state energy of the Rydberg series. A software package for

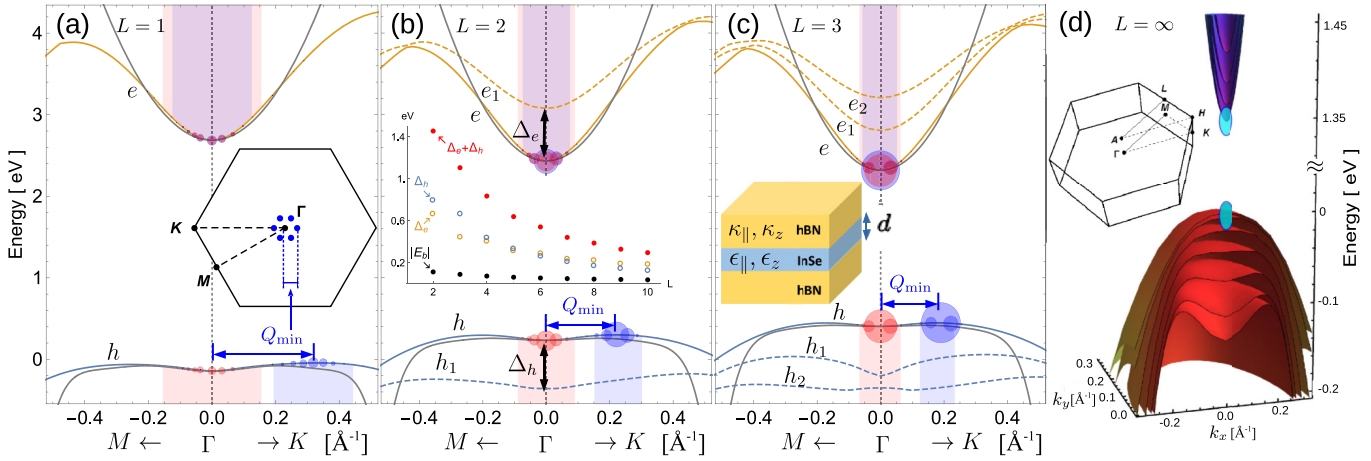

FIG. 2. The bound electron-hole states and the quasiparticle dispersion in momentum space: (a)–(c) The plots for L =1–3 layers film. The solid (dashed) yellow and blue curves are conduction and valence (sub)band tight-binding dispersions [23]. The gray curves are the $\mathbf{k}\cdot\mathbf{p}$ dispersion where ε_c and ε_v are expanded into a polynomial of $\mathbf{k}$. The sizes of the red (blue) circles are proportional to the probability density $|\psi_{\mathbf{Q}}(\mathbf{k})|^2$ with $\mathbf{Q} = 0$ ($\mathbf{Q} = Q_{\rm min}$ being the total momentum of the lowest energy exciton. (d) Plot for bulk InSe dispersion near A point: Each of the bands plotted both in conduction and in valence band correspond to $k_z = 0 - 0.06$ Å^{-1} in steps of 0.01 Å^{-1}. Blue shaded region indicates the region in in-plane momentum and in energy covered by the ground-state exciton in the bulk limit as determined by the size of the Gaussian wave packet and the exciton binding energy. (Insets) (a) Brillouin zone of 2D-InSe, blue circles showing C_6-symmetric localization of holes; (b) a comparison of the $\mathbf{Q} = 0$ exciton binding energy (closed black circles) with the sub-band energy splittings. Δ_e (open yellow circles) and Δ_h (open blue circles) correspond to the e-e_1 and h-h_1 splitting at the Γ point, respectively. The closed black circles are the total splitting, $\Delta_e + \Delta_h$; (c) schematic of hBN-encapsulated InSe, with their different dielectric constants; (d) Brillouin zone of bulk InSe.

the implementation of numerical diagonalization of Eq. (1) with arbitrary parameters for InSe films and encapsulation environment and instructions for interested users are included in the Supplemental Material [45].

With this numerical setting, we solve Eq. (1) using the DFT-parametrized $\mathbf{k}\cdot\mathbf{p}$ theory for InSe films with dispersions illustrated in Fig. 2. In particular, we used a polynomial expansion around Γ point both for the conduction and valence bands [46] computed using the GW-parametrized hybrid $\mathbf{k}\cdot\mathbf{p}$ tight-binding model (see Appendix B), $\varepsilon_{c/v}(\mathbf{k}) = \sum_{i,j=0} A_{ij}^{e/h} k_x^i k_y^j$ also plotted in Figs. 2(a)–2(c). For comparison, in Fig. 2(d), we show the conduction and valence band dispersion of bulk InSe near the band edges (which are at A point in the 3D Brillouin zone), where the inversion of $\varepsilon_v(\mathbf{k}, k_z)$ develops upon the increase of z-axis momentum k_z (counted from A point).

In Fig. 3(a), we show the first eight bound states energies of the Γ-point exciton with $Q = 0$ (solid line) [47] and the lowest-energy momentum-dark state of the exciton at $Q = Q_{\min}$ (dashed line) for $1 \leqslant L \leqslant 3$. A minimum at $Q = Q_{\min}$ in the exciton dispersion for each state [Fig. 3(b)] is due to the sombrero of the h band (see Fig. 2). The non-hydrogen-like energy sequence [48,49] is due to the 2D screening of the e-h interaction in the film leading to a Keldysh-like potential for $L = 1$ and 2.

To illustrate the layer-number dependence of the exciton dispersion, we compare the exciton binding energy at the Γ point, $E_b(0)$, and at its dispersion minimum, $E_b(Q_{\min})$, for L up to 10 layers. In the inset in Fig. 1, we plot the activation energy ε_{act} from the dark exciton state (at $Q = Q_{\min}$) to the optically active state (at $Q = 0$). We find that $\varepsilon_{\text{act}} \to 0$ at $L^* = 7$, which indicates that an indirect to direct crossover for the exciton occurs before the expectation based on a single-particle valence band dispersion (at $L^* = 10$, see Appendix B). For completeness, we also analyzed excitons in bulk 3D InSe using bulk band dispersions shown in Fig. 2(d) and $V(\mathbf{q}, q_z) = -\frac{4\pi e^2/\epsilon_0}{\epsilon_\parallel q^2 + \epsilon_z q_z^2}$. We solve the Bethe-Salpeter equation for bulk InSe using the 3D harmonic oscillator basis, and use dielectric constants [40] $\epsilon_\parallel = 10.9$, $\epsilon_z = 9.9$ for InSe, together with the GW-computed valence band masses ($m_{v\parallel} = -5.35m_0$, $m_{vz} = -0.078m_0$) and the conduction band masses ($m_{c\parallel}/m_0 = 0.16$ and $m_{cz}/m_0 = 0.086$ where m_0 is the free electron mass) which are close to those measured in cyclotron resonance experiments [50]. The examples of computed bulk exciton dispersions, $E_{3D}(\mathbf{Q}, Q_z)$ are shown in Fig. 3(c). Using ($Q_z \approx \frac{\pi}{La_z}$) for the quantization of the transverse exciton motion, we find that the crossover into indirect spectrum should be expected at $L \approx 6$–7 layers, in agreement with the transition number of layers L^* found in the layer dependence of the activation energy ε_{act} (inset in Fig. 1). We note that the computed bulk (3D) exciton binding energy is about 30% lower than the experimentally claimed [51,52] values of 13–15 meV. Binding energy can be increased to 14.6 meV by choosing $\epsilon_\parallel = 9.5$, $\epsilon_z = 8.6$ (with $\sqrt{\epsilon_z/\epsilon_\parallel} = 0.95$ as in Ref. [40]). For this reason we computed and compared the exciton spectra in the films using two choices of dielectric parameters $\epsilon_\parallel = 10.9$, $\epsilon_z = 9.9$ and $\epsilon_\parallel = 9.5$, $\epsilon_z = 8.6$. We find that in thin films $L \leqslant 10$ such a variation of InSe dielectric parameters has a much weaker influence on the exciton bindings than in the

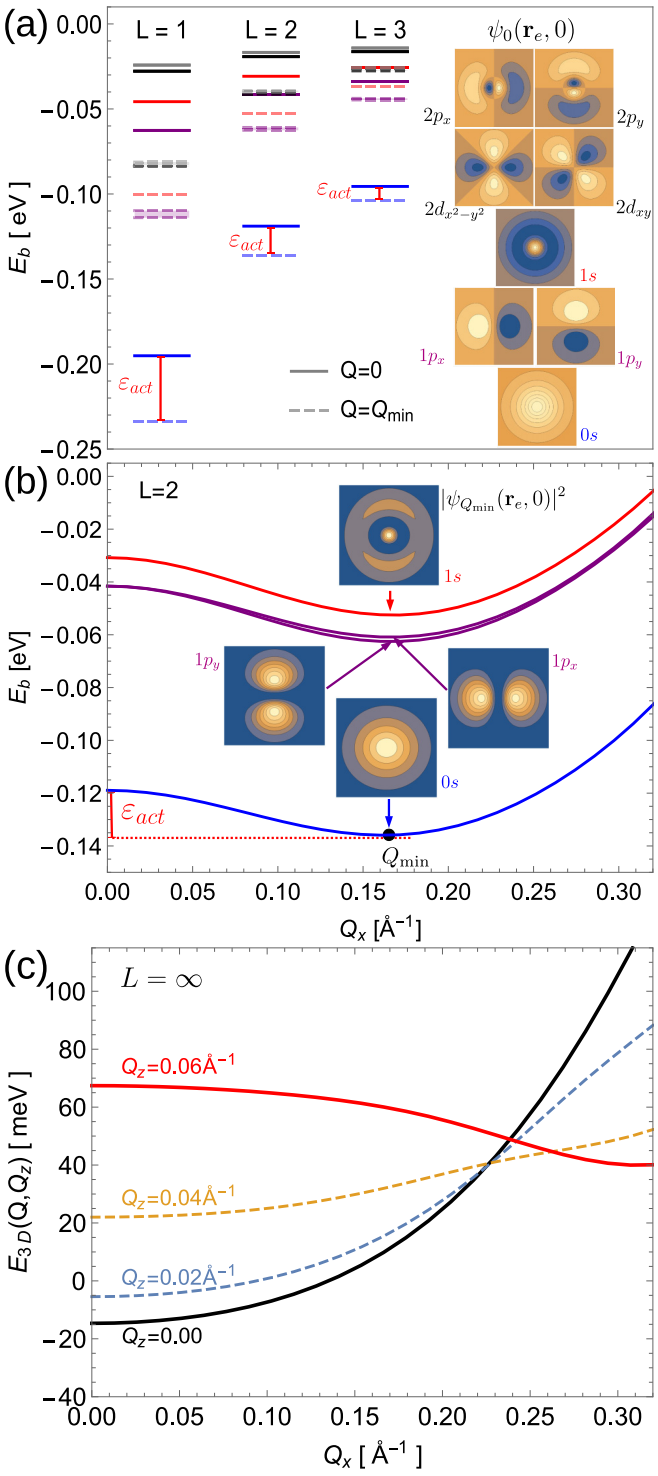

FIG. 3. (a) The first eight low-energy states of the exciton at $Q = 0, Q_{\min}$ in hbN-encapsulated InSe. Insets on the right are the schematic exciton wave functions $\psi_0(\mathbf{r}_e, 0)$ in the real space ($\psi_{\mathbf{Q}}(\mathbf{r}_e, \mathbf{r}_h) \equiv \sum_{\mathbf{k}} \psi_{\mathbf{Q}}(\mathbf{k}) e^{i\mathbf{k}\cdot(\mathbf{r}_e - \mathbf{r}_h)}$) which are sorted from higher to lower binding energies (bottom to top). The dark and bright region correspond to a negative and positive value for the wave-function amplitude. (b) The exciton dispersion for the first four low-energy states. The schematic real-space probability distributions of a bound electron, $|\psi_{Q_{\min}}(\mathbf{r}_e, 0)|^2$, are illustrated by the insets. (c) The energy dispersion of the exciton ground state in bulk InSe with $Q_y = 0$. The different Q_z values are indicated in the plot. We use the adjusted dielectric parameters in the plot which are $\epsilon_\parallel = 9.5$ and $\epsilon_\parallel = 8.6$.

TABLE I. Polynomial fit of the sombrero dispersion as for the topmost valence band and parabolic dispersion of the lowest conduction band. m_0 is the free electron mass.

L	A_8^h (eVÅ^8)	A_6^h (eVÅ^6)	A_4^h (eVÅ^4)	A_2^h (eVÅ^2)	m_c/m_0
1	−1188.591	471.809	−68.601	3.674	0.266
2	−1210.270	388.158	−49.004	1.989	0.223
3	−1308.626	371.401	−43.048	1.372	0.207
4	−1411.696	364.846	−39.437	0.985	0.198
5	−1565.869	366.036	−36.797	0.703	0.193
6	−1745.505	368.254	−34.556	0.487	0.189
7	−1938.337	369.112	−32.543	0.316	0.187
8	−2130.725	367.119	−30.684	0.179	0.184
9	−2302.573	361.073	−28.941	0.068	0.183
10	−2085.138	331.905	−27.004	−0.026	0.181

bulk material. These calculated binding energies compare well with the values observed in the recent experiments [11] on hBN-encapsulated thin InSe films. In summary, we present a mesoscale theory which is particularly useful for investigating the energy spectrum of a Wannier-Mott exciton in large gap semiconductors ($E_g \gg |E_b|$). Most interestingly, this theoretical framework can also be applied to study direct and indirect excitons in complex van der Waals heterostructures [53–61].

ACKNOWLEDGMENTS

The authors would like to thank H. Deng, M. van Schilfgaarde, D. Pashov, and V. Enaldiev for useful discussions. A.C. acknowledges support from EPSRC CDT Graphene NOWNANO. S.J.M., K.W.S., and V.F. acknowledge support from ERC Synergy Grant Hetero2D, EC Quantum Technologies Flagship Project No. 2D-SIPC, EPSRC Grant No. EP/N010345, and the Lloyd Register Foundation Nanotechnology grant.

APPENDIX A: PARAMETRIZATION OF ELECTRON-HOLE DISPERSION IN *L*-LAYER INSE

Here, we give the details on the parametrized electron and hole dispersion by using polynomial fit. The conduction and valence band dispersions near the Γ point are approximated by

$$\varepsilon_c(\mathbf{k}) = \frac{1}{2m_c}\mathbf{k}^2, \tag{A1}$$

$$\varepsilon_v(\mathbf{k}) = A_2^h\mathbf{k}^2 + A_4^h\mathbf{k}^4 + A_6^h\mathbf{k}^6 + A_8^h\mathbf{k}^8, \tag{A2}$$

where the hexagonal wrapping terms are ignored, because the exciton wave function is strongly localized in k-space. These polynomials are obtained by fitting to bands from the GW-parametrized hybrid $\mathbf{k}\cdot\mathbf{p}$ tight-binding (HkpTB) model, Appendix B, and the fitted values for 1- to 10-layer InSe film are listed in Table I. We note for $L \leqslant 9$ that the quadratic term in the valence band dispersion corresponds to negative effective hole masses. This yields a sombrero-shaped dispersion in the valence band and requires one to retain higher-order terms in the expansion for fitting. The hole mass becomes positive at $L = 10$. For the 3D bulk dispersion near the conduction and valence band edges of γ-InSe, we employ the following polynomial of the form,

$$\varepsilon_c(\mathbf{k}, k_z) = \frac{k^2}{2m_{c\parallel}} + \frac{k_z^2}{2m_{cz}}, \tag{A3}$$

$$\varepsilon_v(\mathbf{k}, k_z) = \frac{\mathbf{k}^2}{2m_{v\parallel}} + \frac{k_z^2}{2m_{vz}} + \gamma\mathbf{k}^4 + \alpha\mathbf{k}^2k_z^2 + \gamma_z k_z^4. \tag{A4}$$

Here, k_z is measured from the A point. In the fit, obtained using GW-DFT computed bands, the effective in-plane and out-of-plane masses for the electron are $m_{c\parallel} = 0.16m_0$ and $m_{cz} = 0.086m_0$, close to the experimentally measured [50] values of $m_{c\parallel} \approx 0.14m_0$ and $m_{cz} \approx 0.08m_0$, respectively. For the valence band, the fitted parameters are as follows: $m_{v\parallel} = -5.35m_0$, $m_{vz} = -0.078m_0$, $\gamma = -10.84$ eVÅ^4, $\alpha = 1074$ eVÅ^4, and $\gamma_z = 1688$ eVÅ^4.

APPENDIX B: HYBRID MULTIBAND $\mathbf{k}\cdot\mathbf{p}$ TIGHT-BINDING THEORY WITH PARAMETERS FROM QUASIPARTICLE SELF-CONSISTENT GW CALCULATIONS

1. Hybrid multiband $\mathbf{k}\cdot\mathbf{p}$ tight-binding model

The model used in this study is built using two main components: a multiband $\mathbf{k}\cdot\mathbf{p}$ model describing the monolayer bands (following Refs. [20,62]), and interlayer coupling in few-layer and bulk systems, described using a tight-binding approach based on the monolayer $\mathbf{k}\cdot\mathbf{p}$ bands (similar to the hybrid $\mathbf{k}\cdot\mathbf{p}$ tight-binding approach taken in Refs. [28,63]).

In this description we model the bands of few-layer and bulk InSe near the Γ point using a Hamiltonian with the form,

$$H = \sum_{\mathbf{k},\sigma}\left[\sum_{n=1}^{N} H_{ML,\mathbf{k},\sigma}^{n} + \sum_{n=1}^{N-1} H_{IL,\mathbf{k},\sigma}^{n,n+1} + \text{H.c.}\right], \tag{B1}$$

where $H_{ML,\mathbf{k},\sigma}^{n}$ is the monolayer $\mathbf{k}\cdot\mathbf{p}$ Hamiltonian on layer n of the N-layer crystal, at $\mathbf{k}$ with z projection of spin $\sigma = \pm\frac{1}{2}$. $H_{I-L}^{n,n+1}$ includes the interlayer tight-binding hops between the monolayer bands.

a. Monolayer $\mathbf{k}\cdot\mathbf{p}$ *Hamiltonian*

The monolayer Hamiltonian follows the multiband $\mathbf{k}\cdot\mathbf{p}$ approaches of Refs. [20,62]. While in our previous works [23,28] the basis of monolayer bands was a basis of single-band $\mathbf{k}\cdot\mathbf{p}$ expansions, so that matrix elements such as couplings to electromagnetic fields and the interlayer hops mentioned above had to depend on k, here we follow the multiband approach and take as our basis the bands at Γ, and introduce k-dependent off-diagonal terms to account for the variation of the bands with k. At the expense of an increase in the dimensionality of the parameter space, this allows us to make the approximation that the interlayer hops are independent of k, and assists in the capture of higher-order effects, such as the offset valence band maximum, while keeping the $\mathbf{k}\cdot\mathbf{p}$ expansions to order k^2. The monolayer Hamiltonian for layer

n of an N-layer crystal takes the form,

$$\begin{aligned}H^{n}_{ML,\mathbf{k},\sigma} =& (\varepsilon_{c_1}+\alpha_{c_1}k^2)a^{\sigma\dagger}_{n,c_1,\mathbf{k}}a^{\sigma}_{n,c_1,\mathbf{k}} + (\varepsilon_{c}+\alpha_{c}k^2)a^{\sigma\dagger}_{n,c,\mathbf{k}}a^{\sigma}_{n,c,\mathbf{k}} + (\varepsilon_{v}+\alpha_{v}k^2)a^{\sigma\dagger}_{n,v,\mathbf{k}}a^{\sigma}_{n,v,\mathbf{k}}\\
&+ \left(\varepsilon_{v_1}+\left(\alpha_{v_1}k^2+\alpha'_{v_1}\left(k_x^2-k_y^2\right)\right)a^{\sigma\dagger}_{n,v_{1x},\mathbf{k}}a^{\sigma}_{n,v_{1x},\mathbf{k}} + \left(\varepsilon_{v_1}+\alpha_{v_1}k^2+\alpha'_{v_1}\left(k_y^2-k_x^2\right)\right)a^{\sigma\dagger}_{n,v_{1y},\mathbf{k}}a^{\sigma}_{n,v_{1y},\mathbf{k}}\right.\\
&+ \left(\varepsilon_{v_2}+\left(\alpha_{v_2}k^2+\alpha'_{v_2}\left(k_x^2-k_y^2\right)\right)a^{\sigma\dagger}_{n,v_{2x},\mathbf{k}}a^{\sigma}_{n,v_{2x},\mathbf{k}} + \left(\varepsilon_{v_2}+\alpha_{v_2}k^2+\alpha'_{v_2}\left(k_y^2-k_x^2\right)\right)a^{\sigma\dagger}_{n,v_{2y},\mathbf{k}}a^{\sigma}_{n,v_{2y},\mathbf{k}} + 2\alpha'_{v_1}k_xk_ya^{\sigma\dagger}_{n,v_{1x},\mathbf{k}}a^{\sigma}_{n,v_{1y},\mathbf{k}}\right.\\
&+ 2\alpha'_{v_2}k_xk_ya^{\sigma\dagger}_{n,v_{2x},\mathbf{k}}a^{\sigma}_{n,v_{2y},\mathbf{k}} + \beta_{c_1,v}k^2a^{\sigma\dagger}_{n,c_1,\mathbf{k}}a^{\sigma}_{n,v,\mathbf{k}} + i\beta_{c_1,v_2}\left(k_xa^{\sigma\dagger}_{n,c_1,\mathbf{k}}a^{\sigma}_{n,v_{2x},\mathbf{k}} + k_ya^{\sigma\dagger}_{n,c_1,\mathbf{k}}a^{\sigma}_{n,v_{2y},\mathbf{k}}\right)\\
&+ i\beta_{v,v_2}\left(k_xa^{\sigma\dagger}_{n,v,\mathbf{k}}a^{\sigma}_{n,v_{2x},\mathbf{k}} + k_ya^{\sigma\dagger}_{n,v,\mathbf{k}}a^{\sigma}_{n,v_{2y},\mathbf{k}}\right) + i\beta_{c,v_1}\left(k_xa^{\sigma\dagger}_{n,c,\mathbf{k}}a^{\sigma}_{n,v_{1x},\mathbf{k}} + k_ya^{\sigma\dagger}_{n,c,\mathbf{k}}a^{\sigma}_{n,v_{1y},\mathbf{k}}\right)\\
&- 2\lambda_{v_{1,2}}i\sigma\left(a^{\sigma\dagger}_{n,v_{1x},\mathbf{k}}a^{\sigma}_{n,v_{1y},\mathbf{k}} + a^{\sigma\dagger}_{n,v_{2x},\mathbf{k}}a^{\sigma}_{n,v_{2y},\mathbf{k}}\right) + \lambda_{v,v_1}\left(-2\sigma a^{\sigma\dagger}_{n,v,\mathbf{k}}a^{-\sigma}_{n,v_{1x},\mathbf{k}} + ia^{\sigma\dagger}_{n,v,\mathbf{k}}a^{-\sigma}_{n,v_{1y},\mathbf{k}}\right). \qquad \text{(B2)}\end{aligned}$$

The bands which form the basis of the model are the monolayer Γ-point bands in the absence of spin-orbit coupling (SOC) [23]. The operator $a^{\sigma(\dagger)}_{n,j,\mathbf{k}}$ annihilates (creates) an electron in layer n, band j, with spin $\sigma = \pm\frac{1}{2}$ and in-plane momentum $\mathbf{k}$. As singly degenerate bands which are totally in-plane symmetric at Γ, bands c_1, c, v are assigned Γ-point energies $\varepsilon_{c_1,c,v}$ with quadratic "onsite" dispersions with respective coefficients $\alpha_{c_1,c,v}$. In contrast, in the absence of SOC bands v_1 and v_2, being dominated by p_x and p_y orbitals, are twice degenerate at Γ with energies ε_{v_1,v_2}. The dispersions of their two light- and heavy-hole branches are handled using two components corresponding to a basis of their p_x and p_y components, with quadratic intra- and intercomponent contributions with coefficients $\alpha^{(\prime)}_{v_{1,2}}$. In the multiband $\mathbf{k}\cdot\mathbf{p}$ picture away from Γ the bands are modified by off-diagonal terms between them. These terms must preserve the σ_h symmetry of the monolayer, so only involve the pairs c_1, v, c, v_1 and v, v_2. Of these, c_1, v is between bands which are totally in-plane symmetric at Γ, so the off-diagonal term is quadratic, while terms involving the x and y components of $v_{1,2}$ are linear in k_x and k_y, respectively. The coefficients of these terms are denoted as $\beta_{c_1,v}$, β_{c,v_1}, and β_{v,v_2}, respectively. Finally, spin-orbit coupling (SOC) is included within the components of v_1 and v_2 (l_zs_z with coupling strength $\lambda_{v_{1,2}}$) and between v_1 and v (the "spin-flip" $l_xs_x + l_ys_y$ with coupling strength λ_{v,v_1}). Cross-gap "spin-flip" terms are neglected.

b. Interlayer tight-binding hops

The nonzero interlayer tight-binding hops between the monolayer bands, and their form, can be inferred from the symmetries of the bands involved in the hop. The resulting interlayer contribution to the Hamiltonian takes the form,

$$\begin{aligned}H^{n,n+1}_{IL,\mathbf{k},\sigma} =& \sum_{j=c_1,c,v} t_j a^{\sigma\dagger}_{n,j,\mathbf{k}}a^{\sigma}_{n+1,j,\mathbf{k}}\\
&+ t_{c_1,c}\left(a^{\sigma\dagger}_{n,c_1,\mathbf{k}}a^{\sigma}_{n+1,c,\mathbf{k}} - a^{\sigma\dagger}_{n,c,\mathbf{k}}a^{\sigma}_{n+1,c_1,\mathbf{k}}\right)\\
&+ t_{c,v}\left(a^{\sigma\dagger}_{n,c,\mathbf{k}}a^{\sigma}_{n+1,v,\mathbf{k}} - a^{\sigma\dagger}_{n,v,\mathbf{k}}a^{\sigma}_{n+1,c,\mathbf{k}}\right)\\
&+ t_{v_{1,2}}\sum_{i=x,y}\left(a^{\sigma\dagger}_{n,v_{1i},\mathbf{k}}a^{\sigma}_{n+1,v_{1i},\mathbf{k}} - a^{\sigma\dagger}_{n,v_{1i},\mathbf{k}}a^{\sigma}_{n+1,v_{2i},\mathbf{k}}\right.\\
&\left.- a^{\sigma\dagger}_{n,v_{2i},\mathbf{k}}a^{\sigma}_{n+1,v_{2i},\mathbf{k}} + a^{\sigma\dagger}_{n,v_{2i},\mathbf{k}}a^{\sigma}_{n+1,v_{1i},\mathbf{k}}\right). \qquad \text{(B3)}\end{aligned}$$

Since the γ stacking preserves the C_3 rotational symmetry of the monolayer, the bands may be divided into two groups, with no hopping between the singly and doubly degenerate basis bands, with the x and y components also not mixed by the interlayer hops. We have made the approximation that, since interlayer hops are dominated by interlayer Se-Se pairs [23], they may be taken as $z/-z$ symmetric. As a result, hops between c_1 and c, and between c and v, which are pairs of bands with opposing symmetry under $z/-z$ reflection in the monolayer, are antisymmetric under exchange of layers. We neglect the hop $t_{c_1,v}$ as the bands are well separated in energy, and interlayer hops involving c_1 are expected to be weak owing to the dominance of the c_1 wave function by orbitals on the indium atoms in the center of each layer. Finally, using the domination of v_1 and v_2 by Se p_x and p_y orbitals, we assume that all hops within and between v_1 and v_2 are of the same magnitude, $t_{v_{1,2}}$.

2. Parametrization—bulk γ-InSe

Since DFT can often underestimate band gaps, significantly so in the case of thicker 2D and bulk InSe, a means by which one may obtain spectra of more use in comparison with experiments is the use of a "scissor operator"—a rigid shift upwards in energy of the unoccupied bands with respect to the occupied bands. In other words, one assumes that features of the DFT bands, such as effective masses, band widths, matrix elements, and so on, are all correct, other than the size of the gap itself. This has been shown to be a useful procedure in theoretical studies of semiconductors [64–66], and in 2D InSe [7,23]. However, the magnitude of the underestimation of the gap (approaching a factor of ∼4 in the bulk limit) for InSe can make the procedure more complex. For example, a straight scissor correction without taking into account other effects of the underestimation of the gap can lead to an overestimation of the interband out-of-plane electric dipole matrix element [23], or an underestimation of the band-edge effective masses in the bulk case and hence an overestimation of the splitting of sub-bands in the few-layer case [28]. While there are means by which some of these problems may be overcome (for example, the out-of-plane effective mass was corrected in Ref. [28] by applying a scissor correction to the monolayer bands *after* parametrization of the interlayer hops), the presence of cross-gap off-diagonal matrix elements in even the monolayer Hamiltonian presents challenges in the determination of the appropriate means of compensating for an underestimation of the band gap in a DFT reference.

In this case, therefore, we take as our first-principles reference a quasiparticle self-consistent GW (QSGW) calculation for the bulk crystal. For this we use the QUESTAAL package

[67,68], using the Bethe-Salpeter equation (BSE) to determine the polarization in the calculation of W. Since the bands and gaps of InSe have been shown to be sensitive to strain [69,70], we use an experimental lattice with crystal structure parameters found using x-ray diffraction [71]. The DFT part of the calculation sampled the Brillouin zone with a $24 \times 24 \times 24$ **k**-point grid, while for the QSGW part a $6 \times 6 \times 6$ grid was used. In the calculation of W, nine occupied bands and fifteen unoccupied bands were handled using the BSE, while the rest of the bands were handled at the random-phase approximation level. In the DFT part, the G-vector cutoff for the interstitial density mesh was 9.1 $\mathrm{Ry}^{1/2}$, while in the QSGW part the cutoffs for the plane-wave expansions of the eigenfunctions and the Coulomb integrals were 3.4 a.u. and 2.9 a.u., respectively. The QSGW calculation of the self-energy is carried out without taking SOC into account, with the effects of SOC included at the DFT level afterwards. We choose a calculation of the bulk crystal as a reference for finding model parameters as a QSGW calculation for few-layer InSe would be prohibitively expensive given the number of atoms in a unit cell. The calculation gives a quasiparticle band gap of 1.367 eV for the bulk, close to the experimentally obtained 1.351 eV [72].

In the case of the model, Eq. (B1) is amended to describe the bulk with a unit cell corresponding to a single layer as

$$H = H_{1L}^{1} + H_{lL}^{1,1} e^{ik_z a_z} + \mathrm{H.c.}, \tag{B4}$$

where k_z is the out-of-plane momentum and $a_z = 8.315$ Å is the distance between successive layers [71]. The parametrization is carried out in two steps. First, we fit bands for 50 k_z points between $k_z = 0$ and $k_z = \pi/a_z$ for $\mathbf{k} = 0$, as we show in Fig. 4, then holding the 2D Γ-point parameters fixed, we fit the in-plane dispersions for small **k** near Γ up to $k = \mathrm{K}/5$ for each k_z used in the first stage of the fitting. In Fig. 4 we show the in-plane QSGW and model dispersions for $k_z a_z = 0, \pi/2, \pi$. The model parameters are given in Table II.

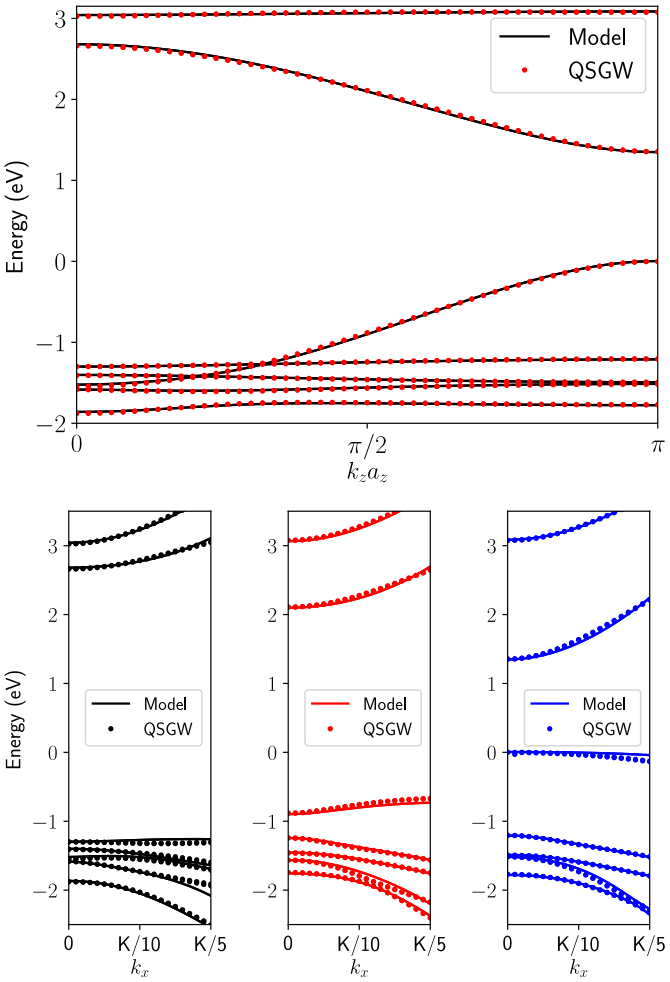

FIG. 4. Upper panel: QSGW (dots) and fitted model (lines) out-of-plane dispersions for bulk γ-InSe, for in plane momentum $\mathbf{k} = 0$. Lower panels: in-plane dispersions (along k_x) for (from left to right) $k_z a_z = 0, \pi/2, \pi$. 0 eV set to valence band edge in all cases.

3. Few-layer bands

Having found a parameter set for the model, we now explore its behavior in the few-layer case, with an overview of some of the key features of the bands of few-layer InSe shown in Fig. 5. The dispersive nature of the bulk conduction and valence bands, arising from the strong interlayer hops t_c, t_v, t_{cv} between bands with strong wave-function contributions from selenium p_z orbitals, translate to large splittings between sub-bands in the few-layer case. It is this strong interlayer hybridization which is responsible for the large variation of band gap with crystal thickness [7,23], reaching >2.8 eV for monolayer films. In contrast, v_1 and v_2, being dominated by $p_{x,y}$ orbitals which lie mostly in the 2D crystal plane, have weak interband hops and exhibit much weaker splitting. As a consequence when the conduction and valence bands acquire contributions from v_1 and v_2 (due to, in the model, interband $\mathbf{k} \cdot \mathbf{p}$ mixing) away from Γ their splitting becomes weaker. In the conduction band this manifests itself as a difference between the effective masses of successive sub-bands, which in Ref. [28] was handled by a k-dependent t_c.

For the valence band the situation is more complex. As has been theoretically predicted [17,19] and shown in ARPES experiments [10], for the thinnest films an offset in the valence band maximum develops, leading to a slightly indirect band gap, in contrast to the direct gap found in thicker films and in the bulk crystal. In the multiband $\mathbf{k} \cdot \mathbf{p}$ picture a key contribution to this phenomenon can be understood [62] as repulsion away from Γ between bands v and v_2. When in the few-layer case v splits much more than v_2 this repulsion becomes much weaker. Coupled with a weaker splitting of v itself at larger k in a similar manner to that of the conduction band, this causes the depth and radius of the "Mexican hat" offset to decrease rapidly with increasing crystal thickness, ultimately leading to a direct gap in the model for $N \geqslant 10$ layers.

APPENDIX C: NUMERICAL IMPLEMENTATION OF HARMONIC OSCILLATOR BASIS

In the harmonic oscillator basis described in the text, the BSE (1) takes the form,

$$\sum_{n_x' n_y'} \left[\mathcal{H}^0_{n_x n_y; n_x' n_y'} - \mathcal{V}_{n_x n_y; n_x' n_y'} \right] \mathcal{A}^{\mathbf{Q}}_{n_x' n_y'} = \Omega \mathcal{A}^{\mathbf{Q}}_{n_x n_y}, \tag{C1}$$

TABLE II. Model parameters for Eqs. (B2) and (B3) fitted to QSGW bands for bulk InSe. 0 eV is set to the valence band edge in the bulk.

ε_{c_1}	3.064 eV
ε_c	2.015 eV
ε_v	−0.855 eV
ε_{v_1}	−1.449 eV
ε_{v_2}	−1.538 eV
$\lambda_{v_{1,2}}$	0.142 eV
λ_{v,v_1}	0.119 eV
t_{c_1}	−0.011 eV
t_c	0.333 eV
t_v	−0.420 eV
$t_{v_{1,2}}$	−0.048 eV
$t_{c_1,c}$	0.019 eV
$t_{c,v}$	0.251 eV
α_{c_1}	1.54 eVÅ^2
α_c	−18.7 eV Å^2
α_v	−4.95 eVÅ^2
α_{v_1}	6.48 eVÅ^2
α'_{v_1}	−10.51 eVÅ^2
α_{v_2}	−0.28 eVÅ^2
α'_{v_2}	−4.20 eVÅ^2
$\beta_{c_1,v}$	3.77 eVÅ^2
β_{c_1,v_2}	8.51 eVÅ
β_{c,v_1}	10.54 eVÅ
β_{v,v_2}	−2.78 eVÅ

with the kinetic energy matrix,

$$\mathcal{H}^0_{n_x n_y; n'_x n'_y}(\mathbf{Q}) = \int d^2k [\varepsilon_c(\mathbf{k}) - \varepsilon_v(\mathbf{k}-\mathbf{Q})] \times \varphi^*_{n_x}(k_x)\varphi^*_{n_y}(k_y)\varphi_{n'_x}(k_x)\varphi_{n'_y}(k_y), \quad \text{(C2)}$$

and the interaction matrix,

$$\mathcal{V}_{n_x n_y; n'_x n'_y} = \int \frac{d^2k d^2q}{(2\pi)^2} V(\mathbf{q}) \times \varphi^*_{n_x}(k_x)\varphi^*_{n_y}(k_y)\varphi_{n'_x}(k_x+q_x)\varphi_{n'_y}(k_y+q_y). \quad \text{(C3)}$$

In the following, we explain how to choose an optimal harmonic oscillator basis set to speed up the convergence in a calculation. We also give the details for how to construct the matrix equation in Eq. (C1).

Choice of basis set. To diagonalize the BSE in Eq. (C1), we first need to specify the harmonic oscillator basis set which is determined by the parameters: λ, the length scale of the oscillator, and $N_{\max}$, the cutoff of the oscillator modes with $n_x + n_y \leqslant N_{\max}$. In principle, λ can be arbitrary since a unique result can be obtained provided that $N_{\max}$ is large enough. In practice, working with a large basis set is undesirable because large matrix diagonalization is a very demanding computational task. In the following, we show that a good convergent result can be obtained with a relatively small basis set if a proper choice of λ is used.

The procedure for obtaining the optimal λ is to maximize the exciton binding energy against λ (inset of Fig. 6). This λ corresponds to the optimal coverage of the exciton by the basis set in the momentum/real space. In Fig. 6, we demonstrate

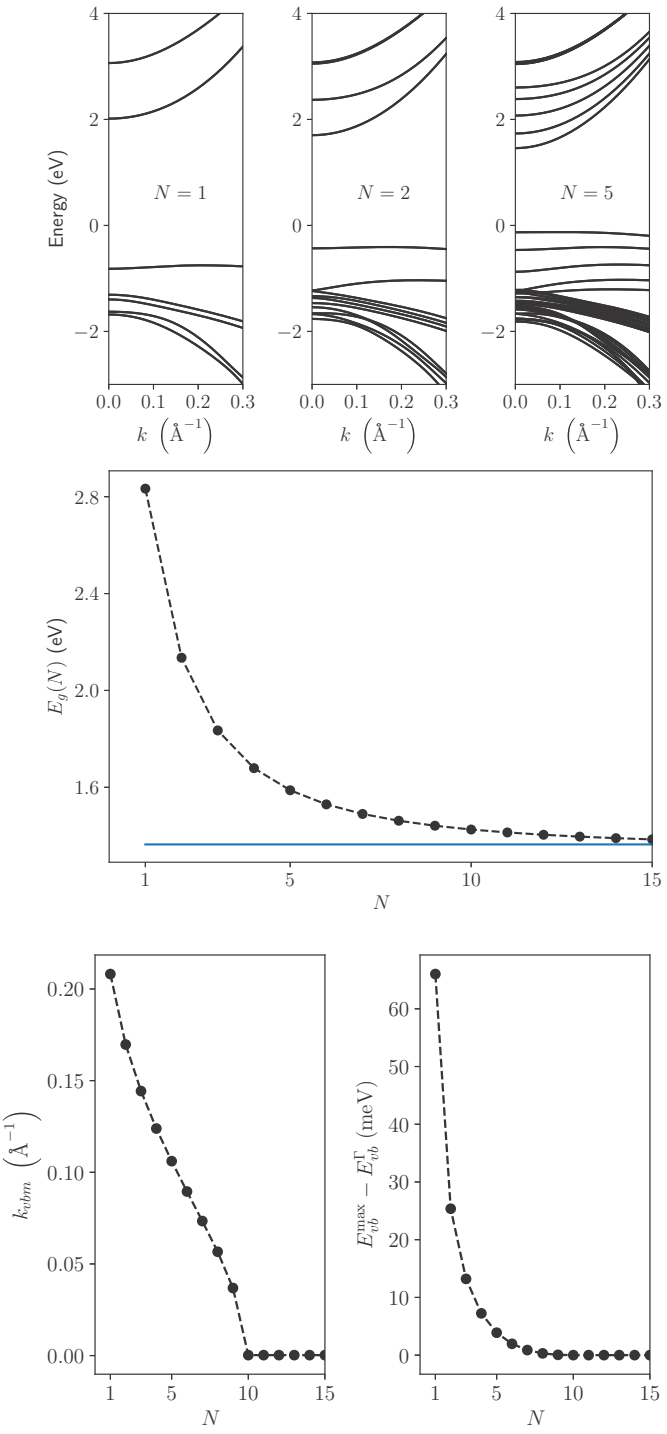

FIG. 5. (Upper panels) 2D model dispersions for monolayer, bilayer, and five-layer InSe. (Middle panel) Vertical band gaps at Γ for N = 1- to 15-layer InSe. Solid line is the bulk band gap. (Lower panels) Position (left) and magnitude (right) of offset of valence band maximum from Γ point for N = 1- to 15-layer InSe, showing indirect-direct gap transition at 10 layers.

how the binding energy depends on λ of a finite basis set with $n_x + n_y \leqslant N_{\max} = 12$. We note that the optimal λ for each different states need to be determined separately since each states have a very different characteristic localized length scale. In Fig. 6, one can see that once the optimal λ is determined, we obtain a good convergent result for the binding energy at

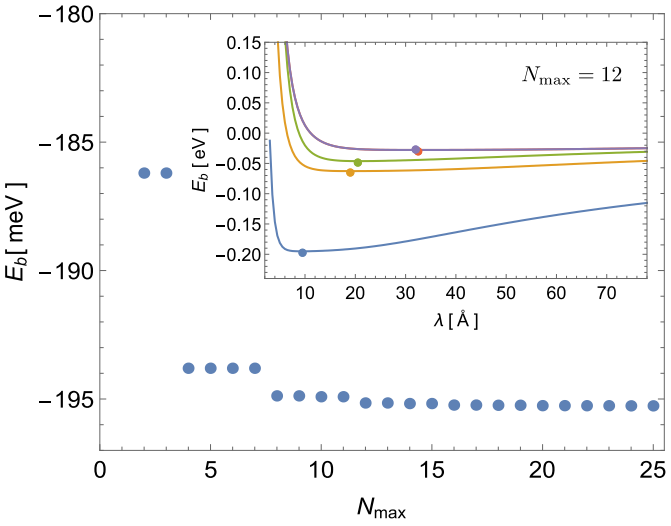

FIG. 6. The convergence in the calculation of exciton ground-state binding energy by using the optimal λ for a monolayer InSe with Keldysh potential. The optimal λ for each state is determined by maximizing their corresponding binding energy which are marked by the closed circles in the inset. The optimization for the first four Γ-point exciton binding energy in the inset is performed with fixed $N_{\max} = 12$.

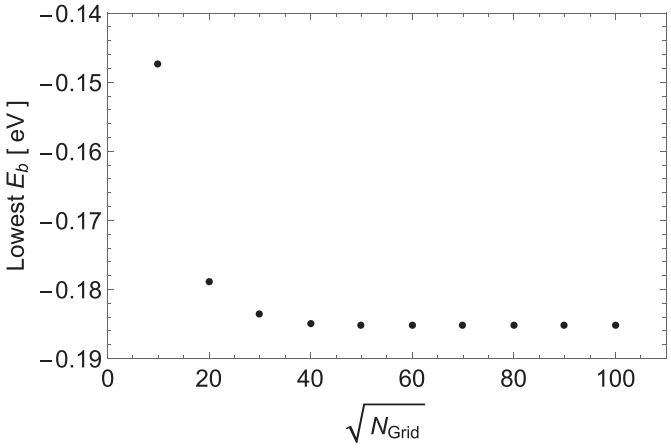

FIG. 7. The convergence of the $\mathbf{Q} = 0$ exciton ground-state energy with different grid size for constructing the Fourier series of ε_c and ε_v.

$N_{\max} \sim 12$. Increasing the number of basis beyond $N_{\max} = 12$ only leads to no more than 2 meV correction.

Kinetic energy matrix. For a general band dispersion such as those in tight-binding model, analytical expression may not be available and the query of the band energy may be computationally expansive. Therefore, a straightforward numerical integration in Eq. (C2) is not a practical approach. A feasible numerical method is to expand the band dispersion (periodic function) into a fast convergent Fourier series. Namely,

$$\varepsilon_c(\mathbf{k}) - \varepsilon_v(\mathbf{k} - \mathbf{Q}) = \sum_{\mathbf{s}=-\infty}^{\infty} [C_{\mathbf{s}} - V_{\mathbf{s}} e^{i2\pi \mathbf{s}\cdot\bar{\mathbf{Q}}}] e^{-i2\pi \mathbf{s}\cdot\bar{\mathbf{k}}}, \quad \text{(C4)}$$

where $\mathbf{s} = (s_x, s_y)$, $\bar{\mathbf{k}} = (k_x/T_x, k_y/T_y)$, and $\bar{\mathbf{Q}} = (Q_x/T_x, Q_y/T_y)$ with the (T_x, T_y) are the periodicity of the dispersion in each dimensions. The Fourier coefficients are therefore defined as

$$\begin{bmatrix} C_{\mathbf{s}} \\ V_{\mathbf{s}} \end{bmatrix} = \int_{-\frac{T_x}{2}}^{\frac{T_x}{2}} \frac{dk_x}{T_x} \int_{-\frac{T_y}{2}}^{\frac{T_y}{2}} \frac{dk_y}{T_y} e^{i2\pi \mathbf{s}\cdot\bar{\mathbf{k}}} \begin{bmatrix} \varepsilon_c(\mathbf{k}) \\ \varepsilon_v(\mathbf{k}) \end{bmatrix}. \quad \text{(C5)}$$

With this expansion, we can integrate out the momentum explicitly. Hence, the band energy matrix in Eq. (C2) become

$$\mathcal{H}^0_{n_x n_y; n'_x n'_y}(\mathbf{Q}) = \sum_{s_x, s_y=-\infty}^{\infty} [C_{\mathbf{s}} - V_{\mathbf{s}} e^{i2\pi \mathbf{s}\cdot\bar{\mathbf{Q}}}] \prod_j^{x,y} \frac{2^{\zeta_j - \frac{1}{2}(n_j + n'_j)} \zeta_j! (\bar{a}_j s_j)^{\Delta_j}}{i^{n'_j - n_j + \Delta_j} \sqrt{n_j! n'_j!}} \times e^{-\frac{1}{4}\bar{a}_j^2 s_j^2} L_{\zeta_j}^{\Delta_j}\left(\frac{1}{2}\bar{a}_j^2 s_j^2\right), \quad \text{(C6)}$$

with $\zeta_j = \min[n_j, n'_j]$, $\Delta_j = |n'_j - n_j|$, $\bar{a}_j = 2\pi/(T_j \lambda)$, and $L_n^{\alpha}(x)$ is the associated Laguerre polynomial. Since the band dispersion is periodic, only a few of the Fourier modes are relevant to the series. Moreover, we note that the higher order term in the sum are exponentially suppressed. This implies that we have transformed the numerical integration problem into a fast convergent summation.

To calculate the Fourier coefficients, we can approximate the integral in Eq. (C5) as a Riemann sum by discretizing the momentum space into a uniform grid. The calculation of Riemann sum is the same as calculating the discrete Fourier transformation which can be very efficiently evaluated by the fast-Fourier transformation. In this numerical approach, the tight-binding Hamiltonian only needs to be diagonalized once in constructing the uniform grid. Depending on the smoothness of the band structure, typically, the grid size greater than 50×50 points is good enough for a desirable convergent result (see Fig. 7). In this paper, we use 100×100 grid points for the calculation.

Although we have used a straightforward method with fast-Fourier transformation. The idea of our method is essentially the same as K-point sampling in Refs. [73–75]. The K-point sampling method is much more efficient since it utilizes all the symmetry in the function and regrouping the Fourier series into a faster convergent series. The Fourier coefficient in the series can be very efficiently calculated by the Monkhorst-Pack grid in the reduced Brillouin zone. This method was originally discussed in Ref. [75] as a "hybrid method."

We can further simplify the calculation in Eq. (C2) if only the low-energy exciton is in our interest. As indicated in Fig. 2, only the low-energy electronic modes (red/blue shaded region) which are well described by the $\mathbf{k}\cdot\mathbf{p}$ model are relevant for exciton binding. In this low-energy regime, one may approximate $\varepsilon_{c/v}$ by expanding it into polynomial. Thus, in this approach, we can use the following identity to calculate Eq. (C2) analytically,

$$\int dk k^l \frac{e^{-k^2} H_m(k) H_n(k)}{\sqrt{\pi m! n! 2^{m+n}}} = \sqrt{\frac{n!}{m!}} \sum_{r=0}^{\lfloor l/2 \rfloor} \sum_{s=0}^{\min[m, l-2r]} \binom{m}{s} \frac{2^{s-l-\frac{1}{2}(m-n)} l!}{r!(l-2r-s)!} \delta_{l+m-2r-2s,n}, \quad \text{(C7)}$$

TABLE III. Comparison of binding energies in meV as obtained from the harmonic oscillator basis against analytical and calculated results [49] for suspended MoS_2. Basis size used in the comparison with MoS_2 monolayer corresponded to $N_{\max} = 12$ (basis size=91 states) and λ was optimized. For the 2D hydrogen atom with a reduced effective mass of $\mu = 0.14$ and $\epsilon = 9$ the basis size used for the comparison was $N_{\max} = 20$ for every states in the table except the $1s$. As for the $1s$ state a greater basis size of $N_{\max} = 24$ as used.

	HO basis	2D hydrogen	HO basis	Suspended MoS_2 [49]
$0s$	92.5	94.2	554	555
$1p_{x,y}$	10.38	10.47	315	316
$1s$	9.6	10.47	257	258
$2d_{xy}$	3.76	3.77	209	209
$2p_{x,y}$	3.69	3.77	184	185

where $\lfloor l/2 \rfloor$ is the largest integer that is equal or smaller than $l/2$.

Interaction matrix. In this paper, we assume in-plane rotational symmetry in the e-h interaction. Hence, the k integration in Eq. (C3) can be carried out explicitly by using $H_n(x+y) = \sum_{s=0}^{n} \binom{n}{s} H_s(x)(2y)^{n-s}$ and this yields

$$\mathcal{V}_{n_x n_y; n_x' n_y'} = \int \frac{qdq}{(2\pi)^2} V(q) e^{-\frac{1}{4}q^2\lambda^2} \prod_{j}^{x,y} \sum_{s_j=0}^{\min[m_j,n_j]} (\lambda q)^{\sigma_j},$$
$$\times \binom{n_j}{s_j}\binom{m_j}{s_j} \frac{\left(-\frac{1}{2}\right)^{\frac{1}{2}\sigma_j} s_j!}{\sqrt{m_j! n_j!}} 2\mathrm{B}\left(\frac{\sigma_x+1}{2}, \frac{\sigma_y+1}{2}\right), \tag{C8}$$

where $\sigma_j = n_j + m_j - 2s_j$ and $\mathrm{B}(x,y)$ is the beta function. For the Keldysh potential, $V(q) = -\frac{2\pi e^2}{\sqrt{\kappa_\parallel \kappa_z} q(1+r_* q)}$, we have the following analytical expression for

$$\int \frac{qdq}{(2\pi)^2} V(q) (\lambda q)^{\sigma_x+\sigma_y} e^{-\frac{1}{4}q^2\lambda^2}$$
$$= \frac{-e^2}{2\pi\sqrt{\kappa_\parallel \kappa_z}} \left(-\frac{\lambda}{r_*}\right)^{\sigma_x+\sigma_y} \left\{ \frac{e^{-\frac{\lambda^2}{4r_*^2}}}{2r_*/\lambda} \left[\pi \,\mathrm{erf}\left(\frac{\lambda}{2r_*}\right) - \mathrm{Ei}\left(\frac{\lambda^2}{4r_*^2}\right)\right] \right.$$
$$\left. - \sum_{j=0}^{\sigma_x+\sigma_y-1} \Gamma\left(\frac{j+1}{2}\right) \left(-\frac{2r_*}{\lambda}\right)^j \right\},$$

where $\Gamma(x)$ is the gamma function, $\mathrm{Ei}(x)$ is the exponential integral, and $\mathrm{erf}(x)$ is the error function.

Comparison with hydrogenlike exciton levels for $V \propto -1/r$ and Keldysh interaction. As shown in Table III, in comparing the binding energy as obtained from the harmonic oscillator basis with the analytically obtained 2D hydrogen atom energy levels, the discrepancy between the two was found smaller than 2% as for the ground-state energy and even lower for the states with $l \neq 0$. The higher excited states with $l = 0$ required a very large basis size in order to accurately calculate the binding energy due to the very sharp singularity of the wave function appearing at $r = 0$ (Kato cusp). This situation is similar to the well-known problem in the Slater-type versus Gaussian-type orbitals in quantum chemistry [76], since the harmonic oscillator is essentially a Gaussian basis. Such a sharp feature in the excitonic wave function is mitigated in the Keldysh potential as the $1/r$ divergence becomes logarithmic. In this case, the harmonic oscillator basis yields better accuracy for each binding state in the spectrum. In comparing our binding energy calculation with the calculated bindings for MoS_2, the error was significantly reduced for the same basis size with <0.3% as for the ground state and lower for the $l \neq 0$ states.

Connection to the real-space formalism. It is also instructive to describe the excitonic problem in terms of real space. To do this, we can Fourier transform the Bethe-Salpeter equation in (1) by using

$$\psi(\mathbf{r}_e, \mathbf{r}_h) = \sum_{\mathbf{k}_e, \mathbf{k}_h} \psi_{\mathbf{Q}}(\mathbf{k}) e^{i(\mathbf{k}_e \cdot \mathbf{r}_e - \mathbf{k}_h \cdot \mathbf{r}_h)}. \tag{C9}$$

We remind that $\mathbf{k}_e = \mathbf{k}$ and $\mathbf{k}_h = \mathbf{k} - \mathbf{Q}$. This transformation turns all momentum in the dispersion in Eq. (1) into derivative operators and yields

$$[\varepsilon_c(-i\nabla_{\mathbf{r}_e}) - \varepsilon_v(i\nabla_{\mathbf{r}_h}) - \Omega + V(\mathbf{r}_e - \mathbf{r}_h)]\psi(\mathbf{r}_e, \mathbf{r}_h) = 0, \tag{C10}$$

where $V(\mathbf{r}) = \int_{\mathbf{q}} e^{i\mathbf{r}\cdot\mathbf{q}} V(\mathbf{q})$ is the Fourier transformation of the potential. The above equation yields the Mott-Wannier model if only the quadratic mass term in $\varepsilon_{c/v}$ is kept. However, in our model, we need to retain higher-order terms in the hole dispersion.

Similar to the Mott-Wannier model, Eq. (C10) can be reduced to a one-body problem by using the canonical transformation. Since the hole effective mass is not well defined due to the sombrero-shaped dispersion, instead of using the center-of-mass frame coordinate system, we choose

$$\begin{bmatrix} \boldsymbol{X} \\ \boldsymbol{x} \end{bmatrix} = \frac{1}{\sqrt{2}} \begin{bmatrix} \mathbf{r}_e + \mathbf{r}_h \\ \mathbf{r}_e - \mathbf{r}_h \end{bmatrix}, \quad \begin{bmatrix} \hat{\mathbf{P}} \\ \hat{\mathbf{p}} \end{bmatrix} = -\frac{i}{\sqrt{2}} \begin{bmatrix} \nabla_{\mathbf{r}_e} + \nabla_{\mathbf{r}_h} \\ \nabla_{\mathbf{r}_e} - \nabla_{\mathbf{r}_h} \end{bmatrix}.$$

The crucial requirement for this transformation is that the new coordinate system satisfies $[x_j, \hat{p}_j] = [X_j, \hat{P}_j] = i$ such that the physical phase space volume is preserved. Using the $(\boldsymbol{X}, \boldsymbol{x})$ coordinate, Eq. (C10) in the real space reads

$$\left[\varepsilon_c\left(\frac{\hat{\mathbf{p}} + \hat{\mathbf{P}}}{\sqrt{2}}\right) - \varepsilon_v\left(\frac{\hat{\mathbf{p}} - \hat{\mathbf{P}}}{\sqrt{2}}\right) - \Omega - V(\sqrt{2}\boldsymbol{x})\right]\psi(\boldsymbol{X}, \boldsymbol{x}) = 0. \tag{C11}$$

We note that, in this coordinate system, the correspondence between momentum and real space representation of the exciton momentum is $\mathbf{Q} = \mathbf{k}_e - \mathbf{k}_h \leftrightarrow -i\nabla_{\mathbf{r}_e} - i\nabla_{\mathbf{r}_h} = \sqrt{2}\hat{\mathbf{P}}$.

First, it is noted that $[\hat{\mathbf{P}}, H] = 0$ where H (independent of $\boldsymbol{X}$) is the electron-hole two-particle Hamiltonian in (C10) indicating that $\mathbf{P}$ is a well-defined quantum number which gives the exciton momentum $\mathbf{Q} = \sqrt{2}\mathbf{P}$. Therefore, the wave function is uniquely dependent on $\boldsymbol{x}$:

$$\psi(\boldsymbol{X}, \boldsymbol{x}) = e^{i\mathbf{P}\cdot\boldsymbol{X}} \chi(\boldsymbol{x}), \tag{C12}$$

which is the eigenfunction of H. Substituting the above ansatz wave function into Eq. (C10), we reduce the equation into a one-body Shrödinger equation as

$$\left[\varepsilon_c\left(\frac{\sqrt{2}\hat{\mathbf{p}}+\mathbf{Q}}{2}\right) - \varepsilon_v\left(\frac{\sqrt{2}\hat{\mathbf{p}}-\mathbf{Q}}{2}\right) - \Omega + V(\sqrt{2}\boldsymbol{x})\right]\chi(\boldsymbol{x}) = 0. \quad \text{(C13)}$$

Expanding $\chi(\boldsymbol{x})$ into the harmonic oscillator basis as $\chi(\boldsymbol{x}) = \sum_{\mathbf{n}} \mathcal{C}^{\mathbf{Q}}_{n_x n_y}\varphi_{n_x}(\rho_x)\varphi_{n_y}(\rho_y)$ where $\boldsymbol{\rho} = \mathbf{r}_e - \mathbf{r}_h = \sqrt{2}\boldsymbol{x}$ is the relative coordinate of electron and hole. The real-space basis function, $\varphi_n(\rho)$, is the Fourier transformation of $\varphi_n(k)$ which is also a harmonic oscillator. Therefore, the matrix representation for Eq. (C13) is

$$\sum_{n'_x n'_y}\left[\mathcal{H}^0_{n_x n_y; n'_x n'_y} + \mathcal{V}_{n_x n_y; n'_x n'_y}\right]\mathcal{C}^{\mathbf{Q}}_{n'_x n'_y} = \Omega \mathcal{C}^{\mathbf{Q}}_{n_x n_y}, \quad \text{(C14)}$$

with the kinetic Hamiltonian,

$$\mathcal{H}^0_{n_x n_y; n'_x n'_y}(\mathbf{Q}) = \int d^2\rho \varphi_{n_x}(\rho_x)\varphi_{n_y}(\rho_y)\left[\varepsilon_c\left(\frac{\sqrt{2}\hat{\mathbf{p}}+\mathbf{Q}}{2}\right) - \varepsilon_v\left(\frac{\sqrt{2}\hat{\mathbf{p}}-\mathbf{Q}}{2}\right)\right]\varphi_{n'_x}(\rho_x)\varphi_{n'_y}(\rho_y), \quad \text{(C15)}$$

and the Coulomb interaction matrix,

$$\mathcal{V}_{n_x n_y; n'_x n'_y} = \int d^2\rho V(\boldsymbol{\rho})\varphi_{n_x}(\rho_x)\varphi_{n_y}(\rho_y)\varphi_{n'_x}(\rho_x)\varphi_{n'_y}(\rho_y).$$

The integration in Eq. (C15) can be carried out exactly by using the chain rule to rewrite $\hat{\mathbf{p}} = -i\nabla_{\boldsymbol{x}} = \sqrt{2}(-i\nabla_{\boldsymbol{\rho}})$ and then using the recursive relation of the Hermite functions. Alternatively, one may also calculate it by turning $-i\nabla_{\boldsymbol{\rho}}$ into the simple harmonic ladder operators and carrying out the commutation algebra. Nevertheless, the calculated result from both methods is identical to the momentum space calculation in Eq. (C7).

[1] G. R. Bhimanapati, Z. Lin, V. Meunier, Y. Jung, J. Cha, S. Das, D. Xiao, Y. Son, M. S. Strano, V. R. Cooper, L. Liang, S. G. Louie, E. Ringe, W. Zhou, S. S. Kim, R. R. Naik, B. G. Sumpter, H. Terrones, F. Xia, Y. Wang, J. Zhu, D. Akinwande, N. Alem, J. A. Schuller, R. E. Schaak, M. Terrones, and J. A. Robinson, ACS Nano **9**, 11509 (2015).

[2] X. Qian, Y. Wang, W. Li, J. Lu, and J. Li, 2D Mater. **2**, 032003 (2015).

[3] K. S. Novoselov, A. Mishchenko, A. Carvalho, and A. H. C. Neto, Science **353**, aac9439 (2016).

[4] G. W. Mudd, S. A. Svatek, T. Ren, A. Patanè, O. Makarovsky, L. Eaves, P. H. Beton, Z. D. Kovalyuk, G. V. Lashkarev, Z. R. Kudrynskyi *et al.*, Adv. Mater. **25**, 5714 (2013).

[5] S. Lei, L. Ge, S. Najmaei, A. George, R. Kappera, J. Lou, M. Chhowalla, H. Yamaguchi, G. Gupta, R. Vajtai, A. D. Mohite, and P. M. Ajayan, ACS Nano **8**, 1263 (2014).

[6] M. Brotons-Gisbert, D. Andres-Penares, J. Suh, F. Hidalgo, R. Abargues, P. J. Rodríguez-Cantó, A. Segura, A. Cros, G. Tobias, E. Canadell, P. Ordejón, J. Wu, J. P. Martínez-Pastor, and J. F. Sánchez-Royo, Nano Lett. **16**, 3221 (2016).

[7] D. A. Bandurin, A. V. Tyurnina, G. L. Yu, A. Mishchenko, V. Zólyomi, S. V. Morozov, R. K. Kumar, R. V. Gorbachev, Z. R. Kudrynskyi, S. Pezzini, Z. D. Kovalyuk, U. Zeitler, K. S. Novoselov, A. Patanè, L. Eaves, I. V. Grigorieva, V. I. Fal'ko, A. K. Geim, and Y. Cao, Nat. Nanotechnol. **12**, 223 (2016).

[8] D. J. Terry, V. Zólyomi, M. Hamer, A. V. Tyurnina, D. G. Hopkinson, A. M. Rakowski, S. J. Magorrian, N. Clark, Y. M. Andreev, O. Kazakova, K. Novoselov, S. J. Haigh, V. I. Fal'ko, and R. Gorbachev, 2D Mater. **5**, 041009 (2018).

[9] J. F. Sánchez-Royo, G. Muñoz-Matutano, M. Brotons-Gisbert, J. P. Martínez-Pastor, A. Segura, A. Cantarero, R. Mata, J. Canet-Ferrer, G. Tobias, E. Canadell, J. Marqués-Hueso, and B. D. Gerardot, Nano Research **7**, 1556 (2014).

[10] M. J. Hamer, J. Zultak, A. V. Tyurnina, V. Zólyomi, D. Terry, A. Barinov, A. Garner, J. Donoghue, A. P. Rooney, V. Kandyba, A. Giampietri, A. Graham, N. Teutsch, X. Xia, M. Koperski, S. J. Haigh, V. I. Fal'ko, R. V. Gorbachev, and N. R. Wilson, ACS Nano **13**, 2136 (2019).

[11] J. Zultak, S. J. Magorrian, M. Koperski, A. Garner, M. J. Hamer, E. Tóvári, K. S. Novoselov, A. A. Zhukov, Y. Zou, N. R. Wilson, S. J. Haigh, A. V. Kretinin, V. I. Fal'ko, and R. Gorbachev, Nat. Commun. **11**, 125 (2020).

[12] X. Li, M.-W. Lin, A. A. Puretzky, J. C. Idrobo, C. Ma, M. Chi, M. Yoon, C. M. Rouleau, I. I. Kravchenko, D. B. Geohegan, and K. Xiao, Sci. Rep. **4**, 5497 (2014).

[13] Z. B. Aziza, D. Pierucci, H. Henck, M. G. Silly, C. David, M. Yoon, F. Sirotti, K. Xiao, M. Eddrief, J.-C. Girard, and A. Ouerghi, Phys. Rev. B **96**, 035407 (2017).

[14] Z. B. Aziza, V. Zólyomi, H. Henck, D. Pierucci, M. G. Silly, J. Avila, S. J. Magorrian, J. Chaste, C. Chen, M. Yoon, K. Xiao, F. Sirotti, M. C. Asensio, E. Lhuillier, M. Eddrief, V. I. Fal'ko, and A. Ouerghi, Phys. Rev. B **98**, 115405 (2018).

[15] A. Budweg, D. Yadav, A. Grupp, A. Leitenstorfer, M. Trushin, F. Pauly, and D. Brida, Phys. Rev. B **100**, 045404 (2019).

[16] D. V. Rybkovskiy, N. R. Arutyunyan, A. S. Orekhov, I. A. Gromchenko, I. V. Vorobiev, A. V. Osadchy, E. Y. Salaev, T. K. Baykara, K. R. Allakhverdiev, and E. D. Obraztsova, Phys. Rev. B **84**, 085314 (2011).

[17] D. V. Rybkovskiy, A. V. Osadchy, and E. D. Obraztsova, Phys. Rev. B **90**, 235302 (2014).

[18] V. Zólyomi, N. D. Drummond, and V. I. Fal'ko, Phys. Rev. B **87**, 195403 (2013).

[19] V. Zólyomi, N. D. Drummond, and V. I. Fal'ko, Phys. Rev. B **89**, 205416 (2014).

[20] M. Zhou, R. Zhang, J. Sun, W.-K. Lou, D. Zhang, W. Yang, and K. Chang, Phys. Rev. B **96**, 155430 (2017).

[21] M. Zhou, D. Zhang, S. Yu, Z. Huang, Y. Chen, W. Yang, and K. Chang, Phys. Rev. B **99**, 155402 (2019).

[22] Y. Sun, S. Luo, X.-G. Zhao, K. Biswas, S.-L. Li, and L. Zhang, Nanoscale **10**, 7991 (2018).

[23] S. J. Magorrian, V. Zólyomi, and V. I. Fal'ko, Phys. Rev. B **94**, 245431 (2016).

[24] T. Cao, Z. Li, and S. G. Louie, Phys. Rev. Lett. **114**, 236602 (2015).

[25] M. Trushin, Phys. Rev. B **99**, 205307 (2019).

[26] B. Skinner, Phys. Rev. B **93**, 235110 (2016).

[27] G. W. Mudd, M. R. Molas, X. Chen, V. Zólyomi, K. Nogajewski, Z. R. Kudrynskyi, Z. D. Kovalyuk, G. Yusa, O. Makarovsky, L. Eaves, M. Potemski, V. I. Fal'ko, and A. Patanè, Sci. Rep. **6**, 39619 (2016).

[28] S. J. Magorrian, A. Ceferino, V. Zólyomi, and V. I. Fal'ko, Phys. Rev. B **97**, 165304 (2018).

[29] G. Onida, L. Reining, and A. Rubio, Rev. Mod. Phys. **74**, 601 (2002).

[30] J. Jiang, R. Saito, G. G. Samsonidze, A. Jorio, S. G. Chou, G. Dresselhaus, and M. S. Dresselhaus, Phys. Rev. B **75**, 035407 (2007).

[31] M. L. Trolle, G. Seifert, and T. G. Pedersen, Phys. Rev. B **89**, 235410 (2014).

[32] F. Wu, F. Qu, and A. H. MacDonald, Phys. Rev. B **91**, 075310 (2015).

[33] T. Deilmann and K. S. Thygesen, 2D Mater. **6**, 035003 (2019).

[34] L. V. Keldysh, Sov. J. Expt. Theor. Phys. Lett. **29**, 658 (1979).

[35] N. S. Rytova, Moscow Univ. Phys. Bull. **3**, 18 (1967).

[36] S. Latini, T. Olsen, and K. S. Thygesen, Phys. Rev. B **92**, 245123 (2015).

[37] M. L. Trolle, T. G. Pedersen, and V. Véniard, Sci. Rep. **7**, 39844 (2017).

[38] R. Geick, C. H. Perry, and G. Rupprecht, Phys. Rev. **146**, 543 (1966).

[39] A. Laturia, M. L. Van de Put, and W. G. Vandenberghe, npj 2D Mater. Appl. **2**, 6 (2018).

[40] N. Kuroda and Y. Nishina, Solid State Commun. **34**, 481 (1980).

[41] P. Cudazzo, I. V. Tokatly, and A. Rubio, Phys. Rev. B **84**, 085406 (2011).

[42] $r_* \approx L \times 7.7$ Å.

[43] F. García Flórez, L. D. A. Siebbeles, and H. T. C. Stoof, arXiv:2002.5921.

[44] The bound electron-hole states in an exciton resemble the two-body system in a hydrogen atom. Therefore, these bound states may be well described by an atomic orbital basis set. For the sake of numerical simplicity, we use harmonic oscillator basis function which is an orthogonal Gaussian-type orbital basis.

[45] See Supplemental Material at http://link.aps.org/supplemental/10.1103/PhysRevB.101.245432 for the software package. The instruction is included in the file.

[46] In the expansion, one has to ensure that the truncated polynomials must not allow $\varepsilon_c(\mathbf{k}_e) - \varepsilon_v(\mathbf{k}_h)$ smaller than the bandgap for all $\mathbf{k}_{e/h}$.

[47] The degeneracies for the non-s-wave states are lifted by less than 1 meV in the tight-binding model which only has the sixfold rotational symmetry.

[48] Z. Ye, T. Cao, K. O'Brien, H. Zhu, X. Yin, Y. Wang, S. G. Louie, and X. Zhang, Nature **513**, 214 (2014).

[49] J.-Z. Zhang and J.-Z. Ma, J. Phys. Condens. Matter **31**, 105702 (2019).

[50] E. Kress-Rogers, R. Nicholas, J. Portal, and A. Chevy, Solid State Commun. **44**, 379 (1982).

[51] N. Kuroda, Y. Nishina, H. Hori, and M. Date, J. Phys. Soc. Jpn. **47**, 1373 (1979).

[52] A. Schindlmayr, Eur. J. Phys. **18**, 374 (1997).

[53] H. Fang, C. Battaglia, C. Carraro, S. Nemsak, B. Ozdol, J. S. Kang, H. A. Bechtel, S. B. Desai, F. Kronast, A. A. Unal, G. Conti, C. Conlon, G. K. Palsson, M. C. Martin, A. M. Minor, C. S. Fadley, E. Yablonovitch, R. Maboudian, and A. Javey, Proc. Natl. Acad. Sci. **111**, 6198 (2014).

[54] P. Rivera, J. R. Schaibley, A. M. Jones, J. S. Ross, S. Wu, G. Aivazian, P. Klement, K. Seyler, G. Clark, N. J. Ghimire, J. Yan, D. G. Mandrus, W. Yao, and X. Xu, Nat. Commun. **6**, 6242 (2015).

[55] P. Rivera, K. L. Seyler, H. Yu, J. R. Schaibley, J. Yan, D. G. Mandrus, W. Yao, and X. Xu, Science **351**, 688 (2016).

[56] Z. Wang, Y.-H. Chiu, K. Honz, K. F. Mak, and J. Shan, Nano Lett. **18**, 137 (2017).

[57] A. Ciarrocchi, D. Unuchek, A. Avsar, K. Watanabe, T. Taniguchi, and A. Kis, Nat. Photonics **13**, 131 (2018).

[58] E. V. Calman, M. M. Fogler, L. V. Butov, S. Hu, A. Mishchenko, and A. K. Geim, Nat. Commun. **9**, 1895 (2018).

[59] N. Ubrig, E. Ponomarev, J. Zultak, D. Domaretskiy, V. Zólyomi, D. Terry, J. Howarth, I. Gutiérrez-Lezama, A. Zhukov, Z. R. Kudrynskyi, Z. D. Kovalyuk, A. Patané, T. Taniguchi, K. Watanabe, R. V. Gorbachev, V. I. Fal'ko, and A. F. Morpurgo, Nat. Mater. **19**, 299 (2020).

[60] K. F. Mak and J. Shan, Nat. Nanotechnol. **13**, 974 (2018).

[61] M. M. Fogler, L. V. Butov, and K. S. Novoselov, Nat. Commun. **5**, 4555 (2014).

[62] P. Li and I. Appelbaum, Phys. Rev. B **92**, 195129 (2015).

[63] D. A. Ruiz-Tijerina, M. Danovich, C. Yelgel, V. Zólyomi, and V. I. Fal'ko, Phys. Rev. B **98**, 035411 (2018).

[64] V. Fiorentini and A. Baldereschi, Phys. Rev. B **51**, 17196 (1995).

[65] K. A. Johnson and N. W. Ashcroft, Phys. Rev. B **58**, 15548 (1998).

[66] N. Bernstein, M. J. Mehl, and D. A. Papaconstantopoulos, Phys. Rev. B **66**, 075212 (2002).

[67] T. Kotani, M. van Schilfgaarde, and S. V. Faleev, Phys. Rev. B **76**, 165106 (2007).

[68] D. Pashov, S. Acharya, W. R. Lambrecht, J. Jackson, K. D. Belashchenko, A. Chantis, F. Jamet, and M. van Schilfgaarde, Comput. Phys. Commun. **249**, 107065 (2020).

[69] Y. Li, T. Wang, M. Wu, T. Cao, Y. Chen, R. Sankar, R. K. Ulaganathan, F. Chou, C. Wetzel, C.-Y. Xu, S. G. Louie, and S.-F. Shi, 2D Materials **5**, 021002 (2018).

[70] C. Song, F. Fan, N. Xuan, S. Huang, G. Zhang, C. Wang, Z. Sun, H. Wu, and H. Yan, ACS Appl. Mater. Interfaces **10**, 3994 (2018).

[71] J. Rigoult, A. Rimsky, and A. Kuhn, Acta Crystallogr. B **36**, 916 (1980).

[72] J. Camassel, P. Merle, H. Mathieu, and A. Chevy, Phys. Rev. B **17**, 4718 (1978).

[73] D. J. Chadi and M. L. Cohen, Phys. Rev. B **8**, 5747 (1973).

[74] S. L. Cunningham, Phys. Rev. B **10**, 4988 (1974).

[75] H. J. Monkhorst and J. D. Pack, Phys. Rev. B **13**, 5188 (1976).

[76] A. L. Magalhães, J. Chem. Educ. **91**, 2124 (2014).

5.3 Supplementary material

As well as using the harmonic oscillator basis projection method presented in Section.5.2 to calculate the excitonic binding energies and exciton dispersions in hBN-encapsulated InSe thin films, in Table III of Appendix.C of the above publication we presented a comparison between our calculated binding energies in a suspended TMD with the binding energies obtained in Ref.[65] using finite-element methods. With our algorithm, we also calculated the exciton binding energy of an indirect exciton in a van der Waals heterostructure, namely, 1L-MoS_2/hBN/1L-MoS_2. Using DFT-calculated effective masses of monolayer MoS_2 provided by Celal Yelgel, we obtained the exciton binding energy as a function of the number of intermediate hBN layers projecting the solution of the Schrödinger equation in the harmonic oscillator basis. The Schrödinger equation for such bound state had the form

$$\left[\frac{\hbar^2 k^2}{2\mu} + \frac{\hbar^2 Q^2}{2M} + V(r_e - r_h)\right]\Phi = E\Phi, \tag{5.1}$$

where $\mu \equiv \frac{m_e m_h}{m_e + m_h}$ is the reduced effective mass of the electron-hole pair, $V(r_e - r_h)$

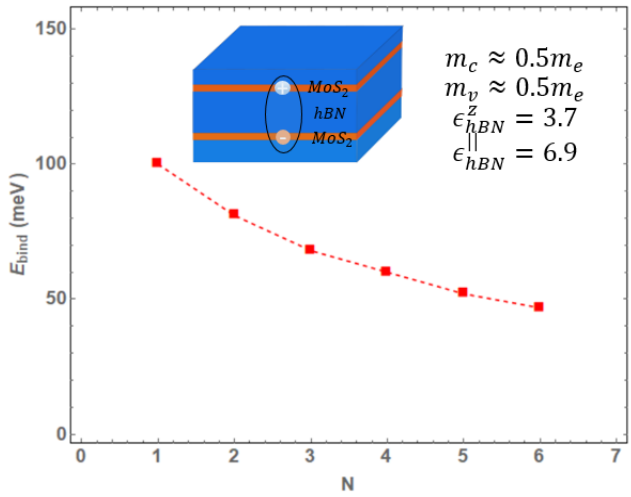

Figure 5.1: Calculation of the indirect exciton binding energy of a 1L-MoS_2/hBN/1L-MoS_2 heterostructure (see Ref.[66] for a comparison)using the electrostatic formalism developed in Ref.[11] for a generalised van der Waals heterostructure. The dielectric constants used for the MoS_2 layers were $\epsilon_{||} = 14$ and $\epsilon_z = 6.8$ (see Ref.[66]) and the thickness of each hBN and MoS_2 layer was assumed to be $d = 0.33$nm.

is the electrostatic electron-hole interaction and $M = m_e + m_h$ is the total mass of the exciton. In Appendix.C.3 of this thesis we show how the electrostatic potential $V(r_e - r_h)$ was obtained using a previously developed method presented in Ref.[11] and Ref.[12] for van der Waals heterostructures.

Chapter 6

Magnetic focusing in twisted bilayer graphene

6.1 Introduction

When a magnetic field is applied to a 2D electron gas, electrons perform closed cyclotron orbits due to the Lorentz force. If electrons rotate very close to the sample edge, the boundary potential may scatter the incident electron and rebound the incoming particle. Such open orbits (known as *skipping orbits*) become really interesting for transport measurements since they provide very clear electronic signals when electrons are injected through a narrow channel in a 2-terminal device (see Fig.6.1). In addition to providing a measurable signal, the concentration of infinitely many skipping orbits forms what is known as *caustics*. Caustics are a continuum of points in the region near the sample edge where the electron density becomes singular due to purely geometrical effects. Therefore, at such points in space, the measured voltage is expected to significantly increase due to the natural tendency of electrons to focus towards those regions. This technique became extremely interesting in transport studies of 2D materials thanks to theoretical predictions in graphene *pn*-junctions[67, 68] of perfectly collimated electron focusing.

For a general band structure, the equations of motion of an electron under an applied electric field $\mathbf{E}$ and a magnetic field $\mathbf{B}$, can be obtained from a purely quasiclassical formulation accounting for the effect of a non-zero Berry curvature Ω_n, [69, 70]

$$\hbar\dot{\mathbf{k}} = -e(\mathbf{E} + \dot{\mathbf{r}} \times \mathbf{B}), \quad \dot{\mathbf{r}} = \frac{1}{\hbar}\frac{\partial\varepsilon(\mathbf{k})}{\partial\mathbf{k}} - \dot{\mathbf{k}} \times \Omega_n(\mathbf{k}). \tag{6.1}$$

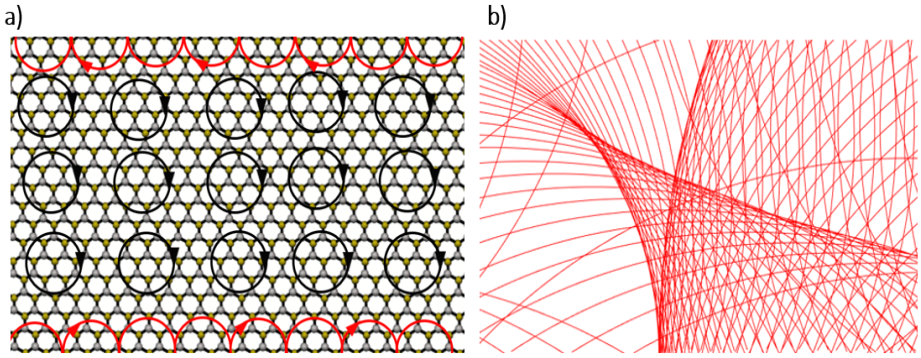

Figure 6.1: a) Skipping orbits (red) and cyclotron orbits (black) in an arbitrary material. The focusing of skipping orbits when electrons are injected is responsible for the formation of caustics and magnetic focusing. b) Formation of caustics and a cusp. The very clear tendency of the cyclotron orbits to concentrate along specific points in space generates these specially high electron density locations.

From the equations of motion, the real space trajectory can be parameterised as a function of time t and θ (i.e. $\mathbf{r}(t,\theta)$) where t labels the time and θ any relevant parameter at the moment of injection. From each of the electron's position at a time t, the electron density at an arbitrary point $\mathbf{r}$ can be obtained from[71]

$$\rho(\mathbf{r}) = \int \delta(\mathbf{r} - \mathbf{r}_n(t)) dt d\theta. \tag{6.2}$$

From the expression above, we can demonstrate after a sequence of substitutions that for circular cyclotron orbits of radius R whose centre after n rebounds is located at $(\zeta_n(\theta), \eta_n(\theta))$, the electron density is singular when

$$F = f(x, y; \zeta_n, \eta_n, R) \equiv (x - \zeta_n)^2 + (x - \eta_n)^2 - R^2 = 0, \quad \frac{dF}{d\theta} = 0. \tag{6.3}$$

Consequently it is expected to observe peaks in the electron current when such high electron concentration curves exactly hit the detector[68].

In this chapter we present how the technique of magnetic focusing was applied to twisted bilayer graphene in order to probe its band structure. Using a self-consistent algorithm similar to the one presented in Section.3, the transverse magnetic focusing signal was calculated at different carrier densities, magnetic fields and displacement fields. The application of a displacement field was shown to generate an opposite shift in the energy of the two different $\mathbf{K}$ and $\mathbf{K}'$ points,

therefore suppressing the contribution from one valley and enhancing the contribution from the opposite one. This has a huge potential in the field of valleytronics as a technique to filter valley currents by means of electrostatic gating.

6.2 Minibands in twisted bilayer graphene probed by magnetic focusing

The results of this publication were reported in Ref.[72]: "Minibands in twisted bilayer graphene probed by magnetic focusing". In:Science Advances 6.16 (2020).

My contribution to this work: A.Ceferino contributed to the theoretical understanding of the magnetic focusing technique and helped with the calculation of the transverse magnetic focusing signal in twisted bilayer graphene.

Full author list: A. I. Berdyugin, B. Tsim, P. Kumaravadivel, S. G. Xu, A. Ceferino, A. Knothe, R. K. Kumar, T. Taniguchi, K. Watanabe, A. K. Geim, I. V. Grigorieva and V. I. Fal'ko.

Author contribution: P. Kumaravidavel and S. G. Xu fabricated the necessary samples. A. I. Berdyugin performed the transport measurements with the help of R. K. Kumar. The transport measurements were analysed by A. I. Berdyugin, B. Tsim, V. I. Fal'ko, and I. V. Grigorieva. B. Tsim made the necessary transverse magnetic focusing calculations with help of V. I. Falko as well as A. Knothe. T. Taniguchi and K. Watanabe provided the hexagonal boron nitride crystals necessary for the device encapsulation. A. I. Berdyugin, B. Tsim, I. V. Grigorieva, and V. I. Fal'ko wrote the manuscript with additional comments from A. K. Geim, P. Kumaravidavel, and S. G. Xu.

CONDENSED MATTER PHYSICS

Minibands in twisted bilayer graphene probed by magnetic focusing

A. I. Berdyugin[1]*, B. Tsim[1,2], P. Kumaravadivel[1,2], S. G. Xu[1,2], A. Ceferino[1,2], A. Knothe[2], R. Krishna Kumar[1,2], T. Taniguchi[3], K. Watanabe[3], A. K. Geim[1,2], I. V. Grigorieva[1,2,4], V. I. Fal'ko[1,2,4]*

Magnetic fields force ballistic electrons injected from a narrow contact to move along skipping orbits and form caustics. This leads to pronounced resistance peaks at nearby voltage probes as electrons are effectively focused inside them, a phenomenon known as magnetic focusing. This can be used not only for the demonstration of ballistic transport but also to study the electronic structure of metals. Here, we use magnetic focusing to probe narrowbands in graphene bilayers twisted at ~2°. Their minibands are found to support long-range ballistic transport limited at low temperatures by intrinsic electron-electron scattering. A voltage bias between the layers causes strong minivalley splitting and allows selective focusing for different minivalleys, which is of interest for using this degree of freedom in frequently discussed valleytronics.

INTRODUCTION

Crystallographic alignment of atomically thin crystals stacked together in a van der Waals heterostructure is a powerful tool that enables fine-tuning of their electronic spectra. For crystals with similar honeycomb lattices, the spectra are modified by the presence of a long-range interference (moiré) pattern with a period λ_S dependent on the twist angle θ between the layers (see Fig. 1A) (*1*–*18*). The additional spatial periodicity reduces the size of the Brillouin zone and introduces secondary Dirac points, as illustrated in Fig. 1B. So far, the most pronounced twist-engineered changes in the electronic properties of two-dimensional (2D) crystals have been achieved in twisted bilayer graphene (TBG), where the twist at discrete "magic" angles results in narrowbands, periodically modulated interlayer hybridization, and strong enhancement of electron correlations, leading to superconductivity and Mott insulator transitions (*6*–*8*). At larger θ, the TBG spectrum corresponds to a metal with several minibands at each K and K′ valley in the Brillouin zone (Fig. 1B). Electronic properties of such a metal are expected to be quite different from

[1]School of Physics and Astronomy, University of Manchester, Manchester M13 9PL, UK. [2]National Graphene Institute, University of Manchester, Manchester M13 9PL, UK. [3]National Institute for Materials Science, 1-1 Namiki, Tsukuba 305-0044, Japan. [4]Henry Royce Institute for Advanced Materials, Manchester M13 9PL, UK.
*Corresponding author. Email: alexey.berdyugin@manchester.ac.uk (A.I.B.); vladimir.falko@manchester.ac.uk (V.I.F.)

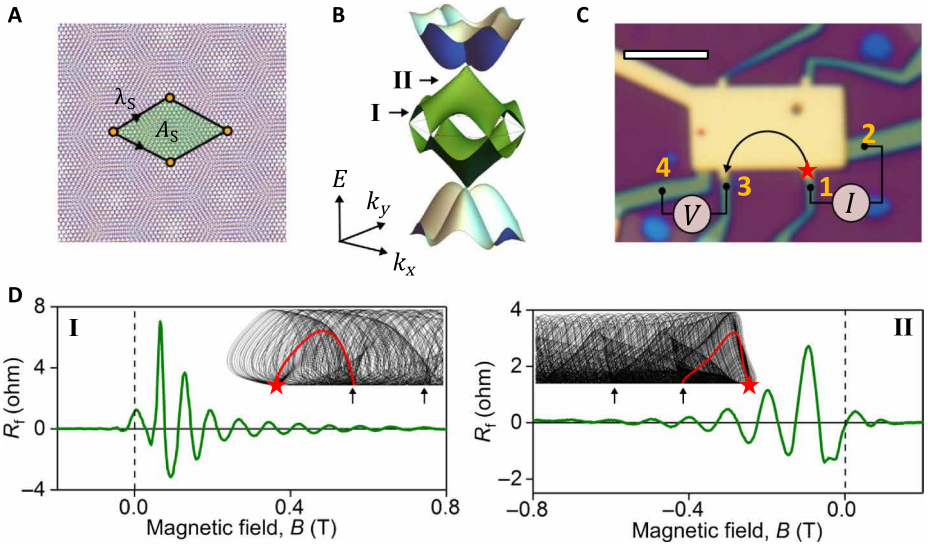

Fig. 1. Moiré minibands and TMF measurements. (**A**) Schematics of the moiré superlattice induced by the twist of graphene layers. Here, two graphene sheets are rotated by an angle θ relative to each other, which creates an additional spatial periodicity $\lambda_S = a/[2 \sin(\theta/2)]$ (a is graphene's lattice constant) with the unit cell area of $A_S = \sqrt{3}/2\lambda_S^2$. (**B**) Band structure of TBG graphene in the K valley of the Brillouin zone calculated for the twist angle θ = 1.87°, as discussed in section S3. (**C**) Optical image of TBG device D1 with θ = 1.87°. Scale bar, 4 μm. (**D**) Two examples of TMF signals measured in device D2 (D = 0 V nm^{-1}) at 5 K for the carrier density 3.7 × 10^{12} cm^{-2} (left) and 9.3 × 10^{12} cm^{-2} (right) at a distance of 4.9 μm from the injector. The latter is close to the main and secondary neutrality points, respectively, as illustrated in (B). The insets are examples of focusing caustics near the main (left) and secondary (right) neutrality points (see more examples in fig. S4). Arrows highlight the focal points for caustics, red star marks the current injection point, and red lines show typical trajectories that extend from the injector to the first focal point.

the behavior of Dirac electrons in monolayer or bilayer (aligned to Bernal stacking) graphene but so far remain largely unexplored. Here, we use transverse focusing of electrons in a perpendicular magnetic field (TMF) (*12*, *19*–*23*) to probe the properties of moiré minibands in TBG and demonstrate an exceptionally high quality of the "artificial metal" in TBG, as well as a possibility to use vertical displacement field, *D*, to break the valley degeneracy in the two constituent layers and selectively enhance transport in one of the minivalley.

RESULTS

Studied devices

We studied two high-quality dual-gated TBG devices encapsulated with ~30- to 50-nm-thick hexagonal boron nitride (hBN) crystals: D1, with $\theta = 1.87° \pm 0.01°$ (shown in Fig. 1C), and D2, with $\theta = 2.60° \pm 0.01°$ (fig. S1A). The procedure used to determine θ is described in section S1. The devices were fabricated using standard dry-transfer (*24*, *25*) and tear-and-stack (*4*, *26*) techniques (see section S2 for details). To ensure a clean interface between the two graphene layers, special care was taken to avoid any contact between graphene and the polymer during the transfer (section S2). In transport measurements, both devices showed similar behavior, with low-temperature mobilities in excess of 400,000 $cm^2\ V^{-1}\ s^{-1}$ for carrier density $n \sim 10^{12}\ cm^{-2}$. All data shown below were obtained at a constant displacement field, *D*, that was achieved by a simultaneous sweep of the top and bottom gates (section S2).

Transverse magnetic focusing

The high mobility for both devices enabled observation of TMF (*12*, *19*–*23*), which is a manifestation of ballistic motion of electrons and had been used to characterize the shape of Fermi surfaces in both 3D (*19*, *20*) and 2D (*12*, *21*–*23*) metals. To measure the effect of TMF in our TBG devices, we used a nonlocal geometry illustrated in Fig. 1C, where narrow contacts 1 and 2 at one end of the device were used for current injection (driving current I_{12}) and contacts 3 and 4 at the other end were used to detect a voltage V_{34}. In the presence of a perpendicular magnetic field, electrons injected from contact 1 propagate along the device edges in skipping orbits and form a characteristic caustic pattern determined by the shape of the Fermi surface, as illustrated in the insets of Fig. 1D. Caustics are focused into equidistant focal points along the sample edge, and the drift direction of the skipping orbits is determined by the sign of the magnetic field such that electron- and hole-like carriers propagate in opposite directions. As the positions of focal points vary with the magnetic field, whenever they coincide with the position of the voltage probe (contact 3 in Fig. 1C), one observes a focusing peak in the nonlocal resistance $R_f = V_{34}/I_{12}$. Figure 1D gives two examples of the observed focusing peaks measured at different carrier densities.

Figure 2A shows a typical dependence of R_f on the carrier density and magnetic field at zero displacement field, $D = 0\ V\ nm^{-1}$. Here, the appearance of an R_f signal in a particular quadrant of the *B*-*n* diagram reflects the sign of the cyclotron mass, while the change of the quadrant upon doping indicates an inversion of the electron dispersion (i.e., a change of sign of the mass from electrons to holes or vice versa). Accordingly, a fan-like pattern in the center of Fig. 2A, which converges and changes direction at zero carrier density, indicates a neutrality point. Two additional, qualitatively similar, changes of the cyclotron mass appear at higher electron and hole densities,

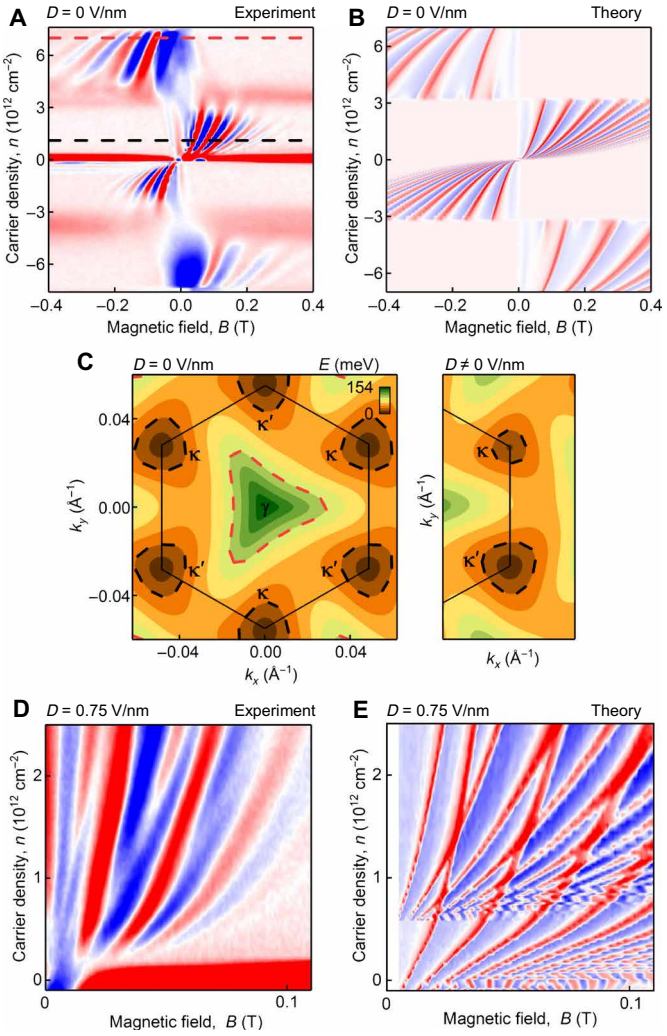

Fig. 2. Transverse magnetic focusing map. (**A**) Focusing signal R_f as a function of the magnetic field and carrier density measured at 2 K for device D1 in zero displacement field, $D = 0\ V\ nm^{-1}$. Color scale: blue to red, ±3 ohms. (**B**) TMF map calculated from the energy spectrum shown in Fig. 1B using a numerical method described in section S4. The angle between the zigzag edge of one of the monolayers and the sample boundary is taken as 45° to avoid any spurious effects of crystallographic alignment. As demonstrated in section S4, the calculated TMF map is only very weakly sensitive to the mutual orientation between graphene and the sample edge, confirming the generality of our results. (**C**) Contour plot of the first conduction miniband shown for the K valley of the Brillouin zone for zero (left) and nonzero (right) displacement fields. Black and red dashed lines outline the shape of the Fermi surfaces for carrier densities marked by black and red dashed lines in (A); the latter corresponds to equivalent doping levels relative to the main (black) and secondary (red) neutrality points. The color scale is from 0 to 154 meV. (**D**) R_f as a function of magnetic field and carrier density for device D2 measured at $T = 2$ K and $D = 0.75\ V\ nm^{-1}$ at a distance of 8.5 μm from the injector (more data are shown in fig. S5). Color scale: blue to red, ±0.2 ohm. (**E**) TMF map calculated numerically for device D2 in a displacement field (see sections S3 to S5 for details), which shows the splitting of the focusing peaks originating from the different miniband dispersion at κ and κ′.

showing inverted fan-like patterns at higher energies. These indicate that the electron dispersion converges toward a new (secondary) neutrality point, such as shown in Fig. 1B. The crossover between these two regimes (at $n \approx 3 \times 10^{12}\ cm^{-2}$ and $-3 \times 10^{12}\ cm^{-2}$) must

correspond to a van Hove singularity (vHS) in the moiré miniband spectrum. For a quantitative comparison, Fig. 2B presents the results of TMF modeling for device D1. Here, we used the model from (*3*) to compute the electron spectrum shown in Fig. 1B (see section S3 for details) and to perform numerical analysis of caustics (*12*), where the contributions to R_f from trajectories of electrons leaving the injection contact at different angles were weighted proportionally to $|\nabla_{\boldsymbol{k}}\boldsymbol{E}|^{-1}$ (section S4). A good agreement between the experiment (Fig. 2A) and theory (Fig. 2B) suggests that the band structure of TBG is well described by the spectrum shown in Fig. 1B.

It is noticeable that the fan-like patterns in Fig. 2 (A and B)—corresponding to the main and secondary neutrality points of the TBG superlattice (around zero carrier density and above the vHS, respectively)—have different periodicities. This difference is caused by different sizes of the Fermi surfaces at equivalent doping levels (black and red dashed lines in Fig. 2A), due to the degeneracy of the miniband dispersion at κ and κ′. The Fermi surface contours are shown in Fig. 2C by black dashed lines around κ and κ′ points of the mini Brillouin zone (main neutrality point) and a red dashed line around the γ point (secondary neutrality point). Furthermore, our theoretical analysis suggests that the Fermi surfaces close to the γ point have a triangular shape (Fig. 2C), which can be traced to the strong interlayer hybridization of those states. At the same time, the Fermi surfaces around κ and κ′ points (that coincide with the valley centers K of the top and bottom graphene layers) are almost isotropic, as in monolayer graphene, pointing toward weak interlayer hybridization of these states.

Effect of the displacement field

The absence of appreciable interlayer coupling at κ and κ′ can be used to disentangle the TMF contributions from different minivalleys. To this end, we used a finite displacement field, up to $D = 0.75$ V nm^{-1} (achievable without a risk of damaging our devices), which shifts the on-layer potential for electrons and therefore shifts the energies of the Dirac cones at κ and κ′, as illustrated in Fig. 2C. Such layer-symmetry breaking lifts the degeneracy between κ and κ′ and separates the motion of electrons from different minivalleys in a magnetic field, as they now have different sizes of cyclotron orbits. This generates two different magneto-oscillation frequencies of R_f at low carrier densities, $|n| < 10^{12}$ cm^{-2}, as seen in Fig. 2D, where separate focusing peaks appear for the electrons from each minivalley.

DISCUSSION

Further information about carrier dynamics in TBG can be obtained by studying the temperature dependence of TMF and its evolution for consecutive focusing peaks. In Fig. 3A, we show how the amplitude of TMF oscillations depends on temperature T in the range 2 K < T < 30 K, in the vicinity of both main and secondary neutrality points. For quantitative analysis, we extract the relative scattering length as (*12*)

$$\frac{L_s}{L_{path}} = \left(\ln\left[\frac{A(T_{base})}{A(T)}\right]\right)^{-1} \quad (1)$$

where L_{path} is the length of trajectories extending from the injector to the first focal point as shown in Fig. 1D, and $A_{1(2)}(T)$ and $A_{1(2)}(T_{base})$ are the areas under the first (second) focusing peak in Fig. 3A at T and $T_{base} = 2$ K, respectively. The results are shown in Fig. 3B. The measured scattering lengths L_s for both carrier densities and all focusing peaks follow a T^{-2} scaling, which is different from the T^{-1} dependence characteristic of phonon-dominated scattering (*23*, *27*). Such scaling points toward the dominance of low-angle electron-electron scattering that was also found to be responsible for the TMF suppression in graphene/hBN superlattices (*12*). Furthermore, the ratio between the areas under the second and first focusing peaks in Fig. 3A, A_2/A_1, characterizes the reflection of electrons at the sample boundary: The closer it is to one, the higher the probability for the incoming electrons to undergo specular reflection. In our experiment, electrons with energies near the main neutrality points ($n \approx 1.8 \times 10^{12}$ cm^{-2}; Fig. 3A, right) undergo almost specular reflection ($A_2/A_1 \approx 0.8$), while reflection of the electrons with energies near the secondary neutrality point ($n \approx 6.6 \times 10^{12}$ cm^{-2}; Fig. 3A, left) is notably less specular ($A_2/A_1 \approx 0.65$). This indicates a higher probability of diffusive scattering in the latter case, which is consistent with the greater sensitivity of the corresponding part of the miniband spectrum to inevitable perturbations of the moiré pattern near the sample edge. Because of little hybridization between the layers near κ and κ′, the scattering of Dirac electrons should be little affected by the termination of

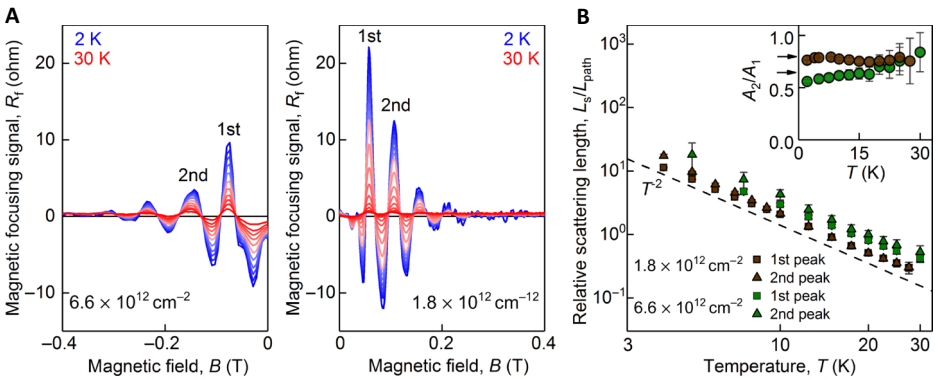

Fig. 3. Temperature dependence of magnetic focusing. (**A**) Temperature dependence of the TMF signal measured at two characteristic carrier densities for device D1 (see legends). T was varied from 2 to 30 K (blue to red). (**B**) T dependence of the relative scattering length (see text) extracted from experimental data for consecutive focusing peaks. Absolute scattering lengths for several relative orientations of the crystallographic axes and the sample edge are shown in fig. S6. Dashed line shows T^{-2} dependence. The inset shows the ratio of the areas under the first and second focusing peaks in (A) as a function of T. Arrows correspond to $A_2/A_1 = 0.8$ and 0.65 (see text). Error bars indicate the accuracy of determining A_2/A_1; large errors at $T > 20$ K are due to the relatively large background signal as the focusing peaks become strongly suppressed.

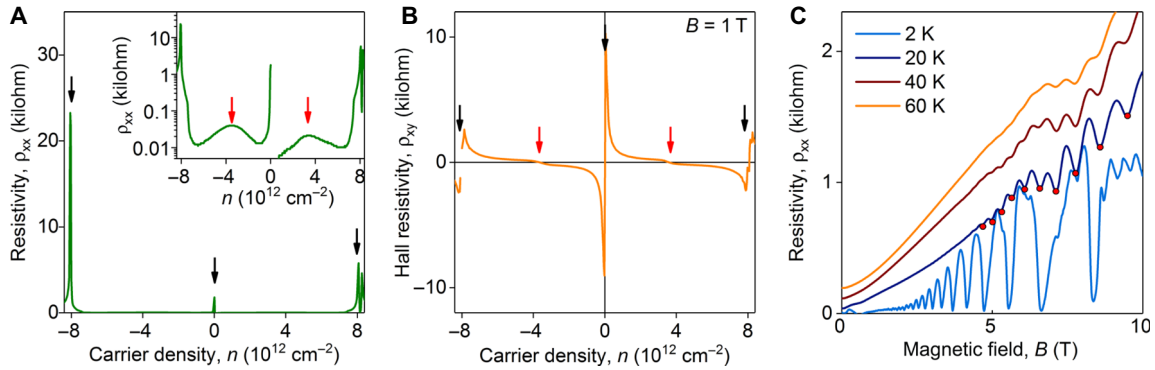

Fig. 4. Bulk transport properties of TBG. (**A**) Resistivity as a function of carrier density measured at 5 K for device D1. The inset shows the same data on a logarithmic scale. (**B**) Hall resistivity as a function of the carrier density for D1. Black arrows in (A) and (B) mark neutrality points, and red arrows mark vHS. (**C**) Resistivity versus magnetic field measured at different temperatures for device D1 at $n = 3.1 \times 10^{12}$ cm^{-2}. Red dots on a 40-K curve highlight the positions of Brown-Zak oscillations.

superlattice periodicity near the edge, while its part near the secondary neutrality points should be affected substantially, promoting diffusive scattering.

Last, we note that the above observations of superlattice effects in TMF correlate well with the bulk transport properties of the same TBG samples studied using local geometry. The longitudinal and Hall resistivity shown in Fig. 4 (A and B) displays secondary neutrality points (indicated by black arrows) and vHS (red arrows) at the same carrier densities as those inferred from the TMF experiments. Furthermore, the presence of a moiré superlattice in the studied TBG samples is seen from the presence of Brown-Zak oscillations (*13*, *14*) that dominate the magnetotransport above $T \sim 30$ K (Fig. 4C): While at low temperatures the magnetoresistance is dominated by Shubnikov–de Haas oscillations (see $T = 2$ K curve in Fig. 4C), these are rapidly suppressed as T increases and give way to another 1/B-periodic oscillations, with period determined by the relation between the magnetic flux through the moiré supercell area, A_S, and the magnetic flux quantum $\phi_0 = h/e$, i.e., $BA_S = \phi_0/q$ (where q is an integer).

To conclude, we have demonstrated that TBG supports ballistic propagation of electrons in multimicrometer devices, with electron transport determined by the reconstruction of the energy spectrum in the presence of a long-period superlattice. This offers new opportunities to study fundamental phenomena, such as Bloch oscillations in moiré superlattices (*28*–*30*) and their use for, e.g., terahertz generation. Moreover, we have shown that the sensitivity of the TBG band structure to the displacement field allows selective manipulation of electrons from different minivalleys, which may be implemented in electronic devices exploiting the valley degree of freedom.

MATERIALS AND METHODS

Device fabrication

To make TBG, we used the standard tear-and-stack method as described in section S2. TBG stacks were encapsulated between hBN crystals and assembled onto SiO_2 substrate with doped silicon underneath, which served as a bottom gate electrode. Then, devices were shaped into hall bars using standard electron-beam lithography and reactive-ion etching techniques (section S2).

Measurement details

We used standard low-frequency lock-in measurement technique with excitation frequency of 10 to 30 Hz. To independently control the carrier density and interlayer displacement field, we used dual-gated geometry, as discussed in section S2.

SUPPLEMENTARY MATERIALS

Supplementary material for this article is available at http://advances.sciencemag.org/cgi/content/full/6/16/eaay7838/DC1

REFERENCES AND NOTES

1. G. Li, A. Luican, J. M. B. Lopes dos Santos, A. H. Castro Neto, A. Reina, J. Kong, E. Y. Andrei, Observation of Van Hove singularities in twisted graphene layers. *Nat. Phys.* **6**, 109–113 (2010).
2. E. Suárez Morell, J. D. Correa, P. Vargas, M. Pacheco, Z. Barticevic, Flat bands in slightly twisted bilayer graphene: Tight-binding calculations. *Phys. Rev. B* **82**, 121407(R) (2010).
3. R. Bistritzer, A. H. MacDonald, Moiré bands in twisted double-layer graphene. *Proc. Natl. Acad. Sci. U.S.A.* **108**, 12233–12237 (2011).
4. Y. Cao, J.. Y. Luo, V. Fatemi, S. Fang, J.. D. Sanchez-Yamagishi, K. Watanabe, T. Taniguchi, E. Kaxiras, P. Jarillo-Herrero, Superlattice-induced insulating states and valley-protected orbits in twisted bilayer graphene. *Phys. Rev. Lett.* **117**, 116804 (2016).
5. K. Kim, A. Da Silva, S. Huang, B. Fallahazad, S. Larentis, T. Taniguchi, K. Watanabe, B. J. Le Roy, A. H. MacDonald, E. Tutuc, Tunable moiré bands and strong correlations in small-twist-angle bilayer graphene. *Proc. Natl. Acad. Sci. U.S.A.* **114**, 3364–3369 (2017).
6. Y. Cao, V. Fatemi, A. Demir, S. Fang, S. L. Tomarken, J. Y. Luo, J. D. Sanchez-Yamagishi, K. Watanabe, T. Taniguchi, E. Kaxiras, R. C. Ashoori, P. Jarillo-Herrero, Correlated insulator behaviour at half-filling in magic-angle graphene superlattices. *Nature* **556**, 80–84 (2018).
7. Y. Cao, V. Fatemi, S. Fang, K. Watanabe, T. Taniguchi, E. Kaxiras, P. Jarillo-Herrero, Unconventional superconductivity in magic-angle graphene superlattices. *Nature* **556**, 43–50 (2018).
8. M. Yankowitz, S. Chen, H. Polshyn, Y. Zhang, K. Watanabe, T. Taniguchi, D. Graf, A. F. Young, C. R. Dean, Tuning superconductivity in twisted bilayer graphene. *Science* **363**, 1059–1064 (2019).
9. M. Yankowitz, J. Xue, D. Cormode, J. D. Sanchez-Yamagishi, K. Watanabe, T. Taniguchi, P. Jarillo-Herrero, P. Jacquod, B. J. Le Roy, Emergence of superlattice Dirac points in graphene on hexagonal boron nitride. *Nat. Phys.* **8**, 382–386 (2012).
10. L. A. Ponomarenko, R. V. Gorbachev, G. L. Yu, D. C. Elias, R. Jalil, A. A. Patel, A. Mishchenko, A. S. Mayorov, C. R. Woods, J. R. Wallbank, M. Mucha-Kruczynski, B. A. Piot, M. Potemski, I. V. Grigorieva, K. S. Novoselov, F. Guinea, V. I. Fal'ko, A. K. Geim, Cloning of Dirac fermions in graphene superlattices. *Nature* **497**, 594–597 (2013).
11. C. R. Dean, L. Wang, P. Maher, C. Forsythe, F. Ghahari, Y. Gao, J. Katoch, M. Ishigami, P. Moon, M. Koshino, T. Taniguchi, K. Watanabe, K. L. Shepard, J. Hone, P. Kim, Hofstadter's butterfly and the fractal quantum Hall effect in moiré superlattices. *Nature* **497**, 598–602 (2013).
12. M. Lee, J. R. Wallbank, P. Gallagher, K. Watanabe, T. Taniguchi, V. I. Fal'ko, D. Goldhaber-Gordon, Ballistic miniband conduction in a graphene superlattice. *Science* **353**, 1526–1529 (2016).
13. R. Krishna Kumar, X. Chen, G. H. Auton, A. Mishchenko, D. A. Bandurin, S. V. Morozov, Y. Cao, E. Khestanova, M. B. Shalom, A. V. Kretinin, K. S. Novoselov, L. Eaves, I. V. Grigorieva, L. A. Ponomarenko, V. I. Fal'ko, A. K. Geim, High-temperature quantum oscillations caused by recurring Bloch states in graphene superlattices. *Science* **357**, 181–184 (2017).

14. R. Krishna Kumar, A. Mishchenko, X. Chen, S. Pezzini, G. H. Auton, L. A. Ponomarenko, U. Zeitler, L. Eaves, V. I. Fal'ko, A. K. Geim, High-order fractal states in graphene superlattices. *Proc. Natl. Acad. Sci. U.S.A.* **115**, 5135–5139 (2018).
15. K. L. Seyler, P. Rivera, H. Yu, N. P. Wilson, E. L. Ray, D. G. Mandrus, J. Yan, W. Yao, X. Xu, Signatures of moiré-trapped valley excitons in $MoSe_2/WSe_2$ heterobilayers. *Nature* **567**, 66–70 (2019).
16. K. Tran, G. Moody, F. Wu, X. Lu, J. Choi, K. Kim, A. Rai, D. A. Sanchez, J. Quan, A. Singh, J. Embley, A. Zepeda, M. Campbell, T. Autry, T. Taniguchi, K. Watanabe, N. Lu, S. K. Banerjee, K. L. Silverman, S. Kim, E. Tutuc, L. Yang, A. H. MacDonald, X. Li, Evidence for moiré excitons in van der Waals heterostructures. *Nature* **567**, 71–75 (2019).
17. C. Jin, E. C. Regan, A. Yan, M. Iqbal Bakti Utama, D. Wang, S. Zhao, Y. Qin, S. Yang, Z. Zheng, S. Shi, K. Watanabe, T. Taniguchi, S. Tongay, A. Zettl, F. Wang, Observation of moiré excitons in WSe_2/WS_2 heterostructure superlattices. *Nature* **567**, 76–80 (2019).
18. E. M. Alexeev, D. A. Ruiz-Tijerina, M. Danovich, M. J. Hamer, D. J. Terry, P. K. Nayak, S. Ahn, S. Pak, J. Lee, J. I. Sohn, M. R. Molas, M. Koperski, K. Watanabe, T. Taniguchi, K. S. Novoselov, R. V. Gorbachev, H. S. Shin, V. I. Fal'ko, A. I. Tartakovskii, Resonantly hybridized excitons in moiré superlattices in van der Waals heterostructures. *Nature* **567**, 81–86 (2019).
19. V. S. Tsoi, Focusing of electrons in a metal by a transverse magnetic field. *JETP Lett.* **19**, 70–71 (1974).
20. V. S. Tsoi, Determination of the dimensions of nonextremal Fermi-surface sections by transverse focusing of electrons. *JETP Lett.* **22**, 197–198 (1975).
21. C. W. J. Beenakker, J. G. Williamson, M. E. I. Broekaart, P. H. M. van Loosdrecht, B. J. van Wees, J. E. Mooij, C. T. Foxon, J. J. Harris, Coherent electron focusing with quantum point contacts in a two-dimensional electron gas. *Phys. Rev. B* **39**, 8556–8575 (1989).
22. J. J. Heremans, M. B. Santos, M. Shayegan, Observation of magnetic focusing in two-dimensional hole systems. *Appl. Phys. Lett.* **61**, 1652–1654 (1992).
23. T. Taychatanapat, K. Watanabe, T. Taniguchi, P. Jarillo-Herrero, Electrically tunable transverse magnetic focusing in graphene. *Nat. Phys.* **9**, 225–229 (2013).
24. A. V. Kretinin, Y. Cao, J. S. Tu, G. L. Yu, R. Jalil, K. S. Novoselov, S. J. Haigh, A. Gholinia, A. Mishchenko, M. Lozada, T. Georgiou, C. R. Woods, F. Withers, P. Blake, G. Eda, A. Wirsig, C. Hucho, K. Watanabe, T. Taniguchi, A. K. Geim, R. V. Gorbachev, Electronic properties of graphene encapsulated with different two-dimensional atomic crystals. *Nano Lett.* **14**, 3270–3276 (2014).
25. I. Meric, P. Y. Huang, Q. Gao, Y. Gao, H. Tran, T. Taniguchi, K. Watanabe, L. M. Campos, D. A. Muller, J. Guo, P. Kim, J. Hone, K. L. Shepard, C. R. Dean, One-dimensional electrical contact to a two-dimensional material. *Science* **342**, 614–617 (2013).
26. K. Kim, M. Yankowitz, B. Fallahazad, S. Kang, H. C. Movva, S. Huang, S. Larentis, C. M. Corbet, T. Taniguchi, K. Watanabe, S. K. Banerjee, B. J. Le Roy, E. Tutuc, van der Waals heterostructures with high accuracy rotational alignment. *Nano Lett.* **16**, 1989–1995 (2016).
27. E. H. Hwang, S. Das Sarma, Acoustic phonon scattering limited carrier mobility in two-dimensional extrinsic graphene. *Phys. Rev. B* **77**, 115449 (2008).
28. L. Esaki, L. L. Chang, New transport phenomenon in a semiconductor "superlattice". *Phys. Rev. Lett.* **33**, 495–498 (1974).
29. K. Leo, P. H. Bolivar, F. Brüggemann, R. Schwedler, K. Köhler, Observation of Bloch oscillations in a semiconductor superlattice. *Solid State Commun.* **84**, 943–946 (1992).
30. C. Waschke, H. G. Roskos, R. Schwedler, K. Leo, H. Kurz, K. Köhler, Coherent submillimeter-wave emission from Bloch oscillations in a semiconductor superlattice. *Phys. Rev. Lett.* **70**, 3319–3322 (1993).
31. P. Rickhaus, J. Wallbank, S. Slizovskiy, R. Pisoni, H. Overweg, Y. Lee, M. Eich, M. H. Liu, K. Watanabe, T. Taniguchi, T. Ihn, K. Ensslin, Transport through a network of topological channels in twisted bilayer graphene. *Nano Lett.* **18**, 6725–6730 (2018).
32. N. W. Ashcroft, N. D. Mermin, *Solid State Physics* (Saunders College, 1976).
33. J. R. Wallbank, A. A. Patel, M. Mucha-Kruczynski, A. K. Geim, V. I. Fal'ko, Generic miniband structure of graphene on a hexagonal substrate. *Phys. Rev. B* **87**, 245408 (2013).
34. H. Schmidt, T. Lüdtke, P. Barthold, E. M. Cann, V. I. Fal'ko, R. J. Haug, Tunable graphene system with two decoupled monolayers. *Appl. Phys. Lett.* **93**, 172108 (2008).
35. S. Slizovskiy, A. Garcia-Ruiz, N. Drummond, V. I. Fal'ko, Dielectric susceptibility of graphene describing its out-of-plane polarizability. arXiv:1912.10067 [cond-mat. mes-hall] (20 December 2019).
36. J. D. Sanchez-Yamagishi, T. Taychatanapat, K. Watanabe, T. Taniguchi, A. Yacoby, P. Jarillo-Herrero, Quantum Hall effect, screening, and layer-polarized insulating states in twisted bilayer graphene. *Phys. Rev. Lett.* **108**, 076601 (2012).
37. B. Fallahazad, Y. Hao, K. Lee, S. Kim, R. S. Ruoff, E. Tutuc, Quantum Hall effect in Bernal stacked and twisted bilayer graphene grown on Cu by chemical vapor deposition. *Phys. Rev. B* **85**, 201408(R) (2012).

Acknowledgments: We thank J. R. Wallbank for helpful discussions. **Funding:** A.I.B., B.T., and A.C. acknowledge support from Graphene NOWNANO Doctoral Training Center, and R.K.K. was supported by an EPSRC fellowship award. This work has been supported by EPSRC grants EP/S019367/1, EP/S030719/1, and EP/N010345/1; EPSRC Doctoral Training Centre Graphene NOWNANO EP/L01548X/1; ERC Synergy Grant Hetero2D; Lloyd's Register Foundation Nanotechnology grant; and European Graphene Flagship Project. **Author contributions:** P.K. and S.G.X. fabricated devices. A.I.B. carried out electrical measurements with the help from R.K.K. A.I.B., B.T., V.I.F., and I.V.G. analyzed the results. B.T. did magnetic focusing simulations with contributions from V.I.F., A.C., and A.K. T.T. and K.W. provided hBN crystals. A.I.B., B.T., I.V.G., and V.I.F. wrote the manuscript with contributions from A.K.G., P.K., and S.G.X. All authors contributed to discussions. **Competing interests:** The authors declare that they have no competing interests. **Data and materials availability:** All data needed to evaluate the conclusions in the paper are present in the paper and/or the Supplementary Materials. Additional data related to this paper may be requested from the authors.

Submitted 17 July 2019
Accepted 22 January 2020
Published 17 April 2020
10.1126/sciadv.aay7838

Citation: A. I. Berdyugin, B. Tsim, P. Kumaravadivel, S. G. Xu, A. Ceferino, A. Knothe, R. K. Kumar, T. Taniguchi, K. Watanabe, A. K. Geim, I. V. Grigorieva, V. I. Fal'ko, Minibands in twisted bilayer graphene probed by magnetic focusing. *Sci. Adv.* **6**, eaay7838 (2020).

Minibands in twisted bilayer graphene probed by magnetic focusing

A. I. Berdyugin, B. Tsim, P. Kumaravadivel, S. G. Xu, A. Ceferino, A. Knothe, R. Krishna Kumar, T. Taniguchi, K. Watanabe, A. K. Geim, I. V. Grigorieva and V. I. Fal'ko

Sci Adv **6** (16), eaay7838.
DOI: 10.1126/sciadv.aay7838

Science Advances
AAAS

advances.sciencemag.org/cgi/content/full/6/16/eaay7838/DC1

Supplementary Materials for

Minibands in twisted bilayer graphene probed by magnetic focusing

A. I. Berdyugin*, B. Tsim, P. Kumaravadivel, S. G. Xu, A. Ceferino, A. Knothe, R. Krishna Kumar, T. Taniguchi, K. Watanabe, A. K. Geim, I. V. Grigorieva, V. I. Fal'ko*

*Corresponding author. Email: alexey.berdyugin@manchester.ac.uk (A.I.B.); vladimir.falko@manchester.ac.uk (V.I.F.)

Published 17 April 2020, *Sci. Adv.* **6**, eaay7838 (2020)
DOI: 10.1126/sciadv.aay7838

This PDF file includes:

Section 1. Determining twist angle.

We used two independent methods to find the actual twist angle θ between the two graphene layers. First, the twist angles were found from $\rho_{xx}(n)$ and $\rho_{xy}(n)$ measurements using the position of the secondary neutrality points (NP):

$$\theta = 2\arcsin\left(\sqrt{\frac{\sqrt{3}a^2}{8A}}\right), \qquad \text{(S1)}$$

where a is graphene's lattice constant, n the carrier density, $A = 4/\Delta n$ the superlattice unit cell area, and Δn the position of the secondary NP. For device D1, NP are shown in Figs 4A and 4B in the main text yielding $\Delta n = 8.1 \times 10^{12}$ cm^{-2} and $\theta = 1.87°$. For device D2 it was impossible to reach secondary NPs using electrostatic gating; to find the twist angle in this case we used the fact that NPs can be found by extrapolation of the reciprocal Hall resistivity, $(\rho_{xy})^{-1}$ as shown in Fig. S1A. The main neutrality point is clearly seen at zero carrier density and two van Hove singularities (vHS) are shown by red arrows. To find the secondary NPs, the linear dependences below and above the vHS were extrapolated as shown in Fig. S1A, with NPs corresponding to the intersections with $(\rho_{xy})^{-1} = 0$. The positions of the secondary NPs for this device, marked by black arrows, give $\Delta n = 15.7 \times 10^{12}$ cm^{-2} corresponding to $\theta = 2.60°$.

Another way to determine the twist angle is from the periodicity of Brown-Zak oscillations (*13*, *14*), which are shown in Fig. 4C for D1 and in Fig. S1B for D2. The superlattice area can be found as $A = \Delta\left(\frac{1}{B}\right)\phi_0$, where $\Delta\left(\frac{1}{B}\right)$ is the period of Brown-Zak oscillations in the reciprocal magnetic field, and ϕ_0 the flux quantum. This gives $\Delta\left(\frac{1}{B}\right) = 0.0119 \pm 0.0005$ T^{-1} for D1 and 0.00616 ± 0.00005 T^{-1} for D2 corresponding to $\theta = 1.87 \pm 0.01°$ for device D1 and $\theta = 2.60 \pm 0.01°$ for D2, in good agreement with the values found from Hall resistivity.

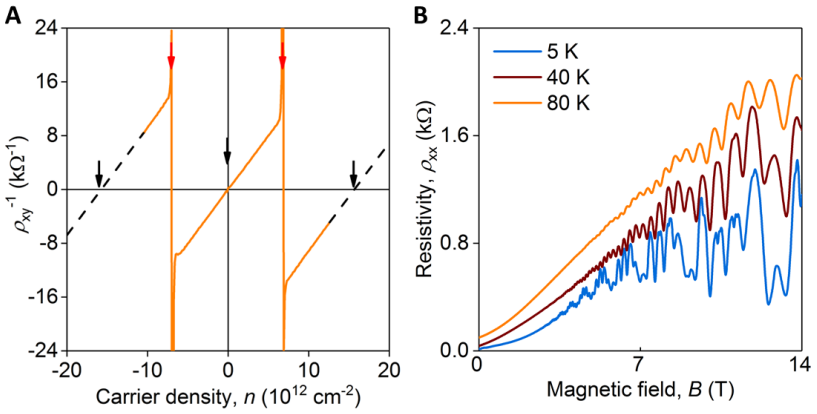

Fig. S1. Hall resistivity and Brown-Zak oscillations in device D2. (**A**), Reciprocal Hall resistivity as a function of carrier density in a magnetic field of 1T measured at 3.5K. Black arrows indicate positions of neutrality points and red arrows show positions of vHS. Black dashed lines are extrapolations that allowed us to find positions of the secondary NPs. (**B**), Longitudinal resistivity vs magnetic field measured at different temperatures for device D2 at the carrier density n = 5.8x10^{12} cm^{-2}.

Section 2. Device fabrication and measurement details

The heterostructures studied in this work were assembled using the standard dry-transfer technique (*24*, *25*), and for the fabrication of the twisted bilayer graphene (TBG) we adapted the tear-and-stack (*26, 4*) method. Details of these methods are outlined below.

First, the top hexagonal boron nitride (hBN) crystal was picked up using a polypropylene carbonate (PPC) polymer spun onto a polydimethylsiloxane (PDMS) film. Then we used a micromanipulator to place the hBN crystal so as to cover only a part of the monolayer graphene located on a SiO_2/Si substrate. Next, hBN was slowly peeled off the substrate, tearing the graphene flake into two pieces while picking up the part covered with hBN. The remaining part of the graphene flake was rotated by 2˚ and picked up with the first half attached to hBN to produce TBG. The temperature of the substrate was kept at 70˚ C throughout this process in order to reduce thermally induced strain or relaxation of the layers. By carefully controlling the micromanipulator, we ensured that graphene layers had no contact with the PPC polymer, guaranteeing a clean interface between the two graphene monolayers. Finally, the bottom hBN crystal was picked up to encapsulate the TBG, and the whole stack released onto a SiO_2/Si substrate. To define 1D contacts, we used reactive ion etching to selectively remove the heterostructures areas, followed by deposition of Cr (3 nm) and Au (60 nm). An additional lithography step was used to make a gold top gate, which also served as an etching mask to define the mesa. An example of the final device is shown in Fig. S2A, where we show one of our dual gated TBG samples. For this sample we used p-doped Si as the bottom gate and Au as the top gate.

Resistance measurements were carried out using the standard low-frequency lock-in technique with a small excitation current ~100 nA; this ensured negligible heating effects down to the lowest measurement temperature, T = 2K. The dual-gated geometry allowed us to control the total carrier density and the displacement field independently. The total carrier density is the sum of carrier densities induced by the top and bottom gates: $n_{\mathrm{total}} = \frac{1}{e}(C_{\mathrm{tg}}V_{\mathrm{tg}} + C_{\mathrm{bg}}V_{\mathrm{bg}})$, where V_{tg} and V_{bg} are the top and bottom gate voltages, e is the electron charge, C_{tg} and C_{bg} are the respective capacitances per unit area of the top and bottom gate (here C_{tg} and C_{bg} were obtained from the Hall measurements). The displacement field is calculated using $D = \frac{1}{2\varepsilon_0}(C_{\mathrm{tg}}V_{\mathrm{tg}} - C_{\mathrm{bg}}V_{\mathrm{bg}})$, where ε_0 is the vacuum permittivity. To achieve a fixed displacement field, V_{tg} and V_{bg} were varied simultaneously according to the above formula, so that only the total carrier density changed. An example of such measurements is shown in Fig. S2B.

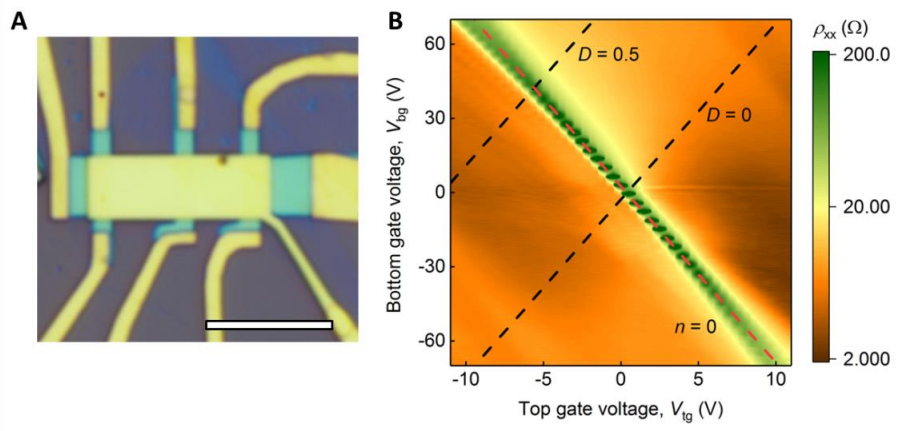

Fig. S2. Dual-gate measurement setup. (**A**)**,** Optical image of device D2. Scale bar, 7 µm. (**B**)**,** ρ_{xx} as a function of top and bottom gate voltages for device D2 at T = 3.5K. Red dashed line corresponds to the conditions of zero carrier density and black dashed lines show the direction of double gate sweeps at D=0 and 0.5 V/nm.

Section 3. Calculations of TBG band structure

To calculate the band structure of TBG, we used the model reported in ref. (*31*), where the Hamiltonian is given by:

$$\hat{\mathrm{H}}_{\mathrm{TBG}} = \begin{pmatrix} \frac{\Delta}{2} & \nu\pi^{\dagger} & & w\sum_{j=0,1,2} e^{-i\,\Delta\mathbf{K}_j\cdot\boldsymbol{r}}\begin{pmatrix} 1 & e^{i\frac{2\pi}{3}j} \\ e^{-i\frac{2\pi}{3}j} & 1 \end{pmatrix} \\ \nu\pi & \frac{\Delta}{2} & & \\ & & -\frac{\Delta}{2} & \nu\pi^{\dagger} \\ w\sum_{j=0,1,2} e^{i\,\Delta\mathbf{K}_j\cdot\boldsymbol{r}}\begin{pmatrix} 1 & e^{i\frac{2\pi}{3}j} \\ e^{-i\frac{2\pi}{3}j} & 1 \end{pmatrix} & & \nu\pi & -\frac{\Delta}{2} \end{pmatrix}. \quad \text{(S2)}$$

This is equivalent to the continuum-model Hamiltonian derived in ref. (*3*) up to a gauge transformation. The on-diagonal blocks describe the top and bottom layers of graphene where ν is the Dirac velocity for the monolayer and Δ the energy shift induced by the perpendicular displacement field. The off-diagonal blocks describe the interactions between the two layers, with the interlayer coupling strength given by w=110 meV.

The original band touching point of the top layer is placed at the corner of the mini Brillouin zone (mBZ) κ, and the band touching point of the bottom layer is placed at κ'. The vectors $\Delta\mathbf{K}_j$ accounting for the shift between Brillouin zone corners for the two layers (as illustrated in Fig. S3) are given by:

$$\Delta\mathbf{K}_j = \frac{4\pi\theta}{3a}\left(-\sin\left(\frac{2\pi j}{3}\right), \cos\left(\frac{2\pi j}{3}\right)\right), \quad \text{(S3)}$$

where θ is the twist angle between the two layers in radians and a=2.46 Å is graphene's lattice constant.

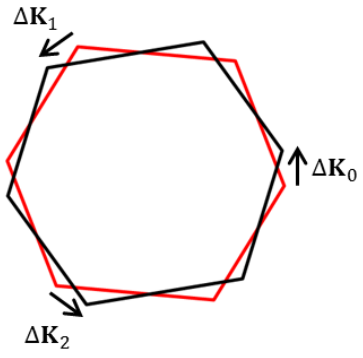

Fig. S3. Brillouin zone of two twisted graphene layers. Red and black hexagons are the original Brillouin zones of the two monolayers overlaid with a relative twist. The vectors $\Delta\mathbf{K}_j$ (defined in Eq. (S3)) account for the shift between the original Brillouin zone corners of the two graphene layers making up a twisted bilayer graphene.

The Hamiltonian in Eq. (S2) is shown for the K valley of the original Brillouin zone. To obtain the band structure in the K' valley, we use a π-rotation of this Hamiltonian.

The miniband spectrum is calculated by zone folding (*32*), i.e., by bringing the states in the K valley with momenta connected by the reciprocal lattice vectors of the moiré pattern to the first mBZ. The basis of *k*-states of the top and bottom layer are formed from the reciprocal lattice vectors $\Delta\mathbf{K}_0 + \mathrm{m}\mathbf{G}_1 + \mathrm{n}\mathbf{G}_2$ and $2\Delta\mathbf{K}_0 + \mathrm{m}\mathbf{G}_1 + \mathrm{n}\mathbf{G}_2$, respectively, where $\mathbf{G}_1 = \Delta\mathbf{K}_0 - \Delta\mathbf{K}_1$ and $\mathbf{G}_2 = \Delta\mathbf{K}_0 - \Delta\mathbf{K}_2$. The number of basis states is chosen to ensure convergence of the first three conduction and valence bands. The resulting Hamiltonian that contains the matrix elements between the basis states is diagonalised using a similar method to ref. (*33*).

Section 4. Numerical simulations of transverse magnetic focusing

To simulate TMF maps shown in Fig. 2 in the main text, we first calculate the band structures to extract the Fermi surfaces and then determine the cyclotron orbits in real space by rotating the Fermi surfaces by 90° and scaling by $\hbar/eB$ *(the scaling factor is obtained from the quasi-classical equations of motion (32)). Charge carriers propagate either clockwise or anticlockwise, depending on the sign of the effective charge. We assume specular boundary conditions, so that in a magnetic field the carriers travel along the edge of the sample following cyclotron (skipping) orbits and caustics of skipping orbits focus onto equidistant points. The drift direction of the skipping orbits depends on the effective charge of the carriers and the direction of the magnetic field.*

To achieve consistency with the experiment we select the states that are moving away from the injection point with energies between ε_f *and* ε_f+eV *(where* ε_f *is the Fermi energy and V the applied voltage). The group velocity is calculated from the band structure using* $v \propto \nabla_{\mathbf{k}}\mathbf{E}$*, i.e., it is related to the energy dispersion (for example, the velocity is smaller in flatter parts of the dispersion). Accordingly, as the applied voltage elevates the Fermi level, it results in extra states being occupied such that the available states are populated with a probability proportional to* $|\nabla_{\mathbf{k}}\mathbf{E}|^{-1}$ *and different injection angles should be weighted with a probability proportional to the density of states.*

The TMF spectra shown in Fig. 2B, E in the main text are calculated numerically by using a similar method to ref. (12). This is achieved by counting how many electrons enter contact 3 (Fig. 1C in the main text) having a finite width w*. The non-local resistance (*$(\mathrm{V}_3-\mathrm{V}_4)/\mathrm{I}_1$ *is then found by calculating* $(\mathrm{N}_3-\mathrm{N}_4)/\mathrm{N}_1$*, where* N_1 *is the total number of injected electrons,* N_3 *is the number of electrons entering contact 3 and* N_4 *is a smooth background given by* $\mathrm{N}_4=\sum_{\mathrm{i}}^{\mathrm{N}_1}\mathrm{w}/\mathrm{d}_{\mathrm{i}}$*. Here the subscripts correspond to the device contacts in Fig. 1C and* d_{i} *is the distance between consecutive skips along the edge of the* i^{th} *trajectory.*

To investigate whether the TMF spectra are sensitive to the crystallographic orientation of graphene layers with respect to the skipping direction (the edge of the sample), Fig. S4 compares TMF maps simulated for different edge orientations characterised by an angle Φ*. To this end, we* fix the orientation of one of the monolayers so that $\Phi=0°$ corresponds to the zig zag edge and $\Phi=90°$ to the armchair edge. The results for parameters of device D1 at $|n|$ = 6.6x10^{12} cm^{-2} give triangular skipping orbits with the distance between the focusing peaks along the sample boundary weakly dependent on Φ – see Fig. S4. Similar results are obtained for all carrier densities where the Fermi surfaces are anisotropic, i.e., for $|n|$ > 3x10^{12} cm^{-2} where the Fermi surface around the γ point has a pronounced triangular shape (see Fig. 2C in the main text). Corresponding TMF maps show focusing peaks at slightly shifted positions relative to each other. The 3-fold symmetry of the triangular Fermi surface means that the TMF maps should repeat after 60° as is indeed seen for Φ = 30° and 90° in Fig. S4, where the results are identical. At low carrier densities, near the main neutrality point, the Fermi surfaces are almost isotropic and the TMF maps are independent of Φ. The positions of vHSs are independent of Φ as well, in agreement with *ref. (12).*

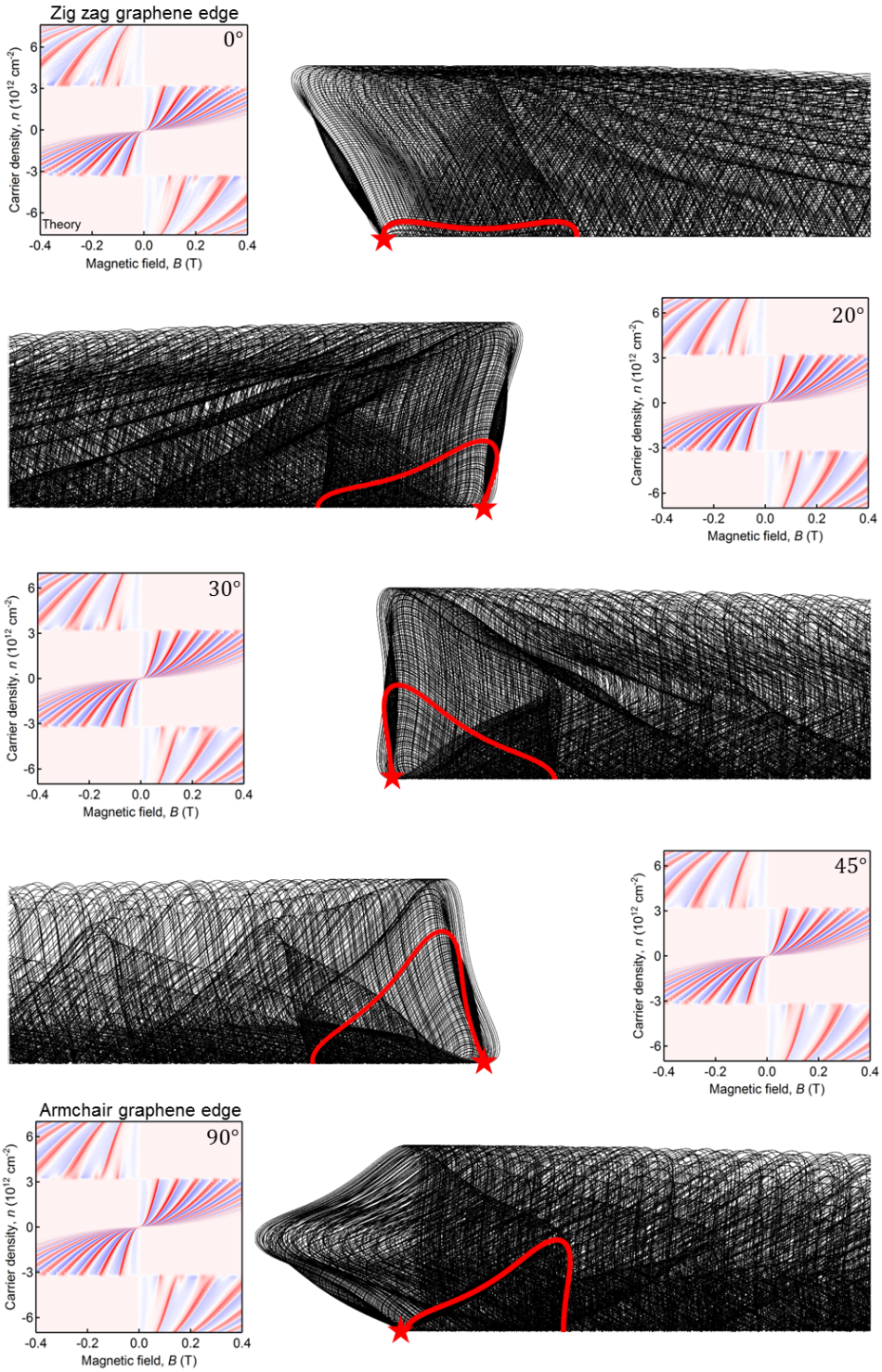

Fig. S4. TMF maps and simulated skipping orbits for different edge alignment. The TMF maps are simulated for $\Phi = \mathbf{0}°, \mathbf{20}°, \mathbf{30}°, \mathbf{45}°$ and $\mathbf{90}°$ for device D1. *T*he orientation of one of the monolayers is fixed such that $\mathbf{0}°$ corresponds to the zig zag edge and $\mathbf{90}°$ to the armchair edge. The skipping orbits are shown at $|n|$ = 6.6x10^{12} cm^{-2}.

Section 5. Electrostatic screening in a finite displacement field

The TMF map in Fig. 2E in the main text shows the effect of a finite displacement field between the two graphene monolayers. To find the effective electric field for each n in this figure, we need to take into account electrostatic screening. At twist angles ~2° and low carrier densities, the two monolayers are almost decoupled. To take into account electrostatic screening in this case, we include a screening term as proposed in ref. (*34, 35*):

$$\frac{ed}{\varepsilon_0 \varepsilon}\left(\varepsilon_0 D - \left(\frac{1+\varepsilon}{4}\right)(n_1 - n_2)e\right) = \frac{hv}{2\sqrt{\pi}}\left(s_1\sqrt{|n_1|} - s_2\sqrt{|n_2|}\right), \qquad \text{(S4)}$$

$$n = n_1 + n_2\,. \qquad \text{(S5)}$$

where n_1 and n_2 are carrier densities in the two parallel graphene layers separated by a distance d, D the applied displacement field, v the Dirac velocity, the band indices s_1 and s_2 are given by $s_i = n_i/|n_i|$, and the electron charge $e < 0$. In case of the TBG, we use $d \approx 0.34$ nm and following Refs. (*35*, *36, 37*), the dielectric constant for twisted bilayer $\varepsilon = 2.7$. The total carrier density n is given by Eq. (S5). To find the effective electric field for each value of n and D used in the experiment, the two equations are solved simultaneously using the Dirac velocity for monolayer graphene, v=10^6 m/s. In our calculations, we take n_1 to be the bottom layer and n_2 to be the top layer. The positive direction of D is from the top to the bottom (pointing downwards).

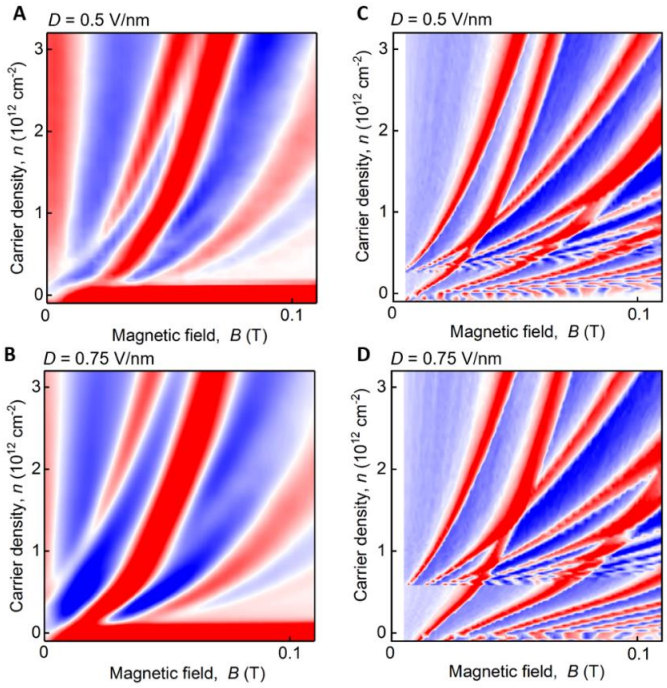

Fig. S5. Further examples of TMF in a displacement field. (**A**), R_f as a function of a magnetic field and carrier density measured for the device D2 at 2K at a distance 4.9 μm from the injector in a displacement field 0.5 V/nm. Colour scale: blue to red ±2.5 Ω. (**B**), R_f as a function of a magnetic field and carrier density measured for the device D2 at 5K at a distance 4.9 μm from the injector in a displacement field 0.75 V/nm. Colour scale: blue to red ±1.5 Ω. (**C**), TMF map calculated numerically for panel (A). (**D**), TMF map calculated numerically for panel (B).

Section 6. Temperature dependence of electron scattering length

Fig. 3B of the main text shows the temperature dependence of the relative scattering length L_S/L_{path} for the electrons near the main and secondary neutrality points, where L_S is the electron scattering length and L_{path} is the length of the trajectories extending from the injector to the first focal point. To extract the absolute scattering lengths we have calculated L_{path} such that the position of the first focal point coincides with the position of the voltage probe. For the electrons near the main neutrality point, $L_{path} \approx \pi \frac{L}{2}$, (see inset in Fig. 1a in the main text), where L is the distance from the current injector to the voltage probe, which is independent of the angle between the crystallographic axes orientation of graphene layers and the sample edge. Near the secondary neutrality point L_{path} is sensitive to the relative orientation of the graphene layers and the sample edge, as can be seen in Fig. S4. We have calculated L_{path} and extracted the corresponding scattering lengths for several characteristic angles between the device edge and zig zag axis of the top graphene layer: $L_{path\,0^\circ} = 1.11\,L$; $L_{path\,10^\circ} = 1.25\,L$; $L_{path\,20^\circ} = 1.58\,L$; $L_{path\,30^\circ} = 1.77\,L$; $L_{path\,45^\circ} = 1.93\,L$. Using these values we extracted the scattering lengths, presuming different crystallographic orientations and compare them in Fig. S6. This showed that in all cases scattering lengths vary between ~100 μm at low *T* and a few μm at *T* =30K, indicating the importance of electron-electron scattering at elevated *T* as discussed in the main text.

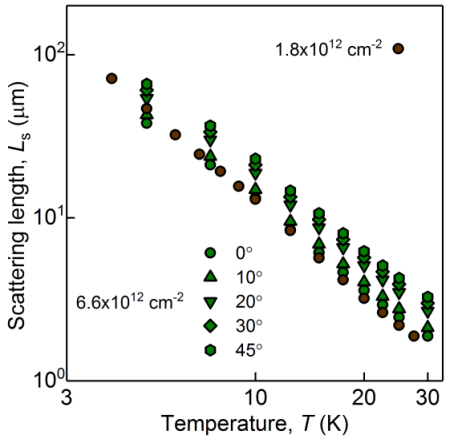

Fig. S6. Temperature dependence of electron scattering length. Electron scattering lengths corresponding to different relative orientations of the graphene's crystallographic axes and the sample edge were extracted from the temperature dependence of the first focusing peak in Fig. 3B of the main text using L_{path} calculated as described in Supplementary section 6.

REFERENCES AND NOTES

1. G. Li, A. Luican, J. M. B. Lopes dos Santos, A. H. Castro Neto, A. Reina, J. Kong, E. Y. Andrei, Observation of Van Hove singularities in twisted graphene layers. *Nat. Phys.* **6**, 109–113 (2010).

2. E. Suárez Morell, J. D. Correa, P. Vargas, M. Pacheco, Z. Barticevic, Flat bands in slightly twisted bilayer graphene: Tight-binding calculations. *Phys. Rev. B* **82**, 121407 (2010).

3. R. Bistritzer, A. H. MacDonald, Moiré bands in twisted double-layer graphene. *Proc. Natl. Acad. Sci. U.S.A.* **108**, 12233–12237 (2011).

4. Y. Cao, J. Y. Luo, V. Fatemi, S. Fang, J. D. Sanchez-Yamagishi, K. Watanabe, T. Taniguchi, E. Kaxiras, P. Jarillo-Herrero, Superlattice-induced insulating states and valley-protected orbits in twisted bilayer graphene. *Phys. Rev. Lett.* **117**, 116804 (2016).

5. K. Kim, A. Da Silva, S. Huang, B. Fallahazad, S. Larentis, T. Taniguchi, K. Watanabe, B. J. Le Roy, A. H. MacDonald, E. Tutuc, Tunable moiré bands and strong correlations in small-twist-angle bilayer graphene. *Proc. Natl. Acad. Sci. U.S.A.* **114**, 3364–3369 (2017).

6. Y. Cao, V. Fatemi, A. Demir, S. Fang, S. L. Tomarken, J. Y. Luo, J. D. Sanchez-Yamagishi, K. Watanabe, T. Taniguchi, E. Kaxiras, R. C. Ashoori, P. Jarillo-Herrero, Correlated insulator behaviour at half-filling in magic-angle graphene superlattices. *Nature* **556**, 80–84 (2018).

7. Y. Cao, V. Fatemi, S. Fang, K. Watanabe, T. Taniguchi, E. Kaxiras, P. Jarillo-Herrero, Unconventional superconductivity in magic-angle graphene superlattices. *Nature* **556**, 43–50 (2018).

8. M. Yankowitz, S. Chen, H. Polshyn, Y. Zhang, K. Watanabe, T. Taniguchi, D. Graf, A. F. Young, C. R. Dean, Tuning superconductivity in twisted bilayer graphene. *Science* **363**, 1059–1064 (2019).

9. M. Yankowitz, J. Xue, D. Cormode, J. D. Sanchez-Yamagishi, K. Watanabe, T. Taniguchi, P. Jarillo-Herrero, P. Jacquod, B. J. Le Roy, Emergence of superlattice Dirac points in graphene on hexagonal boron nitride. *Nat. Phys.* **8**, 382–386 (2012).

10. L. A. Ponomarenko, R. V. Gorbachev, G. L. Yu, D. C. Elias, R. Jalil, A. A. Patel, A. Mishchenko, A. S. Mayorov, C. R. Woods, J. R. Wallbank, M. Mucha-Kruczynski, B. A. Piot, M. Potemski, I. V. Grigorieva, K. S. Novoselov, F. Guinea, V. I. Fal'ko, A. K. Geim, Cloning of Dirac fermions in graphene superlattices. *Nature* **497**, 594–597 (2013).

11. C. R. Dean, L. Wang, P. Maher, C. Forsythe, F. Ghahari, Y. Gao, J. Katoch, M. Ishigami, P. Moon, M. Koshino, T. Taniguchi, K. Watanabe, K. L. Shepard, J. Hone, P. Kim, Hofstadter's butterfly and the fractal quantum Hall effect in moiré superlattices. *Nature* **497**, 598–602 (2013).

12. M. Lee, J. R. Wallbank, P. Gallagher, K. Watanabe, T. Taniguchi, V. I. Fal'ko, D. Goldhaber-Gordon, Ballistic miniband conduction in a graphene superlattice. *Science* **353**, 1526–1529 (2016).

13. R. Krishna Kumar, X. Chen, G. H. Auton, A. Mishchenko, D. A. Bandurin, S. V. Morozov, Y. Cao, E. Khestanova, M. B. Shalom, A. V. Kretinin, K. S. Novoselov, L. Eaves, I. V. Grigorieva, L. A.

Ponomarenko, V. I. Fal'ko, A. K. Geim, High-temperature quantum oscillations caused by recurring Bloch states in graphene superlattices. *Science* **357**, 181–184 (2017).

14. R. Krishna Kumar, A. Mishchenko, X. Chen, S. Pezzini, G. H. Auton, L. A. Ponomarenko, U. Zeitler, L. Eaves, V. I. Fal'ko, A. K. Geim, High-order fractal states in graphene superlattices. *Proc. Natl. Acad. Sci. U.S.A.* **115**, 5135–5139 (2018).

15. K. L. Seyler, P. Rivera, H. Yu, N. P. Wilson, E. L. Ray, D. G. Mandrus, J. Yan, W. Yao, X. Xu, Signatures of moiré-trapped valley excitons in $MoSe_2/WSe_2$ heterobilayers. *Nature* **567**, 66–70 (2019).

16. K. Tran, G. Moody, F. Wu, X. Lu, J. Choi, K. Kim, A. Rai, D. A. Sanchez, J. Quan, A. Singh, J. Embley, A. Zepeda, M. Campbell, T. Autry, T. Taniguchi, K. Watanabe, N. Lu, S. K. Banerjee, K. L. Silverman, S. Kim, E. Tutuc, L. Yang, A. H. MacDonald, X. Li, Evidence for moiré excitons in van der Waals heterostructures. *Nature* **567**, 71–75 (2019).

17. C. Jin, E. C. Regan, A. Yan, M. Iqbal Bakti Utama, D. Wang, S. Zhao, Y. Qin, S. Yang, Z. Zheng, S. Shi, K. Watanabe, T. Taniguchi, S. Tongay, A. Zettl, F. Wang, Observation of moiré excitons in WSe_2/WS_2 heterostructure superlattices. *Nature* **567**, 76–80 (2019).

18. E. M. Alexeev, D. A. Ruiz-Tijerina, M. Danovich, M. J. Hamer, D. J. Terry, P. K. Nayak, S. Ahn, S. Pak, J. Lee, J. I. Sohn, M. R. Molas, M. Koperski, K. Watanabe, T. Taniguchi, K. S. Novoselov, R. V. Gorbachev, H. S. Shin, V. I. Fal'ko, A. I. Tartakovskii, Resonantly hybridized excitons in moiré superlattices in van der Waals heterostructures. *Nature* **567**, 81–86 (2019).

19. V. S. Tsoi, Focusing of electrons in a metal by a transverse magnetic field. *JETP Lett.* **19**, 70–71 (1974).

20. V. S. Tsoi, Determination of the dimensions of nonextremal Fermi-surface sections by transverse focusing of electrons. *JETP Lett.* **22**, 197–198 (1975).

21. C. W. J. Beenakker, J. G. Williamson, M. E. I. Broekaart, P. H. M. van Loosdrecht, B. J. van Wees, J. E. Mooij, C. T. Foxon, J. J. Harris, Coherent electron focusing with quantum point contacts in a two-dimensional electron gas. *Phys. Rev. B* **39**, 8556–8575 (1989).

22. J. J. Heremans, M. B. Santos, M. Shayegan, Observation of magnetic focusing in two-dimensional hole systems. *Appl. Phys. Lett.* **61**, 1652–1654 (1992).

23. T. Taychatanapat, K. Watanabe, T. Taniguchi, P. Jarillo-Herrero, Electrically tunable transverse magnetic focusing in graphene. *Nat. Phys.* **9**, 225–229 (2013).

24. A. V. Kretinin, Y. Cao, J. S. Tu, G. L. Yu, R. Jalil, K. S. Novoselov, S. J. Haigh, A. Gholinia, A. Mishchenko, M. Lozada, T. Georgiou, C. R. Woods, F. Withers, P. Blake, G. Eda, A. Wirsig, C. Hucho, K. Watanabe, T. Taniguchi, A. K. Geim, R. V. Gorbachev, Electronic properties of graphene encapsulated with different two-dimensional atomic crystals. *Nano Lett.* **14**, 3270–3276 (2014).

25. I. Meric, P. Y. Huang, Q. Gao, Y. Gao, H. Tran, T. Taniguchi, K. Watanabe, L. M. Campos, D. A. Muller, J. Guo, P. Kim, J. Hone, K. L. Shepard, C. R. Dean, One-dimensional electrical contact to a two-dimensional material. *Science* **342**, 614–617 (2013).

26. K. Kim, M. Yankowitz, B. Fallahazad, S. Kang, H. C. Movva, S. Huang, S. Larentis, C. M. Corbet, T. Taniguchi, K. Watanabe, S. K. Banerjee, B. J. Le Roy, E. Tutuc, van der Waals heterostructures with high accuracy rotational alignment. *Nano Lett.* **16**, 1989–1995 (2016).

27. E. H. Hwang, S. Das Sarma, Acoustic phonon scattering limited carrier mobility in two-dimensional extrinsic graphene. *Phys. Rev. B* **77**, 115449 (2008).

28. L. Esaki, L. L. Chang, New transport phenomenon in a semiconductor "superlattice". *Phys. Rev. Lett.* **33**, 495–498 (1974).

29. K. Leo, P. H. Bolivar, F. Brüggemann, R. Schwedler, K. Köhler, Observation of Bloch oscillations in a semiconductor superlattice. *Solid State Commun.* **84**, 943–946 (1992).

30. C. Waschke, H. G. Roskos, R. Schwedler, K. Leo, H. Kurz, K. Köhler, Coherent submillimeter-wave emission from Bloch oscillations in a semiconductor superlattice. *Phys. Rev. Lett.* **70**, 3319–3322 (1993).

31. P. Rickhaus, J. Wallbank, S. Slizovskiy, R. Pisoni, H. Overweg, Y. Lee, M. Eich, M. H. Liu, K. Watanabe, T. Taniguchi, T. Ihn, K. Ensslin, Transport through a network of topological channels in twisted bilayer graphene. *Nano Lett.* **18**, 6725–6730 (2018).

32. N. W. Ashcroft, N. D. Mermin, *Solid State Physics* (Saunders College, 1976).

33. J. R. Wallbank, A. A. Patel, M. Mucha-Kruczynski, A. K. Geim, V. I. Fal'ko, Generic miniband structure of graphene on a hexagonal substrate. *Phys. Rev. B* **87**, 245408 (2013).

34. H. Schmidt, T. Lüdtke, P. Barthold, E. M. Cann, V. I. Fal'ko, R. J. Haug, Tunable graphene system with two decoupled monolayers. *Appl. Phys. Lett.* **93**, 172108 (2008).

35. S. Slizovskiy, A. Garcia-Ruiz, N. Drummond, V. I. Fal'ko, Dielectric susceptibility of graphene describing its out-of-plane polarizability. arXiv:1912.10067 [cond-mat.mes-hall] (20 December 2019).

36. J. D. Sanchez-Yamagishi, T. Taychatanapat, K. Watanabe, T. Taniguchi, A. Yacoby, P. Jarillo-Herrero, Quantum Hall effect, screening, and layer-polarized insulating states in twisted bilayer graphene. *Phys. Rev. Lett.* **108**, 076601 (2012).

37. B. Fallahazad, Y. Hao, K. Lee, S. Kim, R. S. Ruoff, E. Tutuc, Quantum Hall effect in Bernal stacked and twisted bilayer graphene grown on Cu by chemical vapor deposition. *Phys. Rev. B* **85**, 201408 (2012).

Chapter 7

Conclusion

This thesis presents a complete description of the electric field-dependent intersubband optical transitions in multilayer InSe, its tunable spin-orbit coupling strength with an applied electric field and the excitonic properties derived from the Mexican hat dispersion in its valence band. Furthermore, we also explored the possibility of filtering valley currents in twisted bilayer graphene.

The intersubband optical absorption peaks in multilayer InSe indicated that the energy difference between the quantum-confined energy levels ranged in the infrared and far-infrared part of the optical spectrum. The electric field was found to be a crucial ingredient to understand the optical properties of the confined electrons as it shifts the resonant frequencies towards higher energies and enhances the magnitude of the absorption peaks. This is due to an increase in the effective mass of the lowest conduction subband and an enhancement of the intersubband oscillator strength. Using a quantum well model, a mathematical description of this phenomena was reached and exact calculations on the effect of an applied displacement on the intersubband energies were performed.

As far as the spintronic properties of multilayer InSe was concerned, the application of a perpendicularly applied electric field was found to enhance or suppress the electron's SOC strength depending on the direction of the electric field relative to the crystal stacking. This makes InSe an excellent platform for new spintronic devices as it was demonstrated that its SOC strength in the conduction band could be tuned up to exactly 0meVÅ. Three main mechanisms were found to affect the conduction band SOC, firstly the intrinsic $z \to -z$ and inversion asymmetry of the crystal, then the wavefunction's $z \to -z$ asymmetry due to an applied electrostatic potential, and finally the intralayer dipole moments which mix bands of opposite z-parity. The extracted SOC strengths

were compared with weak antilocalization measurements and the perturbative calculation was found to slightly overestimate the magnitude of the SOC strength.

Excitons in multilayer InSe were studied projecting the exciton Hamiltonian in the harmonic oscillator basis. The excitonic properties of multilayer InSe were calculated using a hybrid $\mathbf{k} \cdot \mathbf{p}$ tight-binding Hamiltonian around the Γ-point. Using the quantum harmonic oscillator basis, it was found that in the process of decreasing the number of layers from the bulk to the monolayer limit, excitons transitioned from direct to indirect. The harmonic oscillator projection method was used to calculate binding energies in suspended MoS_2 and the obtained results were compared with exact solutions previously obtained with finite element methods. A very good agreement between the two was reached demonstrating the validity of the numerical method proposed. Using a Fourier expansion of the electron and hole dispersion, the exciton binding energy was calculated in monolayer InSe, demonstrating the potential of this method to extract the entire exciton band structure.

Transverse magnetic focusing experiments were performed in twisted bilayer graphene. It was clearly shown how a perpendicularly applied displacement field could filter currents from the two different valleys due to an asymmetric shift in energy at the $\mathbf{K}$ and $\mathbf{K}'$ points. Theoretical calculations using a continuum-model Hamiltonian demonstrated very good agreement between theory and experiment.

Future work on InSe could include studying the effect in the SOC strength of different interfaces other than hBN. This could be useful in order to quantify the effect that interfacial electric fields have on the spin-split bands. From the optics side, one could try to generalise the proposed method to study more complex situations like excitons trapped in impurity potentials or other bound states like trions or biexcitons.

Appendix A

A.1 Self-consistent analysis of bilayer InSe

To obtain a self-consistent expression for bilayer InSe in a similar fashion to bilayer graphene[73, 74, 75, 76, 77], we will apply the Löwdin partitioning method (see Section.4.2 for a more detailed explanation) together with elementary electrostatics. We start with the usual 4×4 hybrid $\mathbf{k}\cdot\mathbf{p}$ tight-binding Hamiltonian matrix of bilayer InSe which, as shown in Eq. (2.23) looks like

$$\hat{H}_{k.p} = \begin{pmatrix} \frac{E_g}{2} + \frac{\hbar^2k^2}{2m} + \frac{\Delta}{2} & t_{cc} & 0 & t_{cv} \\ t_{cc} & \frac{E_g}{2} + \frac{\hbar^2k^2}{2m} - \frac{\Delta}{2} & -t_{cv} & 0 \\ 0 & -t_{cv} & -\frac{E_g}{2} + \gamma_2k^2 + \gamma_4k^4 + \frac{\Delta}{2} & t_{vv} \\ t_{cv} & 0 & t_{vv} & -\frac{E_g}{2} + \gamma_2k^2 + \gamma_4k^4 - \frac{\Delta}{2} \end{pmatrix}. \tag{A.1}$$

For convenience, we simplified the notation as done in Eq. (2.23), where the $t_{cc} \equiv t_c + t_{cc_2}k^2$, $t_{vv} \equiv t_v + t_{vv_2}k^2$ and $t_{cv} \equiv t_{c,v} + t_{cv_2}k^2$. The terms $\pm\frac{\Delta}{2}$ account for the electrostatic energy difference between the two InSe layers in the bilayer. We use Löwdin partitioning up to second order in order to project the t_{cv} hopping into the two blocs corresponding to the two conduction and two valence band states. This results in two 2×2 Hamiltonians for the conduction and valence bands respectively, each one of the form

$$\hat{H}_c = \begin{pmatrix} \frac{E_g}{2} + \frac{\hbar^2k^2}{2m} + \frac{t_{cv}^2}{E_c - E_v} + \frac{\Delta}{2} & t_{cc} \\ t_{cc} & \frac{E_g}{2} + \frac{\hbar^2k^2}{2m} + \frac{t_{cv}^2}{E_c - E_v} - \frac{\Delta}{2} \end{pmatrix}, \tag{A.2}$$

and

$$\hat{H}_v = \begin{pmatrix} -\frac{E_g}{2} + \gamma_2 k^2 + \gamma_4 k^4 - \frac{t_{cv}^2}{E_c - E_v} + \frac{\Delta}{2} & t_{vv} \\ t_{vv} & -\frac{E_g}{2} + \gamma_2 k^2 + \gamma_4 k^4 - \frac{t_{cv}^2}{E_c - E_v} - \frac{\Delta}{2} \end{pmatrix}. \tag{A.3}$$

In these two Hamiltonians, the electrostatic energy difference between the two InSe layers, Δ, is assumed to be negligibly small in comparison to the monolayer InSe band gap (around 2.8eV). The eigenenergies of Eq. (A.2) and Eq. (A.3) result in the following two expressions:

$$\varepsilon_{\pm c} = \frac{E_g}{2} + \frac{\hbar^2 k^2}{2m} + \frac{t_{cv}^2}{E_c - E_v} \pm \sqrt{t_{cc}^2 + \frac{\Delta^2}{4}} \quad , \tag{A.4}$$

and

$$\varepsilon_{\pm v} = -\frac{E_g}{2} + \gamma_2 k^2 + \gamma_4 k^4 - \frac{t_{cv}^2}{E_c - E_v} \pm \sqrt{t_{vv}^2 + \frac{\Delta^2}{4}} \quad . \tag{A.5}$$

The probability amplitudes in layer 1 and 2 for the lowest conduction subband eigenvectors can be obtained from Eq. (A.2) to be

$$|\Psi_{c1}|^2 = \frac{\left(\Delta - \sqrt{4t_{cc}^2 + \Delta^2}\right)^2}{4t_{cc}^2 + \left(\Delta - \sqrt{4t_{cc}^2 + \Delta^2}\right)^2}. \quad \text{and} \quad |\Psi_{c2}|^2 = \frac{4t_{cc}^2}{4t_{cc}^2 + \left(\Delta - \sqrt{4t_{cc}^2 + \Delta^2}\right)^2}. \tag{A.6}$$

For the valence band, its topmost valence subband probability amplitudes follow from Eq. (A.3) as

$$|\Psi_{v1}|^2 = \frac{\left(\Delta + \sqrt{4t_{vv}^2 + \Delta^2}\right)^2}{4t_{vv}^2 + \left(\Delta + \sqrt{4t_{vv}^2 + \Delta^2}\right)^2} \quad \text{and} \quad |\Psi_{v2}|^2 = \frac{4t_{vv}^2}{4t_{vv}^2 + \left(\Delta + \sqrt{4t_{vv}^2 + \Delta^2}\right)^2}. \tag{A.7}$$

The self-consistent calculation then proceeds calculating the carrier density in the conduction band for each layer

$$n_1 = \frac{1}{\pi}\int_0^{p_F} dpp \frac{\left(\Delta - \sqrt{4t_{cc}^2 + \Delta^2}\right)^2}{4t_{cc}^2 + \left(\Delta - \sqrt{4t_{cc}^2 + \Delta^2}\right)^2}, \tag{A.8}$$

and

$$n_2 = \frac{1}{\pi}\int_0^{p_F} dpp \frac{4t_{cc}^2}{4t_{cc}^2 + \left(\Delta - \sqrt{4t_{cc}^2 + \Delta^2}\right)^2}, \tag{A.9}$$

where n_1 and n_2 label the carrier density in layer 1 and 2 such that $n = n_1 + n_2$. On purely electrostatic grounds, for a single-gated geometry we get

$$\Delta = \frac{e^2 n_2 L^2}{C_b} = \frac{e^2 (n - n_1) L^2}{C_b}, \tag{A.10}$$

where C_b is the capacitance of the InSe bilayer of area L^2. In the presence of a back gate, the above formula becomes

$$\Delta = \frac{e^2 (n_2 + n_{back}) L^2}{C_b}. \tag{A.11}$$

Finally we put everything in terms of the total carrier density, which relates to the Fermi wavevector as $n \equiv \frac{p_F^2}{2\pi}$. For the valence band, the analysis is identical, but one has to be slightly more careful about the range of the momentum integration due to the Mexican hat dispersion. As we need to calculate n_2, the first

approximation consist in assuming $\frac{\Delta}{2} << t_{cc}$ and we therefore get

$$n_1 = \frac{2}{(2\pi)^2}\int_0^{p_F} 2\pi dpp \frac{\left(\Delta - \sqrt{4t_{cc}^2+\Delta^2}\right)^2}{4t_{cc}^2 + \left(\Delta - \sqrt{4t_{cc}^2+\Delta^2}\right)^2} = \frac{1}{\pi}\int_0^{p_F} pdp \frac{\left(\Delta - 2t_{cc}\right)^2}{4t_{cc}^2 + \left(\Delta - 2t_{cc}\right)^2} \tag{A.12}$$

$$= \frac{1}{\pi}\int_{t_c}^{t_c+t_{cc2}p_F^2} \frac{dq}{2t_{cc2}} \frac{\left(2q+\Delta'\right)^2}{4q^2 + \left(\Delta' + 2q\right)^2} = \frac{1}{2\pi t_{cc2}}\left(\frac{q}{2} - \frac{\Delta}{8}\ln\left(8q^2 - 4q\Delta + \Delta^2\right)\right)\Bigg]_{t_c}^{t_c+t_{cc2}p_F^2}$$

where $\sqrt{2\pi n} = p_F$ and $\Delta' = -\Delta$. We therefore obtain

$$n_1 = \frac{1}{2\pi t_{cc2}}\left(\frac{t_{cc2}p_F^2}{2} - \frac{\Delta}{8}\ln\left(\frac{8(t_c + t_{cc2}p_F^2)^2 - 4(t_c + t_{cc2}p_F^2)\Delta + \Delta^2}{8t_c^2 - 4t_c\Delta + \Delta^2}\right)\right), \tag{A.13}$$

which is related to Δ through Eq. (A.10), resulting in a self-consistent analytical expression for the electrostatic energy difference in bilayer InSe.

Appendix B

B.1 Localization corrections to conductivity

Localization corrections to conductivity arise due to the self-interference effects between two counter-propagating paths along a closed-loop (see Fig.B.1). Such loop corrections can be diagrammatically represented in the recursive diagram shown in Fig.B.1(a), where the interaction potential between the two counter-propagating electrons (shown in dashed) is an impurity scattering event, and the two counter-propagating solid lines label the two electron propagators. In considering the spin relaxation due to spin-flipping events such as scattering with magnetic impurities or any interband spin-orbit coupling mediated scattering event, a sufficiently short spin relaxation time could alter the coherence between the two counter-propagating electrons and suppress constructive interference. Similarly, the Peierls phase acquired due to an externally applied magnetic field would as well contribute to decohere the counter-propagating electrons, reducing the constructive interference corrections to conductance.

Such contributions can be considered through a two-particle correlator known as the Cooperon and defined as the Green's function of the diffusion equation in the presence of all possible relaxation mechanisms[82]

$$\left[D\left(i\vec{\bigtriangledown}+\frac{2e\mathbf{A}}{c\hbar}\right)^2+\Gamma_j+\tau_\phi^{-1}\right]C_j(\mathbf{r},\mathbf{r}')=\delta(\mathbf{r}-\mathbf{r}'). \tag{B.1}$$

In the above equation, D is defined as the diffusion coefficient, Γ_j is the relaxation rate of the j^{th} component of the Cooperon and $\mathbf{A}$ is the magnetic vector potential. The Cooperon $C_j(\mathbf{r},\mathbf{r}')$ is a four-dimensional vector with C_0 being the spin singlet state formed by the two particles and $C_{1,2,3}$ the three spin triplet states. The

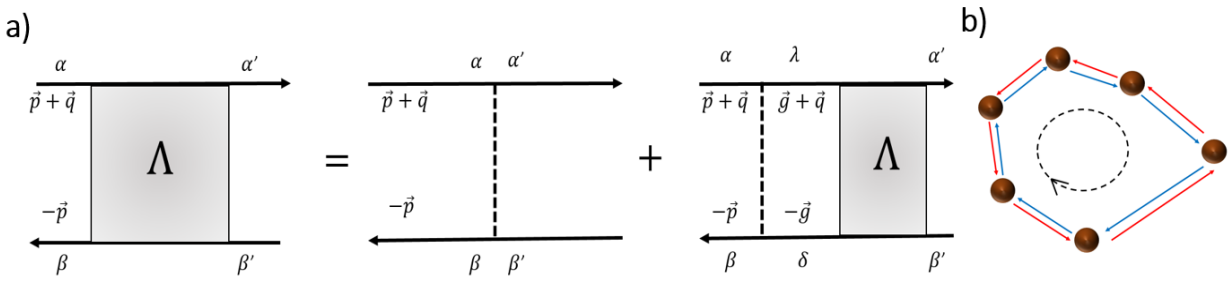

Figure B.1: (Left) Maximally crossed diagram (Λ) for the impurity-loop corrections of conductivity inspired from Ref.[78, 79, 80, 81]. The greek letters label the spin sate of the two particles before and after the impurity scattering processes. (Right) Real space scattering process giving rise to the loop corrections to conductivity. The blue line labels the trajectory of the electron while the red line labels the trajectory of the counter-propagating particle.

two-particle correlator can then be related to the conductivity corrections through

$$\delta\sigma = \frac{e^2 D}{\pi\hbar}\sum_{j=0,x,y,z} c_j C_j(\mathbf{r}=\mathbf{r}') = \frac{-e^2 D}{\pi\hbar}\sum_{j=x,y,z}\int_0^{(\tau D)^{-1/2}} (C_j(q)-C_0(q))\frac{qdq}{2\pi}, \tag{B.2}$$

where τ is the momentum relaxation time and $c_j = 1$ or -1 if $j = 0$ or $j = x, y, z$. In Fourier transforming Eq. (B.1), it is easy to obtain

$$\begin{pmatrix} \Pi & 0 & 0 & 0 \\ 0 & \Pi+\tau_{so}^{-1} & 0 & 0 \\ 0 & 0 & \Pi+\tau_{so}^{-1} & 0 \\ 0 & 0 & 0 & \Pi+\tau_{so}^{-1} \end{pmatrix} \vec{\mathbf{C}} = \vec{\mathbf{1}},$$

where $\Pi \equiv D(i\vec{\bigtriangledown} + 2e\mathbf{A}/c\hbar)^2 + \tau_\phi^{-1}$, τ_{SO} is the spin relaxation time and $\vec{1} \equiv [1,1,1,1]^T$. Isolating the four-vector $\vec{\mathbf{C}}$ and using Eq. (B.2), the following expression for the corrections to magnetoconductance is obtained[83]

$$\Delta\sigma(B) - \Delta\sigma(0) = \frac{e^2}{2\pi h}\left(\frac{1}{2}\Psi\left(\frac{1}{2}+\frac{H_\phi}{B}+\frac{2H_{SO}}{B}\right) - \frac{1}{2}\ln\left(\frac{H_\phi+2H_{SO}}{B}\right)\right. \tag{B.3}$$
$$\left. + \Psi\left(\frac{1}{2}+\frac{H_\phi}{B}+\frac{H_{SO}}{B}\right) - \ln\left(\frac{H_\phi}{B}+\frac{H_{SO}}{B}\right) - \frac{1}{2}\Psi\left(\frac{1}{2}+\frac{H_\phi}{B}\right) + \frac{1}{2}\ln\left(\frac{H_\phi}{B}\right)\right),$$

where $H_{SO} \equiv \frac{c\hbar}{4eD\tau_{so}}$ and $H_{\phi} \equiv \frac{c\hbar}{4eD\tau_{\phi}}$. To correctly account for the backscattering corrections to conductivity, it is crucial to know exactly the dominant spin relaxation mechanism.

In inversion symmetric systems, the spin relaxation is known to be dominated by the presence of magnetic impurities and by momentum scattering events which, in conjunction with the electron's spin-orbit coupling could flip the particle's spin. Therefore, a direct proportionality between the momentum and the spin relaxation time is expected ($\tau_{SO} \propto \tau$)[84]. In non-centrosymmetric systems, the spin relaxation mechanism is expected to come from the spin precession of the electron due to an effective momentum-dependent magnetic field (Dyakonov-Perel spin relaxation mechanism)[85]. Therefore, spin relaxation is expected to occur in the flying time between successive scattering events implying an inverse proportionality between the momentum and the spin relaxation time. Furthermore, as demonstrated in Ref.[85], if such spin relaxation mechanism is dominant, the in-plane spin relaxation time is identically twice as long as the out-of-plane spin relaxation time $\left(\frac{1}{\tau_{s_{xx}}} = \frac{1}{\tau_{s_{yy}}} = \frac{1}{2\tau_{s_{zz}}}\right)$ for [001] quantum wells. In non-centrosymmetric systems, the electrons may acquire a net Berry phase when they undergo closed-loop corrections. This would therefore modify the phase difference between the counter-propagating particles and, by extension, the interference corrections to conductivity.

Depending on whether the electrons have a linear or cubic in momentum spin-splitting, the resulting corrections to conductivity can differ dramatically. This is due to the acquired Berry phase in the precession motion of the electron once it fully completes a 2π rotation. The corrections to magnetoconductance in this situation were first derived by Iordanskii, Larkin and Pitaevskii[80] for a two-dimensional particle. We start from the electron propagator including a general form of the SOC

$$G^{\pm}(k,\omega) = \frac{1}{\omega - E(k) - \vec{\sigma}\cdot\vec{\Omega} \pm \frac{i}{2\tau}}, \tag{B.4}$$

where $E(k)$ is the electron dispersion, $\vec{\sigma}\cdot\vec{\Omega}$ is the **k**-dependent SOC, τ is the momentum relaxation time and ω is the energy of the particle. The following expression was obtained for the Cooperon amplitude $C = C(q,\theta,k_F)$ when expanding it in Fourier harmonics of θ and including higher harmonics terms written in terms of C_0 (0^{th} harmonic):

$$\hat{L}C_0 = \frac{1}{2\pi\nu_0\tau_0}, \tag{B.5}$$

where ν_0 is the density of states in the two-dimensional system and the operator $\hat{L}$ is defined as

$$\hat{L} = \tau\Big(\frac{1}{\tau_\phi} + \frac{1}{2}v_F^2q^2\tau_1 + 2(\Omega_1^2\tau_1 + \Omega_3^2\tau_3)(1+\sigma_+\rho_- + \sigma_-\rho_+) - \tau_1 v_F\Omega_1[(\sigma_+ + \rho_+)q_+ \tag{B.6}$$

$$+ (\sigma_- + \rho_-)q_-]\Big).$$

In the above expression, σ is the spin index of the particle and ρ is the spin index of the counter-propagating particle such that $\sigma_\pm = \frac{1}{2}(\sigma_x \pm i\sigma_y)$ and $\rho_\pm = \frac{1}{2}(\rho_x \pm i\rho_y)$ while Ω_1 and Ω_3 are both the linear and cubic SOC spin splittings in Eq. (B.4). The $q_\pm$ terms are the momentum transfer terms shown in Fig.B.1 and defined as $q_\pm = q_x \pm iq_y$, while the terms τ_0, τ_1 and τ_3 are the different angular harmonics of the scattering probability per unit time at angle ϕ, $W(\phi)$. The terms τ_n are therefore defined as $\frac{1}{\tau_n} = \int W(\phi)(1-\cos(n\phi))d\phi$. Finally, the phase relaxation rate $1/\tau_\phi$ is introduced as an energy cutoff parameter for sufficiently small momentum transfer processes. The solutions of Eq. (B.5) of the Cooperon can be represented in the form[80]

$$C^{\alpha\gamma}_{\beta\delta}(q) = \frac{1}{2\pi\nu_0\tau_0}\sum_{\tau=1}^{\tau=4}\frac{1}{E_\tau}\Psi_{\tau q}(\alpha,\beta)\Psi^*_{\tau q}(\gamma,\delta), \tag{B.7}$$

where $\tau = 1$ stands for the spin singlet state and $\tau = 2,3,4$ for the three spin triplet states. The wavefunction $\Psi_{\tau q}$ and the energy E_τ are the eigenfunctions and eigenenergies of the operator $\hat{L}$ defined in Eq. (B.5). The indices α,β,γ and δ label the spin indices of the initial and final counter-propagating particles.

In the presence of a magnetic field B, the creation and annihilation operator identities used to solve the harmonic oscillator problem can be related to the momentum operator q such that $q_+ = \sqrt{2}Sa$ and $q_- = \sqrt{2}Sa^\dagger$ where $S^2 \equiv 2eB/c$. Such identities are then applied to obtain the Cooperon to solve Eq. (B.5). Projecting $\Psi_{\tau,q}$ in the harmonic oscillator basis and using[86]

$$\delta\sigma^{WL} = \frac{-2\pi e^2 \nu_0 \tau_0^2 D}{\pi} \int_0^{(\tau_1 D)^{-1/2}} \sum_{j=1}^{j=3} C_j - C_0(q) \frac{qdq}{2\pi}, \tag{B.8}$$

where the subindex j labels whether the Cooperon is in a singlet singlet (C_0) or in a triplet state ($C_{1,2,3}$) and D is the diffusion coefficient defined as $D = \frac{1}{2}v_F^2\tau_1$, the following expression for the magnetoconductance corrections to conductivity[87, 80] can be derived from Eq. (B.8)

$$\Delta\sigma(B) = \frac{-e^2}{4\pi^2\hbar}\left(\frac{1}{a_0} + \frac{2a_0 + 1 + (B_{SO}/B)}{a_1[a_0 + (B_{SO}/B)] - 2(B'_{SO}/B))} - \sum_{n=1}^{n=\infty}\left[\frac{3}{n} - \right. \right. \tag{B.9}$$
$$\left. \frac{3a_n^2 + 2a_n(B_{SO}/B) - 1 - 2(2n+1)(B'_{SO}/B)}{[a_n + (B_{SO}/B)]a_{n-1}a_{n+1} - 2(B'_{SO}/B)[(2n+1)a_n - 1]}\right] + 2\ln\left(\frac{B_{tr}}{B}\right)$$
$$\left. + \Psi\left(\frac{1}{2} + \frac{B_\phi}{B}\right) + 3C\right).$$

In the above expression, $B_{so} \equiv \frac{c\hbar}{4eD\tau_{so}}$ where $\frac{1}{\tau_{so}}$ is defined as $\frac{1}{\tau_{so}} \equiv 2(\Omega_1^2\tau_1 + \Omega_3^2\tau_3)$. The terms B'_{so}, B_ϕ, B_{tr} and a_n are defined as $B'_{so} \equiv \frac{c\hbar 2\Omega_1^2\tau_1}{4eD}$, $B_\phi \equiv \frac{c\hbar}{4eD\tau_\phi}$, $B_{tr} \equiv \frac{c\hbar}{4eD\tau}$ and $a_n \equiv n + \frac{1}{2} + \frac{B_\phi}{B} + \frac{B_{so}}{B}$. Finally, the constant C is the Euler-Mascheroni constant defined as $C \equiv 0.57721$ and Ψ the digamma function. In systems such as InSe where the cubic in momentum SOC is negligible, at sufficiently small wavevectors, the fitted parameter τ_{SO} can be directly related to the Rashba SOC strength α and to the precession frequency Ω_1 through $\alpha = \frac{\hbar^2}{2m_c\sqrt{D\tau_{so}}}$ and $\frac{1}{\tau_{so}} = 2\Omega_1^2\tau_1$. Finally it is relevant to point out that the above formalism was developed assuming $B_{tr} << B$ and $\Omega\tau << 1$, so that the accumulated Peierls phase is not strong enough to completely destroy the necessary coherence and that the spin precession frequency is much slower than the momentum scattering rate[88, 81].

Appendix C

C.1 Electron-hole interaction in 2D thin films

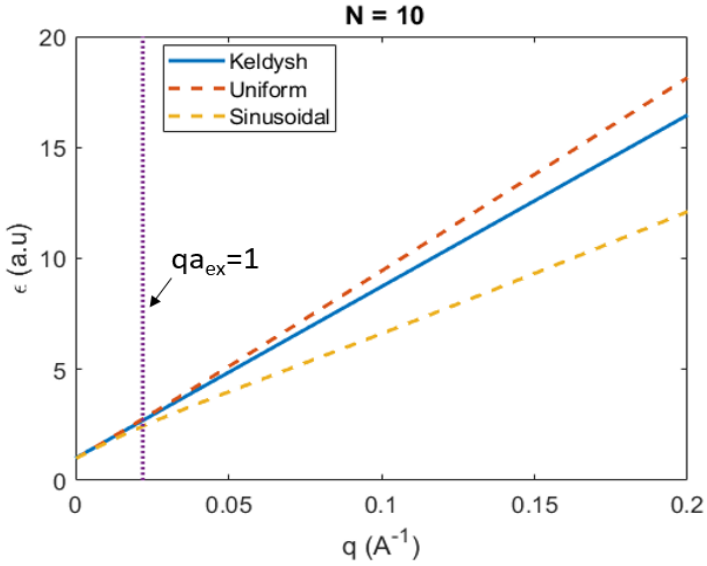

Figure C.1: Dielectric constants as a function of momentum transfer for the three different types of electrostatic potentials under consideration. For a general 2D electrostatic potential $V(q)$ the dielectric constant follows from $V(q) = \frac{2\pi e^2}{\sqrt{\epsilon_{||s}\epsilon_{zs}}q\epsilon_{2D}(q)}$.

To perform accurate calculations of the excitonic binding energies, it is necessary to account for the distribution along the z-direction of the electron and hole wavefunction, as they may enhance or suppress the electrostatic interaction between the two particles. Knowing the approximately sinusoidal distribution of the wavefunction along the z-direction of the InSe thin film, three different approximations were used to consider both the electron and hole wavefunction profile along the confinement direction. Firstly, electrons and holes were modelled with a uniform distribution and then a sinusoidal distribution was used to model the quantum-confined eigenstates. Finally, the usual Keldysh interaction which considers both the electrons and holes as point-like particles was employed (see

Table C.1 for a comparison between the exciton binding energies according to the three different approximations and Fig.C.1 for the dependence of the dielectric constant on the wavevector k according to each electrostatic model).

Distribution	$N=1$	$N=2$	$N=3$	$N=4$	$N=5$	$N=6$	$N=7$
Keldysh	195.4	119.0	90.4	74.2	63.9	56.2	50.7
Sinusoidal	202.3	124.9	95.8	79.2	68.6	60.6	55.1
Uniform	201.9	125.2	95.8	79.2	68.6	59.9	55.2

Table C.1: Binding energies in meV of different InSe few-layer systems according to the different form of the electrostatic interaction considered to account for the wavefunction profile along the confinement direction. The dielectric constants used for the InSe thin film were $\epsilon_{||}^{InSe}=9.9$ and $\epsilon_{z}^{InSe}=10.9$ and for the hBN substrate $\epsilon_{||}^{hBN}=6.8$ and $\epsilon_{z}^{hBN}=3.5$.

C.1.1 Keldysh interaction

In 2D materials, the dielectric tensor of the encapsulating environment (most often, hexagonal boron nitride) crucially reduces the electrostatic screening in the electron-hole coulombic[63] interaction therefore hugely increasing the binding energy of the exciton as well as its lifetime. While in the 2D hydrogen atom problem[89] the electrostatic interaction is the usual $1/r$ potential, a slightly more accurate potential is needed to account for the dielectric contrast between the substrate and the thin film[90, 91]. The electrostatic interaction for a thin film of thickness d and a point charge located at $z=z'$ inside the thin film, can be obtained from solving the Poisson equation (in cgs units) in the three different regions:

$$\left(\epsilon_{||hBN}\left(\frac{\partial^2}{\partial^2 x}+\frac{\partial^2}{\partial^2 y}\right)+\epsilon_{zhBN}\frac{\partial^2}{\partial^2 z}\right)\Phi_{h\uparrow}(\vec{r},z)=0, \tag{C.1}$$

$$\left(\epsilon_{||a}\left(\frac{\partial^2}{\partial^2 x}+\frac{\partial^2}{\partial^2 y}\right)+\epsilon_{za}\frac{\partial^2}{\partial^2 z}\right)\Phi_{a}(\vec{r},z)=-4\pi e\delta^{(3)}(z-z'), \quad \text{and}$$

$$\left(\epsilon_{||hBN}\left(\frac{\partial^2}{\partial^2 x}+\frac{\partial^2}{\partial^2 y}\right)+\epsilon_{zhBN}\frac{\partial^2}{\partial^2 z}\right)\Phi_{h\downarrow}(\vec{r},z)=0.$$

In the above expression, $h\uparrow$ and $h\downarrow$ label the hBN on top and on the bottom of the thin film, labelled with the subscript a. After adding the continuity equations for both the electrostatic potential and the electric field at $\pm d/2$, four boundary condition equations are obtained, and the electrostatics problem can be solved exactly. Upon performing an in-plane Fourier transform of $\Phi_a(\vec{r},z), \Phi_{h\uparrow}(\vec{r},z)$ and $\Phi_{h\downarrow}(\vec{r},z)$ (i.e. $\Phi_i(\vec{r},z) \rightarrow \phi_i(k,z)$) and isolating $\phi_a(k,z)$ we get the following electrostatic potential for the thin film when $z \geq z'$

$$V(k,z,z') = \frac{-4\pi e^2 \cosh\Big[k\Big(d/2-z\Big)+\eta\Big]\cosh\Big[k\Big(d/2+z'\Big)+\eta\Big]}{\sqrt{\epsilon_{||a}\epsilon_{za}}k\sinh\Big[kd+2\eta\Big]}, \text{ therefore} \tag{C.2}$$

$$V(k,0,0) \approx \frac{-2\pi e^2}{\sqrt{\epsilon_{||hBN}\epsilon_{zhBN}}k(1+r_0k)},$$

where $\eta \equiv \frac{1}{2}\ln\left(\frac{\sqrt{\epsilon_{||a}\epsilon_{za}}+\sqrt{\epsilon_{||hBN}\epsilon_{zhBN}}}{\sqrt{\epsilon_{||a}\epsilon_{za}}-\sqrt{\epsilon_{||hBN}\epsilon_{zhBN}}}\right)$ and $r_0 = \frac{\sqrt{\epsilon_{||a}\epsilon_{za}}d}{\sqrt{\epsilon_{||hBN}\epsilon_{zhBN}}}$. The last step in Eq. (C.2) required to consider the limit when the dielectric constant of the thin film is much larger than the substrate dielectric constant ($\sqrt{\epsilon_{||a}\epsilon_{za}} >> \sqrt{\epsilon_{||hBN}\epsilon_{zhBN}}$) and when the film thickness to tend to zero ($d \rightarrow 0$). Upon inverse Fourier transforming Eq. (C.2) to extract the dependence on real space coordinates, we get the following expression for the electrostatic interaction[63]

$$V(r) = \frac{-e^2\pi}{2\sqrt{\epsilon_{||hBN}\epsilon_{zhBN}}r_0}\left(H_0\Big(\frac{r}{r_0}\Big) - Y_0\Big(\frac{r}{r_0}\Big)\right). \tag{C.3}$$

In Eq. (C.3), $\epsilon \equiv \sqrt{\epsilon_{||a}\epsilon_{za}}$, $r_0 \equiv \frac{\sqrt{\epsilon_{||a}\epsilon_{za}}d}{2\sqrt{\epsilon_{||hBN}\epsilon_{zhBN}}}$ and H_0 and Y_0 are the zero-order Struve and Neumann special functions.

C.1.2 Electrostatic interaction between two uniform charge distributions

We aim at calculating the electrostatic energy between two uniform rods embedded in a substrate as a function of the in-plane wavevector k. This can

be done integrating over the entire electron and hole distribution a Keldysh-like interaction at each point of the two uniform rods assuming both of them have a uniform density ρ. We start considering $z \geq z'$ to calculate the total electrostatic potential, ignoring any prefactor in Eq. (C.2) included in the term ρ^2,

$$\phi(k) = \rho^2 \int_{-d/2}^{d/2} \int_{-d/2}^{z} \frac{\cosh\left(k(d/2 - z) + \eta\right) \cosh\left(k(d/2 + z') + \eta\right) dz dz'}{k \sinh\left(kd + 2\eta\right)}. \quad \text{(C.4)}$$

The first integral with respect to z' simplifies to

$$\int_{-d/2}^{z} \cosh\left(kz' + kd/2 + \eta\right) dz' = \frac{1}{k}\Bigg[\sinh\left(kz + kd/2 + \eta\right) - \sinh\left(\eta\right)\Bigg],$$

where

$$\eta = \frac{1}{2} \ln\left(\frac{\epsilon + \epsilon_1}{\epsilon - \epsilon_1}\right),$$

and $\epsilon = \sqrt{\epsilon_{||a}\epsilon_{za}}$, $\epsilon_1 = \sqrt{\epsilon_{||hBN}\epsilon_{zhBN}}$. We now integrate with respect to z, and the resulting expression will have two terms, which look like

$$\phi(k) \propto \frac{1}{k}\Bigg(\int_{-d/2}^{d/2} \cosh\left(k(d/2 - z) + \eta\right) \sinh\left(kz + kd/2 + \eta\right) dz \quad \text{(C.5)}$$
$$- \int_{-d/2}^{d/2} \cosh\left(k(d/2 - z) + \eta\right) \sinh\left(\eta\right) dz \Bigg).$$

For the second term, we obtain

$$\sinh\left(\eta\right) \int_{-d/2}^{d/2} \cosh\left(k(d/2 - z) + \eta\right) dz = \frac{1}{k} \sinh\left(\eta\right) \Bigg[\sinh\left(kd + \eta\right) - \sinh\left(\eta\right)\Bigg], \quad \text{(C.6)}$$

while for the first term we get

$$\int_{-d/2}^{d/2} \cosh\left(k(d/2-z)+\eta\right)\sinh\left(kz+kd/2+\eta\right)dz = \tag{C.7}$$
$$\int_{-d/2}^{d/2}(\cosh\left(a\right)\cosh\left(kz\right)-\sinh\left(a\right)\sinh\left(kz\right))\times(\sinh\left(a\right)\cosh\left(kz\right)+\cosh\left(a\right)\sinh\left(kz\right)) =$$
$$A\int_{-d/2}^{d/2}\cosh\left(kz\right)^2dz - A\int_{-d/2}^{d/2}\sinh\left(kz\right)^2dz = Ad,$$

where $a \equiv kd/2+\eta$ and $A \equiv \cosh\left(a\right)\sinh\left(a\right) = \sinh\left(2a\right)/2$. Putting all terms together, we therefore obtain the final result for the situation $z \geq z'$:

$$V_\epsilon(k) = \rho^2\left(\frac{-\sinh\left(\eta\right)\Big(\sinh\left(kd+\eta\right)-\sinh\left(\eta\right)\Big)}{k^3\sinh\left(kd+2\eta\right)}+\frac{d}{2k^2}\right). \tag{C.8}$$

We then have to add the situation when $z < z'$ which requires to swap z and z' in Eq. (C.4)

$$\phi(k) = \rho^2\int_{-d/2}^{d/2}\int_z^{d/2}\frac{\cosh\left(k(d/2+z)+\eta\right)\cosh\left(k(d/2-z')+\eta\right)dzdz'}{k\sinh\left(kd+2\eta\right)} \tag{C.9}$$
$$= \rho^2\left(\frac{-\sinh(kd+\eta)\sinh(\eta)+\sinh^2(\eta)}{k^3\sinh\left(kd+2\eta\right)}+\frac{d}{2k^2}\right).$$

The total result therefore yields to the following electrostatic interaction

$$V_\epsilon(k) = \rho^2\left(\frac{-2\sinh\left(\eta\right)\Big(\sinh\left(kd+\eta\right)-\sinh\left(\eta\right)\Big)}{k^3\sinh\left(kd+2\eta\right)}+\frac{d}{k^2}\right). \tag{C.10}$$

If we were to properly include the dielectric anisotropy, the result will be modified as follows:

$$V_\epsilon(k) = \rho^2\left(\frac{-2\sinh\left(\eta\right)\Big(\sinh\left(\tilde{k}d+\eta\right)-\sinh\left(\eta\right)\Big)}{\tilde{k}^3\sinh\left(\tilde{k}d+2\eta\right)}+\frac{d}{\tilde{k}^2}\right), \tag{C.11}$$

where $\tilde{k} = \sqrt{\frac{\epsilon_{a||}}{\epsilon_{za}}}k$, accounting for the dielectric anisotropy in the momentum variable.

C.1.3 Electrostatic interaction between two sinusoidal charge distributions

The distribution of the electrons and holes considered here has the form $P_e(z) = A\cos^2(\frac{\pi z}{d})$ and $P_h(z) = A\cos^2(\frac{\pi z'}{d})$. We therefore use the same integration procedure as used for the uniform distribution including all the prefactors in ρ,

$$V(k) = \rho^2 \int_{-d/2}^{d/2}\int_{-d/2}^{d/2} \frac{\cos^2(\frac{\pi z}{d})\cos^2(\frac{\pi z'}{d})\cosh(k(d/2-z)+\eta)\cosh(k(d/2+z')+\eta)dzdz'}{k\sinh(kd+2\eta)}. \tag{C.12}$$

This integral can be evaluated exactly by splitting the integral limits into two and repeatedly using the two identities

$$\int \cosh(ax+b)\sin(cx+d)dx = \frac{a}{a^2+c^2}\sinh(ax+b)\sin(cx+d) \tag{C.13}$$
$$-\frac{c}{a^2+c^2}\cosh(ax+b)\cos(cx+d)+C,$$
$$\int \cosh(ax+b)\cos(cx+d)dx = \frac{a}{a^2+c^2}\sinh(ax+b)\cos(cx+d)$$
$$+\frac{c}{a^2+c^2}\cosh(ax+b)\sin(cx+d)+C. \tag{C.14}$$

Using Wolfram Mathematica, the following electrostatic potential was derived from Eq. (C.12)

$$V(k) = \frac{\rho^2}{k}\left[\frac{-4\sinh^2(\tilde{k}d/2)\sinh^2(\eta)-\sinh(2\eta)\sinh(\tilde{k}d)}{(1+\frac{\tilde{k}^2d^2}{4\pi^2})\tilde{k}^2d^2\sinh(\tilde{k}d+2\eta)} + \frac{(1+\frac{3\tilde{k}^2d^2}{8\pi^2})}{(1+\frac{\tilde{k}^2d^2}{4\pi^2})\tilde{k}d}\right]. \tag{C.15}$$

C.2 Relevant integrals for the calculation of the full excitonic dispersion

In the tight-binding calculation, we expanded both the conduction and the valence band dispersion in a Fourier series such that:

$$\varepsilon_c(\mathbf{k}) - \varepsilon_v(\mathbf{k}-\mathbf{Q}) = \sum_{s=-\infty}^{s=\infty} (C_s - V_s e^{i2\pi \mathbf{s}\tilde{\mathbf{Q}}}) e^{-i2\pi \mathbf{s}\tilde{\mathbf{k}}}. \tag{C.16}$$

where $\tilde{Q} \equiv (Q_x/T_x, Q_y/T_y)$ and $\tilde{k} \equiv (k_x/T_x, k_y/T_y)$. T_x and T_y are defined as the periodicity in reciprocal space of the Fourier harmonics as described in Section.5.2. We then projected this term into the harmonic oscillator basis obtaining

$$H_{n_x,n_y;n'_x,n'_y}(\mathbf{Q}) = \int d^2k \sum_{s=-\infty}^{s=\infty} (C_s - V_s e^{i2\pi \mathbf{sQ}}) e^{-i2\pi \mathbf{sk}} \phi_{n_x}(k_x)\phi_{n_y}(k_y)\phi_{n'_x}(k_x)\phi_{n'_y}(k_y). \tag{C.17}$$

Firstly the x and y coordinates were separated such that each integral had the form

$$\int e^{-x^2} H_{n_x}(x) e^{iq_x x} H_{m_x}(x) dx = \int e^{-x^2 + iq_x x} H_{n_x}(x) H_{m_x}(x) dx \tag{C.18}$$

and then we used the following integral identity[92]

$$\int_{-\infty}^{\infty} e^{-(x-y)^2} H_m(x) H_n(x) dx = 2^n \sqrt{\pi} m! y^{n-m} L_m^{n-m}(-2y^2). \tag{C.19}$$

Performing a coordinate transformation of the form $x' = x - \frac{iq_x}{\sqrt{2}}$ the following result is obtained

$$\int e^{-x^2} H_n(x) e^{iq_x x} H_m(x) dx = 2^n \sqrt{\pi} m! \left(\frac{iq_x}{\sqrt{2}}\right)^{n-m} L_m^{n-m}\left(-2\left(\frac{iq_x}{\sqrt{2}}\right)^2\right) e^{-\frac{q_x^2}{4}}. \tag{C.20}$$

The final result for the dispersive term therefore had the form

$$H_{n_x,n_y;n'_x,n'_y}(\mathbf{Q}) = \sum_{s_x,s_y=-\infty}^{\infty} \Big[C_{\mathbf{s}} - V_{\mathbf{s}} \mathrm{e}^{i2\pi \mathbf{s}\cdot\bar{\mathbf{Q}}}\Big] \times \prod_{j}^{x,y} \frac{2^{\zeta_j - \frac{1}{2}(n_j+n'_j)} \zeta_j! (\bar{a}_j s_j)^{\Delta_j}}{i^{n'_j - n_j + \Delta_j} \sqrt{n_j! n'_j!}}$$
$$\mathrm{e}^{-\frac{1}{4}\bar{a}_j^2 s_j^2} L_{\zeta_j}^{\Delta_j}(\tfrac{1}{2}\bar{a}_j^2 s_j^2), \tag{C.21}$$

where $\Delta_j = |n'_j - n_j|$, $\zeta_j = min[n'_j, n_j]$ and $\tilde{a}_j = \frac{2\pi}{T_j \lambda}$. The Keldysh potential is then projected in the harmonic oscillator basis. Each matrix element therefore has the form

$$V_{n_x,n_y;n'_x,n'_y} = \int \frac{d^2k d^2q}{(2\pi)^2} V(q) \phi_{n_x}(k_x) \phi_{n_y}(k_y) \phi_{n'_x}(k_x + q_x) \phi_{n'_y}(k_y + q_y) = \tag{C.22}$$
$$\int \frac{q \mathrm{d}q}{(2\pi)^2} V(q) \mathrm{e}^{-\frac{1}{4}q^2\lambda^2} \prod_{j}^{x,y} \sum_{s_j=0}^{\min[m_j,n_j]} (\lambda q)^{\sigma_j} \binom{n_j}{s_j} \binom{m_j}{s_j} \frac{(-\frac{1}{2})^{\frac{1}{2}\sigma_j} s_j!}{\sqrt{m_j! n_j!}} 2\mathrm{B}(\tfrac{\sigma_x+1}{2}, \tfrac{\sigma_y+1}{2}).$$

Using the following Hermite polynomial identity for $H_n(x+y)$

$$H_n(x+y) = \sum_{s=0}^{s=n} \binom{n}{s} H_s(x) (2y)^{n-s} \tag{C.23}$$

we rewrite Eq. (C.22) in polar coordinates and remove the angular integral through the substitution $t = \cos(\theta)$, which results in a Beta function given the following identity

$$B(x,y) = \int_0^1 t^{x-1}(1-t)^{y-1} dt. \tag{C.24}$$

Finally, the radial integral was explicitly evaluated using Wolfram Mathematica as:

$$\int \frac{q \mathrm{d}q}{(2\pi)^2} \frac{-2\pi e^2}{\sqrt{\kappa_\parallel \kappa_z} q(1 + r^* q)} (\lambda q)^{\sigma_x + \sigma_y} \mathrm{e}^{-\frac{1}{4}q^2\lambda^2} = \frac{-e^2}{2\pi\sqrt{\kappa_\parallel \kappa_z}} \Big(- \frac{\lambda}{r_*} \Big)^{\sigma_x+\sigma_y} \Bigg\{ \frac{\mathrm{e}^{-\frac{\lambda^2}{4r_*^2}}}{2r_*/\lambda} \Big[\pi \mathrm{erf}(\tfrac{\lambda}{2r_*}) - \tag{C.25}$$
$$\mathrm{Ei}(\tfrac{\lambda^2}{4r_*^2}) \Big] - \sum_{j=0}^{\sigma_x+\sigma_y-1} \Gamma(\tfrac{j+1}{2}) (-\tfrac{2r_*}{\lambda})^j \Bigg\}.$$

C.3 Electron-hole interaction in van der Waals heterostructures

In Ref.[11], the electron-hole interaction for a general van der Waals heterostructure was calculated using the method of electrostatic transfer matrices (ETM). This method models the van der Waals heterostructure as a sequence of dielectric slabs each one with an in-plane and an out-of-plane dielectric constant. This method consists in rewriting the Poisson equation at each dielectric slab and to match both the electric field and electrostatic potential at each interface, turning a complex electrostatic problem into a system of matrix equations. For each dielectric slab, the Poisson equation (in SI units) reads as[11]

$$\epsilon_j^{\parallel}\nabla^2_{\rho,\theta}\Phi_j + \epsilon_j^{\perp}\frac{\partial^2\Phi_j}{\partial^2 z} = \delta(z-z_j)q_j. \tag{C.26}$$

where q_j is a point charge located at z_j and $\Phi_j(\rho,\theta,z)$ is the electrostatic potential at the j^{th} slab written in cylindrical coordinates. The solution at any layer n given a charge located in layer c is written as:

$$\Phi_n(\rho,z) = \frac{e}{4\pi\epsilon_c\epsilon_0}\int_0^\infty J_0(k\rho)[A_n(k)e^{kz} + B_n(k)e^{-kz} + e^{-k|z|}\delta_{n,c}]dk. \tag{C.27}$$

We will only look at the effect that a charge in layer c has on every other layer of the heterostructure. Its potential in its most general form would look like

$$V_{eh}^{n,c}(\rho) = \frac{e^2}{4\pi\epsilon_0}\int_0^\infty \frac{J_0(k\rho)}{\epsilon_{n,c}(k)}dk, \tag{C.28}$$

given that the potential is isotropic in the in-plane direction. The effective dielectric constant at a distance z_t from a point charge in layer c is therefore given by[11]

$$\epsilon(k)_{n,c} = \frac{\epsilon_c}{A_n(k)e^{kz_n} + B_n(k)e^{-kz_n} + \delta_{n,c}}. \tag{C.29}$$

Boundary conditions at the 1^{st} and last layers are also added preventing any unphysical divergence of the electrostatic potential as $z \to \pm\infty$. This is done by setting $B_1 = A_N = 0$. The boundary conditions can be proven to generate a matrix system of equations of the form[11]:

$$M_n \begin{pmatrix} A_{n+1} \\ B_{n+1} \end{pmatrix} = \tilde{M}_n \begin{pmatrix} A_n \\ B_n \end{pmatrix} - \begin{pmatrix} e^{kd_{c-1}} \\ \epsilon_c e^{kd_{c-1}} \end{pmatrix} \delta_{n,c-1} + \begin{pmatrix} e^{-kd_c} \\ -\epsilon_c e^{-kd_c} \end{pmatrix} \delta_{n,c}, \quad \text{(C.30)}$$

where

$$\tilde{M}_n = \begin{pmatrix} e^{kd_n} & e^{-kd_n} \\ \epsilon_n e^{kd_n} & -\epsilon_n e^{-kd_n} \end{pmatrix} \quad \text{and} \quad M_n = \begin{pmatrix} e^{kd_n} & e^{-kd_n} \\ \epsilon_{n+1} e^{kd_n} & -\epsilon_{n+1} e^{-kd_n} \end{pmatrix}. \quad \text{(C.31)}$$

Combining all boundary conditions together, the following equation is obtained relating A_1 and B_N

$$\begin{pmatrix} 0 \\ B_N \end{pmatrix} = M \begin{pmatrix} A_1 \\ 0 \end{pmatrix} - M' \begin{pmatrix} e^{kd_{c-1}} \\ \epsilon_c e^{kd_{c-1}} \end{pmatrix} + M'' \begin{pmatrix} e^{-kd_c} \\ -\epsilon_c e^{-kd_c} \end{pmatrix}, \quad \text{(C.32)}$$

where

$$\begin{aligned} M &= M_N^{-1} \tilde{M}_{N-1} \dots M_1^{-1} \tilde{M}_1, \\ M' &= M_{N-1}^{-1} \tilde{M}_{N-1} \dots M_c^{-1} \tilde{M}_c M_{c-1}^{-1}, \\ M'' &= M_{N-1}^{-1} \tilde{M}_{N-1} \dots M_{c+1}^{-1} \tilde{M}_{c+1} M_c^{-1}. \end{aligned} \quad \text{(C.33)}$$

The previous expression allowed us to obtain the coefficients A_1 and the B_N for a charge in layer c in a very straightforward way, namely

$$\begin{aligned} A_1 &= \frac{(M'_{11} + \epsilon_c M'_{12}) e^{kd_{c-1}} - (M''_{11} - M''_{12}\epsilon_c) e^{-kd_c}}{M_{11}}, \quad \text{and} \quad \text{(C.34)} \\ B_N &= A_1 M_{21} - (M'_{21} e^{kd_{c-1}} + \epsilon_c M'_{22} e^{kd_{c-1}}) + (M''_{21} e^{-kd_c} - \epsilon_c e^{-kd_c} M''_{22}). \end{aligned}$$

The coefficients A_j and B_j for the j^{th} layer can be obtained recursively using Eq. (C.30) to extract (A_{n+1}, B_{n+1}) from every (A_n, B_n).

Bibliography

[1] T.R. Wei et al. “Exceptional plasticity in the bulk single-crystalline van der Waals semiconductor InSe”. In: *Science* 369.6503 (2020), pp. 542–545.

[2] C.H. Ho and Y.J. Chu. “Bending photoluminescence and surface photovoltaic effect on multilayer InSe 2D microplate crystals”. In: *Advanced Optical Materials* 3.12 (2015), pp. 1750–1758.

[3] S. R. Tamalampudi et al. “High performance and bendable few-layered InSe photodetectors with broad spectral response”. In: *Nano letters* 14.5 (2014), pp. 2800–2806.

[4] A. Politano et al. “The influence of chemical reactivity of surface defects on ambient-stable InSe-based nanodevices”. In: *Nanoscale* 8.16 (2016), pp. 8474–8479.

[5] Y. Ma et al. “Engineering a topological phase transition in β-InSe via strain”. In: *New Journal of Physics* 15.7 (2013), p. 073008.

[6] D. Bandurin et al. “High electron mobility, quantum Hall effect and anomalous optical response in atomically thin InSe”. In: *Nature nanotechnology* 12.3 (2017), pp. 223–227.

[7] J. Shang et al. “Tunable electronic and optical properties of InSe/InTe van der Waals heterostructures toward optoelectronic applications”. In: *Journal of Materials Chemistry C* 6.27 (2018), pp. 7201–7206.

[8] Y. Li et al. “Ultrasensitive tunability of the direct bandgap of 2D InSe flakes via strain engineering”. In: *2D Materials* 5.2 (Jan. 2018), p. 021002.

[9] L. Li and M. Wu. “Binary Compound Bilayer and Multilayer with Vertical Polarizations: Two-Dimensional Ferroelectrics, Multiferroics, and Nanogenerators”. In: *ACS Nano* 11.6 (2017), pp. 6382–6388.

[10] A. Budweg et al. “Control of excitonic absorption by thickness variation in few-layer GaSe”. In: *Phys. Rev. B* 100 (4 July 2019), p. 045404.

[11] M. Van der Donck and F. M. Peeters. “Interlayer excitons in transition metal dichalcogenide heterostructures”. In: *Phys. Rev. B* 98 (11 Sept. 2018), p. 115104.

[12] L. Cavalcante et al. “Electrostatics of electron-hole interactions in van der Waals heterostructures”. In: *Physical Review B* 97.12 (2018), p. 125427.

[13] K. Novoselov et al. “2D materials and van der Waals heterostructures”. In: *Science* 353.6298 (2016).

[14] A.K. Geim and I.V. Grigorieva. “Van der Waals heterostructures”. In: *Nature* 499.7459 (2013), pp. 419–425.

[15] M.J. Hamer et al. “Indirect to Direct Gap Crossover in Two-Dimensional InSe Revealed by Angle-Resolved Photoemission Spectroscopy”. In: *ACS Nano* 13.2 (2019), pp. 2136–2142.

[16] D. J. Terry et al. “Infrared-to-violet tunable optical activity in atomic films of GaSe, InSe, and their heterostructures”. In: *2D Materials* 5.4 (Sept. 2018), p. 41009.

[17] C. Song et al. “Largely tunable band structures of few-layer InSe by uniaxial strain”. In: *ACS applied materials & interfaces* 10.4 (2018), pp. 3994–4000.

[18] D. Shcherbakov et al. “Layer-and gate-tunable spin-orbit coupling in a high-mobility few-layer semiconductor”. In: *Science Advances* 7.5 (2021), eabe2892.

[19] S.V. Eremeev et al. “Insight into the electronic structure of semiconducting $\epsilon-$GaSe and $\epsilon-$InSe”. In: *Phys. Rev. Materials* 4 (8 Aug. 2020), p. 084603.

[20] S.R. Tamalampudi et al. “High performance and bendable few-layered InSe photodetectors with broad spectral response”. In: *Nano letters* 14.5 (2014), pp. 2800–2806.

[21] C.H. Ho and Y.J. Chu. “Bending photoluminescence and surface photovoltaic effect on multilayer InSe 2D microplate crystals”. In: *Advanced Optical Materials* 3.12 (2015), pp. 1750–1758.

[22] J. Zultak et al. “Ultra-thin van der Waals crystals as semiconductor quantum wells”. In: *Nature Communications* 11 (Jan. 2020), p. 125.

[23] S.J. Magorrian et al. “Hybrid $\mathbf{k} \cdot \mathbf{p}$ tight-binding model for intersubband optics in atomically thin InSe films”. In: *Phys. Rev. B* 97 (16 Apr. 2018), p. 165304.

[24] Z. Kudrynskyi et al. “Resonant tunnelling into the two-dimensional subbands of InSe layers”. In: *Communications Physics* 3 (Jan. 2020), p. 16.

[25] T. Cao, Z. Li, and S. G. Louie. “Tunable Magnetism and Half-Metallicity in Hole-Doped Monolayer GaSe”. In: *Phys. Rev. Lett.* 114 (23 June 2015), p. 236602.

[26] A.V. Lugovskoi, M.I. Katsnelson, and A.N. Rudenko. “Strong Electron-Phonon Coupling and its Influence on the Transport and Optical Properties of Hole-Doped Single-Layer InSe”. In: *Phys. Rev. Lett.* 123 (17 Sept. 2019), p. 176401.

[27] T. Shubina et al. “InSe as a case between 3D and 2D layered crystals for excitons”. In: *Nature communications* 10.1 (2019), pp. 1–8.

[28] N. Ubrig et al. “Design of van der Waals interfaces for broad-spectrum optoelectronics”. In: *Nature Materials* 19 (Mar. 2020), pp. 1–6.

[29] S.J. Magorrian, V. Zólyomi, and V.I. Fal’ko. “Electronic and optical properties of two-dimensional InSe from a DFT-parametrized tight-binding model”. In: *Phys. Rev. B* 94 (24 Dec. 2016), p. 245431.

[30] S.J. Magorrian, V. Zólyomi, and V.I. Fal’ko. “Spin-orbit coupling, optical transitions, and spin pumping in monolayer and few-layer InSe”. In: *Phys. Rev. B* 96 (19 Nov. 2017), p. 195428.

[31] A. Kormányos et al. “Monolayer MoS_2: Trigonal warping, the Γ valley, and spin-orbit coupling effects”. In: *Phys. Rev. B* 88 (4 July 2013), p. 45416.

[32] G.B. Liu et al. “Electronic structures and theoretical modelling of two-dimensional group-VIB transition metal dichalcogenides”. In: *Chemical Society Reviews* 44.9 (2015), pp. 2643–2663.

[33] D. Kochan, S. Irmer, and J. Fabian. "Model spin-orbit coupling Hamiltonians for graphene systems". In: *Phys. Rev. B* 95 (16 Apr. 2017), p. 165415.

[34] J. Srour et al. "Comparative study of structural and electronic properties of GaSe and InSe polytypes". In: *The Journal of chemical physics* 149.5 (2018), p. 054106.

[35] M. Zhou et al. "Multiband $\mathbf{k} \cdot \mathbf{p}$ theory of monolayer XSe (X = In, Ga)". In: *Phys. Rev. B* 96 (15 Oct. 2017), p. 155430.

[36] M. Arzakantsyan et al. "Growth of large 90 mm diameter Yb:YAG single crystals with Bagdasarov method". In: *Opt. Mater. Express* 2.9 (Sept. 2012), pp. 1219–1225.

[37] P. W. Bridgman. "Certain Physical Properties of Single Crystals of Tungsten, Antimony, Bismuth, Tellurium, Cadmium, Zinc, and Tin". In: *Proceedings of the American Academy of Arts and Sciences* 60.6 (1925), pp. 305–383.

[38] K. J. Xiao, A. Carvalho, and A. H. Castro Neto. "Defects and oxidation resilience in InSe". In: *Phys. Rev. B* 96 (5 Aug. 2017), p. 054112.

[39] D.G. Hopkinson et al. "Formation and healing of defects in atomically thin GaSe and InSe". In: *ACS nano* 13.5 (2019), pp. 5112–5123.

[40] A.S. Kumar et al. "Interfacial Charge Transfer and Gate-Induced Hysteresis in Monochalcogenide InSe/GaSe Heterostructures". In: *ACS Applied Materials & Interfaces* 12.41 (2020), pp. 46854–46861.

[41] H. Pathan et al. "Preparation and characterization of indium selenide thin films from a chemical route". In: *Materials Chemistry and Physics* 93.1 (2005), pp. 16–20.

[42] P. Li and I. Appelbaum. "Symmetry, distorted band structure, and spin-orbit coupling of group-III metal-monochalcogenide monolayers". In: *Phys. Rev. B* 92 (19 Nov. 2015), p. 195129.

[43] P.A.M. Dirac. *The principles of quantum mechanics*. 27. Oxford university press, 1981.

[44] Z. Ben Aziza et al. "Valence band inversion and spin-orbit effects in the electronic structure of monolayer GaSe". In: *Phys. Rev. B* 98 (11 Sept. 2018), p. 115405.

[45] S. J. Magorrian, V. Zólyomi, and V. I. Fal'ko. "Erratum: Electronic and optical properties of two-dimensional InSe from a DFT-parametrized tight-binding model [Phys. Rev. B 94, 245431 (2016)]". In: *Phys. Rev. B* 96 (7 Aug. 2017), p. 079905.

[46] M. Dresselhaus. "Solid state physics part ii optical properties of solids". In: *Lecture Notes (Massachusetts Institute of Technology, Cambridge, MA)* 17 (2001), pp. 15–16.

[47] M. Willatzen and L. Lew Yan Voon. *The kp method: electronic properties of semiconductors*. Springer Science & Business Media, 2009.

[48] G.L. Bir and G.E. Pikus. "Symmetry and strain-induced effects in semiconductors". In: 1974.

[49] M. Zhou et al. "Spin-charge conversion in InSe bilayers". In: *Phys. Rev. B* 99 (15 Apr. 2019), p. 155402.

[50] J.C. Rojas Sánchez et al. In: *Nature communications* 4 (Dec. 2013), p. 2944.

[51] M. Zhou et al. "Current-induced spin polarization in monolayer InSe". In: *Phys. Rev. B* 100 (24 Dec. 2019), p. 245409.

[52] V.M. Edelstein. "Spin polarization of conduction electrons induced by electric current in two-dimensional asymmetric electron systems". In: *Solid State Communications* 73.3 (Jan. 1990), pp. 233–235.

[53] T. Kotani, M. van Schilfgaarde, and S.V. Faleev. "Quasiparticle self-consistent *GW* method: A basis for the independent-particle approximation". In: *Phys. Rev. B* 76 (16 Oct. 2007), p. 165106.

[54] D. Pashov et al. "Questaal: A package of electronic structure methods based on the linear muffin-tin orbital technique". In: *Computer Physics Communications* 249 (2020), p. 107065.

[55] G. Allwright and D.M. Jacobs. "Robin Boundary Conditions Are Generic in Quantum Mechanics". In: *arXiv: Quantum Physics* (2016).

[56] T. Berkelbach, M. Hybertsen, and D. Reichman. "Bright and dark singlet excitons via linear and two-photon spectroscopy in monolayer transition-metal dichalcogenides". In: *Phys. Rev. B* 92 (8 Aug. 2015), p. 085413.

[57] Z. Devizorova and V. Volkov. "Spin splitting of two-dimensional states in the conduction band of asymmetric heterostructures: Contribution from the atomically sharp interface". In: *Soviet Journal of Experimental and Theoretical Physics Letters* 98 (Sept. 2013), pp. 101–106.

[58] Z. Devizorova et al. "Interface contributions to the spin-orbit interaction parameters of electrons at the (001) GaAs/AlGaAs interface". In: *JETP letters* 100.2 (2014), pp. 102–109.

[59] J.R. Schrieffer and P.A. Wolff. "Relation between the Anderson and Kondo Hamiltonians". In: *Physical Review* 149.2 (Sept. 1966), pp. 491–492.

[60] P.O Löwdin. "Partitioning technique, perturbation theory, and rational approximations". In: *International Journal of Quantum Chemistry* 21.1 (1982), pp. 69–92.

[61] P. Löwdin. "A Note on the Quantum-Mechanical Perturbation Theory". In: *Journal of Chemical Physics* 19 (1951), pp. 1396–1401.

[62] A. Ceferino et al. *Tunable spin-orbit coupling in two-dimensional InSe*. 2021. arXiv: `2106.04719 [cond-mat.mes-hall]`.

[63] L.V. Keldysh. "Coulomb interaction in thin semiconductor and semimetal films". In: *ZhETF Pisma Redaktsiiu* 29 (June 1979), p. 716.

[64] A. Ceferino et al. "Crossover from weakly indirect to direct excitons in atomically thin films of InSe". In: *Phys. Rev. B* 101 (24 June 2020), p. 245432.

[65] J.Z Zhang and J.Z Ma. "Two-dimensional excitons in monolayer transition metal dichalcogenides from simple models and variational calculations". In: *arXiv preprint arXiv:1809.00843* (2018).

[66] M. Fogler, L Butov, and K Novoselov. “High-temperature superfluidity with indirect excitons in van der Waals heterostructures”. In: *Nature communications* 5 (July 2014), p. 4555.

[67] V. Cheianov, B. Altshuler, and V.I. Falko. In: *Science* 315.5816 (Mar. 2007), pp. 1252–1255.

[68] A. Patel et al. “Classical and quantum magneto-oscillations of current flow near a *p-n* junction in graphene”. In: *Phys. Rev. B* 86 (8 Aug. 2012), p. 081413.

[69] M.V. Berry. “Quantal phase factors accompanying adiabatic changes”. In: *Proceedings of the Royal Society of London. A. Mathematical and Physical Sciences* 392.1802 (1984), pp. 45–57.

[70] P. Gosselin et al. “Semiclassical dynamics of electrons in magnetic Bloch bands: A Hamiltonian approach”. In: *Europhysics Letters (EPL)* 76.4 (Nov. 2006), pp. 651–656.

[71] N. Davies et al. “Skipping and snake orbits of electrons: singularities and catastrophes”. In: *Physical Review B* 85.15 (2012), p. 155433.

[72] A. Berdyugin et al. “Minibands in twisted bilayer graphene probed by magnetic focusing”. In: *Science Advances* 6.16 (2020), eaay7838.

[73] E. McCann. “Asymmetry gap in the electronic band structure of bilayer graphene”. In: *Phys. Rev. B* 74 (16 Oct. 2006), p. 161403.

[74] E. Castro et al. “Electronic properties of a biased graphene bilayer”. In: *Journal of physics. Condensed matter : an Institute of Physics journal* 22 (May 2010), p. 175503.

[75] M. Fogler and E. McCann. “Comment on “Screening in gated bilayer graphene””. In: *Phys. Rev. B* 82 (19 Nov. 2010), p. 197401.

[76] E. Castro et al. “Biased Bilayer Graphene: Semiconductor with a Gap Tunable by the Electric Field Effect”. In: *Phys. Rev. Lett.* 99 (21 Nov. 2007), p. 216802.

[77] H. Min et al. “Ab initio theory of gate induced gaps in graphene bilayers”. In: *Phys. Rev. B* 75 (15 Apr. 2007), p. 155115.

[78] X.Z. Yan and C. S. Ting. “Weak Localization of Dirac Fermions in Graphene”. In: *Phys. Rev. Lett.* 101 (12 Sept. 2008), p. 126801.

[79] H.Z. Lu, J. Shi, and S.Q. Shen. “Competition between Weak Localization and Antilocalization in Topological Surface States”. In: *Phys. Rev. Lett.* 107 (7 Aug. 2011), p. 076801.

[80] S.V. Iordanskii, Yu. B. Lyanda-Geller, and G.E. Pikus. “Weak localization in quantum wells with spin-orbit interaction”. In: *ZhETF Pisma Redaktsiiu* 60 (Aug. 1994), p. 199.

[81] M. Nestoklon, N. Averkiev, and S. Tarasenko. “Weak localization of two-dimensional Dirac fermions beyond the diffusion regime”. In: *Solid state communications* 151.21 (2011), pp. 1550–1553.

[82] E. McCann and V.I. Fal’ko. “$z \to -z$ Symmetry of Spin-Orbit Coupling and Weak Localization in Graphene”. In: *Phys. Rev. Lett.* 108 (16 Apr. 2012), p. 166606.

[83] S. Hikami, A. I. Larkin, and Y. Nagaoka. “Spin-orbit interaction and magnetoresistance in the two dimensional random system”. In: *Progress of Theoretical Physics* 63.2 (1980), pp. 707–710.

[84] Y. Yafet. “g Factors and Spin-Lattice Relaxation of Conduction Electrons”. In: *Journal of Physics C: Solid State Physics* 14 (1963), pp. 1–98.

[85] M. Dyakonov and V. Kachorovskii. “Spin relaxation of two-dimensional electrons in noncentrosymmetric semiconductors”. In: 20 (Jan. 1986), p. 110.

[86] W. Knap et al. “Weak antilocalization and spin precession in quantum wells”. In: *Physical Review B* 53.7 (1996), p. 3912.

[87] B. Altshuler et al. “Magnetoresistance and Hall effect in a disordered two-dimensional electron gas”. In: *Phys. Rev. B* 22 (11 Dec. 1980), pp. 5142–5153.

[88] L.E. Golub. "Weak antilocalization in high-mobility two-dimensional systems". In: *Phys. Rev. B* 71 (23 June 2005), p. 235310.

[89] D. Parfitt and M. Portnoi. "The two-dimensional hydrogen atom revisited". In: *Journal of Mathematical Physics* 43.10 (2002), pp. 4681–4691.

[90] P. Rivera et al. "Observation of long-lived interlayer excitons in monolayer $MoSe_1$-WSe_2 heterostructures". In: *Nature communications* 6.1 (2015), pp. 1–6.

[91] J. Ross et al. "Electrical control of neutral and charged excitons in a monolayer semiconductor". In: *Nature communications* 4 (Feb. 2013), p. 1474.

[92] I. S. Gradshteyn and I. M. Ryzhik. *Table of integrals, series, and products*. Seventh edition. Elsevier/Academic Press, Amsterdam, 2007.